

CHEMIA

STUDIA UNIVERSITATIS BABEȘ-BOLYAI CHEMIA

4/2024

ISSN (print): 1224-7154;
ISSN (online): 2065-9520; ISSN-L: 2065-9520

© STUDIA UBB CHEMIA

Published by Babeș-Bolyai University

EDITORIAL BOARD OF STUDIA UNIVERSITATIS BABEȘ-BOLYAI CHEMIA

ONORARY EDITOR:

IONEL HAIDUC – Member of the Romanian Academy

EDITOR-IN-CHIEF:

LUMINIȚA SILAGHI-DUMITRESCU

EXECUTIVE EDITOR:

CASTELIA CRISTEA

ASSOCIATE EDITOR:

ALEXANDRU LUPAN

EDITORIAL BOARD:

PAUL ȘERBAN AGACHI, Babeș-Bolyai University, Cluj-Napoca, Romania

LIVAIN BREAU, UQAM University of Quebec, Montreal, Canada

HANS JOACHIM BREUNIG, Institute of Inorganic and Physical Chemistry,
University of Bremen, Bremen, Germany

JEAN ESCUDIE, HFA, Paul Sabatier University, Toulouse, France

ION GROSU, Babeș-Bolyai University, Cluj-Napoca, Romania

EVAMARIE HEY-HAWKINS, University of Leipzig, Leipzig, Germany

FLORIN DAN IRIMIE, Babeș-Bolyai University, Cluj-Napoca, Romania

FERENC KILAR, University of Pecs, Pecs, Hungary

BRUCE KING, University of Georgia, Athens, Georgia, USA

ANTONIO LAGUNA, Department of Inorganic Chemistry, ICMA, University of
Zaragoza, Zaragoza, Spain

JURGEN LIEBSCHER, Humboldt University, Berlin, Germany

KIERAN MOLLOY, University of Bath, Bath, UK

IONEL CĂȚĂLIN POPESCU, Babeș-Bolyai University, Cluj-Napoca,
Romania

CRISTIAN SILVESTRU, Babeș-Bolyai University, Cluj-Napoca, Romania

YEAR
MONTH
ISSUE

Volume 69 (LXIX) 2024
December
4

PUBLISHED ONLINE: 2024-12-18
PUBLISHED PRINT: 2024-12-30
ISSUE DOI: [10.24193/subbchem.2024.4](https://doi.org/10.24193/subbchem.2024.4)

S T U D I A

UNIVERSITATIS BABEȘ–BOLYAI

CHEMIA

4

CONTENT/ SOMMAIRE/ INHALT/ CUPRINS

- Sorina MOLDOVAN, Marieta MUREȘAN-POP, Claudia Andreea COJAN, Réka BARÁBAS, Liliana BIZO, Vickers Microhardness and Structural Evaluation of Experimental Dental Porcelain with Zirconia Addition..... 7
- Chahinaz ZOUBEIDI, Ali OURARI, Elhafnaoui LANEZ, Touhami LANEZ, Electrochemical Characterization And DNA Interaction Studies of a Novel Copper Schiff Base Complex: Insights from Cyclic Voltammetry and Molecular Docking 21
- Xi LI, Yanwen CHEN, Hong LI, Jiahao DING, Ya WANG, Jin MO, Mi ZHOU, Yaning LI, Qiuhan LIN, Boliang WANG, Fabricating and Properties of Rifampicin-Loaded Ethyl Cellulose Composites Via Electrospray..... 37
- Issiaka SANOU, Saada ZOUNGRANA, Moussa OUEDRAOGO, Ali SANOU, Younoussa MILLOGO, Evaluation of the Pozzolan Activity of Metakaolin, Glass Powder and Silica Powder for use in Cementitious Mortars..... 49

Emőke Margit RÉDAI, Orsolya PÉTERFI, Robert Alexandru VLAD, Paula ANTONOAEA, Nicoleta TODORAN, Adriana CIURBA, Ibolya FÜLÖP, Enikő BARABÁS, Emese SIPOS, Formulation and Evaluation of Antifungal Miconazole Nitrate Medicated Soap	67
Melinda-Emese LÁSZLÓ, Matild PAP, Gabriel KATONA, Electrospinning as Tool for Enzyme Immobilization	85
Ana-Elena CHIRALI, Iulia Maria CIOCOTIȘAN, Ana-Maria VLASE, Dana Maria MUNTEAN, Laurian VLASE, Insights into Clozapine's Kinetic Interactions: Enzymatic Inhibition of CYP1A2 by Ciprofloxacin and Norfloxacin	99
İbrahim Seyda URAS, Murat KÜRŞAT, Belma KONUKLUGIL, Murat ŞENTÜRK, Effects Of Some Turkish Plant Extracts On Carbonic Anhydrase and Cholinesterase Enzymes	115
Milan MITIĆ, Vesna STANKOV-JOVANOVIĆ, Jelena MITIĆ, Jelena NIKOLIĆ, Anastasia KARIOTI Diamanto LAZAR, Chemometric Insights Into Grape Stems: Antioxidant Capacity, Phenolic Composition, and Mineral Profile	129
Adrian PATRUT, Laszlo RAKOSY, Karl F. VON REDEN, Radiocarbon Dating of the Historic Derby Boab Tree from Derby, Kimberley, Australia	145
Roxana MITROI, Cristina Ileana COVALIU-MIERLĂ, Cristina-Emanuela ENĂȘCUȚĂ, Grigore PSHENOVSCHIB, Iuliana DELEANU, Valuation of the Energy Potential of Agrozootehnic Waste	159
Cerasella INDOLEAN, Silvia BURCĂ, Biosorption Of Cu (II) Ions Using Residual Tomato Pomace Biomass. A Study of Isotherms and Kinetics	171
Maria CODREANU, Diana IACOB, Maria Ioana ONOFREI, Ana-Maria VLASE, Dana Maria MUNTEAN, Laurian VLASE, <i>In Vitro – In Vivo</i> Correlation of Pentoxifylline: a Comprehensive Kinetic Analysis.....	191

Studia Universitatis Babes-Bolyai Chemia has been selected for coverage in Thomson Reuters products and custom information services. Beginning with V. 53 (1) 2008, this publication is indexed and abstracted in the following:

- Science Citation Index Expanded (also known as SciSearch®)
- Chemistry Citation Index®
- Journal Citation Reports/Science Edition

VICKERS MICROHARDNESS AND STRUCTURAL EVALUATION OF EXPERIMENTAL DENTAL PORCELAIN WITH ZIRCONIA ADDITION

Sorina MOLDOVAN^a, Marieta MUREȘAN-POP^{b,c},
Claudia Andreea COJAN^a, Réka BARÁBAS^{d,e},
Liliana BIZO^{a,e,*}

ABSTRACT. This work aimed to investigate the effect of ZrO₂ addition on the structural and mechanical properties of an experimental dental porcelain (DP) prepared from natural raw materials. ZrO₂ was added in different amounts (1, 3, and 5 wt.%) to the DP mass with the initial composition of 80 wt.% feldspar, 15 wt.% quartz, and 5 wt.% kaolin, obtained by sintering the mixture at 1200 °C. The raw materials and raw materials mixture were analyzed by laser diffraction to obtain the typical particle size distribution (PSD). Subsequently, the obtained phases in the elaborated samples were investigated by X-ray powder diffraction (XRPD), Fourier transform infrared spectroscopy (FTIR), differential scanning calorimetry (DSC) and microhardness tests. The structural analyses revealed that the obtained DP mainly comprised quartz and amorphous phases. In addition, certain peaks of weak corresponding to mullite and zirconia were detected. The measured Vickers microhardness (VMH) of DP sintered at 1200 °C was 794.07±106.56 kgf/mm², which is comparable with those reported for conventional porcelains. Moreover, ZrO₂ addition leads to an overall increase of

^a Babeș-Bolyai University, Faculty of Chemistry and Chemical Engineering, Department of Chemical Engineering, 11 Arany Janos str., RO-400028, Cluj-Napoca, Romania

^b Interdisciplinary Research Institute on Bio-Nano-Sciences, Babeș-Bolyai University, 42 Treboniu Laurian str., RO-400271, Cluj-Napoca, Romania

^c Babeș-Bolyai University, INSPIRE Research Platform, 11 Arany Janos str., RO-400028, Cluj-Napoca, Romania

^d Babeș-Bolyai University, Faculty of Chemistry and Chemical Engineering, Department of Chemistry and Chemical Engineering of Hungarian Line of Study, 11 Arany Janos str., RO-400028, Cluj-Napoca, Romania

^e Babeș-Bolyai University, Institute for Research, Development and Innovation in Applied Natural Sciences, 30 Fântânele str., RO-400327, Cluj-Napoca, Romania

* Corresponding author: liliana.bizo@ubbcluj.ro



the VMH, with the best value of 912.91 ± 30.76 kgf/mm² obtained for the sample with 5 wt.% ZrO₂. In conclusion, the DP studied here exhibits good mechanical properties and could be potentially used in restorative dentistry.

Keywords: dental porcelain, zirconia, structural analyses, Vickers microhardness

INTRODUCTION

Besides many dental materials, porcelain continues to play a significant role in restorative dentistry. The most common applications include teeth full coverage as crowns, inlays and onlay porcelain bridges, veneering agents, castable ceramics, and porcelain fused to metal. Dental porcelain has very stable chemical properties and outstanding esthetics which are not influenced by their use over time. It has similar thermal conductivity and coefficient of thermal expansion to enamel and dentine and exhibits high compressive strength [1].

A classification of dental porcelains could be made based on their composition, fusion temperature, microstructure, translucency, fracture resistance, abrasiveness, and processing technique [2, 3]. The classification of dental porcelain based on composition includes feldspathic porcelains, leucite-reinforced feldspathic porcelain, leucite-reinforced glass ceramics, aluminous ceramics, glass infiltrated composites, alumina polycrystals, glass ceramics, lithium disilicate reinforced glass ceramics and zirconium oxide ceramics [4]. According to their fusion temperature, porcelains are classified into three categories namely high (1300-1400 °C), medium (1100-1300 °C), and low (850-1100 °C) fusing dental porcelains [4, 5]. The high-fusing dental porcelains are used for denture teeth, whereas the medium and low-fusing porcelain are used for crowns and bridges.

The composition of typical feldspathic dental porcelain (DP) by weight is feldspar (75 - 85%), quartz (12 - 22%), kaolin (3 - 5%) and metallic pigments which increase the opacity of dental porcelain (<1 %), including significant amount of feldspar (KAlSi₃O₈), quartz (SiO₂), and kaolin (Al₂O₃·2SiO₂·2H₂O). Feldspar, a greyish crystalline mineral found in rocks rich with iron and mica, is grounded, and after using strong magnets to remove iron compounds, it is milled to obtain the purest powder. Quartz, the matrix component is responsible for the translucency of the restoration, whereas kaolin is used in a limited amount as it has opaque properties, unlike the human teeth which are translucent. It is used in the composition of dental ceramics as it binds the loosely held ceramic particles together [6-9]. The main difference in composition between porcelain used in dentistry and that used in other products (*i.e.* dishes and china houseware) is in the proportions of the main raw materials [6]. The

exact compositions of dental porcelains differ between various products, but in general, there is a trend towards using less kaolin and more feldspar to improve translucency. This suggests that dental porcelain should be described more accurately as glasses. Compositions with low kaolin content require closely controlled firing times and temperatures to produce a satisfactory result due to the large glassy phases they develop [10].

Many attempts have been made to study the addition of different materials like metal oxides (MgO, ZnO, TiO₂ and ZrO₂) or AgVO₃ to DP powders to improve resistance to thermal shock, color, mechanical or antibacterial properties [1, 11-15]. Regarding the mechanical properties, one problem with the use of ceramics in tooth replacement is the fact that fracture occurs at a very low strain of ~ 0.1%, which means that the ceramic structure only exhibits a very low flexibility before fracture [16, 17]. Therefore, the mechanical behavior of dental porcelains still needs to be improved, and consequently, a lot of researchers are trying to develop the mechanical properties of ceramics. Some attempts have been made to overcome these shortcomings.

The research of Kaiyum et al. indicates that the MgO addition in a dental ceramic composition (70 wt.% feldspar, 20 wt.% quartz, and 10 wt.% kaolin) increases mechanical properties up to 1%, and indicates a fixed sintering temperature of 1100 °C. They conclude that MgO has great effects on grain growth, second-phase formation, and densification, which are the key factors that improve mechanical properties [18].

The effect of TiO₂ additions on the densification and mechanical properties of multifunction-resistant (MFR) porcelain prepared from economic raw materials was studied by Harabi et al. The chosen composition was 30 wt.% kaolins (20 wt.% kaolin halloysite type + 10 wt.% kaolin Tamazart), 45 wt.% k-feldspar and 25 wt.% quartz [19]. It has been found that the best three-point flexural strength (3PFS) and Vickers micro-hardness (VMH) values may recommend the use of multifunction-resistant porcelains for dental porcelains and abrasive materials. The best VMH value (12.30 GPa) achieved for the new MFR porcelain is nearly doubled when compared to that obtained by Santos et al. for porcelain-30% ZrO₂ composite (6.5 GPa) [20].

The influence of temperature and boric oxide (B₂O₃) addition on sintering and mechanical properties of dental porcelain prepared by using local Algerian raw materials was studied for the composition of 75 wt.% feldspar, 20 wt.% quartz and 5 wt.% kaolin [6]. It has been found that the sintering temperature was lowered by about 25 and 50 °C for 3 and 5 wt.% B₂O₃ additions, respectively. Moreover, the authors stated that B₂O₃ additions induce a glass matrix composition variation which hindered the leucite formation during sintering, knowing that the leucite is the most significant phase especially when mechanical properties of dental porcelain are concerned [6].

Serragdj et al. have studied the effect of ZrO_2 additions on the densification and mechanical properties of modified resistant porcelains using economic raw materials [21]. The selected composition was 25 wt.% feldspar, 25 wt.% quartz, and 50 wt.% kaolin (25 wt.% kaolin Algerian nano-sized halloysite type + 25 wt.% kaolin Tamazart) and different amounts of ZrO_2 (5 and 8 wt.%). The authors found that the best VMH value of 13.08 GPa obtained for DP is higher than that found by other researchers for porcelain sample or porcelain containing 30 wt.% Al_2O_3 sintered at 1200 °C.

Briefly, many attempts have been made to increase the mechanical properties of dental ceramics by adding different metal oxide particles like MgO, TiO_2 , B_2O_3 or ZnO. Apart from them, ZrO_2 -reinforced glass-ceramic showed the improvement of the flexural strength and fracture toughness [20]. Although different dental porcelain compositions have been extensively studied, there are few investigations on the influence of zirconium oxide additive on the processing, structural and mechanical properties (*i.e.* microhardness). The novelty and major contribution of this study lies in its exploration of the synergistic properties of kaolin, quartz, feldspar and their tailored applications across various sectors, besides the biomedical domain occupy an important place. On the other hand, the novelty of this study arises from the newly developed composition considering two abundantly available and cheaper local raw materials, like quartz (Văleni, Romania) and feldspar (Muntele Rece, Romania). The chosen composition for DP in this work was 80 wt.% feldspar, 15 wt.% quartz, and 5 wt.% kaolin, using economic raw materials [10, 22]. Considering the important role played by zirconia particles in improvement of mechanical properties of dental porcelain this work aims to study the effect of ZrO_2 additions on the structural and mechanical properties of experimental feldspathic dental porcelain prepared from natural raw materials, as zirconia-reinforced porcelain represents a promising alternative to conventional feldspathic porcelains for the fabrication of prosthetic restorations.

RESULTS AND DISCUSSION

The PSD of the granules is of particular interest, fine particles will react completely while large particles will only partially react, and only a part of them will end up participating in the reaction. It is well known that particle size distribution (PSD) of powders affects the sintering behavior, physical and mechanical properties of ceramic materials. Therefore, the results of the granulometric analyses are presented below. Both the raw materials and raw materials mixture after wet homogenization were analyzed using laser diffraction with the results presented in **Table 1** and **Figure 1**. The results of PSD analyses are summarized in **Table 1**, where the modal and median diameters, defined for the cumulative distribution, are also shown.

Table 1. The results of PSD analyses performed on raw materials and raw materials mixture.

Sample	Modal D (μm)	Median D (μm)	Mean V (μm)	50.0% D (μm)	Standard Deviation (SD)
Feldspar	0.224	0.222	0.305	0.222	0.305
Kaolin	0.178	0.171	0.209	0.171	0.171
Quartz	0.708	1.227	1.545	1.227	2.589
Raw materials mixture	0.708	1.169	1.399	1.169	0.395

The results presented in **Figure 1a** showed that kaolin and feldspar show a bimodal distribution presenting two maximum points, which are centered at around 0.15 - 0.2 μm , respectively 0.8 μm , whereas the quartz shows a wide distribution with fractions ranged from 0.1 to 50 μm . The raw materials mixture has a wide and monomodal PSD, with an average particle value of 1.399 μm with particle sizes of the powder falling in a wide size range between 0.3 and 10 μm (**Figure 1b**). This specifies that width of the PSD offers good mixing and uniform distribution between the particles.

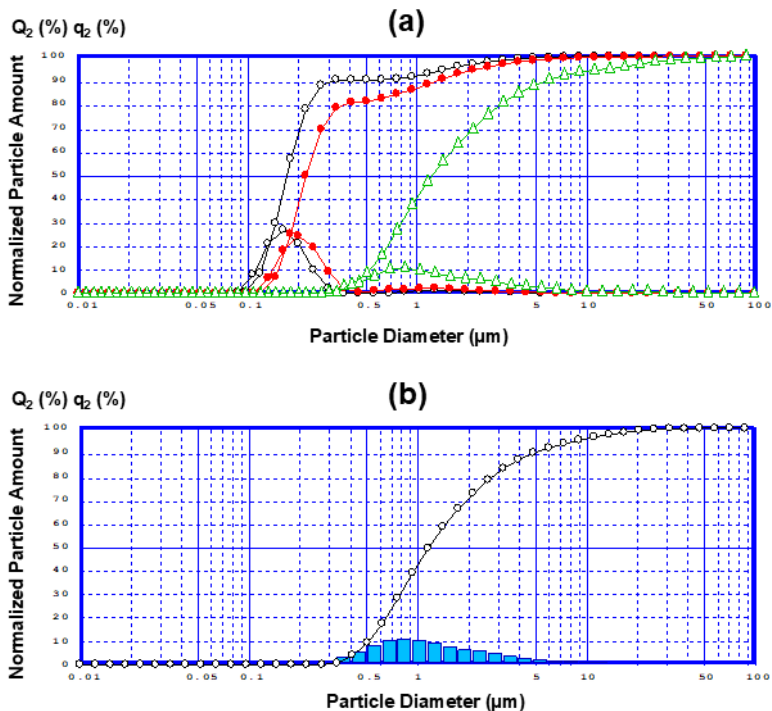


Figure 1. PSD (cumulative and differential curves) for (a) kaolin (black), feldspar (red), quartz (green), and (b) raw materials mixture.

All the prepared samples were analyzed using XRPD. The corresponding diffractograms of the samples DP0 and those with 1%, 3%, and 5% ZrO₂ additions are presented comparatively in **Figure 2**. The presence of quartz (Q) is observed as the main phase in all the analyzed spectra (PDF # 96-901-0145). The evidenced diffraction peaks belong to its β form resulted after the high temperature sintering.

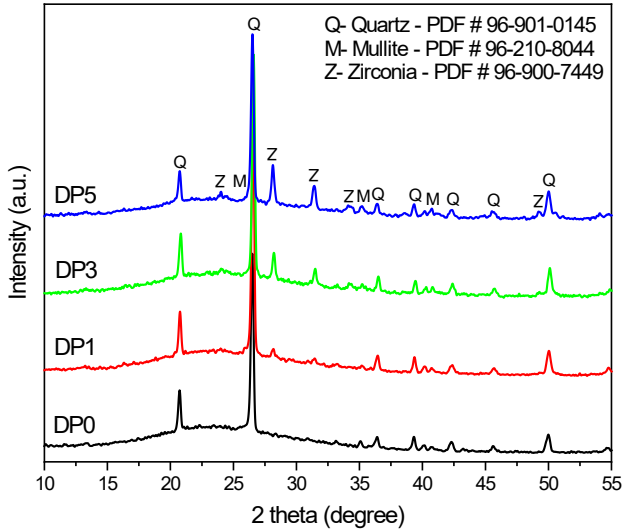


Figure 2. XRPD patterns of DP samples sintered at 1200 °C.

The intensities of the diffraction peaks of quartz did not change in the DP samples with ZrO₂, but a new phase was identified as zirconium oxide (Z; PDF # 96-900-7449). The intensity of the peaks corresponding to ZrO₂ increases with the increase of the percentage of ZrO₂. ZrO₂ leads to an increase in the intensity of the maxima presented at $2\theta \sim 24, 28.2, \text{ and } 31.5$, which belongs to baddeleyite. Certain peaks of weak intensity were identified as corresponding to mullite (M, Al₆Si₂O₁₃; PDF# 96-210-8044). It is known that mullite is responsible for the DP microstructure and mechanical properties. Therefore, the formation of mullite mainly depends on the type and proportion of kaolin used [23]. There is a competition effect between the formation of mullite and the crystallization of the amorphous silica present in the matrix during sintering. Besides, the fraction and nature of the quartz used in the porcelain composition batch influences the amount of unreacted residual quartz during sintering. Quartz has a higher coefficient of thermal expansion as compared to that of the surrounding glassy phase. Therefore, it gives rise to thermal stresses

which affect the porcelain strength [24, 25]. In addition, at this sintering temperature the feldspar melted and its diffractogram presented a large band related to the amorphous phase, as revealed in the XRPD patterns [14].

The FTIR spectra obtained for all samples appear to be almost similar (**Figure 3**). In the spectra of DP0, the broad absorption peak with a maximum of around 3449 cm^{-1} is assigned to the stretching modes of O–H bond vibrations, which is related to surface absorbed water, whereas the broad absorption band around 1624 cm^{-1} is assigned to H–O–H bending vibrations related to the surface chemically adsorbed water [26, 27]. In the spectra of DP1, DP3, and DP5 this vibration is located at 1630 and respectively at 1626 cm^{-1} .

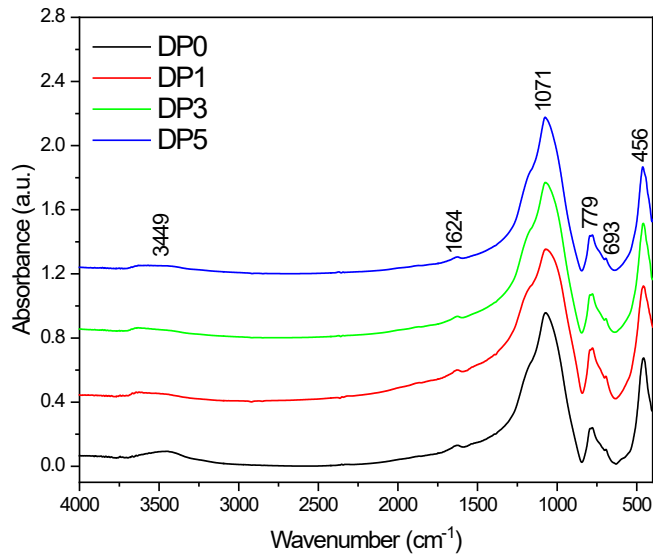


Figure 3. FTIR spectra of DP samples.

In function of the composition of the samples, the region of great interest is in the spectral range between $1400\text{--}845\text{ cm}^{-1}$, which is the specific region for the bands corresponding to the vibration of the bonds in SiO_2 . The maximum of the dominant bands identified in the FTIR spectra of DP is situated around 1624 , 1071 , 779 , 693 , and 456 cm^{-1} . The band located around 1071 cm^{-1} could be attributed to asymmetric stretching vibrations of Si–O–Si bridges in amorphous SiO_2 while the absorption peak around 779 cm^{-1} is ascribed to symmetric stretching vibrations of the same bonds [27–29]. These vibrations are also found in the spectra obtained for the three samples, DP1, DP3, and DP5, but with small shifts. Our results agree with the results previously reported, which identified absorption bands ranging from 400 to 1400 cm^{-1}

associated with the quartz bending band [6, 30]. In the spectral range $1400\text{--}845\text{ cm}^{-1}$ there are changes in FWHM, which compared to the value obtained for sample DP, increases in DP1, but decreases in DP3 and DP5.

DSC was used to investigate the thermal stability and behavior of the prepared DP. The results of the DSC analyses for the investigated samples are presented in **Figure 4**.

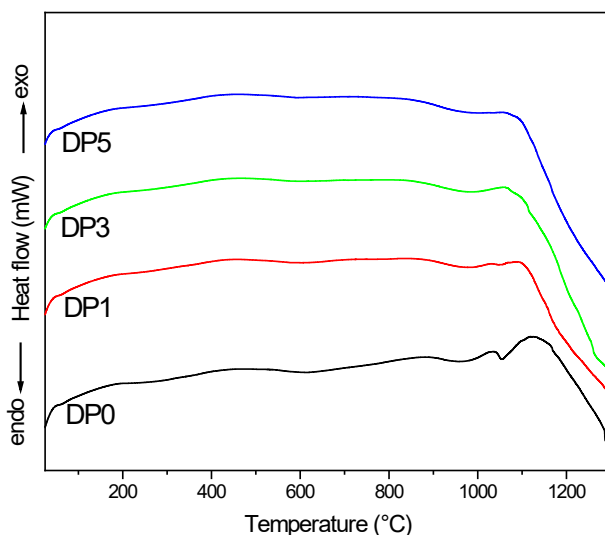


Figure 4. The DSC thermograms of DP samples.

It was observed that the addition of ZrO_2 caused broadening of exothermic peaks between 1000 and $1100\text{ }^\circ\text{C}$, which may be due to overlapping of peaks. The exothermic peaks shifted into a single broad peak with further ZrO_2 addition to the DP. No sharp exothermic effect was observed for DP1, DP2, and DP3 samples in the DSC curves, it means that the number of crystalline phases developed during the DSC run was small, in agreement with XRPD analysis revealed in **Figure 2**. It is evident from DSC results that the addition of ZrO_2 caused a progressive inhibition of the second thermal event confirmed by a reduction in intensity of the exothermic peaks [31, 32].

The surface microhardness of a material refers to its resistance to permanent indentation. It is an important property for restorative materials as it reflects their mechanical strength [33], resistance to wear, and abrasiveness to opposing dental tissues and restorative materials [34]. A change in the surface microhardness indicates structural degradation or solubility, which is associated with a reduction in the material's strength and mechanical performance. Microhardness is generally dependent on the mechanical

strength of the microstructure. When there are weak points such as defects or micro-cracks, the hardness will be lower due to the presence of these cracks. The determined Vickers microhardness (VMH) values of DP samples containing 0, 1, 3, and 5 wt.% ZrO₂ are revealed in **Table 2**.

Table 2. VMH values (mean and standard deviation-SD) obtained for the prepared DP compositions.

Sample ID	DP0	DP1	DP3	DP5
Mean VMH	794.07 ± 106.56	868.83 ± 18.97	846.49 ± 38.85	912.91 ± 30.76

As observed from **Table 2**, an overall increase of VMH in all samples with ZrO₂ addition if compared to DP was observed. The VMH value obtained for DP was slightly influenced by ZrO₂ additions. The higher VMH value of 912.91 ± 30.76 (8.953 GPa) was measured for sample DP5, containing 5 wt.% ZrO₂. The presence of ZrO₂ increased the microhardness of porcelain. A comparison between mechanical properties values of the prepared materials in this study and for those reported in the literature are reported in **Table 3**.

Table 3. Comparative values of the VMH of the dental porcelain obtained from this study and those reported in the literature.

Material	Temperature (°C)	Vickers microhardness (GPa)	Reference
P (porcelain)	1200 °C	7.6 ± 2.0	Serragdj et al.
P	1200 °C	9.3 ± 0.2	Kitouni et al.
P + 30 wt.% alumina and 5 wt.%TiO ₂	1200 °C	7.3	Kimura et al.
P + 5 wt.% ZrO ₂	1200 °C	12.8 ± 2.0	Serragdj et al.
P + 8 wt.% ZrO ₂	1200 °C	13.1 ± 1.0	Serragdj et al.
Dental porcelain (DP)	1200 °C	7.787	present work
DP + 1 wt.% ZrO ₂	1200 °C	8.521	present work
DP + 3 wt.% ZrO ₂	1200 °C	8.302	present work
DP + 5 wt.% ZrO ₂	1200 °C	8.953	present work

The best VMH value achieved for the DP5 sample is higher compared to that obtained by Santos et al. (6.5 GPa) for porcelain of 30 wt.% ZrO₂ composite, even though their mixtures were hot pressed in vacuum at 970 °C for 2 min [20]. Moreover, this VMH value is comparable to that reached by both Kitouni

and Harabi (9.3 GPa) for porcelain samples and greater compared to the works carried out by Kimura et al. (7.3 GPa) for porcelain containing 30 wt.% Al_2O_3 sintered at 1200 °C [35, 36]. Therefore, replacing the more expensive starting materials like Al_2O_3 , whose price is much higher, by other low-cost raw materials, is significantly important.

Most ceramics have comparatively higher hardness values than human enamel and metal alloys [37, 38]. It is known that dental hard tissue comprises a combination of enamel and dentin, both of which have different compositions and structures.

Enamel, which has a glossy surface and varies in color from light yellow to grayish white, is mainly made of the mineral hydroxyapatite, which is crystalline calcium phosphate. It is the hardest tissue in the human body because it contains almost no water. Structurally, enamel covers the entire anatomic crown of the tooth above the gum and protects the dentin. Dentin consists of the mineral hydroxyapatite (70%), organic material (20%), and water (10%). Dentin is harder than bone but softer than enamel, and it is mostly made of phosphoric apatite crystallites. Following the results of Chun et al., the measured hardness value of enamel specimens ($\text{HV} = 274.8 \pm 18.1$) was around 4.2 times higher than that of dentin specimens ($\text{HV} = 65.6 \pm 3.9$) [39]. The Vickers microhardness of the DP prepared in this study is superior to that of dentin and enamel.

Further, the microhardness values of the DP prepared in this study were compared with three commercial CAD/CAM ceramics: IPS e.max CAD (lithium disilicate), VITA ENAMIC (polymer-infiltrated ceramic), and Celtra Duo CAD (zirconia-reinforced lithium silicate). The reported mean microhardness values are 853.82 (± 16.89) for IPS e.max CAD, 342.79 (± 25.69) for VITA ENAMIC, and 853.68 (± 19.46) for Celtra Duo CAD [40]. It was observed that all the new formulations from the present work showed a significant increase in microhardness if compared with VITA ENAMIC. Concerning both IPS e.max CAD and Celtra Duo CAD, a slight increase of 1.7% was observed even at low percentages of material added (1 wt.% ZrO_2), but an increase of microhardness values with 7% at high percentages of material added (5 wt.% ZrO_2). In conclusion, the microhardness values of the experimental dental porcelain developed in this research demonstrated a greater level of microhardness compared to several commercially available dental porcelains. This enhanced microhardness is likely due to the incorporation of the ZrO_2 crystalline phase, which may contribute to the material's performance in dental applications.

CONCLUSIONS

In this study, a newly developed dental porcelain (DP) using economic raw materials was proposed. The selected composition was 80 wt.% feldspar, 15 wt.% quartz, and 5 wt.% kaolin. Additionally, the effect of zirconium oxide (ZrO_2) addition on the structural and mechanical properties of DP was studied. Structural analyses reveal that quartz, mullite and amorphous phases are present on the obtained DP. In the samples with ZrO_2 addition, some peaks of zirconia were identified. The measured Vickers microhardness (VMH) of DP sintered at 1200 °C was 794.07 ± 106.56 kgf/mm², a value comparable with those reported for conventional porcelains. Moreover, the addition of ZrO_2 improved the overall microhardness with the best value of 912.91 ± 30.76 kgf/mm² obtained for the sample with 5 wt.% ZrO_2 . Finally, these VMH values may recommend the use of the DP material for dental applications, as feldspathic porcelains are the most used ceramic materials in dentistry for the manufacture of indirect restorations and as a veneering material for bilayer prostheses over metallic or ceramic infrastructures. Further studies are required to completely elucidate the effect of ZrO_2 as a candidate for potentially improving the mechanical properties of the prepared ceramic dental material.

EXPERIMENTAL SECTION

Raw materials

The raw materials used to prepare DP are kaolin (Zettlitz, Czech Republic), quartz (Văleni, Romania), and feldspar (Muntele Rece, Romania) with the chemical composition presented in **Table 4**. All the raw materials were used as received without any further purification and serve for different functional attributes: feldspar provides natural translucency and forms the main structure of the porcelain, quartz prevents shrinkage during firing, provides stability, and increases durability, whereas kaolin, present in only 1-5% of the powder, is heat-resistant, provides elasticity to the porcelain paste, and helps bind other materials together.

The reinforcing material used in this study was high-purity zirconium oxide (ZrO_2 , Riedel-de Haën AG, Seelze, Germany, 99%) which played a crucial role as improving agent.

Table 4. Chemical compositions of raw materials (wt.%).

Raw materials	SiO ₂	Al ₂ O ₃	Fe ₂ O ₃	TiO ₂	CaO	MgO	Na ₂ O	K ₂ O	LOI*
Kaolin	47.27	35.62	0.66	0.38	0.75	0.20	0.20	0.87	14.2
Feldspar	76.41	12.61	0.31	-	0.42	0.4	0.4	8.5	0.95
Quartz	97.08	0.24	0.02	-	0.96	0.06	0.03	0.03	1.17

*Loss on ignition

Dental porcelain preparation

The composition of the experimented dental porcelain was 80 wt.% feldspar, 15 wt.% quartz, and 5 wt.% kaolin, following the procedure previously reported [14]. The selected raw materials were wet milled and homogenized in a planetary ball mill (Pulverisette 6, Fritsch, Germany) for 30 min at 250 rpm to obtain the typical size distribution. Afterward, the obtained slurry was dried at 105 °C for 1 day using a Memmert incubator. Different ZrO₂ amounts, 1, 3, and 5 wt.%, have been added to the raw materials mixture to improve the mechanical properties of the sintered DP samples. The specimens in the form of discs of 2 g and about 10 mm in diameter were obtained by uniaxially cold press using a metallic dye and a pressure of about 0.5 tons, by a Carver Inc., hydraulic press (Carver Inc., Wabash, IN, USA). The obtained pellets were subsequently sintered at 1200 °C for 12h using a Nabertherm LHT 04/16 (Lilienthal, Germany) furnace, with a constant heating and cooling rate of 5 °C/min. The obtained samples, in the form of powder or pellets, were further used for different analyses. Depending on the amount of ZrO₂ used, 0, 1, 3, and 5 wt.%, the samples have been named as follows: DP0 (without ZrO₂ addition), DP1, DP3, and DP5, respectively.

Characterization methods

Particle size analysis by laser diffraction was performed with a nanoparticle size analyzer SALD-7101 (Shimadzu, Japan). The samples were dispersed in a water medium to form a suspension and drawn into the size analyzer. The particle aggregation was reduced using treatment with ultrasounds.

XRPD analysis was performed to investigate the structure of the samples using a Shimadzu XRD-6000 diffractometer operating at 40 kV, 30 mA, with Ni- filter and graphite monochromator for CuK α ($\lambda=1.54060$ Å). The diffraction patterns were recorded in the 2 θ range of 10-80° at a scan speed of 2 °/min. The phase identifications and crystallographic information files corresponding to the quartz (Q, PDF # 96-901-0145), zirconium oxide (Z;

PDF # 96-900-7449) and mullite (M, PDF# 96-210-8044) phases were selected from the Crystallography Open Database (COD) using version 3.13 (Build 220) of Match! software.

The FTIR measurements were carried out using a Jasco FTIR 6200 spectrometer. The spectra were recorded from KBr pellets, with a spectral resolution of 4 cm⁻¹.

The TA Instruments SDT Q600 Thermogravimetric Analyzer (TGA) & Differential Scanning Calorimeter (DSC) was used to investigate the thermal properties of the samples. The analyses were performed from room temperature to 1300 °C with a ramp of 10 °C/min, using alumina pans.

Vickers microhardness (VMH) values were measured with a Micro Hardness Tester (FALCON 600G2FAO2). Indentations were conducted in the air with loads of 3 kgf. The indentation time was 15 s. For all experiments only well-defined indents, without chipping or cracks, were considered. The samples were thoroughly inspected with a magnifying lens to exclude specimens with any surface defect. The Vickers microhardness (VMH) value of each indent was automatically calculated. Each sample was subjected to 5 indentations and the mean VMH value was calculated in kgf/mm².

REFERENCES

1. I. Naert, 2017. *In Comprehensive Biomaterials II, Materials in Fixed Prosthodontics for Indirect Dental Restorations*, P. Ducheyne Ed.; Elsevier, pp. 467-481.
2. E. A. McLaren; P. T. Cao; *Inside Dentistry*, **2009**, 5(9), 94-105.
3. G. A. Helvey; *Inside Dentistry*, **2013**, 9(4), 62-76.
4. E. H. J. Lugwisha; S. I. Siafu; *Int. J. Dev. Res.*, **2014**, 4, 11, 2260-2265.
5. J. P. Moffa; *Adv. Dent. Res*, **1988**, 2(1), 3-6.
6. A. Harabi; F. Guerfa; E. Harabi; M.-T. Benhassine; L. Foughali; S. Zaiou; *Mat. Sci. Eng. C*, **2016**, 65, 33-42.
7. G. W. Ho; J. P. Matinlinna; *Silicon*, **2011**, 3, 109-115.
8. E. Bajraktarova-Valjakova; A. Grozdanov; Lj. Guguvcevski; V. Korunoska-Stevkovska; B. Kapusevska; N. Gigovski; A. Mijoska; C. Bajraktarova Misevska, *Open Access Maced. J. Med. Sci.*, **2018**, 6(3), 568-573.
9. B. W. Darvell, 2009. *In Materials science for dentistry*, 8th ed., CRC Press LLC, Boca Raton, FL, pp. 547-567.
10. J. F. McCabe; A. W. G. Walls, 2008. *In Applied dental materials*, 9th ed., Blackwell Publishing Ltd., Oxford, UK, pp. 89-100.
11. L. M. Uehara; I. Ferreira; A. L. Botelho; M. L. D. C. Valente; A. C. D. Reis; *Dent. Mater.*, **2022**, 38(6), e174-e180.
12. I. Ferreira; C. L. Vidal; A. L. Botelho; P. S. Ferreira; M. L. C. Valente; M. A. Schiavon; O. L. Alves; A. C. dos Reis; *J. Prosthet. Dent.*, **2020**, 123(3), 529.e1-529.e5.

- 13.L. Vidal; I. Ferreira; P. Ferreira; M. Valente; M. Teixeira; A. Reis; *Antibiotics*, **2021**, 10(2), 1-13.
- 14.B. E. Sakhkhane; M. Mureșan-Pop; L. Barbu-Tudoran; T. Lovász; L. Bizo; *Crystals*, **2024**, 14(7), 616.
- 15.M. M. Salman, S. M. Badr, H. T. Nhabih, *The Iraqi Journal for Mechanical and Materials Engineering*, **2024**, 23(1), 1–10.
- 16.D. W. Jones, *J. Can. Dent. Assoc.*, **1998**, 64, 648-650.
- 17.I. M. Hamouda; N. A. El-Waseffy, A. M. Hasan; A. A. El-Falal; *J. Mech. Behav. Biomed. Mater.*, **2010**, 3(8), 610-618.
- 18.M. A. Kaiyum; A. Ahmed; M. H. Hasnat; S. Rahman; *J. Korean Ceram. Soc.*, **2021**, 58, 42-49.
- 19.A. Harabi; S. Kasrani; L. Foughali; I. Serradj; M. T. Benhassine; S. Kitouni; *Ceram. Int.*, **2017**, 43(7), 5547-5556.
- 20.R. L. P. Santos; F. S. Silva; R. M. Nascimento; F. V. Motta; J. C. M Souza; B. Henriques; *Ceram. Int.*, **2016**, 42, 14214-14221.
- 21.I. Serradj; A. Harabi; S. Kasrani; L. Foughali; N. Karboua. *J. Aust. Ceram. Soc.*, **2019**, 55, 489-499.
- 22.I. Teoreanu, N. Ciocca, A. Barbulescu, N. Ciontea, *In Tehnologia produselor ceramice și refractare Vol.1, Tehnologia produselor ceramice (In Romanian)*, Ed. Tehnică, **1985**, pp. 494-496.
- 23.E. Kamseu; C. Leonelli; D. N. Boccaccini; P. Veronesi; P. Miselli; G. Pellacani; U. Chinje Melo; *Ceram. Int.* **2007**, 33, 851-857.
- 24.M. J. Jackson; B. Mills; *Br. Ceram. Trans.* **2001**, 100, 1-8.
- 25.N.G. Holmstroem; *Am. Ceram. Soc. Bull.* **1981**, 60, 470-473.
- 26.F. Kooli; L. Yan; S. X. Tan; J. Zheng; *J Therm. Anal. Calorim.* **2014**, 115, 1465-1475.
- 27.P. Komadel; *Clay Miner.*, **2003**, 38, 127-138.
- 28.M. Todea; M. Muresan-Pop; A. Vulpoi; S. Simon; D. Eniu; *Appl. Surf. Sci.*, **2018**, 457, 838-845.
- 29.Y. Liu; F. Zeng; B. Sun, P. Jia; I. T Graham; *Minerals*, **2019**, 9, 358.
- 30.S. Kieffer; *Rev. Geophys. Space Phys.*, **1979**, 17, 20-34.
- 31.Y. Sawadog; M. Sawadogo; M. Ouédraogo; M. Seynou; G. Lecomte-Nana; P. Blanchart; M. Gomina; L. Zerbo; *J. Mat. Sci. Chem. Eng.*, **2022**, 10, 41-58.
- 32.S. Yilmaz; Z. Engin Erkmén; *Am. Ceram. Soc. Bull.*, **2007**, 86, 9301-9034.
- 33.B. T. Leun; J. K. Tsoi; J. P. Matinlinna; E. H. Pow; *J. Prosthet. Dent.*, **2015**, 114, 440-446.
- 34.R. S. Asaad; S. Salem; *Egypt. Dent. J.*, **2012**, 67, 485-495.
- 35.S. Kitouni; A. Harabi, *Cerâmica*, **2011**, 57, 453-460.
- 36.I. Kimura; N. Hotta; K. Sato; N. Saito; S. Yasukawa; *Ceram. Int.*, **1988**, 14(4), 217-222.
- 37.G. E. Monasky; D. F. Taylor; *J. Prosthet. Dent.*, **1971**, 25, 299-306.
- 38.R. M. Fisher; B. K. Moore; M. L. Swartz; R. W. Dykema; *J. Prosthet. Dent.* **1983**, 50, 627-631.
- 39.K. J. Chun; H. H. Choi; J. Y. Lee; *J. Dent. Biomech.* **2014**, 5, 1-6.
- 40.R. Z. Alshali; M. A. Alqahtani; *Materials*, **2022**, 15, 5948.

ELECTROCHEMICAL CHARACTERIZATION AND DNA INTERACTION STUDIES OF A NOVEL COPPER SCHIFF BASE COMPLEX: INSIGHTS FROM CYCLIC VOLTAMMETRY AND MOLECULAR DOCKING

Chahinaz ZOUBEIDI^a, Ali OURARI^b,
Elhafnaoui LANEZ^c, and Touhami LANEZ^{c,*}

ABSTRACT. In this study, we investigate the electrochemical properties of a novel copper complex (CuL₂) derived from the Schiff base ligand N-3-bromopropylsalicylaldimine (LH). We also examine its interaction with chicken blood double-stranded DNA (cb-ds DNA) in phosphate buffer solution (PB) at physiological pH 7.2 using cyclic voltammetry (CV) techniques. The interaction mechanism of nitrite with CuL₂, involving the CuI/Cu redox system, is explored. The CuL₂ complex was electropolymerized on glassy carbon (GC) and fluorine tin oxide (FTO). The morphology of PolyCuL₂ formed on FTO was analyzed using scanning electron microscopy (SEM) and its elemental composition determined by EDX analysis. The modified electrode polyCuL₂/GC exhibited efficient catalytic activity for the electroreduction of oxygen (O₂) in homogeneous electrocatalytic media. The binding constant (K_b) of the DNA-CuL₂ adduct, determined from CV measurements, was found to be 1.33×10⁵, closely matching the value obtained from molecular docking studies (1.75×10⁵). Docking studies indicate that the CuL₂ complex binds to DNA in the minor groove binding mode. The anodic peak potential shift in the negative direction suggests an electrostatic interaction between CuL₂ and DNA.

Keywords: Copper(II) complex; Electro-polymerization; catalytic reduction; DNA binding affinity; AutoDock.

^a Department of Renewable Energies, Faculty of Hydrocarbons, Renewable Energies and Earth and Universe Sciences, University of Ouargla, BP.511, 30000, Ouargla, Algeria

^b Laboratory of Electrochemistry, Molecular Engineering and Redox Catalysis (LEIMCR), Faculty of Technology, Ferhat ABBAS University of Sétif-1, Sétif 19000, Algeria

^c VTRS Laboratory, Department of Chemistry, Faculty of Sciences, University of El Oued, B.P.789, 39000, El Oued, Algeria

* Corresponding author: touhami-lanez@univ-eloued.dz



INTRODUCTION

Numerous Schiff base ligands have been investigated as starting materials for coordinating transition metals. The increased interest in their metal complexes is due to their usefulness in various fields. A new class of ligands containing two coordination sets (N and O atoms) with a carbon-bromide function (C-Br) has garnered attention due to their prominent chemical reactivity [1–3].

Moreover, there has been growing interest in the synthesis, characterization, and crystal structures of Cu(II) Schiff base complexes [2–6]. These complexes exhibit interesting properties and structural diversity, making them useful for many applications[7,8], including the preparation of supramolecular assemblies[9,10] and the development of highly sensitive carbon paste electrodes modified with copper complexes for electrocatalytic reduction of nitrite (NO_2^-) [11] and bromate (BrO_3^-) in aqueous media [12].

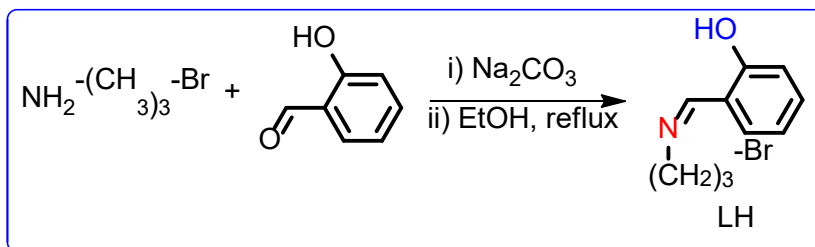
Transition metal coordination compounds have been extensively used as DNA structural probes [13], DNA cleaving agents [14], DNA molecular light switches [15], and for various other applications [16,17]. They form very stable complexes with peculiar properties and reactivity, particularly in binding small molecules [18,19]. These chelating ligands with O and N donor atoms and their complexes also show broad biological activity [20,21]. Furthermore, some dibromide-bridged binuclear Cu(II) complexes, based on Schiff base ligands, have been investigated for their potential as anticancer agents [22,23].

Continuing from our previous work, where the Cu(II) complex and its ligand were characterized by microanalysis, UV–Vis, FT-IR, ^1H NMR, and ^{13}C NMR spectroscopy, with structures confirmed by single crystal X-ray crystallography[24], we now report on the investigation of the electrocatalytic properties of a new copper Schiff base complex (CuL_2). This complex appears in polymer matrices as pendant functional groups covalently grafted by bromide atoms. We also examine the interaction of CuL_2 with chicken blood double-stranded DNA using cyclic voltammetry (CV) techniques and molecular docking simulation.

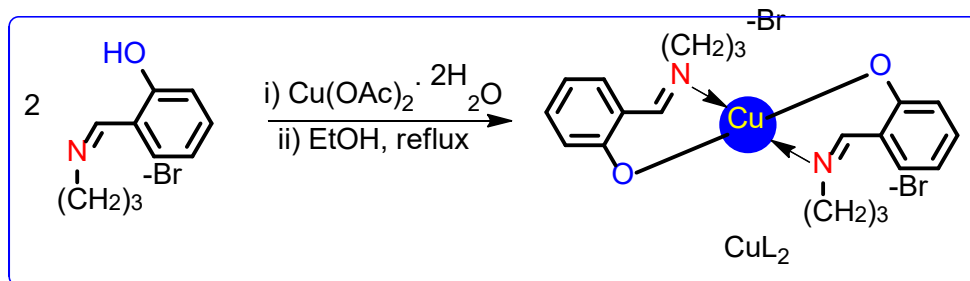
RESULTS AND DISCUSSION

The ligand LH was synthesized by reacting 3-bromopropylamine hydrobromide with 2-hydroxybenzaldehyde in a 1:1 molar ratio, using a base to enhance the nucleophilicity of the amino group ($-\text{NH}_2$)[24]. The CuL_2 complex was then prepared by refluxing the ligand with Cu(II) acetate tetrahydrate in

absolute ethanol, resulting in a dark green precipitate from the exchange reaction between LH and the copper salt. The reaction pathways for the formation of LH and the CuL_2 complex are shown in Schemes 1 and 2.



Scheme 1. Synthetic route of Schiff base ligand LH.



Scheme 2. Synthetic route of Schiff base-copper complex CuL_2 .

Electrochemical study of CuL_2 complex

The CuL_2 complex was investigated using cyclic voltammetry in an acetonitrile solution with a scan rate of $100 \text{ mV}\cdot\text{s}^{-1}$, within the potential range of -1.80 to 1.80 V against a Saturated Calomel Electrode (SCE).

Upon sweeping the voltage to oxidizing potentials, CuL_2 (Figure 1) shows two anodic waves at $+1.08$ (I) and $+1.24 \text{ V}$ (II). The first peak (I) corresponds to the quasi-reversible oxidation of the $\text{Cu}(\text{II})$ to $\text{Cu}(\text{III})$ [6, 25]. LH_2 , being the most electron donating as the dianionic form/ $(\text{L}^-)_2$, stabilizes the copper ion in the higher oxidation state $\text{Cu}(\text{III})$ and disfavors reduction of the copper(II) cation. The active species of $\text{Cu}(\text{III})$ is likely to oxidize the ligand LH_2 via an intermediate electron transfer process, by electrochemical reaction LH_2 with ligand Schiff base. The second peak (II) is observed at nearly the same potential value as the corresponding ligand and can be attributed

to irreversible oxidation of phenolic groups of the ligand [1,6,26]. LH_2 , being the most electron donating as the dianionic (L^-)₂, stabilizes the copper ion in the higher oxidation state and disfavors reduction of the copper(II) cation. Also, the oxidation potential of the copper complex seems to be more positive than the value observed for the ligand, which may be related to the relative stability of the coordination bonding between the oxygen and the azote atom with copper (II) ion. Two overlapping reduction peaks at -0.78 (III) and -1.07 (IV) V/SCE, which are assigned to the Cu(II)/Cu(I) redox couple and the reduction the imine groups of the Schiff base, respectively [25]. The latter reduction wave is significantly shifted to less cathodic potentials compared to the ligand alone, indicating a decrease in the electron density of the imine group after the coordination process with the copper complex [28].

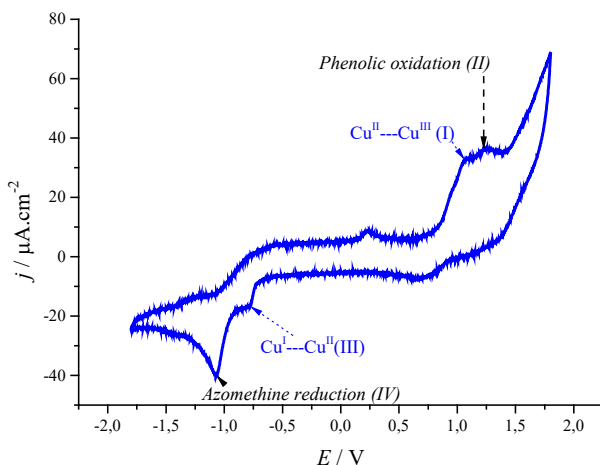


Figure 1. Cyclic voltammogram of 1 mM of CuL_2 at GC electrode in acetonitrile solution 0.1 M TBAP. Scan rate $100 \text{ mV}\cdot\text{s}^{-1}$.

Figure 2 displays a pair of oxidation-reduction peaks corresponding to the Cu(III)/Cu(II) redox couple at 1.08 V and 0.64 V. The ΔE_p data being larger than the theoretical value for an electrochemically reversible one-electron process. Thus, for this complex the large ΔE_p value expressing an electrochemical oxidation of Cu(II) would be due to a quasi-reversible behavior of the couple $Cu(III)L + e^- = Cu(II)L$ yielding an average formal potential of $E_{1/2} = 0.86 \text{ V}$. The difference between the anodic and cathodic potentials is $\Delta E_p = 0.44 \text{ V}$ and the current ratio (I_{pc3}/I_{pa3}) exceeds unity at 4.83 confirm the irreversibility electrochemistry of this redox couple.

The Cu(III)/Cu(II) redox couple appears to be scan-rate-dependent, particularly for the anodic wave. At lower scan rates (10-100 $\text{mV}\cdot\text{s}^{-1}$), this anodic wave splits into two. As the scan rate increases, the first wave shifts to more anodic potentials, while the second wave shifts to more cathodic potentials, resulting in an increase in current intensities. These two redox couples are likely irreversible, consistent with previous reports in the literature [29,30].

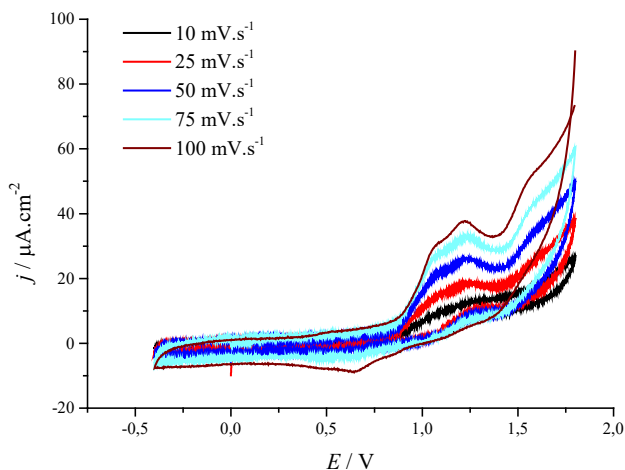
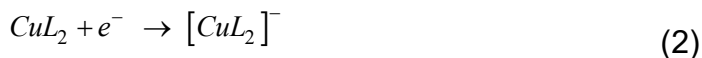


Figure 2. Cyclic voltammogram of 1 mM CuL_2 in 0.1 M TBAP/ CH_3CN showing scan rate dependence of Cu(II) / Cu(III) redox couple.

The electroreduction polymerization process of the copper complex CuL_2 on optically transparent electrodes was observed by a continuous increase in peak currents during the initial cathodic sweep scans (Figure 3A). In subsequent scans, the current decreases, and after several cycles, the initial reduction peaks disappear, replaced by two new peaks around -0.6 V/SCE, indicating the formation of a deposited film on the electrode surface. These redox processes correspond to the Cu(II)/Cu(I) redox couple and increase with the number of cycles [31,32]. As the number of cycles increases, not only does the peak current intensity rise, but the potential also shifts to more negative values [33,34]. It has been proposed that the oxidative polymerization of Salen-type metal units is primarily a ligand-based process, where radical-radical coupling between the phenol rings is responsible for polymer formation. This new material can be considered a modified electrode [$\text{PolyCuL}_2/\text{GC}$]. Comparing the electrochemical processes, such as anodic oxidation or cathodic reduction, the monomer involved in these reactions leads to the formation of intermediate radical-cations and radical-anions, respectively (see Eq. 1 and Eq. 2).



Similarly, the electrochemical process described in Eq. 2 initially produces radical-anions. These radical species participate in radical-radical coupling, resulting in the formation of polymer films and thereby producing modified electrodes [33,34]. The PolyCuL₂ film is deposited and grows on an optically transparent FTO-coated glass electrode, as evidenced by the continuous increase in the peak currents of the copper complex (Figure 3B).

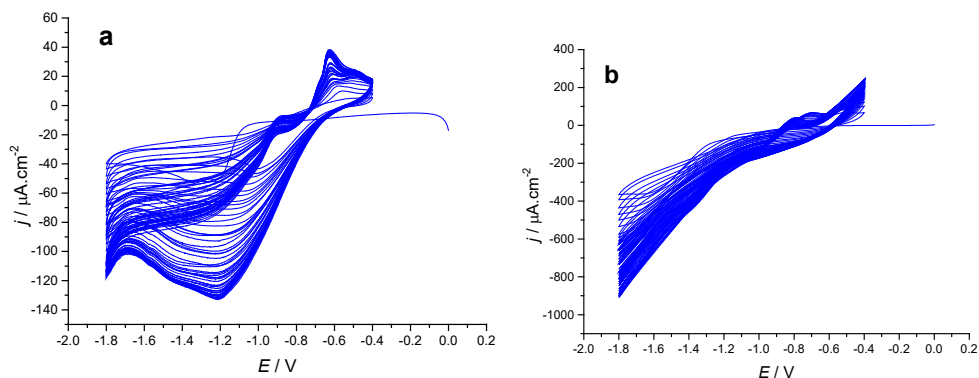


Figure 3. (a) Cyclic voltammogram showing electropolymerization of 0.1 M of CuL₂, 0.1 M TBAP/CH₃CN by: cycling between -0.4 and -1.8 V/SCE in acetonitrile solution using GC-electrode at 75 Mv. s⁻¹ in (100 cycles). (b) and FTIO electrode at 100 mV s⁻¹ (100 cycles).

Energy dispersive X-ray (EDS) analysis of the PolyCuL₂/FTO was conducted to investigate the adsorption of Cu on the surface of the modified electrode within the polymer catalyst structure (Figure 4). The EDS images display peaks corresponding to copper, oxygen, and nitrogen, confirming the presence of these elements. Furthermore, the analysis indicated that the coating of copper on the surface of the modified electrode PolyCuL₂ was successful.

The scanning electron microscopy (SEM) images presented in Fig. 5 were used to explore the morphology of the film electropolymerized onto an FTO substrate. The surface of the PolyCuL₂ film, obtained by cycling 100 times between -0.4 and -1.8 V, displays high porosity, which becomes apparent at high magnifications.

ELECTROCHEMICAL CHARACTERIZATION AND DNA INTERACTION STUDIES OF A NOVEL COPPER SCHIFF BASE COMPLEX

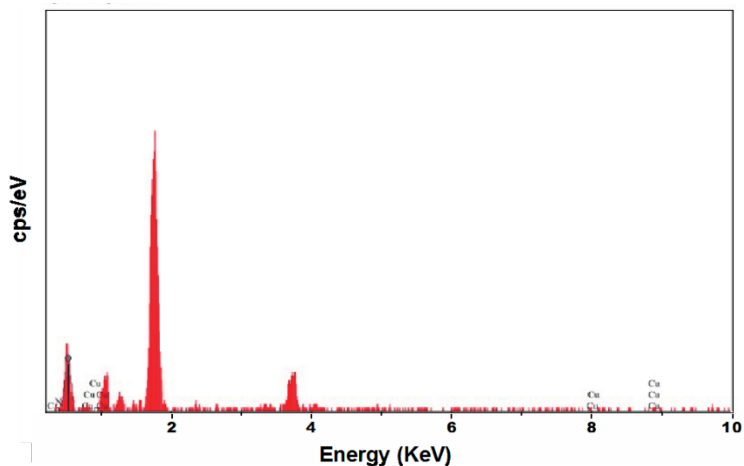


Figure 4. EDAX spectrum of polyCuL₂/FTO.

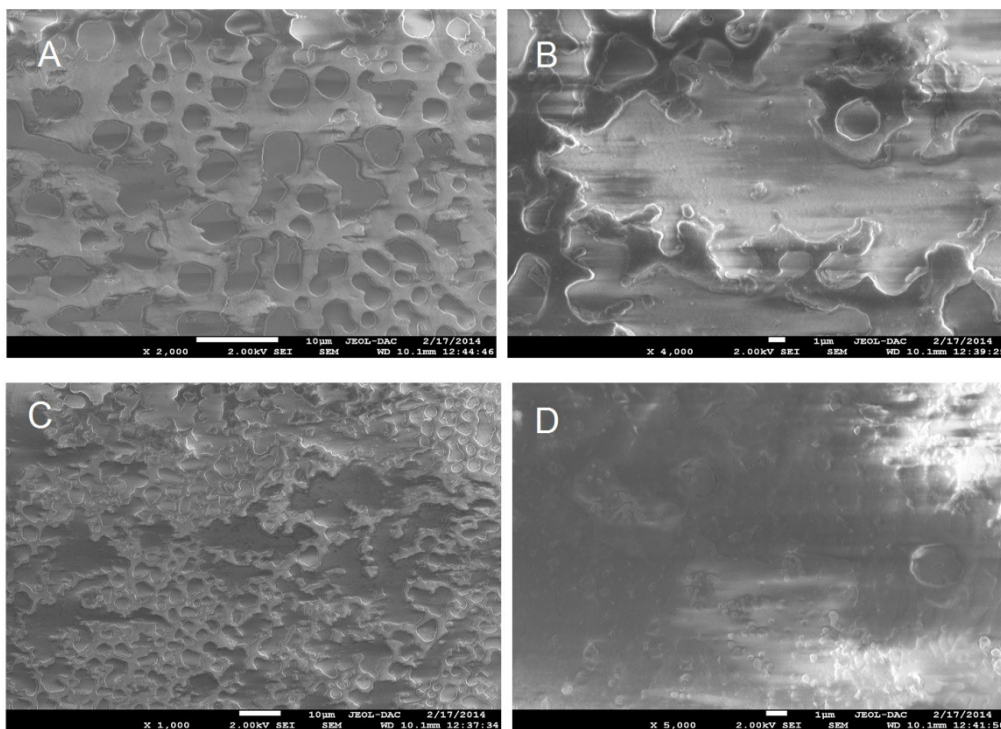


Figure 5. Scanning electron micrographs of the FTO modified electrode surface with polyCuL₂/FTO, (a) X 2,000, 2.0 Kv 10 μm, (b) X 4,000, 2.0 Kv 1 μm (c) X 2,000, 2.00 Kv 10 μm, (d) X 5,000, 2.0 Kv 1 μm.

Catalytic effect of polyCuL₂

The electrochemical determination of the efficient catalytic activity for the reduction of oxygen by a CG electrode modified with a polyCuL₂ film was conducted in a mixture containing 9.2 mg.L⁻¹ of oxygen (O₂) and 0.5 mol.L⁻¹ KCl solution (Fig. 6). Under a controlled nitrogen atmosphere, the signal was almost zero (Curve A). However, in an air medium, the signal became significant (Curve B). This indicates that the electrocatalytic efficiency was drastically affected by the modification of the electrode surface, resulting in polyCuL₂/GC films [35–37]. The results showed a significant enhancement of the redox system, observed at -0.8 V vs. SCE, which has been attributed to oxygen reduction by the Cu(II)/Cu(I) couple[38].

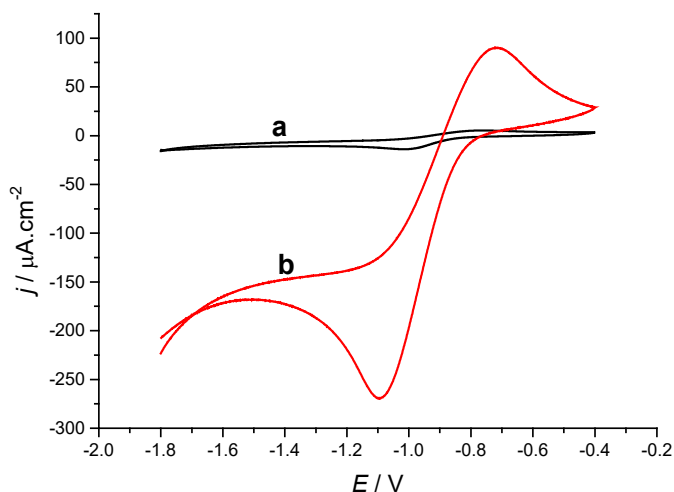


Figure 6. Cyclic voltammograms recorded in 0.1 M TBAP/CH₃CN solution at 100 mV/s with polyCuL₂/GC Modified electrode: (a) under saturated nitrogen atmosphere, (b) under saturated air atmosphere.

It is postulated that the catalytic efficiency for a given catalyst can be assessed from the ratios of the cathodic peak (*ipc*) currents under oxygen and nitrogen atmospheres, denoted as *ipc*(O₂)/*ipc*(N₂). As shown in Table 2, higher values for the *ipc*(O₂)/*ipc*(N₂) ratios were observed at various scan rates. This indicates a reproducible and efficient electrocatalytic effect, especially at lower scan rates, suggesting that more time allows for the chemical reaction necessary for oxygen reduction [39].

Table 1. Catalytic efficiency data for electrode modified polyCuL₂/GC.

Rates (mV/s)	100	75	50	25
$i_{pc}(O_2)/i_{pc}(N_2)$	19.28	18.57	20.12	13.67

DNA Binding Study of CuL₂ via Cyclic Voltammetry

The cyclic voltammetry technique was applied to study the interaction between the CuL₂ complex and DNA. When an increasing concentration of DNA was added to a solution of the CuL₂ complex, the anodic peak current height of the complex decreased, and the anodic peak potential exhibited a negative shift. This result suggests that the CuL₂ complex interacts with DNA via an electrostatic mode [40]. Cyclic voltammograms of the CuL₂ complex in the absence and presence of DNA are shown in Fig. 7a. To avoid acidic or basic denaturation of DNA, the pH of the solution was fixed at the physiological pH of 7.2 using a 0.1 M phosphate buffer solution (KH₂PO₄/K₂HPO₄).

From this observation, it can be noted that in the absence of DNA, the voltammograms of the CuL₂ complex show an anodic peak potential at 1.335 V. In the presence of DNA, this peak appears at 1.288 V, with a negative shift of 47 mV, indicating an interaction between the CuL₂ complex and DNA. The voltammograms further show a drop in the anodic peak current densities, which can be attributed to the slow diffusion of the DNA–CuL₂ adduct [41].

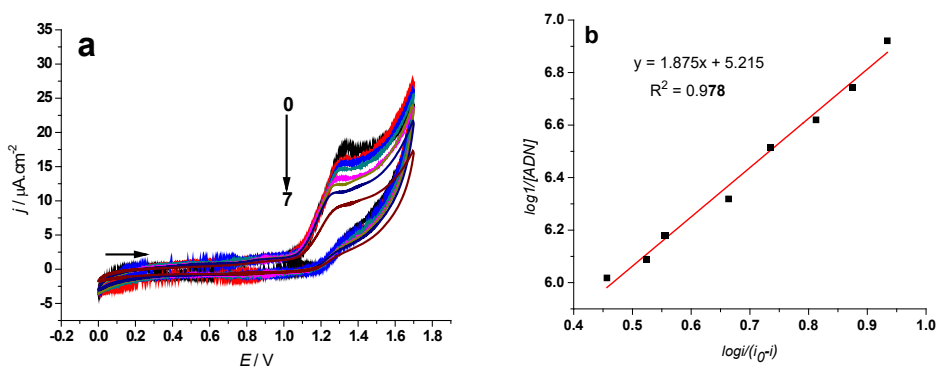


Figure 7. (a) Cyclic voltammograms of 0.1 mM CuL₂ in 0.1 M buffer phosphate solution recorded at 0.1 V·s⁻¹ potential sweep rate on GC disk electrode in the absence of DNA(0), and in presence of 0.12 (1), 0.24 (2), 0.48 (3), 0.96 (4), 1.44 (5), 1.92 (6) and 2.40 μM DNA (7), (b) the plot of $\log 1/i - (i/i_0)$ versus $\log 1/[DNA]$ used to calculate the binding constant of ligand CuL₂ with DNA.

Binding constant and binding free energy

The decrease in anodic peak current density of the DNA–CuL₂ adduct relative to the free CuL₂ complex is used to calculate the binding constant and binding free energy, using equation 3 [42].

$$\log \frac{1}{[DNA]} = \log K_b + \log \frac{j}{j_0 - j} \quad (3)$$

where j_0 and j are the anodic peak current densities of the free CuL₂ complex and the DNA–CuL₂ adduct, respectively, K_b is the binding constant, and $[DNA]$ is the concentration of the free ligand.

By plotting $\log 1/[DNA]$ versus $\log 1/1-(j/j_0)$, the binding constant value $K_b = 1.33 \times 10^5 \text{ M}^{-1}$ is obtained from the intercept of the plot, and the binding free energy $\Delta G = -29.72 \text{ kJ.mol}^{-1}$ at $\sim 25 \text{ }^\circ\text{C}$ is calculated using equation 4.

$$\Delta G = -RT \ln K_b \quad (4)$$

where R is the universal gas constant and T is the temperature in Kelvin.

DNA Binding Study of CuL₂ via molecular docking studies

Molecular docking studies of the CuL₂ complex with DNA were performed to predict the binding site and favored orientation of the ligand within the DNA. The three-dimensional crystal structures of DNA (PDB ID: 1W0T) and the CuL₂ complex (CCDC ID: 1044698) were obtained from the Protein Data Bank (<http://www.pdb.org>) [43] and The Cambridge Crystallographic Data Centre (<https://www.ccdc.cam.ac.uk>), respectively.

Before performing the docking calculations, crystallographic water molecules and protein molecules were removed from the DNA crystal structure, hydrogen atoms were added, and partial charges were assigned to the DNA structure file. The PDB file format of the CuL₂ complex structure was obtained from the CIF file and imported into the AutoDock molecular docking software.

Fig. 8 shows the 3D conformation structure of the CuL₂ complex. All docking studies were conducted on a Pentium 3.30 GHz microcomputer with 4.00 GB of RAM and running the Windows 7 operating system.

At the end of the docking runs, various binding energies of the ligand were obtained with their respective conformations. The most stable conformation corresponding to the strongest binding energy was selected as the best pose for docking analysis. The binding energy of the docked structure of the CuL₂ complex with DNA was found to be $-29.93 \text{ kJ.mol}^{-1}$ at the 19th run. The magnitude of the calculated binding free energy indicates a

high binding affinity between DNA and the CuL_2 complex, our results are in good agreement with the previously published work by Ebtisam Alolayqi and coworkers [44]. A binding constant of $1.75 \times 10^5 \text{ M}^{-1}$ at $\sim 25^\circ \text{C}$ was derived from the binding energy value. The DNA binding propensity of the complex could be attributed to the presence of the imino-phenyl system.

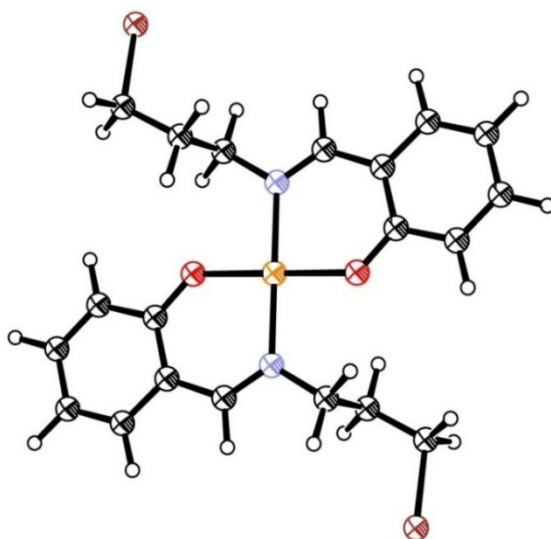


Figure 8. ORTEP of the compound Copper(II) complex of Schiff base N-3-bromopropylsalicylaldimine.

The results indicate that the CuL_2 complex interacts with DNA via its oxygen atom through a hydrogen bond to the hydrogen atom of deoxyadenosine DA11 (Figure 9).

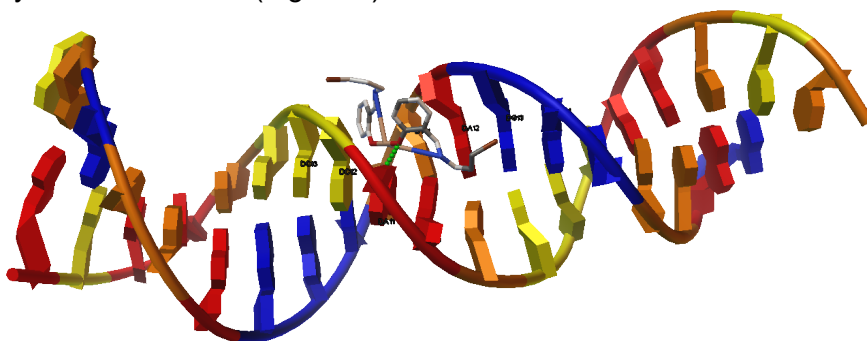


Figure 9. Docking poses of CuL_2 complex with DNA (PDB ID: 1W0T) illustrating the interactions between DNA and the examined complex. It shows the CuL_2 is attached in the minor groove via H-bonding.

CONCLUSIONS

This work describes the electrochemical behavior of the copper(II) complex of the Schiff base, N-3-bromopropylsalicylalimine, and its electroreduction activity. This complex behaves as a monomer and is easily electropolymerized by an electroreduction process, likely involving radical-radical coupling at the para-positions of the phenoxy groups of the Schiff base moieties or the reduction of C-Br bonds. The efficient electrocatalytic activity of this new material (polyCuL₂) has been demonstrated through its electroreduction in the presence of dioxygen.

Furthermore, the interaction of the copper complex with calf thymus double-stranded (cb-ds) DNA was investigated. DNA interaction studies were conducted using cyclic voltammetry and electronic spectroscopic techniques, and the obtained experimental results were confirmed by molecular docking calculations using the AutoDock 4.2 program. Molecular docking calculations further visualized the interactions and clearly confirmed the groove mode of binding of the Cu(II) complex to cb-ds DNA.

Both experimental results and molecular docking calculations indicated that the CuL₂ complex possesses significant binding affinity with DNA via electrostatic interactions as the dominant mode. Additionally, the magnitude of the binding energy confirms the electrostatic interaction of the studied complex with DNA.

EXPERIMENTAL SECTION

Synthesis

The CuL₂ complex was synthesized following our previously reported procedure [24].

DNA Extraction

DNA was extracted from chicken blood using the Falcon method [45]. The UV absorbance ratio at 260 and 280 nm was 1.97, indicating high purity and minimal protein contamination [45]. The DNA concentration per nucleotide was measured using electronic spectroscopy, applying the known molar extinction coefficient value of 6600 M⁻¹ cm⁻¹ at 260 nm [46].

Cyclic Voltammetry and Software

Cyclic voltammograms were recorded at room temperature (~25 °C) using a mono-compartment cell with a 5 mL capacity. The instrumentation included a VoltaLab 50 Potentiostat/Galvanostat controlled by a microcomputer.

A conventional three-electrode system was used for all experiments in CH₃CN solutions containing 0.1 M TBAP and 0.001 M of the CuL₂ complex to identify the electrochemical profile of the copper complex ligand. For the DNA interaction study, experiments were conducted in phosphate buffer solution at physiological pH 7.2.

The interactions between the CuL₂ complex and DNA were analyzed using the AutoDock 4.2 program [47]. For docking calculations, the AutoDock 4.2 program was used, employing the Lamarckian Genetic Algorithm (LGA) with a genetic algorithm (GA) search. Docking simulations were performed using default parameters, with the number of runs set to 50, 150 individuals, and 2,500,000 energy evaluations. The grid size was set at 70 × 60 × 126 Å, with points separated by 1.000 Å. The grid centers were set at X = 30.562, Y = 37.946, and Z = 18.681. The search was carried out on a grid of 41 and 51 points per dimension with a step size of 0.375 Å, centered on the DNA binding site. The best conformation was selected based on the lowest docking energy.

ACKNOWLEDGMENTS

This work was supported by the directorate-general of scientific research and technological development (DGRSDT) and the laboratory of valorization and technology of Saharan resources (VTRS) (project code: B00L01UN390120150001).

REFERENCES

1. A. Ourari; C. Zoubeidi; W. Derafa; S. Bouacida; H. Merazig; E. Morallon; *Res. Chem. Intermed.*, **2017**, *43*, 3163–3182.
2. A. Ourari; K. Ouari; W. Moumeni; L. Sibous; G. M. Bouet; M. A. Khan; *Transit. Met. Chem.*, **2006**, *31*, 169–175.
3. C. Santos; M. Vilas-Boas; M. F. M. Piedade; C. Freire; M. T. Duarte; B. De Castro; *Polyhedron*, **2000**, *19*, 655–664.
4. A. D. Khalaji; *Curr. Trends X-Ray Crystallogr. Chandrasekaran, Q., Ed.*, **2011**, 161–190.
5. R. K. Parashar; R. C. Sharma; A. Kumar; G. Mohan; *Inorg. Chim. Acta*, **1988**, *151*, 201–208.
6. J. Losada; I. del Peso; L. Beyer; *Transit. Met. Chem.*, **2000**, *25*, 112–117.
7. Z. Li; J.-T. Hou; S. Wang; L. Zhu; X. He; J. Shen; *Coord. Chem. Rev.*, **2022**, *469*, 214695.
8. A. Fazal; S. Al-Fayez; L. H. Abdel-Rahman; Z. S. Seddigi; A. R. Al-Arfaj; B. El Ali; M. A. Dastageer; M. A. Gondal; M. Fettouhi; *Polyhedron*, **2009**, *28*, 4072–4076.
9. L. J. Childs; M. Pascu; A. J. Clarke; N. W. Alcock; M. J. Hannon; *Chem. Eur. J.*, **2004**, *10*, 4291–4300.

10. L. J. Childs; J. Malina; B. E. Rolfsnes; M. Pascu; M. J. Prieto; M. J. Broome; P. M. Rodger; E. Sletten; V. Moreno; A. Rodger; *Chem. Eur. J.*, **2006**, *12*, 4919–4927.
11. A. A. Amer; H. Ilikti; C. Beyens; J. Lyskawa; U. Maschke; *Eur. Polym. J.*, **2019**, *112*, 569–580.
12. A. Ourari; B. Ketfi; S. I. R. Malha; A. Amine; *J. Electroanal. Chem.*, **2017**, *797*, 31–36.
13. G. Mahalakshmi; K. N. Vennila; B. Selvakumar; P. L. Rao; R. Malwade; S. Deval; S. Madhuri; M. Seenivasaperumal; K. P. Elango; *J. Biomol. Struct. Dyn.*, **2020**, *38*, 3443–3451.
14. P. U. Maheswari; M. Palaniandavar; *J. Inorg. Biochem.*, **2004**, *98*, 219–230.
15. C. Metcalfe; J. A. Thomas; *Chem. Soc. Rev.*, **2003**, *32*, 215–224.
16. K. Abdi; H. Hadadzadeh; M. Weil; M. Salimi; *Polyhedron*, **2012**, *31*, 638–648.
17. H. Hadadzadeh; M. Salimi; M. Weil; Z. Jannesari; F. Darabi; K. Abdi; A. D. Khalaji; S. Sardari; R. Ahangari; *J. Mol. Struct.*, **2012**, *1022*, 172–180.
18. S. Dhar; F. X. Gu; R. Langer; O. C. Farokhzad; S. J. Lippard; *Proc. Natl. Acad. Sci.*, **2008**, *105*, 17356–17361.
19. S. Dhar; Z. Liu; J. Thomale; H. Dai; S. J. Lippard; *J. Am. Chem. Soc.*, **2008**, *130*, 11467–11476.
20. I. M. A. Mohamed; A. M. Abu-Dief; **2015**.
21. S. Sathiyaraj; G. Ayyannan; C. Jayabalakrishnan; *J. Serbian Chem. Soc.*, **2014**, *79*, 151–165.
22. T. J. Kistenmacher; T. Sorrell; L. G. Marzilli; *Inorg. Chem.*, **1975**, *14*, 2479–2485.
23. J. A. Carrabine; M. Sundaralingam; *J. Am. Chem. Soc.*, **1970**, *92*, 369–371.
24. A. Ourari; C. Zoubeydi; S. Bouacida; W. Derafa; H. Merazig; *Acta Crystallogr. Sect. E Crystallogr. Commun.*, **2015**, *71*, m33–m34.
25. S. Rayati; S. Zakavi; M. Koliaei; A. Wojtczak; A. Kozakiewicz; *Inorg. Chem. Commun.*, **2010**, *13*, 203–207.
26. F. Bedioui; E. Labbe; S. Gutierrez-Granados; J. Devynck; *J. Electroanal. Chem.*, **1991**, *301*, 267–274.
27. A. Jozwiuk; Z. Wang; D. R. Powell; R. P. Houser; *Inorg. Chim. Acta*, **394** (2013) 415–422
28. M. Roelsgaard; P. Nørby; E. Eikeland; M. Søndergaard; B. B. Iversen; *Dalt. Trans.*, **2016**, *45*, 18994–19001.
29. M. Vilas-Boas; C. Freire; B. De Castro; A. R. Hillman; *J. Phys. Chem. B*, **1998**, *102*, 8533–8540.
30. H. Kianfar; L. Keramat; M. Dostani; M. Shamsipur; M. Roushani; F. Nikpour; *Spectrochim. Acta Part A Mol. Biomol. Spectrosc.*, **2010**, *77*, 424–429.
31. C. S. Martin; T. R. L. Dadamos; M. F. S. Teixeira; *Sensors Actuators B Chem.*, **2012**, *175*, 111–117.
32. T. R. L. Dadamos; M. F. S. Teixeira; *Electrochim. Acta.*, **2009**, *54*, 4552–4558.
33. I. A. Chepurnaya; M. P. Karushev; E. V. Alekseeva; D. A. Lukyanov; O. V. Levin; *Pure Appl. Chem.*, **2020**, *92*, 1239–1258.
34. P. Audebert; P. Hapiot; P. Capdevielle; M. Maumy; *J. Electroanal. Chem.*, **1992**, *338*, 269–278.

35. J. H. Cameron; S. C. Turner; *J. Chem. Soc. Dalt. Trans.*, **1992**, 3285–3289.
36. A. Pui; I. Berdan; I. Morgenstern-Badarau; A. Gref; M. Perrée-Fauvet; *Inorg. Chim. Acta*, **2001**, *320*, 167–171.
37. J.-C. Moutet; A. Ourari; *Electrochim. Acta*, **1997**, *42*, 2525–2531.
38. M. Martins; M. V. Boas; B. de Castro; A. R. Hillman; C. Freire; *Electrochim. Acta*, **2005**, *51*, 304–314.
39. M. A. Thorseth; C. E. Tornow; C. M. Edmund; A. A. Gewirth; *Coord. Chem. Rev.*, **2013**, *257*, 130–139.
40. N. Li; Y. Ma; C. Yang; L. Guo; X. Yang; *Biophys. Chem.*, **2005**, *116*, 199–205.
41. A. Shah; M. Zaheer; R. Qureshi; Z. Akhter; M. F. Nazar; *Spectrochim. Acta Part A Mol. Biomol. Spectrosc.*, **2010**, *75*, 1082–1087.
42. G.-C. Zhao; J.-J. Zhu; J.-J. Zhang; H.-Y. Chen; *Anal. Chim. Acta*, **1999**, *394*, 337–344.
43. P. W. Rose; A. Pričić; A. Altunkaya; C. Bi; A. R. Bradley; C. H. Christie; L. Di Costanzo; J. M. Duarte; S. Dutta; Z. Feng; et al.; *Nucleic Acids Res.*, **2017**, *45*, D271–D281.
44. E. Alolayqi; M. Afzal; A. Alarifi; A. Beagan; M. Muddassir; *Crystals*, **2022**, *12*(1), 15.
45. E. Lanez; L. Bechki; T. Lanez; *Chem. Chem. Technol.*, **2019**, *13*, 11–17.
46. T. Lanez; H. Benaicha; E. Lanez; M. Saidi; *J. Sulfur Chem.*, **2018**, *39*, 76–88.
47. R. Vijayalakshmi; M. Kanthimathi; V. Subramanian; B. U. Nair; *Biochem. Biophys. Res. Commun.*, **2000**, *271*, 731–734.
48. C. Steffen; K. Thomas; U. Huniar; A. Hellweg; O. Rubner; A. Schroer; *J. Comput. Chem.*, **2010**, *31*, 2967–2970.

FABRICATING AND PROPERTIES OF RIFAMPICIN- LOADED ETHYL CELLULOSE COMPOSITES VIA ELECTROSPRAY

Xi LI^{a,b,c,d,e*} , Yanwen CHEN^a, Hong LI^a, Jiahao DING^a,
Ya WANG^a , Jin MO^f, Mi ZHOU^{a,d}, Yaning LI^e,
Qiuhan LIN^{e*} , Boliang WANG^e

ABSTRACT. Rifampin (Rif) is usually applied as first-line anti-tubercular drugs but has limited bioavailability. Herein, Rif-loaded ethyl cellulose (EC) composites was designed and fabricated by electrospray to improve therapy effectiveness and duration. A novel stable disk-like drug delivery system was prepared, and characterized by scanning electron microscopy (SEM), X-ray diffraction (XRD), Fourier transform infrared (FTIR) spectroscopy, differential scanning calorimetry (DSC), thermogravimetric (TG) analysis as well as *in vitro* release tests in phosphate buffer solution (PBS) at pH= 4.0 and pH= 7.4. The SEM results suggested EC/Rif composites had uniform circular surface and particle size distribution with an average size ranged from 7.11 μm to 7.37 μm . Rif can be physically and molecularly dispersed and incorporated into the EC matrix, as confirmed by the XRD, FTIR, DSC, and TG results. At pH 7.4, the rate of Rif release in EC/Rif composites improved with the increasing Rif content. For EC/Rif sample with equal mass ratio, the highest cumulative release of Rif

^a Bengbu University, Functional Powder Material Laboratory of Bengbu City, Bengbu 233030, P.R. China

^b University of Science and Technology of China, State Key Laboratory of Fire Science, Hefei 230026, P.R. China

^c Anhui University, Anhui Province Key Laboratory of Environment-friendly Polymer Materials, Hefei 230601, P.R. China

^d Anhui Xiangyuan Science and Technology Co., Ltd. Bengbu 233030, P.R. China

^e Nanjing University of Science and Technology, School of Chemical Engineering, Nanjing 210094, P.R. China

^f Bengbu Third People's Hospital Affiliated to Bengbu Medical University, intensive care unit, Bengbu 233030, P.R. China

* Corresponding authors: lixivip89@163.com, linqh@njust.edu.cn



reached 64.6% at the end of 24 h, while at pH 4.0 the Rif release was slower to 24.8% at 24h. These results suggested that EC/Rif composites fabricated by electro spray could be a promising strategy for controlling Rif delivery.

Keywords: *ethyl cellulose; rifampicin; electro spray; amorphous, drug delivery.*

INTRODUCTION

Tuberculosis (TB) caused by *Mycobacterium tuberculosis* seriously threatens public health around the world. 10.6 million new TB infections and 1.6 million deaths were reported in 2021 [1]. TB is a major global health concern and the incidence is still on the rise [2]. Many anti-TB agents have been developed and applied for the treatment of TB infections [3]. Rifampicin (Rif) with ansa ring structure represents one of the most powerful first-line anti-tubercular drugs because of its unique activity to inhibit bacterial RNA polymerase [4]. However, the Rif efficacy is limited mainly due to its insoluble in water, relatively short plasma half-life (2h) after oral administration and hepatotoxicity [5-6]. An effective strategy to improve therapy effectiveness and duration of Rif is to form micro/nano drug delivery systems by various methods. Rif-loaded nanoparticles with branched poly(lactic-co-glycolic acid) (PLGA) were prepared by nanoprecipitation method [7]. The research showed that Rif was molecularly dispersed and sustained Rif release could be ensured. Many steps such as centrifugation, redispersion cycles and freeze-dry involved in preparing samples may be the applicable limitation of the method. In another study, Rif-loaded PLGA particles were fabricated by solvent evaporation method [8]. The drawback during the sample preparation may be the excessive use of solvents. Tse J. Y. et al prepared Rif-loaded in branched cyclic dextrin dry powder inhalers using the spray-drying technique [9]. The relatively high inlet temperature at 130 °C may be detrimental to the activity of Rif during the preparation course.

Electrospraying, as a cost-effective and one-step technique, uses electrostatic force to prepare non-agglomerated micro/nanoparticles under room temperature [10]. At the moment, electrospraying has been a promising platform for pharmaceutical development and biomedical application [11-12]. Ethyl cellulose (EC) is permitted in good manufacturing without limited acceptable daily intake and widely used in pharmaceutical industry for controlled release of drugs [13]. Regrettably, there are few published reports on preparing EC/Rif drug delivery systems by electro spray method. Therefore, in this study, we loaded Rif into EC matrix by electrostatic spray. The detail properties of the EC/Rifs were explored through the characterization of morphology, structure

and thermal properties, as well as release behavior under acidic (pH 4.0) and physiological (pH 7.4) conditions. This study would add insights for the further development and application of EC/Rif delivery systems.

RESULTS AND DISCUSSION

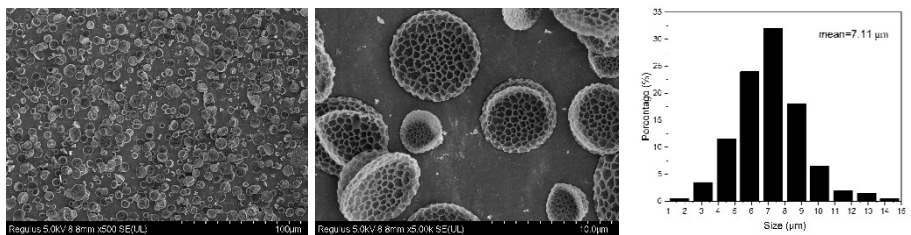
Morphology

Figure 1 shows representative SEM (Hitachi Regulus 8100) images of EC/Rif composites with different mass ratios of EC and Rif prepared by electrospay. Particle size distributions were obtained through the Nano Measurer software by counting 200 particles randomly. As shown in Figure 2, all EC/Rif particles exhibited circular surface with dense surface voids. As illustrated in Figure 1, mean particle sizes of 7.11, 7.13, and 7.49 μm were obtained for EC:Rif 3:1, EC:Rif 2:1, and EC:Rif 1:1, respectively. The results suggested that no significant change was found for the average particle sizes of prepared different EC/Rif composites.

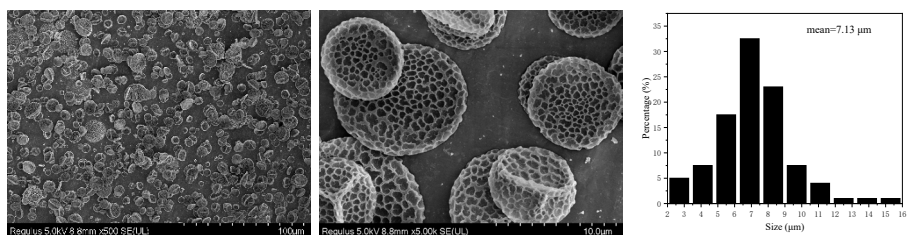
Structure analysis

Figure 2 shows the XRD (Rigaku Corporation SmartLab SE) and FTIR (Thermo Scientific Nicolet IS-10) measurements of EC, Rif, and EC/Rif composites. As shown in Fig. 2a, main peaks appeared approximately 7.5, 11.9, 13.8, 14.5, 16.3, 18.6, 20.5, 21.3, 22.3, 26.1, 29.4 and 36.7° in 2θ , indicating the crystalline nature of Rif [14]. There existed peaks at 2θ of 8.5° and 20.0° for pure EC with properties of semi-crystalline structures [12]. For EC/Rif composites prepared by electrospay, similar XRD patterns with EC and no peaks of Rif were found, which further confirming that the prepared composites are in amorphous state.

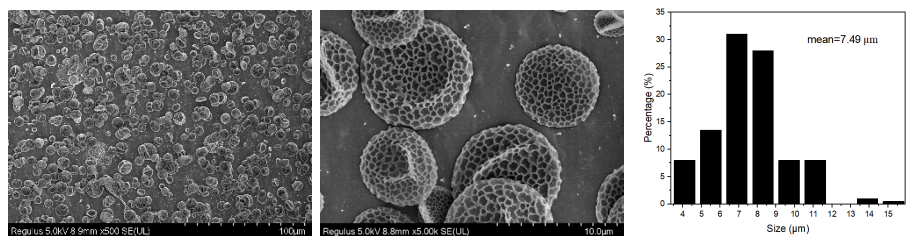
From the FTIR spectra of Rif in Figure 2b, characteristic peaks at 1725 cm^{-1} (C=O stretching of ester bond), 1244 cm^{-1} (C–O–C), and 941 cm^{-1} (–NH rocking) were observed [15]. For EC, the absorption about 1378 and 1110 cm^{-1} were found and related to C–H bending and C–O–C stretching at low wavenumber, respectively. The peak about 3480 cm^{-1} was related to –OH stretching and the peaks at 2975 cm^{-1} and 2862 cm^{-1} were corresponding to diverse C–H stretching modes [16]. For the FTIR spectra of EC/Rif composites, the main characteristic peaks of Rif became weaker than pure Rif, and the spectra were found similar to EC, and no new characteristic peak was observed. The results suggested that no new compounds were generated during the preparation of EC/Rif composites.



(1) F1



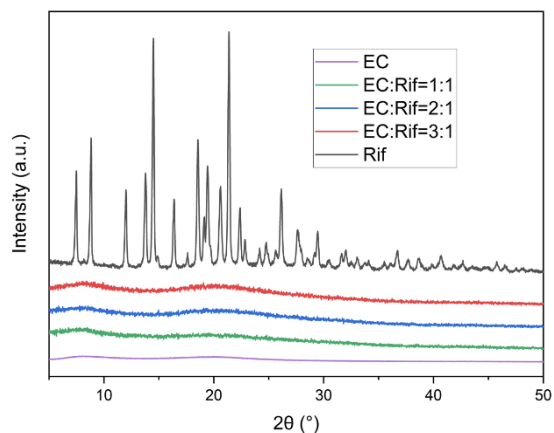
(2) F2



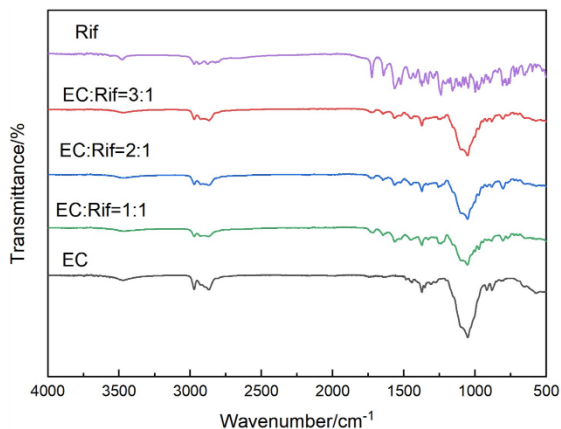
(3) F3

Figure 1. SEM results and particle size distribution of prepared EC/Rif composites

FABRICATING AND PROPERTIES OF RIFAMPICIN-LOADED ETHYL CELLULOSE COMPOSITES VIA ELECTROSPRAY



(a) XRD records



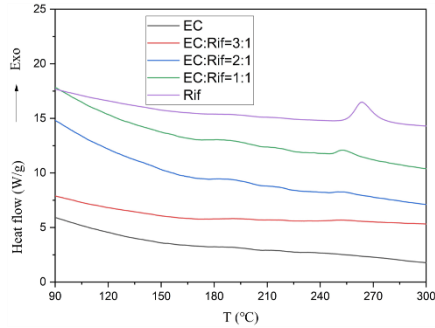
(b) FTIR results

Figure 2. XRD and FTIR records of pure EC, Rif, and EC/Rif composites

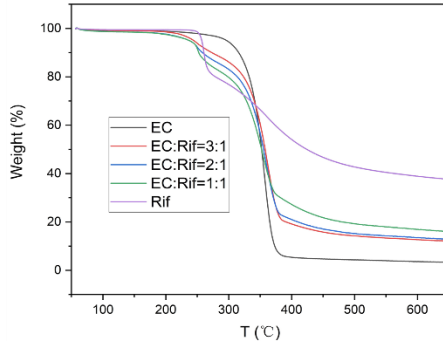
Thermal properties

Figure 3 shows the thermal behaviors of pure EC, Rif, and EC/Rif composites at different ratios measured by differential scanning calorimeter (DSC) (Mettler-Toledo DSC823e) and thermogravimetric (TG) analysis (Mettler-Toledo TGA/SDTA851e) with a heating rate of 10°C/min and N₂ flow rate of 50 ml/min. As shown in Figure 3a, there exhibits an obvious exothermic process [17] at 263.6 °C, and slighter lighter than the value of 240 °C reported in the literature [18]. Perhaps some of the other 3 % within the used Rif with 97 % purity might cause a slow increase of the exothermic temperature. For EC, no obvious melting and exothermic process were found. For EC/Rif composites,

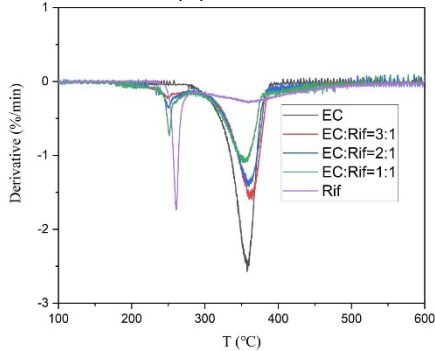
as the content of EC increases, the exothermic event belonging to Rif weakens significantly and even almost disappeared. The absence of a peak can be the indicator of complete conversion into an amorphous state [19]. The thermal events from DSC curves of the EC/Rif composites were similar to that of pure EC, indicating that Rif incorporated into EC in amorphous state, especially at higher EC content.



(a) DSC



(b) TGA



(c) DTG

Figure 3. DSC, TG/DTG thermograms of pure EC, Rif, and EC/Rif composites

The TG and derived thermogravimetry (DTG) profiles of pure EC, Rif and EC/Rif formulations are shown in Figure 3b and Figure 3c, respectively. The TG and DTG curves indicated that pure Rif was thermally stable until 240 °C, and two stages occurred for the thermal decomposition process. The first stage occurred rapidly between 240 and 280 °C with a mass loss about 20%, while the second occurred slowly between 280 and 550 °C with mass loss of 40%. Pure EC was found thermally stable up to 280 °C and the thermal decomposition event occurred in one sharp step in the ranges of 280–400 °C with mass loss of 95%. EC/Rif formulations presents two weight loss events, which could be corresponding to the thermal decomposition of the Rif, Rif and EC, respectively. The weight loss values for EC:Rif 3:1, EC:Rif 2:1, and EC:Rif 1:1 were about 11%, 14% and 17% for a temperature range of 200–280 °C, respectively. The first thermal decomposition event of the EC/Rif composites was advanced and became slow compared to that of pure Rif obtained from TG/DTG analysis. The results could be due to the presence of the dilution of Rif in the prepared EC/Rif formulations powders in the present work and corroborate with the characteristics presented by the literature [20]. The second weight loss event for EC:Rif 3:1, EC:Rif 2:1, and EC:Rif 1:1 were about 75%, 72% and 65% for a temperature range of 280–550 °C, respectively. These thermal analysis corroborating with the XRD and FTIR results of the EC/Rif composites evidenced that Rif was molecularly dispersed in EC matrix.

In vitro release behavior

In vitro drug release profiles of EC/Rif composites with different Rif contents are illustrated in Figure 4. Figure 4 showed that all EC/Rif composites exhibited a relatively fast release of Rif within 8 h, followed by a slow and sustained release as the time increased. As for EC:Rif 3:1 composite, nearly 12.8% of Rif was released at 8 h and 15.6% at 24h. The sample EC:Rif 2:1 showed about 17.2% Rif released at 8 h and 24.4% at 24h. In contrast, sample EC:Rif 1:1 showed the greatest burst release with approximately 54.1% of Rif over a 8 h period, and the highest cumulative release value with 64.6% at the end of 24h. Compared to about 63% of the Rif released after only 30 min from equal mass ratio of EC/Rif composites through supercritical anti-solvent process [21], the release behavior of the prepared EC/Rif composites by electrospray has a significant advantage.

The release profiles of Rif from the EC:Rif 1:1 microparticles for pH 7.4 and 4.4 buffer are presented in Figure 5. As seen, compared to pH 7.4, the Rif release value from the EC:Rif 1:1 particle was substantially reduced to 16.3 % at 8h and 24.8% at 24h at pH 4.0, respectively. Under acidic conditions,

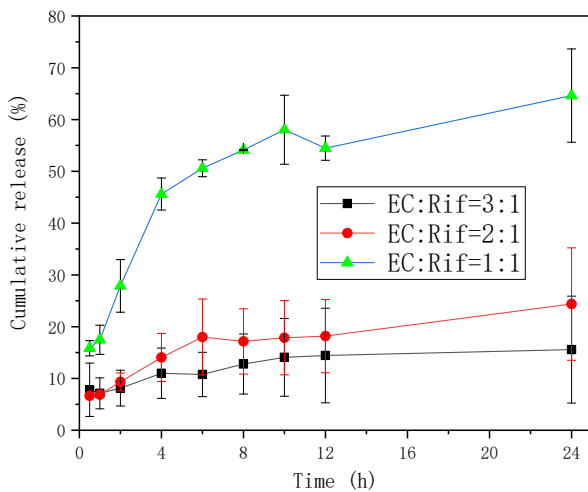


Figure 4. Rif release profile from EC/Rif composites

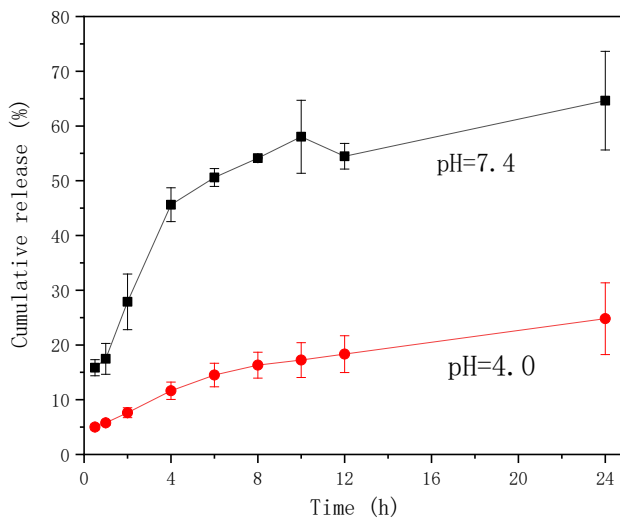


Figure 5 Comparison of Rif release profile from EC: Rif=1:1 formulation at pH with 7.4 and 4.0

the higher retention of Rif in the EC structure was pronounced. It was noticeable that all EC/Rif formulations behaved incomplete release after 24 h. The Rif release from EC/Rif matrices is proposed to be driven by the diffusion of Rif through the semicrystalline structure of EC at pH 7.4 [22]. The higher dissolution rate could be partly attributed to the increased amount of Rif located in the outer surface of EC/Rif composites [23] and the partial amorphous conversion of Rif at higher content, as confirmed by DSC. In addition, the increasing Rif content in the EC/Rif systems could result in a large concentration gradient, then the effective driving strength for diffusion increases, leading to an increase in Rif release rate and cumulative release [24]. While under the acidic condition of pH 4.0, the prevailing factors for the Rif release could be regarded as the solubilization of the EC matrix and the diffusion mechanism become less important [25].

CONCLUSIONS

In this research, we focused on improving the bioavailability and therapeutic efficacy of rifampin, also known as rifampicin, a first-line drug (antibiotic) used in tuberculosis treatment, by developing a novel drug delivery system using ethyl cellulose as a matrix, fabricated using electrospray technology, resulting in disk-like rifampin-loaded ethyl cellulose composites at micro-nano scale. The study suggests that this newly fabricated composite offer potential for controlled the antibiotic release, improving tuberculosis therapy by prolonging drug release and responding to varying pH conditions, thus enhancing rifampin's bioavailability. Notably, the study has limitations or potential challenges, such as scalability, interaction mechanism, and/or biocompatibility, which are crucial for translating these findings to real world applications (e.g. pharmaceutical products conditioning, dosage forms). Future researches will focus on the exploration of testing in *in vivo* models or investigating specific polymers other than cellulose.

EXPERIMENTAL SECTION

Materials

EC with chemically purity and Rif with 97% were purchased from Shanghai Aladdin Biochemical Technology Co., Ltd. China. Dichloromethane (DCM) with analytical grade was bought from Sinopharm Chemical Reagent Co., Ltd, China. Phosphate buffer solution (PBS) with pH = 7.4 was produced by Beijing Labgic Technology Co., Ltd. PBS with pH = 4.0 was bought from by Shanghai Yifen Scientific Instrument Co., Ltd.

Sample preparations

As shown in Figure 6, the EC/Rif composites was prepared by electro spray method, and the preparation process are as follows. Total mass of 0.3 g mixture with EC and Rif were weighted forming the mass ratio of 3:1, 2:1 and 1:1, respectively, and fully dissolved in 10 mL DCM. Magnetic stirring was applied to form uniform solution and named EC:Rif 3:1, EC:Rif 2:1, and EC:Rif 1:1, respectively. The prepared solution was pumped by a syringe pump (TYD01-02, Baoding Leifu Fluid Technology Co., Ltd) with 10-mL plastic syringe of 0.6 mm inner diameter stainless needle. A high-voltage power source (DW-P303-1, TianJin Dongwen High Voltage Power supply Corp) was applied to generate the electric field between the stainless nozzle and the collector with aluminum foil. Other electro spray parameters of prepared EC/Rif composites were as follows: flow rate was 1.5 ml/h, voltage value was 18 kV, collection distance was 15 cm. The EC/Rif composites were collected from the aluminum foil and then dried in a 50 °C oven for 2~3 hours before further use.

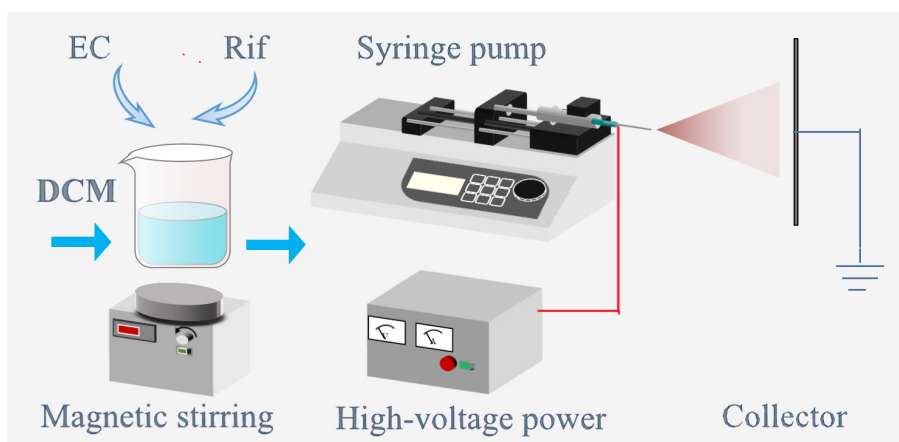


Figure 6. The schematic diagram of the EC/Rif preparation process

Drug release

Standard curve determination

Pure Rif was weighed in PBS solutions and fully dissolved to prepare a series of concentrations (5, 10, 15, 20, 30, and 50 mg/L). Absorbance was determined by a UV–Vis spectrophotometer (U3900 Hitachi, Japan) at 477 nm with pure PBS solution as reference. The equation of the standard curve of Rif was fitted and given below between the Rif concentration in the PBS solution

against the absorbance record (Figure 7): $C=0.03442\times\text{Abs}-0.07768$. The correlation coefficient R^2 was 0.9992, and the linear relation met well with the Beer–Lambert law.

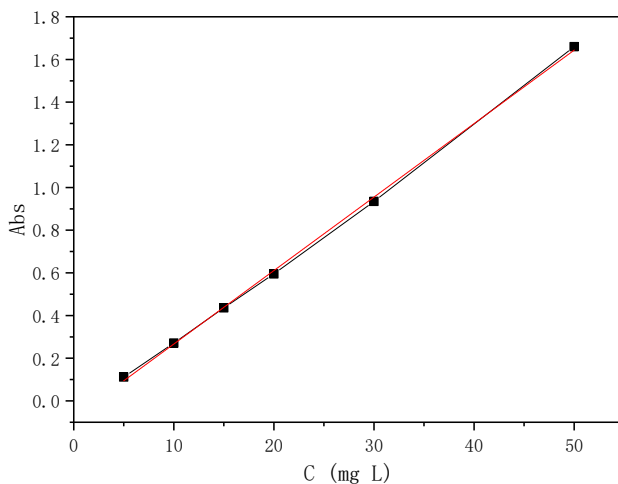


Figure 7. Standard calibration curve of Rif at 477 nm

In vitro drug release behavior

About 30 mg EC/Rif composites with three replicate samples were fully submerged in 100 mL of PBS buffer solution at a temperature of $37\pm 1^\circ\text{C}$ and 100 rpm using a desktop constant temperature oscillator (TH2-312, Shanghai Jinghong Experimental Equipment Co., Ltd, China). Fluid samples were obtained at 0.5 h, 1 h, 2 h, 4 h, 6 h, 8 h, 10 h, 12 h, and 24 h. Equal fresh PBS medium was added after each sampling time to maintain the volume of buffer. The absorbance of the fluid samples was measured by UV-vis spectrophotometer and then the released Rif content could be computed based on the standard curve of Rif.

ACKNOWLEDGMENTS

The project is funded by the Natural Science Research Projects of Universities of Anhui Province (2023AH052944), the Horizontal Subject (00011861, 00011860, 00013351, 00013356), and the applied research projects of Bengbu University (2024YYX48QD, 2024YYX36pj).

REFERENCES

1. S. Bagcchi. *The Lancet Microbe*, **2023**, 4: e20.
2. L. Yang; L. Zhuang; Z. Ye; L. Li; J. Guan; W. Gong. *Iscience*. **2023**, 26: 107881
3. Fernandes, G. F.; Thompson, A. M.; Castagnolo, D; Denny, W. A.; Dos Santos, J. L. *J. Med. Chem.*, **2022**, 65: 7489-7531.
4. L. Musciacchio; M. Mardirossian; B. Guagnini; A. Raffini; M. Rizzo; C. Trombetta; G. Liguori; G. Turco; D. Porrelli. *Mater. Design.*, **2022**, 224: 111286.
5. N. B. Bhatt, C. Barau, A. Amin, E. Baudin, B. Meggi, C. Silva, V. Furlan, B. Grinsztejn, A. Barrail-Tran, M. Bonnet, A. M. Taburet. *Antimicrob. Agents Ch.*, **2014**, 58: 3182-3190.
6. K.M. Kainat; M. Ansari; N. Bano; P.R. Jagdale; A. Ayanur; M. Kumar; P.K. Sharma. *Life Sci.*, **2023**, 333: 122164.
7. E. Snejdrova; J. Loskot; J. Martiska; T. Soukup; L. Prokes; V. Frolov; T. Kucera. *J. Drug. Deliv. Sc. Tech.* **2022**, 73: 103435.
8. C. Castañeda-Fernandez; R. M. Chávez-Santos; M. Silva-Miranda; C. Espitia-Pinzón; R. Martínez; A. Kozina. *Int. J. Pharmaceut.*, **2022**, 622: 121844.
9. J. Y. Tse. K. Kadota; Y. Hirata; M. Taniguchi; H. Uchiyama; Y. Tozuka. *J. Drug. Deliv. Sc. Tec.*, **2018**, 48: 137-144.
10. A. Tanhaei; M. Mohammadi; H. Hamishehkar; M.R. Hamblin. *J. Controll. Release.*, **2021**, 330: 851-865.
11. S. Liu; Z. Fang; K. Ng. *Food. Biosci.*, **2023**, 56: 103307.
12. Q. Wang; W. Xu; Q. Li; C. He; Y. Liu; J. Liu; R. Wang; J. Wu; D. C. Chen. *Int. J. Pharmaceut.*, **2023**, 643: 123220.
13. X. Ma; Y. Liu; L. Fan; W. Yan. *Carbohydr. Polym.*, **2021**, 252: 117169.
14. D. Jing; Y. Gu; H. Xia. *Chem. Eng. Techno.*, **2018**, 41: 1236-1243.
15. J. Shi; H. Zhao; F. Wu, X. Gan. *J. Mater. Res.*, **2021**, 36: 487-498.
16. J.T. Orasugh; N. R. Saha; G. Sarkar; D. Rana; R. Mishra; D. Mondal; S.K. Ghosh; D. Chattopadhyay. *Carbohydr. Poly.*, **2018**, 188: 168-180.
17. O. Londhe; S. S. Mane; B. U. Hirlekar; A. Subbevarapu; A. E. Viju; V. A. Dixit; S. J. Dengale. *Eur. J. Pharm. Biopharm.* **2023**, 188, 54-65.
18. S.Q. Henwood; W. Liebenberg; L.R. Tiedt; A.P. Lötter; M.M. De Villiers. *Drug. Dev. Ind. Pharm.*, **2001**, 27: 1017-1030.
19. M. Fujimori; K. Kadota; K. Shimono; Y. Shirakawa; H. Sato; Y. Tozuka. *J. Food Eng.*, **2015**, 149: 248-254.
20. P. Khadka; P. C. Hill; B. Zhang; R. Katare; J. Dummer; S. C. Das. *Int. J. Pharmaceut.*, **2020**, 587: 119602.
21. R. Djerafi; A. Swanepoel; C. Crampon; L. Kalombo; P. Labuschagne; E. Badens; Y. I. Masmoudi. *Eur. J. Pharm. Sci.*, **2017**, 102: 161-171.
22. B. S. Rao; K. V. R Murthy. *Int. J. Pharmaceut.*, **2002**, 231: 97-106.
23. C. Sun; L. Zou; Y. Xu; Y. Wang. *Macromol. Mater. Eng.*, **2020**, 305: 2000457.
24. P. Pankongadisak; S. Sangklin; P. Chuysinuan; O. Suwanton; P. Supaphol. *J. Drug. Deliv. Sc. Tech.* **2019**, 53: 101121.
25. M. L. Manca; G. Loy; M. Zaru; A. M. Fadda; S. G. Antimisiaris. *Colloids Surfaces B*, **2008**, 67: 166-170.

EVALUATION OF THE POZZOLANIC ACTIVITY OF METAKAOLIN, GLASS POWDER AND SILICA POWDER FOR USE IN CEMENTITIOUS MORTARS

Issiaka SANOU^a, Saada ZOUNGRANA^a, Moussa OUEDRAOGO^a ,
Ali SANOU^{b,c,*} , Younoussa MILLOGO^a 

ABSTRACT. The objective of this study is to evaluate the pozzolanic activity of metakaolin, glass powder and silica powder for use in cementitious mortars. Thus, metakaolin was produced by calcination at 700 °C of a clay soil from Burkina composed of kaolinite (62 wt.%), quartz (30 wt.%) and goethite (6 wt.%). Glass powder consists of amorphous silica and silica powder essentially contains quartz. The chemical characterization of materials showed that the metakaolin and the silica powder belong to the category of type F pozzolans while the silica powder would be type N. The lime saturation test reveals low kinetics of lime fixation by the silica powder. On the other hand, the rate of lime fixation by metakaolin and glass powder increases with treatment time. The pozzolanic index of metakaolin and glass powder at 28 and 90 days is higher than the minimum value of 75% required by the ASTM C618 standard. The presence of metakaolin and glass powder within the cement matrix improves the compressive strength of the resulting mortars due to their good pozzolanic reactivity inducing the formation of calcium silicates hydrated (CSH). Metakaolin and glass powder are therefore suitable for replacing cement in the production of mortars in the construction field.

Keywords: Glass powder, Metakaolin, Silica powder, Cementitious mortars, Compressive strength.

^a Université Nazi BONI, Unité de Formation et de Recherche en Sciences Exactes et Appliquées (UFR/SEA), Laboratoire de Chimie et Energies Renouvelables (LaCER), Bobo-Dioulasso, B.P. 1091 Bobo 01, Burkina Faso.

^b Institut National Polytechnique Félix Houphouët Boigny, Unité Mixte de Recherche et d'Innovation en Sciences Agronomiques et Procédés de Transformation (SAPT), Laboratoire des Procédés Industriels de Synthèses de l'Environnement et des Energies Nouvelles (LAPISEN), BP 1313 Yamoussoukro, Côte d'Ivoire.

^c Ecole Normale Supérieure, Laboratoire des Sciences Physiques Fondamentales et Appliquées (LSFPA), 08 BP 10 Abidjan, Côte d'Ivoire.

* Corresponding author: ali.sanou@inphb.ci / sanouali2007@yahoo.fr



INTRODUCTION

Cement is a necessary material for carrying out construction projects. Unfortunately, its production is energy-intensive and not ecological [1-3]. Also, cementitious materials are confronted with certain pathologies such as alkaline reactions, attacks by sulfate ions and the diffusion of chloride ions, which considerably reduce the lifespan of cementitious products [4, 5]. To remedy these problems linked to cement, several solutions are being considered, including the use of pozzolanic additions to cement production [6]. Among these pozzolanic additives, metakaolin and glass powder have been the subject of several scientific studies [7–10].

Indeed, metakaolin is a material obtained by dehydroxylation of kaolinite between 650 °C and 850 °C [11]. Its use as a cement additive makes it possible to improve the properties of composites in terms of durability, mechanical strength and resistance to chemical attack [12, 13]. This is how the studies carried out by Sinngu et al showed an increase of approximately 30% in the long-term compressive mechanical strength of mortars containing metakaolin compared to the reference mortar [14]. Also, the drying shrinkage of the mortars was reduced by approximately 50%, after the incorporation of 10 to 15 wt.% of metakaolin in the mixtures. As for the glass powder, it comes from the crushing of glass bottles. In most developing countries, glass bottles are most often thrown into the environment after use, which constitutes environmental waste. Its use as a pozzolan constitutes a solution to preserving the environment. The work carried out on glass powder has also produced convincing results [7, 15]. For Wang et al, the initial mechanical strength of mortars containing glass powder is greater than that of the reference mortar not containing glass powder [15]. Furthermore, to our knowledge, little work has been devoted to the pozzolanic reactivity of silica powder [16]. Although glass powder and metakaolin have been the subject of studies with a view to their valorization as cement additives, the substitution rates vary from one author to another author. Thus, according to Harbi et al, the addition of 25 wt.% metakaolin in mortars contributes to improving their mechanical resistance and durability thanks to its pozzolanic character which reduces porosity and also water absorption [7]. For Malla et al, the addition of 12 wt.% metakaolin and 10 wt.% glass powder leads to a considerable improvement in the split tensile strength of concrete and can therefore be recommended as a potential mixture [17].

Thus, the objective of this present work is to evaluate the pozzolanic activity of metakaolin, glass powder and silica powder for use in cementitious mortars. This involves developing ecological materials that can optimally replace cement in the formulation of mortars. To do this, the materials will first

be characterized and then their pozzolanic activity will be evaluated through Frattini tests, lime saturation and determination of the pozzolanic index. Finally, their influence on the compressive mechanical strength of mortars will be studied.

RESULTS AND DISCUSSION

Materials characterization

The heat treatment of clayey materials results in the dehydration of some of its components. Thus, the hydroxyl groups of goethite and kaolinite become detached from the initial structures. In order to better understand the dehydroxylation process, infrared spectra of raw clay and metakaolin obtained by calcination at 700 °C with a heating rate of 10 °C/min for 2 hours were carried out. Figure 1 highlights the comparison of the infrared spectra of the raw clayed material and that thermally activated at 700 °C.

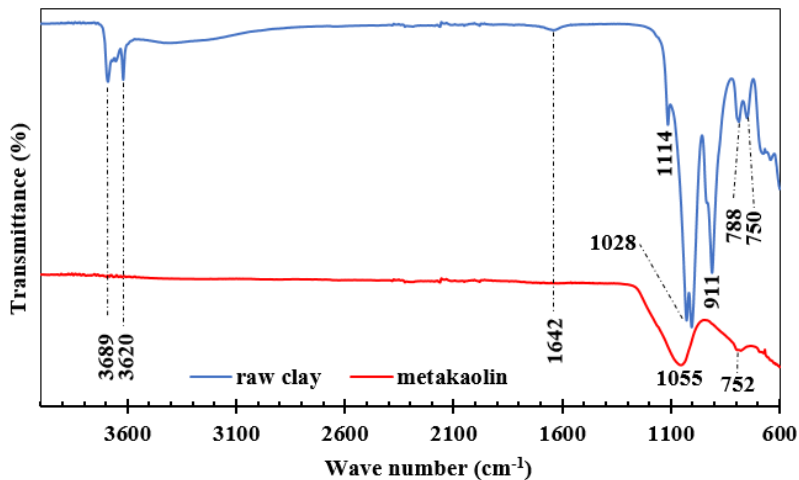


Figure 1. Infrared spectra of raw clay and metakaolin

The analysis of Figure 1 shows that all the characteristic bands of kaolinite have disappeared. Thus, at high frequencies, the disappearance of the bands at 3689 cm⁻¹ and 3620 cm⁻¹ of the hydroxyl groups of kaolinite is due to the effect of heat treatment [9,18]. Furthermore, the characteristic bands of the Si-O bond of kaolinite at 1114 cm⁻¹ and 1028 cm⁻¹, initially present in the raw clay, were transformed into a single wide band around 1055 cm⁻¹ attributed to the asymmetry of Si-O-Al and Si-O-Si vibrations of amorphous

silica [19]. The deformation vibration band of adsorbed water contained in the raw material at 1642 cm^{-1} also disappeared [20]. The band at 911 cm^{-1} of the Al-OH bond of kaolinite is also absent. The disappearance of the Si-O-Al bands (788 cm^{-1} and 750 cm^{-1}) of kaolinite against the band at 752 cm^{-1} for metakaolin seems to indicate a distortion of the tetrahedral layers of the SiO_4 group and the octahedral layers. The infrared spectrum of the glass powder (Figure 2) shows only two bands around 1000 cm^{-1} and 764 cm^{-1} which could be attributed to amorphous silica. The bands at 1140 cm^{-1} and 775 cm^{-1} of the silica powder are due to the Si – O – Si bond of the quartz [9].

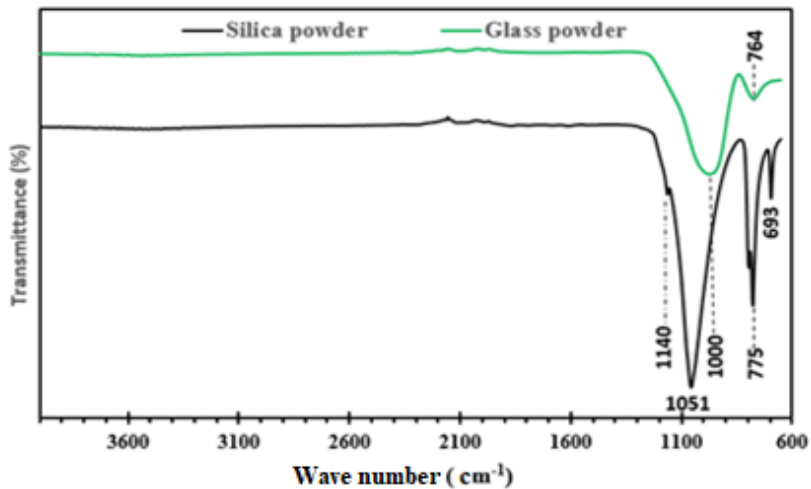


Figure 2. Infrared spectra of glass powder and silica powder

It appears from the analysis of the infrared spectra that the heat treatment at $700\text{ }^{\circ}\text{C}$ results in the transformation of the kaolinite from the clay raw material into an amorphous phase which is metakaolinite.

The diffractogram of the glass powder in Figure 3 shows a halo around 22° (2θ) showing the disorder reigning in the material. This disorder could characterize the presence of amorphous phases within the glass powder [21]. Silica, the main element of glass powder, is then in amorphous form and will give it good pozzolanic reactivity [22]. Analysis of the diffractogram (Figure 4) of the silica powder shows that it is essentially made up of quartz. The chemical composition of the materials is recorded in Table 1. Analysis of the table shows that the samples are mainly composed of silica. Metakaolin is particularly rich in alumina and iron oxide due to the mineralogical composition of the clayey raw material. Glass powder contains a high content of SiO_2 ,

EVALUATION OF THE POZZOLANIC ACTIVITY OF METAKAOLIN, GLASS POWDER AND SILICA POWDER FOR USE IN CEMENTITIOUS MORTARS

CaO and Na₂O. Furthermore, the sum of the oxides SiO₂, Al₂O₃ and Fe₂O₃ is greater than 70 wt.%, according to the ASTM C 618 standard, metakaolin, and silica powder belong to the class of type F pozzolans [23]. However, the CaO content of the glass powder is greater than 10 wt.%, so it belongs to the category of N-type pozzolans [24].

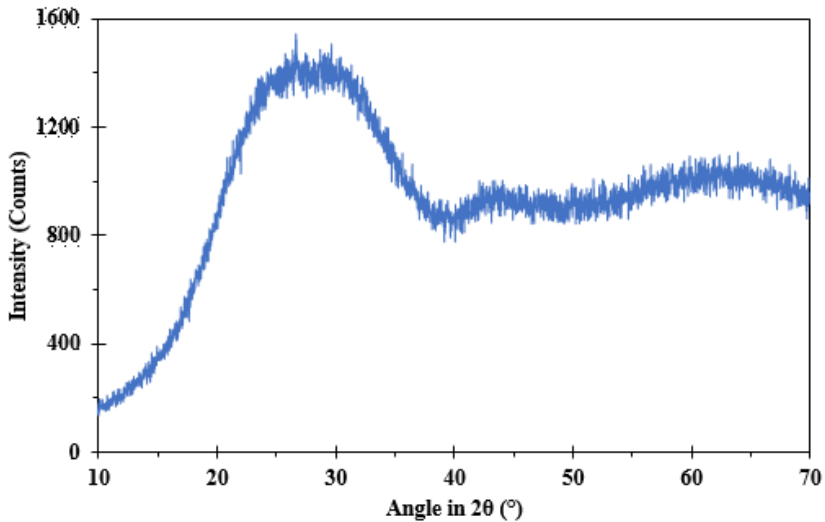


Figure 3. Diffractogram of glass powder

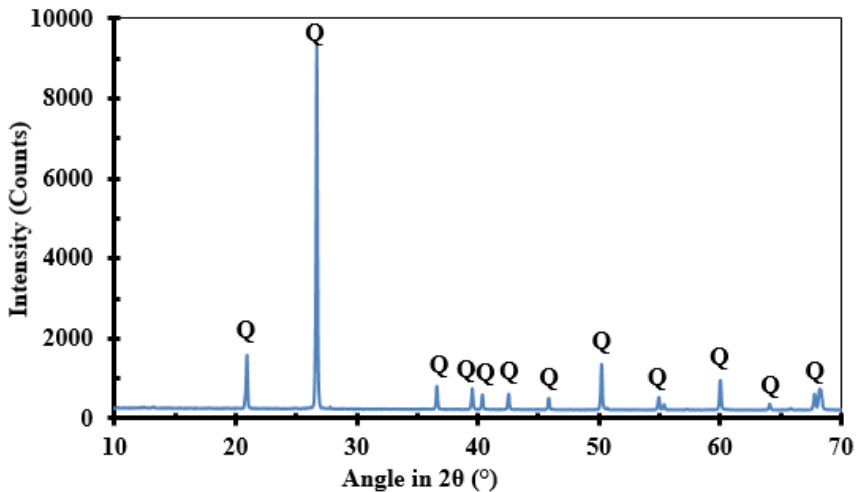


Figure 4. The diffractogram of silica powder

Table 1. Chemical composition of materials

Oxide (wt.%)	SiO ₂	Al ₂ O ₃	Fe ₂ O ₃	MgO	CaO	Na ₂ O	K ₂ O	TiO ₂	LOI ^a
MK	59.38	24.64	5.36	0.08	0.04	0.08	0.10	0.47	9.68
GP	76.77	1.17	0.48	1.65	11.15	10.28	0.40	-	0.57
SP	86.67	9.82	0.10	0.05	0.13	0.16	0.07	0.3	2.7

MK : metakaolin ; GP : glass powder ; SP : silica powder ; ^a Loss on ignition at 1000 °C

Pozzolan activity of materials

Results of Frattini and lime saturation tests

The results of the Frattini test are shown in Figure 5. Analysis of the figure shows that the silica powder does not exhibit any pozzolan activity because it is above the solubility curve of portlandite. On the other hand, glass powder and metakaolin are found below the solubility curve of portlandite, which highlights their pozzolan activity [1, 24]. The results of the lime saturation test are presented in Figure 6. Analysis of the figure shows that the lime fixation rate of the materials is a function of the treatment time. From the first 24 hours, metakaolin presents strong lime consumption kinetics with a fixation rate greater than 50%. This strong reactivity of metakaolin is due to its chemical composition. In fact, metakaolin is rich in silica, alumina and iron oxide which constitute the reactive phases of a pozzolan. According to Seynou et al, pozzolan reactivity at a young age is governed by the chemical composition, more precisely the silica, alumina and iron oxide content of a pozzolan [9]. Glass powder and silica powder have a rate fixation of 35.26 and 36.92% respectively, these values are slightly higher than the value of 35% which constitutes the lime fixation rate at this age of commercial metakaolins [16]. From 3 days, the pozzolan reactivity of the glass powder increases significantly with a lime fixation rate of more than 99% at 28 days. The good pozzolan reactivity of glass powder would be due to its amorphous character [22]. Also, metakaolin has good reactivity between 7 and 28 days but less than glass powder. The lime fixation rate of silica powder is low from the 3rd day and becomes almost constant between 7 and 28 days. This low reactivity would be due to the high quartz content in the silica powder which would constitute an impurity and therefore hamper the pozzolan reactivity.

EVALUATION OF THE POZZOLANIC ACTIVITY OF METAKAOLIN, GLASS POWDER AND SILICA POWDER FOR USE IN CEMENTITIOUS MORTARS

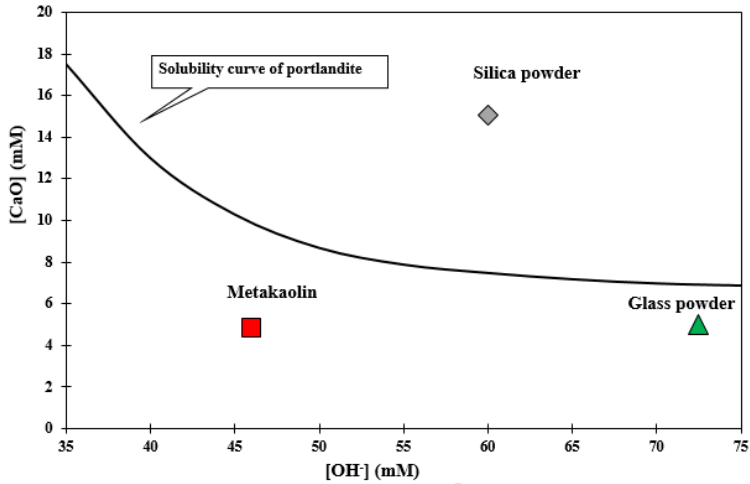


Figure 5. Results of the Frattini test of materials

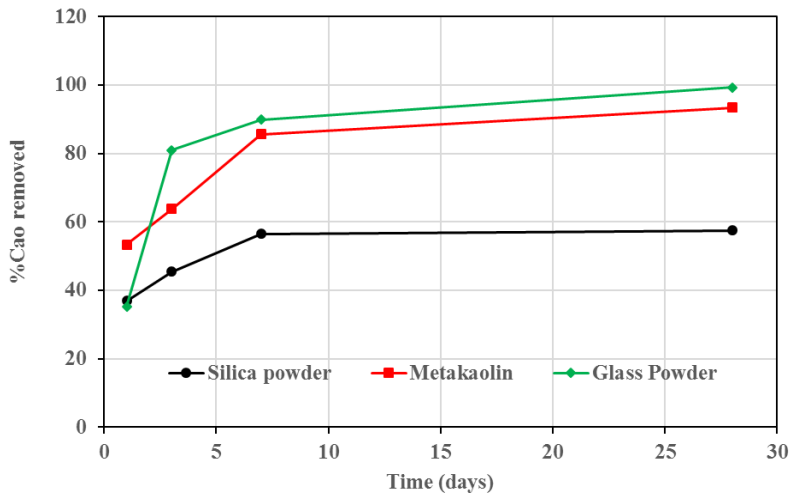


Figure 6. Results of lime saturation test of materials

Pozzolanic activity index

The pozzolanic activity index was evaluated from the mechanical compressive strength at 7, 28 and 90 days of age of the mortars containing a partial replacement of 25 wt.% of Portland cement by the materials and those containing only cement. The various results obtained are recorded in

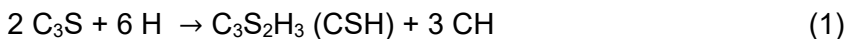
Table 2. Analysis of the table shows that the evolution of the pozzolanic index of the materials is almost similar to their lime fixation kinetics highlighted by the lime saturation test. Thus at 7 days, metakaolin displays the best pozzolanic index. From 28 days to 90 days, glass powder presents the highest value of the pozzolanic index followed by metakaolin. Silica powder has a pozzolanic index that is almost low and constant over time. The pozzolanic index values of the materials are then due to their pozzolanic reactivity. Indeed, pozzolanic reactivity favors the consumption of portlandite in favor of calcium silicates hydrated (CSH), hydrates responsible for the mechanical strength of the mortar. Mortars containing metakaolin and glass powder at 28 and 90 days of age display a pozzolanic index higher than the minimum value of 75% required by the ASTM C 618 standard for a pozzolanic material [23].

Table 2. Pozzolanic index of materials

Materials	Pozzolanic index		
	7 days	28 days	90 days
Glass powder	71.43	92.52	106.19
Metakaolin	78.12	82.64	93.99
Silica powder	67.59	73.35	74.86

Mineralogical characterization

The pozzolanic reactivity of the materials was monitored through the analysis of infrared spectra (Figure 7) carried out on the specimens produced after 28 days of curing. Table 3 summarizes the different bands obtained as well as their attribution. The portlandite (CH) band at 3600 cm^{-1} is intense at the level of the specimens containing silica powder, thus showing its strong release in this mixture. On the other hand, this band is present in metakaolin-lime and glass-lime powder mixtures but less intense. Also, we note an absence of the band around 3500 cm^{-1} of calcium silicates hydrated for the mixture containing silica powder and lime. This reflects the low or non-pozzolanic reactivity of this material as highlighted by the Frattini tests, lime saturation and the pozzolanic index. Indeed, in the presence of water, amorphous silica reacts with lime to form CSH, thus reflecting the pozzolanic reactivity of the material. The calcium silicates hydrated are obtained in two ways. First, when mixing cement with water, the dicalcium silicates (C_2S) and tricalcium silicates (C_3S) of cement react with the water molecules, thereby producing hydrated calcium silicates (CSH) and portlandite (CH) following reactions (1) and (2) [18, 25]:



EVALUATION OF THE POZZOLANIC ACTIVITY OF METAKAOLIN, GLASS POWDER AND SILICA POWDER FOR USE IN CEMENTITIOUS MORTARS

CSH are also formed by pozzolanic reactions involving amorphous silica and portlandite previously released by the hydration of cement. This pozzolanic reaction takes place in three phases described by reactions (3), (4) and (5) [26]:

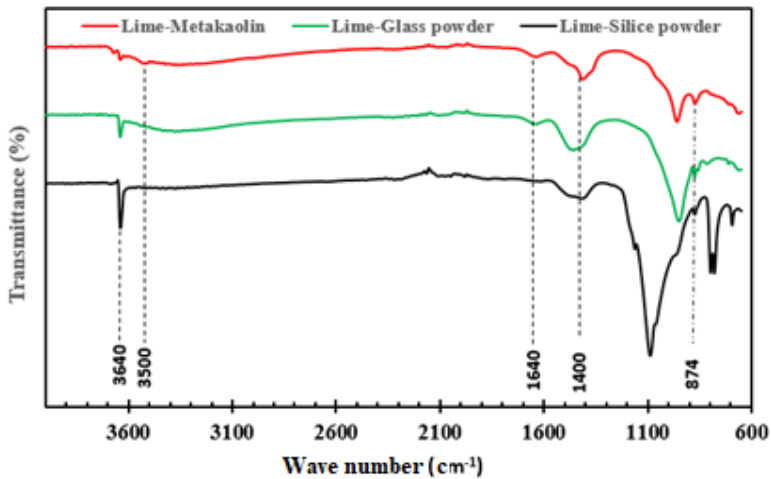
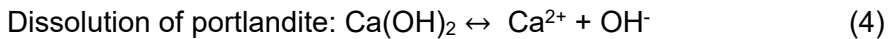


Figure 7. Infrared spectra of specimens

Formation of CSH after solubilization of silica:



The presence of calcite is highlighted through the bands around 1400 and 874 cm^{-1} . This calcite (CaCO_3) comes from the carbonation of portlandite (Ca(OH)_2) following the chemical reaction (6) [18]:



Table 3. Bands attribution

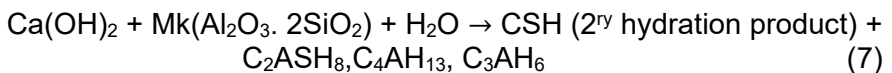
Wave number (cm^{-1})	attribution	References
3640	Portlandite (CH)	[9]
3500-3400	CSH hydrate	[9,26]
1640	Hydration water	[27]
1400-1440	Calcite (CaCO_3)	[28]
874	Calcite (CaCO_3)	[26]

Influence of materials on the mechanical strength of cement mortars

After the study of pozzolanic reactivity, cementitious mortars were manufactured by partial substitution of cement with different materials. Then, their mechanical compressive behavior was studied. Figure 8 shows the evolution of the mechanical compressive strength after 90 days of curing depending on the content of the materials in the cementitious mortars. Analysis of the figure shows that the evolution of the mechanical strength is of the same order as the pozzolanic reactivity of the materials. Indeed, according to the results of the lime saturation test in Figure 6, glass powder had the best lime fixation rate followed by metakaolin. Similarly, the pozzolanic indices from 28 days of glass powder (Table 2) were higher than those of metakaolin and silica powder.

Thus, mortars containing 20 wt% of glass powder present the best compressive strength values (54.8 MPa) followed by mortars amended with 15 wt% of metakaolin (49.55 MPa). The mechanical compressive strength of mortars containing silica powder drops beyond 10 wt.% substitution. The improvement in the mechanical resistance of mortars would be due to the formation of CSH resulting from the hydration reaction of the anhydrous compounds of cement (C_3S and C_2S) and by pozzolanic reaction following reactions (1), (2), (3), (4) and (5) described previously [18, 25].

For Suzan et al, the improvement in the compressive strength of cement mortars amended with metakaolin is mainly attributed to the pozzolanic effect of metakaolin present in the cement matrix which could be detailed as follows: when water is added to the cement-metakaolin mixture, free calcium hydroxide (CH) is released and its concentration increases due to the initial hydration of the cement [29]. The silica and alumina of metakaolin react with calcium hydroxide to form secondary hydration products mainly in the form of hydrated calcium silicate (CSH) with the formation of calcium aluminate hydrates (C_2ASH_8 , C_4AH_{13} , C_3AH_6) which were precipitated upon saturation according to the reaction equation (7):



With : C = CaO ; S = SiO₂ , A = Al₂O₃ and H = H₂O

These secondary hydration products serve as micro-fillings which leads to a reduction in the total porosity of the pastes and therefore an increase in the total content of the bonding centers in the mortars consequently causing an increase in their compressive strength values. According to Wang et al, the improvement in the mechanical compressive strength of cement

EVALUATION OF THE POZZOLANIC ACTIVITY OF METAKAOLIN, GLASS POWDER AND SILICA POWDER FOR USE IN CEMENTITIOUS MORTARS

mortars amended with glass powder would be attributed not only to their pozzolanic reaction but also to the filler effect of filling the pores of the mortars with the powder [15]. The low mechanical resistance values of mortars containing silica powder are due to their low pozzolanic reactivity which would be attributable to their crystalline structure. According to studies carried out by Seynou et al, quartz has no pozzolanic reactivity, only its filler character can contribute to improving the mechanical resistance of mortars [9].

The reduction in the mechanical compressive strength of mortars amended with metakaolin and glass powder would be due to the excessive presence of these materials in the mortars. Indeed, the presence of impurities in metakaolin could negatively influence the formation of hydrates responsible for the good mechanical strength of mortars. The drop in mechanical strength beyond 20 wt.% of the glass powder would be due to the low presence of portlandite to ensure pozzolanic reactivity.

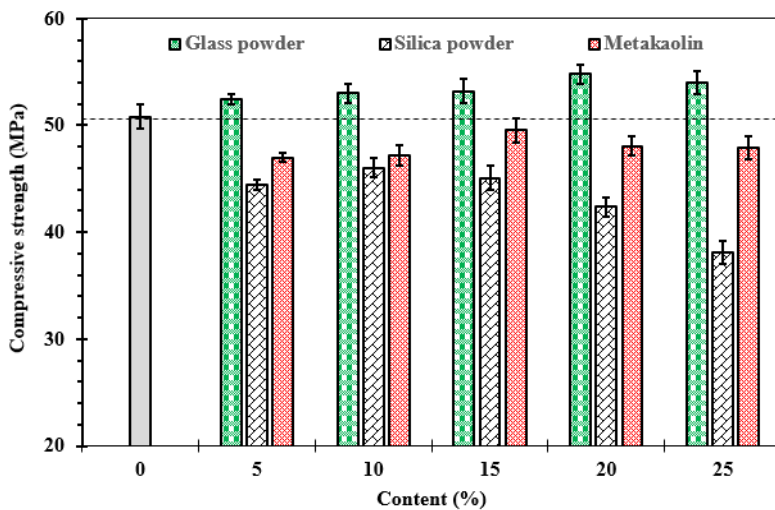


Figure 8. Mechanical compressive strength at 90 days of different mortars

CONCLUSIONS

The objective of this study was to evaluate the pozzolanic activity of metakaolin, glass powder and silica powder for use in cementitious mortars. From the various results obtained, the following remarkable conclusions emerge:

(1) Glass powder and metakaolin consist of amorphous silica and silica powder contains crystalline quartz. Metakaolin and silica powder belong to the class of type F pozzolans and glass powder belongs to the category of type N pozzolans.

(2) the Frattini test showed that metakaolin and glass powder have pozzolanic activity while silica powder does not. The results of the lime saturation test showed rapid lime fixation kinetics of metakaolin at 1 day and from 3 days the glass powder, due to the amorphous structure, fixes lime more than other materials. Silica powder has a low and almost constant lime fixation rate over time.

(3) the values of the pozzolanic index of the materials are of the same order of evolution as their pozzolanic reactivity with an index higher than the minimum value of 75% fixed by the ASTM C618 standard from 28 days for glass powder and metakaolin.

(4) the partial replacement of cement with glass powder and metakaolin improves their compressive strength after 90 days of curing. This improvement is due to the pozzolanic reactivity of these materials and their effect of filling the pores within the cement matrix.

In short, the metakaolin and glass powder obtained could be used at respective contents of 15 wt.% and 20 wt.% as cement substitutes in the elaboration of mortars.

EXPERIMENTAL SECTION

Raw materials

Metakaolin was produced from Burkina clayey soil taken from the rural commune of Saaba (12° 22' North and 1° 26' West). This raw material has been the subject of previous scientific work [18,30]. Analysis of the diffractogram (Figure 9) of this raw material shows that it contains kaolinite, quartz and goethite as crystalline phases. The content of each of these phases is recorded in Table 4. The presence of kaolinite in high content in the clay raw material shows that it can be used for the formulation envisaged. Indeed, kaolinite is a precursor for obtaining metakaolinite, which is the reactive phase of metakaolins. Quartz improves the hydration of cement and contributes to the pozzolanic reaction [1]. Thus, metakaolin was produced by calcination at a temperature of 700 °C with a heating rate of 10 °C/min for 2 hours. The choice of this temperature is based on the analysis of the Differential thermal analysis (DTA) curve of the clay raw material so as to be located between the phenomena of dehydroxylation of kaolinite at 538 °C

and recrystallization of metakaolinite at 973 °C (Figure 10). Also, this value is between 650 and 850 °C which constitutes the temperature interval provided by the literature [11].

Indeed, thermal activation leads to the dehydroxylation of the kaolinite of the raw material into metakaolinite according to the reaction equation (8) [18, 31]:

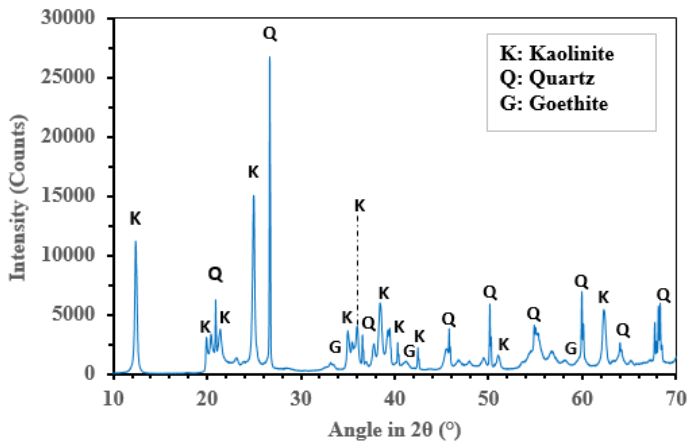
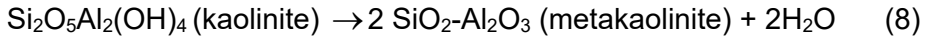


Figure 9. X-ray diffractogram of clayey raw material

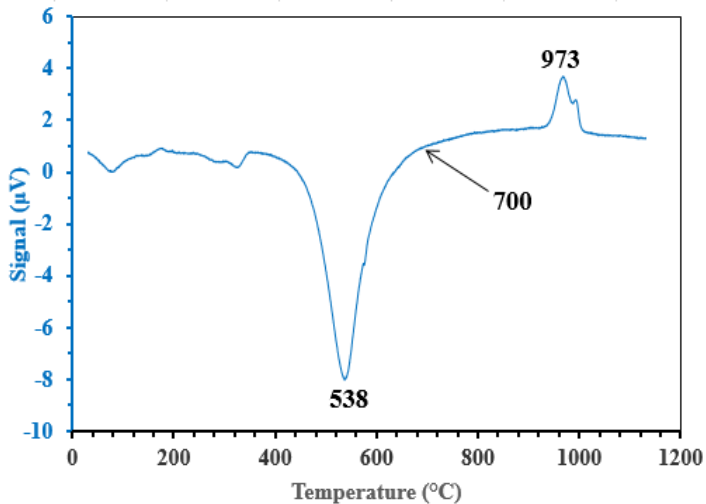


Figure 10. DTA curve of the clayey raw material

Table 4. Mineral phases composition of clayey raw material

Mineral	Kaolinite	Quartz	Goethite	Total	Balance
Composition (wt. %)	62	30	6	98	2

The glass powder was obtained by grinding to a particle size of 45 μm used glass which was collected from landfills in the town of Bobo Dioulasso in Burkina Faso.

As for the silica powder, it was taken from a quarry in the town of Bobo Dioulasso in Burkina Faso and it has also been the subject of previous work [32]. The cement used for the mortars manufacturing is a CEM II with strength class 42.5 MPa from the manufacturing company CIMAF in Burkina Faso. The chemical, mineralogical composition and some physical properties of this cement are recorded in Table 5.

Table 5. Chemical, mineralogical composition and some physical properties of the cement used

Chemical composition	SiO ₂	Al ₂ O ₃	Fe ₂ O ₃	CaO	MgO	SO ₃	K ₂ O	N ₂ O
(wt. %)	21.44	5.38	2.93	55.45	4.87	1.8	0.65	0.23
Mineralogy	C ₃ S		C ₂ S		C ₃ A		C ₄ AF	
(wt. %)	17.38		48.36		9.3		8.92	
Physical Properties	Apparent density	Specific area (cm ² /g)		Water content (%)		Setting start time (min)		
Value	1.18	3969		29		≤ 120		

Chemical and mineralogical characterization

The chemical composition of the materials was determined by inductively coupled plasma atomic emission spectrometry (ICP-AES) using an ICPE-9800 type spectrometer. The solutions were carried out by dissolving the samples with lithium tetraborate (Li₂B₄O₇). The mineral phases within the samples were identified by coupling X-ray diffraction (XRD) and Fourier transform infrared spectrometry (FT-IR). The powder diffractogram was recorded with a Bruker AXS diffractometer using CuK α radiation as the radiation source and graphite monochromator. The infrared spectrometer used for the identification of the functional groups of mineral species is of the Perkin Elmer FT-IR type.

Chemical methods of pozzolanic activity

The effectiveness of a pozzolan in a cementitious matrix depends on its ability to react with the portlandite released during the hydration of the cement in order to form cementitious hydrates. This reactivity defines its pozzolanic activity. Chemically, this reactivity can be carried out by Frattini and lime saturation tests [16].

The Frattini test is one of the commonly used chemical methods to determine the pozzolanicity of a material. The Frattini test procedure involves preparing a 20 g mixture, consisting of 80 wt.% Portland cement with 20 wt.% material added to 100 mL of distilled water. The mixture is stored at a temperature of 40 °C for eight (08) days in tightly closed plastic bottles. After these eight days, the mixture is filtered. The OH⁻ ions contained in the filtrate are then measured with a dilute solution of hydrochloric acid at 10⁻¹ mol.L⁻¹ using methyl orange as a colored indicator. Then, the calcium ions (Ca²⁺) will in turn be measured by X-ray fluorescence (XRF). The results obtained are illustrated by a graph giving the concentration of Ca²⁺ ions expressed in mmol.L⁻¹, equivalent to the quantity of CaO as a function of the concentration of OH⁻ ions also expressed in mmol.L⁻¹. Additionally, from the lime solubility isotherm, the pozzolanicity of the material is determined. Indeed, any material whose coordinates ([OH⁻], [CaO]) are located below the solubility isotherm of portlandite has pozzolanic activity and any material whose coordinates ([OH⁻], [CaO]) are located above the solubility isotherm of portlandite has no pozzolanic activity.

A simpler approach to studying pozzolanic reactivity is to use the lime saturation test. Its procedure consists of preparing a mixture consisting of 1 g of material and 75 mL of saturated lime solution initially prepared by dissolving 2 g of hydrated lime in 1 liter of distilled water. The hermetically sealed mixture is kept for the test period set at 1, 3, 7 and 28 days. The concentration of Ca²⁺ ions in the different mixtures is determined by X-ray fluorescence. Thus, from the quantity of calcium ions available in the initial mixture, the CaO content fixed by the material can be determined as a function of the period of the essay.

Pozzolanic activity index

The pozzolanic index constitutes the ratio of the mechanical compressive strength of the specimens containing pozzolan and those not containing it, called reference specimens. The value of the pozzolanic index is obtained from equation 9

$$I_P = \frac{R_P}{R_T} \times 100 \quad (9)$$

With, I_p : pozzolanic index ; R_p : mechanical compressive strength in MPa of mortars containing pozzolan; R_T : mechanical compressive strength in MPa of the reference mortar.

To do this, the mortar specimens were manufactured according to standard NF-P-15-403 [33]. First the cement, the pozzolan ground to 80 μm and distilled water are introduced into a mixer to mix for one minute at a speed of 140 rpm. Afterwards, standardized sand is added and the mixture is mixed again for 3 minutes at a speed of 280 rpm. Then a manual scraping of the walls of the mixer tank was carried out. Finally, the cycle ends with a three-minute mixing session at 280 rpm. The kneaded mixture is introduced into 40x40x160 mm³ prismatic molds and compacted mechanically. Once leveled, the molds containing the samples are covered with plastic film and stored in the cold room at a temperature of 20 \pm 1 °C. Unmolding is carried out after 24 hours and the specimens are kept in the laboratory at 20 \pm 1 °C in a vase containing distilled water until the day of the test set at 7, 28 days and 90 days. Then, the mechanical compressive strength is determined using a CONTROLAB S type press according to standard NF P 15-471 [34]

Mineralogical reactivity

During pozzolanic reactivity, hydrates similar to those of cement are formed. Thus, monitoring the formation of these hydrates makes it possible to ensure the pozzolanic reactivity of the different materials. To do this, specimens consisting of lime, pozzolan and water were developed according to mass ratios: pozzolan/lime = 1 and water/(pozzolan + lime) = 0.5. After maturing for 28 days, the different composites were subject to mineralogical characterization by infrared spectrometry.

ACKNOWLEDGMENTS

The authors thank Pr. Jean Emmanuel Aubert (Laboratoire Matériaux et Durabilité des Constructions (LMDC), Université de Toulouse, INSA/UPS Génie Civil, 135 Avenue de Rangueil, 31077 Toulouse cedex 04 France de Toulouse) for providing the XRD analysis of the samples.

REFERENCES

1. F. Ganon; A. Yameogo; B. Sorgho; L. Zerbo; M. Seynou; Y. Millogo; R. Ouedraogo; *ChIBA*. **2015**, *16*, 371–383.
2. T. Halmagyi, E. Mosonyi, J. Fazakas, *Studia UBB Chemia*, LXIII, 1, 2018 (p. 73-86).

EVALUATION OF THE POZZOLANIC ACTIVITY OF METAKAOLIN, GLASS POWDER
AND SILICA POWDER FOR USE IN CEMENTITIOUS MORTARS

3. K.L. Scrivener; V.M. John; E.M. Gartner; *Cement and Concrete Research*. **2018**, 114, 2–26.
4. M.Z. Al-mulali; H. Awang; H.P.S. Abdul Khalil; Z.S. Aljournaily; *Cement and Concrete Composites*. **2015**, 55, 129–138.
5. A.P. Fantilli; D. Józwiak-Niedźwiedzka; *Materials*. **2021**, 14, 2291.
6. O. Chaib; M. Mouli; M. Hanifi; M. Hamadache; *J. Mater. Environ. Sci.* **2016**, 7, 422–428.
7. R. Harbi; R. Derabla; Z. Nafa; *Construction and Building Materials*. **2017**, 152, 632–641.
8. M. Kamali; A. Ghahremaninezhad; *Construction and Building Materials*. **2015**, 98, 407–416.
9. M. Seynou; Y. Millogo; L. Zerbo; I. Sanou; F. Ganon; R. Ouedraogo; K. Kaboré; *JMMCE*. **2016**, 04, 195–209.
10. Y. Wang; Z. Shui; Y. Huang; T. Sun; R. Yu; G. Wang; *Construction and Building Materials*. **2018**, 172, 19–28.
11. K.A. Melo; A.M.P. Carneiro; *Construction and Building Materials*. **2010**, 24, 1529–1535.
12. F. Cassagnabère; G. Escadeillas; M. Mouret; *Construction and Building Materials*. **2009**, 23, 775–784.
13. K. Weise; N. Ukrainczyk; E. Koenders; *Materials & Design*. **2023**, 231, 112062.
14. F. Sinngu; S.O. Ekolu; A. Naghizadeh; H.A. Quainoo; *Developments in the Built Environment*. **2023**, 14, 100154.
15. Y. Wang; Y. Li; Y. Su; X. He; B. Strnadel; *Advanced Powder Technology*. **2022**, 33, 103690.
16. S. Donatello; M. Tyrer; C.R. Cheeseman; *Cement and Concrete Composites*. **2010**, 32, 121–127.
17. M. C. Sekhar, M. H. Kumar, S. L. Raju, *Materials Today: Proceedings*. **2023**, 03, 713
18. I. Sanou; M. Ouedraogo; H. Bamogo; N. Meité; M. Seynou; J.-E. Aubert; Y. Millogo; *Emergent Mater.* **2024**, 7, 1203–1217.
19. S.O. Sore; A. Messan; E. Prud'homme; G. Escadeillas; F. Tsobnang; *Construction and Building Materials*. **2018**, 165, 333–345.
20. G. Jozanikohan; M.N. Abarghooei; *J Petrol Explor Prod Technol.* **2022**, 12, 2093–2106.
21. C. Nicolăescu, L. Olar, R. Stefan, M. Todica, C-V. Pop, *Studia UBB Chemia*, LXIII, 2, **2018** (p. 63-70)
22. I. Sanou; M. Sawadogo; M. Seynou; L. Zerbo; R. Ouedraogo; *JMMCE*. **2019**, 07, 373–384.
23. ASTM; *ASTM-C618-08: Standard Specification for coal Fly Ash and Raw or Calcined Natural Pozzolan for Use in Concrete*, West Conshohocken, PA : Annual Book of ASTM standards, **2008**
24. M. Ouedraogo; M. Sawadogo; I. Sanou; M. Barro; S. Nassio; M. Seynou; L. Zerbo; *Results in Materials*. **2022**, 14, 100275.
25. K. Dao; M. Ouedraogo; Y. Millogo; J.-E. Aubert; M. Gomina; *Construction and Building Materials*. **2018**, 158, 84–96.

26. Y. Millogo; J.-C. Morel; K. Traoré; R. Ouedraogo; *Construction and Building Materials*. **2012**, 26, 663–669.
27. G. Dal Poggetto; P. Kittisayarm; S. Pintasiri; P. Chiyasak; C. Leonelli; D. Chaysuwan; *Polymers*. **2022**, 14, 5091.
28. Y. Millogo; M. Hajjaji; R. Ouedraogo; *Construction and Building Materials*. **2008**, 22, 2386–2392.
29. S.S. Ibrahim; A.A. Hagrass; T.R. Boulos; S.I. Youssef; F.I. El-Hossiny; M.R. Moharam; *JMMCE*. **2018**, 06, 86–104.
30. I. Sanou; M. Seynou; L. Zerbo; R. Ouedraogo; *SJC*. **2019**, 7, 1.
31. N. Méité; L.K. Konan; M.T. Tognonvi; B.I.H.G. Doubi; M. Gomina; S. Oyetola; *Carbohydrate Polymers*. **2021**, 254, 117322.
32. M. Sawadogo; I. Sanou; Y. Dah; B. Traoré; Y. Sawadogo; D. Samaké; C. Dembelé; L. Zerbo; M. Seynou; *Journal de la Société Ouest-Africaine de Chimie*. **2021**, 050, 50–56.
33. AFNOR; *NF P15-403 : Sable normal et mortier normal*, **1996**.
34. AFNOR; *NF P15-471 - Méthodes d'essais des ciments: Détermination des résistances mécaniques*, **1990**.

FORMULATION AND EVALUATION OF ANTIFUNGAL MICONAZOLE NITRATE MEDICATED SOAP

Emőke Margit RÉDAI^{a#}, Orsolya PÉTERFI^{a#},
Robert Alexandru VLAD^a, Paula ANTONOAEA^a,
Nicoleta TODORAN^a, Adriana CIURBA^a, Ibolya FÜLÖP^{b*},
Enikő BARABÁS^c, Emese SIPOS^d

ABSTRACT. Miconazole nitrate containing soaps were formulated using one commercially available soap base and three cold process soap bases with various lipids. The aim of our work was to investigate the antimicrobial activity and physicochemical properties of the obtained formulations. The water loss and hardness of the soaps was determined 1, 2, 4 and 9 weeks after preparation. The pH and foamability were determined after 9 weeks of curing time. Two Gram-positive, four Gram-negative bacteria and two yeast (*Candida* spp.) strains were used in the microbial study. The miconazole content was determined with HPLC-UV analysis. Antimicrobial assay showed that all medicated soaps were effective against *Candida albicans*. The API had minimal influence on the physicochemical properties (water loss, pH, foamability and consistency) of the soaps. All soaps possessed

^a University of Medicine, Pharmacy, Science and Technology “George Emil Palade” of Targu Mures, Faculty of Pharmacy, Department of Pharmaceutical Technology and Cosmetology, 38 Gheorghe Marinescu Street, 540142, Targu Mures, Romania

^b University of Medicine, Pharmacy, Science and Technology “George Emil Palade” of Targu Mures, Faculty of Pharmacy, Department of Toxicology and Biopharmacy, 38 Gheorghe Marinescu Street, 540142, Targu Mures, Romania

^c University of Medicine, Pharmacy, Science and Technology “George Emil Palade” of Targu Mures, Faculty of Pharmacy, Department of Cellular Biology and Microbiology, 38 Gheorghe Marinescu Street, 540142, Targu Mures, Romania

^d University of Medicine, Pharmacy, Science and Technology “George Emil Palade” of Targu Mures, Faculty of Pharmacy, Department of Drugs Industry and Pharmaceutical Management, 38 Gheorghe Marinescu Street, 540142, Targu Mures, Romania

* Corresponding author: ibolya.fulop@umfst.ro

Equal contribution



good lathering properties and an alkaline pH (9.2-11.3). The miconazole content of the soaps varied from 2.72 % to 5.12 % as revealed by HPLC-UV analysis.

Keywords: *miconazole, medicated soap, Candida albicans, olive oil.*

INTRODUCTION

The aim of our work was to formulate and obtain miconazole containing medicated soaps using different soap bases (containing various natural oils), and to investigate the antimicrobial activity and physicochemical properties of the obtained formulations, such as water loss, consistency, pH and foamability. To determine the active substance content, HPLC method was applied.

Superficial mycoses

Superficial fungal infections, involving cutaneous stratum corneum, hair and nails are estimated to affect billions of people worldwide, thus being among the most frequent forms of infections. Due to the lack of regular and national surveillance, poor diagnostic and no reporting obligations, incidence rates are usually underestimated and determined by extrapolating local and literature data [1]. The fungal pathogens causing skin mycoses are dermatophytes (*Epidermophyton spp.*, *Microsporum spp.*, *Trichophyton spp.*), yeasts (*Candida spp.*, *Malessezia spp.*) and molds (*Aspergillus spp.*). The most common clinical manifestations of these infections are dermatophytosis, onychomycosis, superficial candidiasis and pityriasis versicolor [2].

Their prevalence depends on socio-economic conditions, geographical location and environmental and cultural habits [3]. Several factors predispose to superficial fungal infections, including physiological factors (infancy, pregnancy, aging, menses), dermatoses, trauma, endocrine diseases (diabetes mellitus, hypothyroidism), immunological dysfunctions (HIV), chemotherapy, antibiotics and immunosuppressant therapy [2,4].

In order to invade healthy human tissue, fungi have to adapt to various environmental factors. Hence, fungal pathogens can respond to host-derived stresses, grow at temperatures of 37°C, take up and metabolize nutrients from their host [5]. In addition, fungal pathogenicity also depends on virulence factors, such as dimorphism, biofilm formation, the expression of adhesins, invasins and virulence enzymes (keratinase, cellulase, protease) [6]. Fungal pathogens adapt to changing environmental pH and modulate the skin surface pH from acidic (4.7) to alkaline through various mechanisms [7]. Most fungi take up amino acids and alkalinize their environment by releasing urea

or ammonia; as an additional mechanism, *C. albicans*, seems to neutralize the pH of its environment through the utilization of carboxylic acids (such as pyruvate, α -ketoglutarate and lactate) [8]. The resulting neutral-alkaline pH disturbs the regulation of the keratinization enzymes required for the renewal of the stratum corneum, leading to host tissue damage and increased virulence [9].

Candida strains such as *C. parapsilosis*, *C. krusei*, *C. tropicalis*, *C. albicans* and *C. glabrata* have also been found on healthy skin, *C. parapsilosis* being the most prevalent species [10]. *C. albicans* is seldom an inhabitant of healthy skin, yet it was identified as the most common infectious agent of this genus, followed by *C. parapsilosis* [11,12]. When examining the skin microbiome of patients with atopic dermatitis or primary immunodeficiencies, *Malassezia spp.* remained the predominant species, however the abundance of *Candida* genus increased [13,14]. In the case of diabetic patients, a high number of *Cladosporium herbarum* and *C. albicans* was found in chronic non healing wounds, *C. parapsilosis* and *C. tropicalis* were also identified [15].

The most frequent forms of superficial candidiasis are intertrigo, interdigital candidiasis, diaper dermatitis, perianal dermatitis, paronychia and onychomycosis. Intertrigo or inflammatory dermatosis is the result of friction and irritation created by opposing skin surfaces, which often occur in infancy, obesity, diabetes mellitus, hyperhidrosis and in those who are bedridden. Due to the damaged epidermal tissue, warm and moist medium, secondary fungal infections with *Candida* are frequent [4,16]. Diapers also ensure favorable conditions for *C. albicans* due to moisture, elevated pH and the presence of irritating urine and stool enzymes. As a result, diaper candidiasis often complicates non-infectious diaper dermatitis in infants, small children and elderly people [17].

To treat superficial fungal infections, antifungal drugs can be administered topically and systematically. Topical treatment of fungal skin infections is preferred to systemic delivery due to direct drug administration onto the infection site, high local drug concentration, reduced systemic adverse effects, ease of administration and improved patient compliance [18].

Pharmacological use of miconazole nitrate

Miconazole nitrate (1-[2-(2,4-dichlorophenyl)-2-[(2,4-dichlorophenyl)-methoxy]-ethyl]-1H-imidazole mononitrate) is a lipophilic imidazole derivative with a broad-spectrum of fungistatic activity [19, 20]. Imidazole derivatives target the ergosterol biosynthesis in yeast through lanosterol 14- α -demethylase (CYP51).

Ergosterol, a 5,7-diene oxysterol is an essential fungal cell membrane sterol synthesized in the endoplasmic reticulum, which maintains the fluidity, permeability and thickness of plasma membranes and protects the phospholipid bilayer against mechanical and oxidative stress [21, 22]. Besides plasma membranes, ergosterol has been found in the membranes of intracellular organelles such as endoplasmic reticulum (ER), mitochondria, peroxisomes and vacuoles, where it regulates the localization and activity of enzymes within the membrane (Cdr1 efflux pump, H⁺-ATPase, V-ATPase) [23]. To form ergosterol, CYP51 catalyzes the three-step C14-demethylation of lanosterol [24]. This step of the ergosterol synthesis is inhibited by imidazole derivatives, which bind to the haem group of CYP51 enzyme through the free nitrogen atom in the imidazole ring [25]. Takahashi et al. used miconazole soaps for cleaning diaper-covered sites of elderly patients, which significantly reduced the pseudohyphae/blastoconidia of *Candida spp.* when compared to control [26]. Jagdale et al. demonstrated the effect of medicated soap strips prepared by dipping paper in miconazole soap solutions [27].

Miconazole also exerts antibacterial effect against gram-positive aerobic bacteria including *Enterococcus spp.*, *Streptococcus spp.*, *Staphylococcus aureus*, methicillin-susceptible, methicillin-resistant and fusidic acid-resistant *S. aureus* [28, 29]. The antibacterial activity of miconazole is attributed to its ability to bind to the haem group of flavohemoglobin, thus inhibiting its NO dioxygenase and alkyl hydroperoxide reductase activity and increasing the intracellular oxidative stress [30]. Miconazole has rapid clearance and low oral bioavailability due to its poor aqueous solubility and low gastrointestinal absorption [31], therefore topical administration is preferred. Topical pharmaceutical dosage forms such as cream, gel, ointment, powder, spray and tincture usually contain 2% miconazole, which are generally well tolerated and effective in the treatment of superficial fungal infections [32].

Soap obtaining: saponification process, lipids and alkali

Natural soaps are anionic surfactants defined as the alkali salts of fatty acids obtained from plant oils and animal fats [33]. The triglycerides, esters and fatty acids contained in these lipids are saponified using a warm aqueous base, typically potassium hydroxide (KOH) or sodium hydroxide (NaOH). Triglycerides (triesters of fatty acids with glycerin) and fatty acid esters are converted to fatty acids, which are then neutralized to produce the salts [34]. Glycerin is a by-product of the saponification process that is left in or sometimes added to soaps for skin conditioning, enhancing product quality (softness, appearance), and as a processing aid [35].

Soaps can be manufactured via cold, hot (semi-boiled) or fully boiled process considering the temperature whereas the saponification reaction takes place. In the cold process, an exact amount of lye is used in order to avoid excess unreacted lye in the finished soap. The saponification index of the lipids is used to ensure the correct ratios of water, oils and lye, as the various fat and oil sources contain different types and amounts of triglycerides, esters and fatty acids [36]. Once the lye and lipids are mixed, saponification takes 18 to 24 hours to complete, and no additional heat is required [37]. Soaps are often formulated to contain an excess of fatty acids (approximately 5%) in order to ensure the absence of unneutralized lye and to reduce the harshness of the soap [38]. Superfatted soaps with 2-5% excess fats or oils are harder, less prone to cracking, and show good leathering and moisturizing ability [39, 40]. In the hot process, the mixture is heated to 80-100 °C (near boiling temperature) in order to accelerate the reaction. In the fully boiled process, the reactants are boiled, and the mixture is washed to remove any impurities, spent lye and glycerin [41, 42].

Besides the manufacturing process, the chemical properties of soaps depend on the composition and the nature of the lipids, and the alkali used in the saponification process. Unsaturated fats are susceptible to oxidation, slowly become rancid, reduce soap hardness, but also provide moisturizing and skin nourishing properties [43,44]. To balance out the soap formula, saturated fatty acids are used to produce harder soaps [39]. Short chain fatty acids (C10-C14) produce more soluble and harder soaps with good foamability. Longer chain fatty acids (C16-C18) contribute to the cleansing property of soap and provide a longer lasting soap [34, 45]. Very long-chain fatty acids (C22 and higher) provide bar integrity [46].

Animal fats (lard, tallow) tend to be richer in long chain saturated fats (C16:0, C18:0) and monounsaturated fats (C18:1), hence these are often combined with coconut oil which contains shorter chain length (C8:0–C14:0) saturated fatty acids. The ratio of tallow/coconut oil used for soap manufacture generally ranges from 85:15 to 75:25. Lather quickness improves, while foam stability decreases with the increase of the coconut oil content [37, 47]. Beeswax contains approximately 12% free fatty acid and 40-45% monoesters of C24-C34 alcohols [48, 49]; it produces harder soaps with high foamability, which have lower foam stability at higher concentrations (35%) [50]. High beeswax content causes the soap to solidify quickly during preparation [36].

The most used oil sources in natural soaps are coconut, palm kernel, palm, olive, rice bran and sunflower seed [51]. Nut oils such as coconut and palm kernel oil are found in a variety of commercial soaps due to their low cost. Short chain saturated fatty acids from these oils produce harder soaps which lather readily but not stably; however, saturated fatty acids with 10 or fewer

carbons confer objectionable odors, irritate and dry out the skin [44]. Palm oil is often used as an alternative for tallow as it also contains C16-C18 fatty acids, which produce slow-lathering soaps with more resistant foam [52]. Kuntom et al. found that the foamability and hardness of soaps derived from palm and palm kernel oil blends is reduced as the palm oil content increases [45].

Olive oil is composed mainly of triacylglycerols of unsaturated free fatty acids, yet it still produces hard soaps with stable lather and skin conditioning properties. Cocoa butter is used for its moisturizing effect, and it also helps to produce harder soaps with good lather [53].

The aqueous solutions of natural soaps neutralized with NaOH have an alkaline pH of 10-11 due to the quantity of alkali released after the dissociation of fatty acid salts. The pH can be further increased when residual amount of alkali is retained in the soap during manufacture [49]. Most commercial soaps have a pH ranging between 9 and 11 with a few soaps having higher pH levels (up to 11.5) [54]. The physiological skin pH is normally acidic (pH 4.1-5.8); elevated values have been detected in infant and elderly skin due to reduced buffer capacity [55]. The skin surface pH also increases after a single washing procedure with alkaline soaps; however, these increases are recovered gradually in 6 hours [56]. Anionic surfactants interact with lipids and keratin filaments of the skin causing reversible expansion of the cell membranes and enhancing the permeability of the skin for active pharmaceutical ingredients [57].

Soap monographs are official in Austrian Pharmacopoeia (ÖAB 2008), British Pharmacopoeia (BP 2019), Korean Pharmacopoeia (KP 10), Japanese Pharmacopoeia (JP XVII), Swiss Pharmacopoeia (Ph. Helv. 11) and US Pharmacopoeia (USP 42-NF 37). Medicinal soap mentioned in both Korean Pharmacopoeia and Japanese Pharmacopoeia is defined as the sodium salts of fatty acids. The British Pharmacopoeia includes a monograph for soft soap, which is “made by the interaction of potassium hydroxide or sodium hydroxide with a suitable vegetable oil or oils or with fatty acids derived there from. It yields not less than 44.0% of fatty acids”. Hard soap (*Sapo durus*) in Austrian Pharmacopoeia is prepared by melting together lard and olive oil, adding a mixture of sodium hydroxide solution and ethanol. US Pharmacopoeia also mentions soaps and shampoos as a dosage form with surface-active properties that facilitate the topical administration of the active pharmaceutical ingredient (usually antimicrobial agents).

RESULTS AND DISCUSSION

Weight loss observed during soap curing can be attributed to the evaporation of water. The soaps were kept at room temperature at a relative humidity of 40-60%. Water loss was followed by comparing the weekly weight decrease to the initial weight measured one week after preparation (**Table 1**). Soaps prepared using the melt-and-pour method do not require curing time as they are ready to use after they harden [58]. Cold process soaps are generally cured for 4 to 6 weeks [59]. The maturation process for castile soap (made from olive oil) is longer, sometimes up to 6 months [60]. At 2 weeks MIX-1-M soaps had the smallest decrease in weight. At 4 weeks soap MIX-2 lost the most amount of water. After the 9-week period the commercial soap had the highest weight loss. OLI and OLI-M soaps present the same weight loss, and the lowest one from all compositions.

Table 1. Weekly weight loss during a 9-week period, and physicochemical and active substance measurements at the end of the curing time.

Soap type	Weekly weight loss (%) compared to initial measurements			pH	Foam volume ml	Miconazole content %±SD
	Week 2 AVG±SD	Week 4 AVG±SD	Week 9 AVG±SD			
COM	5.2%±0.003	6.1%±0.004	13.3%±0.007	9.2	80	
COM-M	5.1%±0.001	6.3%±0.003	13.9%±0.003	9.3	66	2.72%± 0.5
OLI	5.0%±0.006	6.3%±0.008	8.1%±0.009	10.2	50	
OLI-M	4.6%±0.002	7.1%±0.003	8.1%±0.005	10.2	57	2.85%± 1.69
MIX-1	3.0%±0.002	6.4%±0.001	10.9%±0.011	11.3	59	
MIX-1-M	3.0%±0.006	6.5%±0.014	9.2%±0.015	10.1	65	4.92%± 1.68
MIX-2	4.9%±0.001	8.7%±0.002	12.4%±0.007	11.1	56	
MIX-2-M	4.6%±0.006	8.2%±0.005	10.7%±0.008	9.2	80	5.12%± 0.65

Penetration depth value reflects the hardness of the product. Low penetration value indicates harder consistency, high penetration value indicates softer soap. Initial penetration values (**Figure 1**) indicate that soaps were softer immediately after production.

The hardness of medicated soaps was different from control soap during the first period of curing. At 9 weeks each soap had similar consistency, the commercial soaps being softer when compared to cold process soaps. The two commercial soaps and OLI control showed mild changes in their consistency during the maturation process. MIX-1-M medicated soaps had

the highest penetration values from 1 to 4 weeks, suggesting soft consistency despite it losing the most amount of moisture out of the cold process soaps. Medicated cold process soaps were initially softer than control, this tendency remained the same in the case of MIX-1-M and MIX-2-M blends at the end of the maturation process. In the case of the OLI soaps, control had higher penetration values, indicating softness compared to medicated OLI soap.

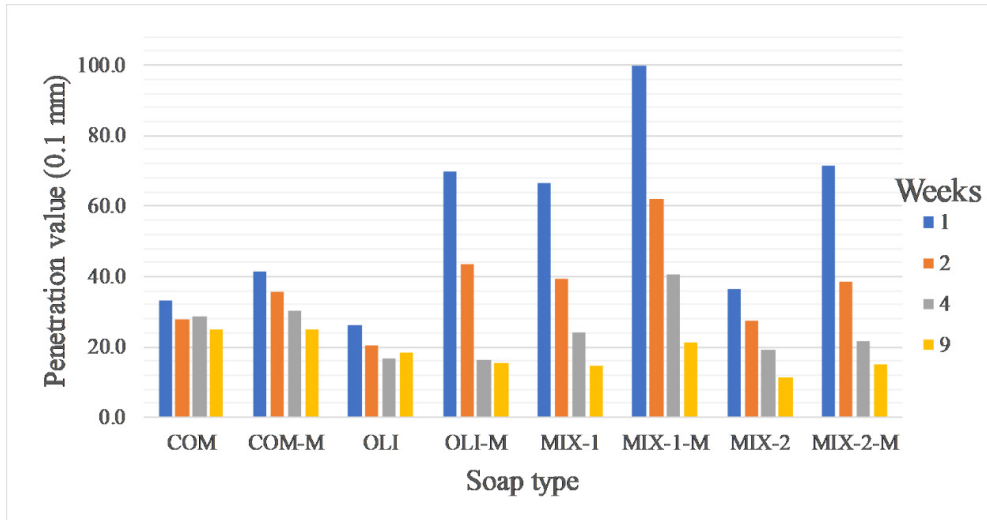


Figure 1. Initial penetration values measured at 1, 2, 4 and 9 weeks

The overall homogeneity of the soap was evaluated at the end of the maturation process (9 weeks) by comparing the difference between the penetration values measured at 5, 10, 15, 20, 25 and 30 s. As the needle entered deeper in the soap, the penetration value increased but with a different amount. The difference between the penetration values of two timestamps (5-10, 10-15, 15-20, 20-25 and 25-30, respectively) decreases with the depth of penetration, suggesting that the soaps were harder in the centre. Soaps with similar penetration value differences dried more homogeneously. OLI soaps showed almost no difference between the penetration values of two different timestamps further suggesting the hardness of the soap. The penetration values of medicated MIX-1-M blend indicate the largest variation in the soap consistency compared to other soaps.

Penetration values probably depend on the composition of the soaps. Olive oil containing soaps are known for their unique properties that may be explained by the components of the oil (fatty acids present in olive oil are palmitic, palmitoleic, stearic, oleic, linoleic, and linolenic acids) [61]. Beeswax

and cocoa butter are solid soap components modifying the consistency of the soaps MIX, MIX-1-M, MIX-2 and MIX-2-M (**Figure 2**). The foamability and pH of the various soap samples are represented in **Table 1**. Each soap showed great lathering properties. Cold process soaps with active pharmaceutical ingredient had better foamability than control, while the contrary was observed in the case of commercial soap. The commercial control soap exhibited the highest foamability followed by the medicated MIX-2-M blend. High foamability does not mean high cleansing, however, most consumers think that way, therefore it is important for product desirability [46].

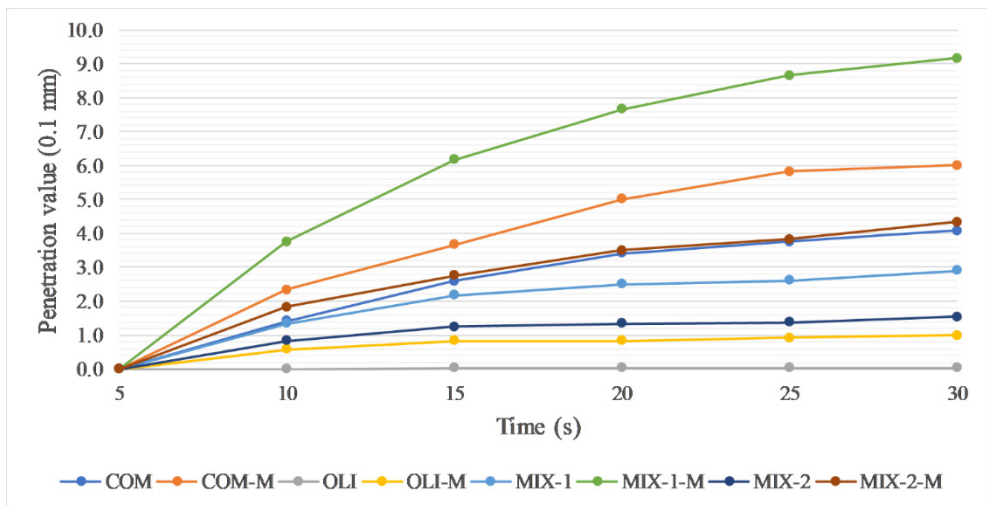


Figure 2. Penetration values measured at 9 weeks

The pH of the medicated soaps was within the normal range for commercial soaps (9-11). Two control soaps had higher pH values (MIX-1-M and MIX-2-M); these were still under 11.5. The pH of the commercial soap was the lowest. Among the prepared soaps OLI and OLI-M have the lowest pH.

Table 2 shows antimicrobial activity of the soap samples. Each medicated soap was effective against *C. albicans*, commercial and OLI soap having the largest inhibition zones (**Figure 3**).

Table 2. Microbial test results

Microorganism	Diameter of zone of inhibition (mm)							
	COM	COM-M	OLI	OLI-M	MIX-1	MIX-1-M	MIX-2	MIX-2-M
<i>Staphylococcus aureus</i>	R	11 ^a	R	R	R	R	R	R
<i>Enterococcus sp.</i>	R	R	11	11	R	R	R	R
<i>Escherichia coli</i>	R	R	R	R	R	R	R	R
<i>Klebsiella sp.</i>	R	R	R	R	R	R	R	R
<i>Salmonella typhimurium</i>	R	R	R	R	R	R	R	R
<i>Pseudomonas aeruginosa</i>	R	R	R	R	R	R	R	R
<i>Candida albicans</i>	R	20	R	20	R	19	R	15 ^a
<i>Candida parapsilosis</i>	R	11	R	R	R	R	R	R

The diameters of the soap solution drops were 10 mm, R – resistance, a – drop with a 9 mm diameter

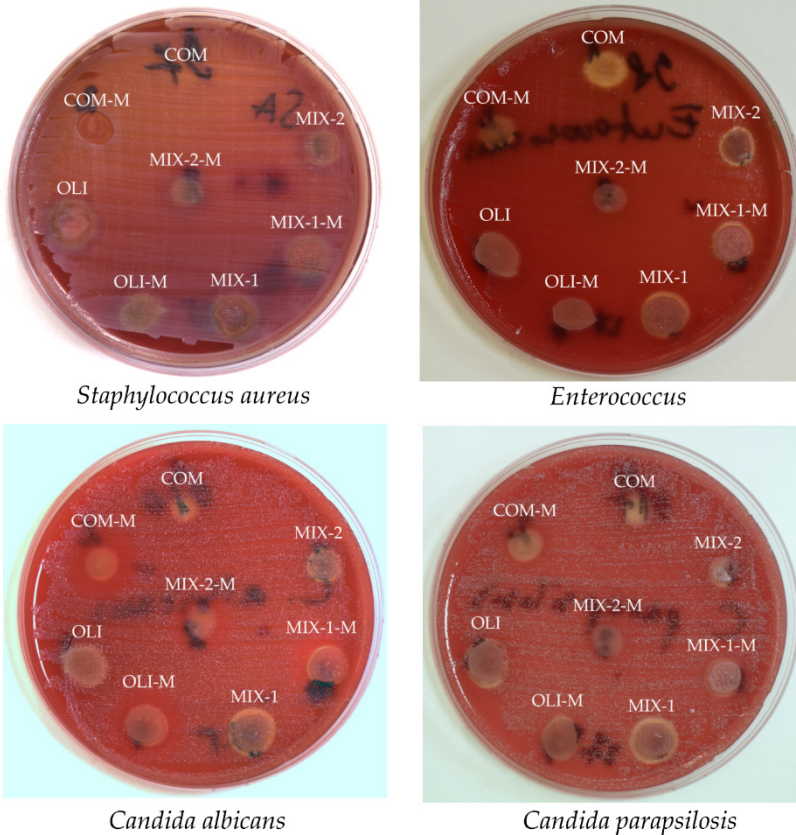


Figure 3. Plates showing zone of inhibition

HPLC method validation

Miconazole shows a linear response between 5-100 µg/ml. The accuracy was tested at three concentration level by adding known amount of miconazole to the soap matrix: then dissolving it in 10% methanol aqueous solution to obtain solutions with 20 µg/ml, 40 µg/ml and 60 µg/ml concentration, respectively. The precision of the method tested at 40 µg/ml expressed in CV% is 0.76. The LOD and LOQ concentrations were 1.25 µg/ml and 4.16 µg/ml, respectively.

The validation parameters of the method are shown in **Table 3**.

Table 3. The validation parameters of the method

Parameter	Result	Statistical analysis	Comment
Linearity	5-100 µg/ml	$R^2=0.9990$	Shapiro-Wilk test accepted range 0.787-1.0 $p<0.05$
		$W=0.918$ ($p=0.51$)	
		$F=5017.80$	
Accuracy (%)			
20 µg/ml	101.7 - 102.3	$R^2=0.9991$	-
40 µg/ml	101.5 - 102.6		
60 µg/ml	100.2 - 101.3		
Precision (CV%)	0.76%	-	-
LOD	1.25 µg/ml	-	-
LOQ	4.16 µg/ml	-	-

Figure 4 shows a typical chromatogram of a soap sample (t_r miconazole 7.14 ± 0.10 min), a spiked sample and the matrix solution, no interference from the matrix can be observed on the retention time of miconazole.

The miconazole content of the soaps shows a content of 2.72 % to 5.12 %. Uniformity content is influenced by the preparation method and the conservation of the soaps. The uniformity had been determined after more than 9 weeks of preparation. In the meantime, the soaps lost water, presented weight loss, which leads to the increase of miconazole content. Miconazole had been suspended in the soap base and the turn into moulds, then allowed to cool. At sampling from the soaps, probes were collected from different places, heights of the soaps. Miconazole might have sedimented during the cooling phase of preparation.

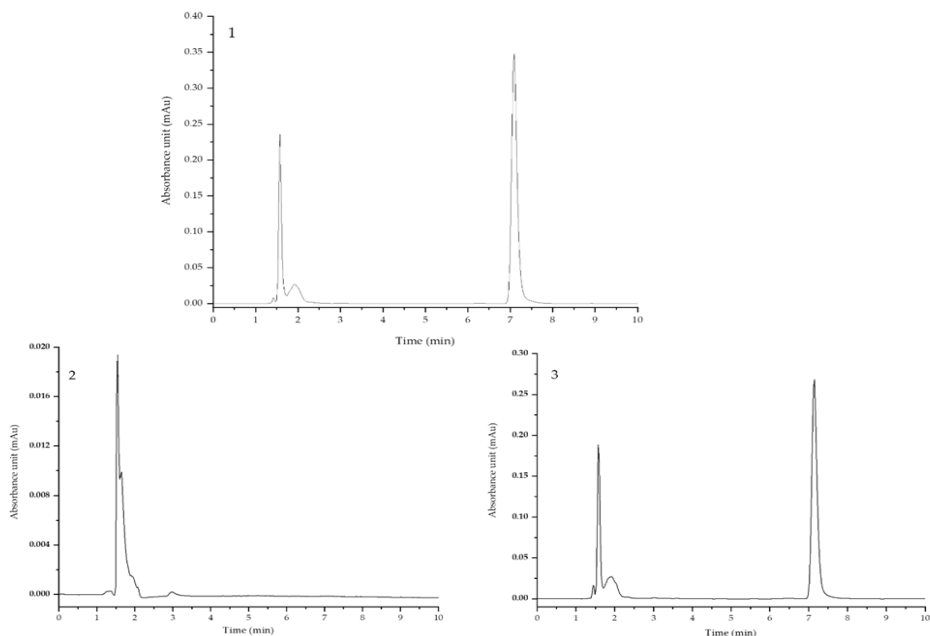


Figure 4. Chromatogram of a soap sample (1 – 60 µg/ml spiked matrix solution; 2 – matrix; 3 – sample OLI-M)

CONCLUSIONS

Medicated, miconazole nitrate containing soaps may be used by medical staff for handwashing and for cleaning skin zones of patients predisposed to fungal infections, the active pharmaceutical ingredient inhibiting the growth of *Candida albicans* in microbiological study. The influence of miconazole nitrate seems to be minor on the properties of the soaps. Olive oil containing soaps presented the lowest weight loss, the lowest pH, and proper consistency during conservation.

EXPERIMENTAL SECTION

Lipids and alkali used for soap preparation

Medicated and control soaps were prepared using four soap bases, three of which were formulated using various lipids and a 25% sodium hydroxide (NaOH) solution. Solid NaOH was weighed and dissolved in distilled

water to prepare the 25% NaOH solution. Each formulation contained olive oil, which was combined with beeswax, cocoa butter and sunflower oil in some of the mixtures (**Table 4**). A commercial ly4e calculator X was used to select the composition of the different formulations considering their saponification index [62]. An approximately 1:2 ratio of lipid and alkaline solution was used with a 5% excess lipid. A commercial soap base was used for comparison, containing coconut oil, palm oil, safflower oil, glycerin, water, sodium hydroxide, sorbitol, propylene glycol, sorbitan oleate, oat protein.

Table 4. Composition of various soap samples

Ingredient (g)	Soap type							
	COM	COM-M	OLI	OLI-M	MIX-1	MIX-1-M	MIX-2	MIX-2-M
Miconazole nitrate	-	0.67	-	0.89	-	0.89	-	0.89
Commercial soap base	33	30	-	-	-	-	-	-
Olive oil	-	-	30	29.1	12	11.1	9	8.11
25% NaOH solution	-	-	15.4	15.4	14.3	14.3	14.5	14.5
Sunflower oil	-	-	-	-	12	12	12	12
Beeswax	-	-	-	-	6	6	3	3
Cocoa butter	-	-	-	-	-	-	6	6

Cold process soap formulation

The oils and butters were mixed in an evaporating dish and heated to 70 °C on an electronic water bath. In the case of the beeswax containing mixtures, the lipids were melted at 85°C to get a homogenous liquid. The olive oil content of medicated soap bases was reduced and replaced with the active pharmaceutical ingredient (2% miconazole nitrate) which was added after melting the lipids. The required amount of alkali solution with the same temperature as the lipid mixtures was slowly poured into the melted lipids, while stirring vigorously until the trace stage, which corresponds to the mixture thickening to the consistency of pudding. Then the mixture was poured gradually into molds and dried for 48 h before unmolding. The soap bars were cured at room temperature for several weeks and the maturation process was followed at 1, 2, 4 and 9 weeks.

To prepare the medicated soap from commercial soap base the melt-and-pour method was used, during which the soap base was melted at 50°C, then mixed with miconazole nitrate and poured into molds.

Following water loss

To measure water loss from soap overtime, the weight of each soap sample was determined 1, 2, 4 and 9 weeks after soap preparation with Kern ABJ 220-4NM analytical balance at room temperature. Three parallel samples were measured.

Hardness measurement by penetrometry

The hardness of the soaps was determined using an automatic penetrometer (VEB Feinmess Dresden) equipped with a penetration needle with a 1 mm diameter and 40 mm exposed needle length. The penetration rate was recorded in penetration units (0,1 mm). The penetration depth was measured at room temperature every 5 seconds during a 30 second period. The measurements were repeated at 1, 2, 4 and 9 weeks after soap preparation with three samples.

pH measurement

50 ml solutions were prepared by dissolving 2.0 g of each soap sample in distilled water. The pH value of each sample was measured after 30 minutes at 25°C using a pH meter (Consort C831 multi-parameter analyzer).

Foamability test

The foamability of the soap samples was determined by dissolving 2.0 g of soap in distilled water for 30 minutes to prepare 50 ml solutions in a graduated cylinder. Later, the solutions were shaken vigorously for 1 minute, allowed to settle for 10 minutes; then the foam volume was measured in ml.

Antimicrobial assay

Two Gram-positive (*Staphylococcus aureus*, *Enterococcus*), four Gram-negative (*Escherichia coli*, *Klebsiella sp.*, *Salmonella typhimurium*, *Pseudomonas aeruginosa*) and two yeast (*Candida albicans*, *C. parapsilosis*) strains were used in microbial study. Each strain was inoculated in a sterile saline solution to make a suspension equal to 0.5 McFarland (1,5x10⁸ CFU/ml) and plated on Mueller Hinton Agar supplemented with 10% defibrinated sheep blood. 1:10 soap solutions were prepared by dissolving the soaps in distilled water for 24 h. 10 µl of each soap solution was placed on the plate at 2.5 cm distance from each other. The inoculated plates were kept at room temperature for 30

minutes to allow diffusion of the agent into the agar; this was followed by 24 h incubation at 37 °C. After incubation, the zone of inhibition and the diameter of the 10 µl soap solution were measured in millimeters.

HPLC measurement of drug content

The HPLC-UV (Merck Hitachi HPLC system: D-7000 interface, L-7100 quaternary pump, L-7612 solvent degasser, L-7200 autosampler, L-7455 DAD detector and HSM 4.0 software) determination of miconazole nitrate content of the soap samples was performed isocratically on EC HPLC column 150 x 4.6 mm NUCLEODUR® PolarTec, 3 µm (Macherey Nagel, Germany) and 5 mM phosphate buffer (pH=8.73±0.02) and acetonitrile (25:75 w/w%) as mobile phase, with a flow rate of 0.75 ml/min. Detection and best chromatogram extraction were carried out at 222 nm. The column was maintained at an ambient temperature and an injection volume of 30 µl was used.

Analytical validation parameters such as linearity, precision, accuracy, specificity, LOD and LOQ were tested. For these parameters a stock solution of miconazole nitrate in 1 mg/ml concentration was prepared by dissolving the active ingredient in methanol, and this was diluted with blank solution (suitable amount of soap, without active ingredient, dissolved in 10% methanol solution in purified water) to obtain standard solutions. The linearity of the method was tested in 5-100 µg/ml concentration range. The accuracy was verified at three concentration levels by adding known amount of miconazole to the soap matrix: then dissolving it in 10% methanol aqueous solution to obtain solutions with 20 µg/ml, 40 µg/ml and 60 µg/ml concentrations, respectively. The precision of the method, tested at 40 µg/ml was expressed in CV%. The LOD and LOQ values were evaluated at a 3:1 and 10:1 signal-to-noise ratio.

REFERENCES

1. F. Bongomin, S. Gago, R.O. Oladele, *J Fungi*, **2017**, 3(4), 57.
2. R.J. Hay, Superficial Mycoses, In: Hunter's Tropical Medicine and Emerging Infectious Disease, 10th Ed. Elsevier Inc, **2020**, 648–652.
3. B. Havlickova, V.A. Czaika, M. Friedrich, *Mycoses*, **2009**, 51 Suppl 4(4),2–15.
4. A. Metin, N. Dilek, S.G. Bilgili. *Clin Cosmet Investig Dermatol*, **2018**, 11, 175–185.
5. C. Braunsdorf, D. Mailänder-Sánchez, M. Schaller, *Cell Microbiol*, **2016**, 18, 1188–1200.
6. D. Chinnapun, *J Sci Technol*, **2015**, 12, 573–580.
7. F.L. Mayer, D. Wilson, B. Hube, *Virulence*, **2013**, 4, 119–128.
8. O. Blechert, H. Zheng, X. Zang, *PLoS One*, **2019**, 14, 1–12.
9. N.M. Martinez-Rossi, G.F. Persinoti, N.T.A. Peres, *Mycoses*, **2012**, 55, 381–387.

10. Z. Rafat, S.J. Hashemi, K. Ahamdikia, *J Mycol Med*, **2017**, 27, 501–505.
11. Z. Ghasemi, S.J. Hashemi, S. Rezaei *Jundishapur J Microbiol*, **2020**, 10 (2), e41030
12. A.L. Byrd, Y. Belkaid, J.A. Segre, *Nat Rev Microbiol*, **2018**, 16, 143–155.
13. E. Zhang, T. Tanaka, M. Tajima, *Microbiol Immunol*, **2011**, 55, 625–632.
14. J. Oh, A.F. Freeman, M. Park, *Genome Res*, **2013**, 23, 2103–2114.
15. L. Kalan, M. Loesche, B.P. Hodkinson, *Healing*, **2016**, 7, 1–12.
16. M.G. Kalra, K.E. Higgins, B.S. Kinney, *Am Fam Physician*, **2014**, 89, 569–573
17. A. Bonifaz, R. Rojas, A. Tirado-Sánchez, *Mycopath*, **2016**, 181, 671–679.
18. N. Akhtar, A. Verma, K. Pathak, *Curr Pharm Des*, **2015**, 21, 2892–2913.
19. G.E. Piérard, T. Hermanns-Lê, P. Delvenne, *Expert Opin Pharmacother*, **2012**, 13, 1187–1194.
20. P.R. Sawyer, R.N. Brogden, R.M. Pinder, T.M. Speight, G.S. Avery, *Drugs*, **1975**, 9(6), 406–423.
21. Y.Q. Zhang, R. Rao, *Virulence*, **2010**, 1, 551–554.
22. M.L. Rodrigues, *MBio*, **2018**, 9, 1–5.
23. Q.Z. Lv, L. Yan, Y.Y. Jiang, *Virulence*, **2016**, 7, 649–659.
24. J. Zhang, L. Li, Q. Lv, *Front Microbiol*, **2023**, 10: 691–697.
25. V.W. Rabelo, T.F. Santos, L. Terra, *Fundam Clin Pharmacol*, **2017**, 31, 37–53.
26. H. Takahashi, N. Oyama, I. Tanaka, *J Dermatol*, **2017**, 44, 760–766.
27. S. Jagdale, D. Bhavsar, M. Gattani, R.K. Anuruddha, C. Anuruddha, R. Chabukswar, *Int J Pharm Sci*, **2011**, 3(3), 299–302.
28. J.S. Weese, M. Walker, T. Lowe, *Vet Dermatol*, **2012**, 23, 1–4.
29. P. Nenoff, D. Koch, C. Krüger, *Mycoses*, **2017**, 60, 552–557.
30. L.S. Nobre, S. Todorovic, A.F.N. Tavares, *J Bacteriol*, **2010**, 192, 1527–1533.
31. B.M. Aljaeid, K.M. Hosny, *Int J Nanomedicine*, **2016**, 11, 441–447.
32. DrugBank. 2021.. <https://www.drugbank.ca/drugs/DB01110> (accessed 23 March 2024).
33. J. Steber, H. Berger, *Biodegrad Surfactants*, **1995**, 134–182.
34. J. Chupa, S. Misner, A. Sachdev, Soap. fatty acids. and synthetic detergents. *Handb Ind Chem Biotechnol Twelfth Ed.* **2012**, 2, 1431–1471.
35. E. Jungermann, O.V. Sonntag, Glycerine: A key Cosmetic Ingredient. Marcel Dekker Inc, New York, **1991**, 395–407.
36. S. Félix, J. Araújo, A.M. Pires, *Waste Manag*, **2017**, 66, 190–195.
37. M.R. Burke, *Bailey's Industrial Oil and Fat Products*. In: Shahidi F (ed) *Bailey's Industrial Oil and Fat Products*. Wiley Interscience, New York. **2005**, 103–136.
38. A. Warra, L. Hassan, S. Gunu, *Niger J Basic Appl Sci*, **2011**, 18, 315–321.
39. A. Kuntom, I. Ahmad, H. Kifli, *J Surfactants Deterg*, **1999**, 2, 325–329.
40. S.E. Benjamin A. Abbass, *J Oil Palm Res*, **2019**, 31, 304–314.
41. M. Shahinuzzaman, Z. Yaakob, M. Moniruzzaman, *J Cosmet Dermatol*, **2016**, 15, 185–193.
42. NPCS Board of Consultants & Engineers. *Soaps. Detergents and Disinfectants Technology Handbook- 2nd Revised Edition*. 2nd Ed. Niir Project Consultancy Services. Delhi, **2019**, 87–89.

43. J.B Marcus, *Lipids Basics: Fats and Oils in Foods and Health*. 1st Ed. Academic Press, **2013**, 231–277.
44. N. Prieto Vidal, O. Adeseun Adigun, T. Huong Pham, *Molecules*, **2018**, 23, 1–20.
45. A. Kuntom, H. Kifli, P.K. Lim *JAOCs. J Am Oil Chem Soc*, **1996**, 73, 105–108.
46. L. Spitz, *Soap Manufacturing Technology*, 1st Ed, Elsevier Science, **2016**, 276–277.
47. E.D. George *J Am Oil Chem Soc*, **1994**, 71, 789–791.
48. F.D. Gunstone, F.B. Padley (eds), *Lipid Technologies and Applications*. Marcel Dekker Inc, New York. **1997**, 245–246.
49. M.A. Jackson, F.J. Eller, *J Supercrit Fluids*, **2006**, 37, 173–177.
50. R. Marquez, S. Balsamo, F. Morales, *Cienc E Ing*, **2019**, 4(1), 17-26.
51. M. Friedman, R. Wolf, *Clin Dermatol*, **1996**, 14, 7–13.
52. D. Mishra, *J Am Oil Chem Soc*, **2013**, 6, 185–192.
53. F.P. Borhan, S.S. Abd, R. Gani Shamsuddin, *Sci World J*, **2014**, 173979, 1-8.
54. S.A Mahesar, R. Chohan, S.T.H. Sherazi, *Pakistan J Anal Environ Chem*. **2019**, 20, 177–183.
55. S.M. Ali, G. Yosipovitch, *Acta Derm Venereol*, **2013**, 93, 261–267.
56. Y. Takagi, K. Kaneda, M. Miyaki, *Ski Res Technol*, **2015**, 21, 144–148.
57. A. Pandey, *J Mol Pharm Org Process Res*, **2022**, 2(2), 2-10.
58. M. Browning, *Melt and Pour Soap making*. Sterling Publishing Company. New York, **2002**, 28-34.
59. S. Sutheimer, J.M. Caster, S.H. Smith, *J Chem Educ*, **2015**, 92, 1763–1765.
60. A.Y. Girgis, *Grasas y Aceites*, **2003**, 54, 226–233.
61. F.D. Gunstone, *Vegetable Oils in Food Technology: Composition. Properties and Uses*. 2nd Ed. John Wiley and Sons Ltd. Chicester, **2011**, 444-456.
62. Házikence. 2016 <https://www.hazikence.hu/kalkulatorok/osszetevo-kalkulator/> (accessed 23 March 2024).

ELECTROSPINNING AS TOOL FOR ENZYME IMMOBILIZATION

Melinda-Emese LÁSZLÓ^a, Matild PAP^a, Gabriel KATONA^{ak} 

ABSTRACT. Enzyme immobilization (covalent or noncovalent) on solid supports such as nanomaterials, resins or polymers can enhance the enzyme activity-, and selectivity, improving their stability. The present research is focused on the non-covalent immobilization of lipase B from *Candida antarctica* (CaL-B) into polyvinyl alcohol (PVA) nanofibers *via* electrospinning with the aim to prepare a stable and reusable biocatalyst compatible with organic reaction media. Polymer solutions of 8, 10 and 12 *w/w* % concentrations were used to investigate the effect of the polymer concentration on the biocatalyst's activity. The immobilized enzyme amount was determined using the Bradford assay, while structural characterization was performed by transmission electron microscopy. The immobilized enzyme preparates were tested in the enzymatic kinetic resolution of (*rac*)-1-phenylethanol and its halogenated derivatives through transesterification with vinyl acetate in batch mode. The highest conversion was obtained in case of CaL-B entrapped in electrospun nanofibers prepared from 10 *w/w* % PVA solution (noted as 10%–PVA–CaL-B) and its high stability was confirmed in recycling experiments. It was found that after the 5th cycle the biocatalyst maintained 88% of its initial activity.

Keywords: *CaL-B, immobilization, electrospinning, PVA, (rac)-1-phenylethanol, EKR.*

INTRODUCTION

Electrospinning is a voltage-driven versatile method for ultrathin fiber production with diameters ranging from a few nanometers to several micrometers [1]. Morton [2] and Cooley [3] patented the first devices to spray liquids in 1902

^a Babeş-Bolyai University, Faculty of Chemistry and Chemical Engineering, 11 Arany János street, RO-400028, Cluj-Napoca, Romania

* Corresponding author: gabriel.katona@ubbcluj.ro



and 1903, and other findings related to this topic were published in the next decades, but despite this early discovery, the procedure was not exploited commercially until the commercialization of electrospun nanofibers for filter applications has been reported for the first time in 1991 [4]. This technique involves the use of high voltage to generate the formation of a liquid jet from a positively charged polymer solution from the emitter, which is solidified by evaporating the solvent to ensure nanofiber formation on the negatively charged collector. Natural and synthetic polymers or polymer alloys are suitable for this process, leading to the production of porous, hollow, core-shell or helical-structured nanofibers. Their quality is influenced by several parameters such as solvent evaporation rate, nature of the polymer, drawing speed and distance between the emitter and collector. The procedure is controllable, parameters can be set and does not involve high costs [5].

Electrospun nanofibers (NFs) are good candidates in numerous fields, the most important being drug delivery [6], filtration [7], tissue engineering [8], biotechnology [9] and green chemistry [10]. Due to their large surface-to-volume ratio and elevated porosity, they are suitable carriers for enzyme immobilization [11-15]. For electronic devices, it is mandatory that the nanofibers produced via electrospinning have controlled fiber structure and ordered fiber orientation [16]. Among biopolymers polycaprolactone, chitosan, polylactic acid and polyvinyl alcohol were reported to be proper for obtaining nanofibers through this technique with applicability in biomedical fields due to their biocompatibility and biodegradability [16-19].

The major advantage of lipases (EC 3.1.1.3) or triacylglycerol ester hydrolases is represented by their extraordinary chemo-, regio- and stereoselectivity. In nature this class of enzymes catalyzes the hydrolysis of triglycerides into glycerol and fatty acids but is also broadly used in esterification reactions. Free lipase is not beneficial in industry because it is difficult to recover for reuse, has poor stability and does not exhibit activity in organic solvents [20], [21]. These inconveniences can be avoided if lipase is immobilized on different types of solid carriers. Over the past years, it has been reported the use of numerous materials [22] which proved to be efficient as support for various lipases immobilization including octyl sepharose [23], Immobead 150 [24] or macroporous resin NKA [25]. The immobilized enzyme should be active and insoluble in the reaction media allowing its reuse in several consecutive catalytic cycles.

Lipase B from *Candida antarctica* yeast belongs to the α/β hydrolase fold family, its catalytic triad consists of serine, histidine and aspartic acid / glutamic acid [26]. The enzyme in its immobilized form exhibits activity in non-polar organic solvents (e. g. toluene, hexane) in broad pH range and temperature. CaL-B is widely utilized in biotransformation, such as enzymatic kinetic resolution (EKR), transesterification, esterification, organic synthesis, and hydrolysis since presents

enantio- and stereo-specificity, a good stability in organic solvents [27-32]. Lipase-catalysed kinetic resolution carried out in organic solvents proved to be effective in obtaining enantiomerically enriched secondary 1-arylethan-1-ols [33], which are important chiral building blocks for the synthesis of a vast number of biologically active compounds. Related to the CaL-B covalent and non-covalent immobilization on solid carriers, a significant number of publications reported the use of different carbon-based nanomaterials such as graphene oxide [34], derivatized single-walled carbon nanotubes [35], core-shell polymeric supports based on polystyrene, methyl polymethacrylate [36], stearic acid-modified nanoparticles [37], different resins [38], [39] or biopolymeric nanofibers such as chitosan [40] [41].

One of the most used commercially available immobilized CaL-B, suitable biocatalyst for biotransformations such as transesterification, is Novozym 435, reported for the first time in 1992. In this case Lewatit VP OC 1600 resin represents the carrier while interfacial activation stands for immobilization method. The active center of the lipase is surrounded by a large hydrophobic pocket, covered by a lid (polypeptide chain), which in its "closed" form inactivates the lipase due to its internal hydrophobic face and interacts with the reaction medium *via* its external hydrophilic face. This immobilization technique may facilitate lipase desorption under specific conditions such as high temperature, in the presence of detergents or organic co-solvents since it is based on hydrophobic interactions. The main disadvantages are linked to the nature of the support's: mechanical fragility under rigorous stirring, moderate hydrophilicity because it can retain hydrophilic by-products such as water and dissolution in certain organic solvents leading to product contamination generated by its degradation [42-44]. In comparison PVA being a water-soluble biopolymer, the electrospun nanofibers produced from its aqueous solution are excellent candidates for non-polar organic reaction media such as hexane and lipase desorption is unlikely to occur due to the entrapment technique used for immobilization by electrospinning. Spelmezan *et al.* reported the immobilization of CaL-B *via* entrapment into polyvinyl alcohol-poly(lactic acid) copolymer [45] and polyvinyl alcohol-chitosan bipolymer electrospun nanofibers [46] while Sóti *et al.* [47] used for the same purpose PVA and PLA nanofibers obtained upon electrospinning.

Herein we propose the fabrication of nanofiber-based reusable biocatalysts by immobilization of CaL-B *via* entrapment into PVA electrospun nanofibers using different polymer concentration solutions, with the aim to determine the effect of polymer concentration on the enzyme's activity while using the same amount of CaL-B in each case. The prepared biocatalysts were tested for EKR of (*rac*)-1-phenylethanol and its halogenated derivatives with vinyl acetate as acylating agent in hexane in batch mode and reusability experiments were also conducted.

RESULTS AND DISCUSSION

Transmission electron microscopy (TEM) served as tool for the structural characterization of the prepared PVA nanofibers and the PVA-based biocatalysts. According to the measurements, PVA nanofibers diameter was found to range between 132 and 176 nm (**Figure 1.A., 1.B.**) and structural changes can be observed upon immobilization of lipase by entrapment into NFs (**Figure 1.C.**).

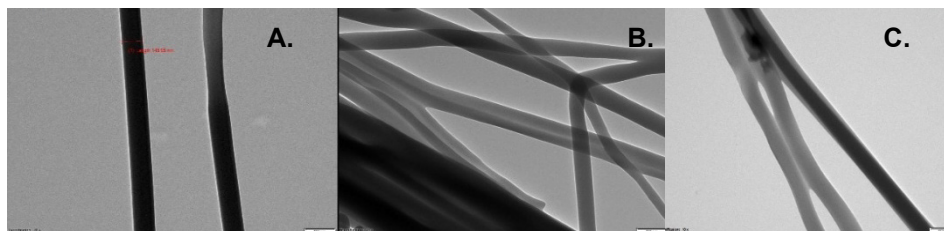


Figure 1. TEM images of PVA nanofibers
(**A.** 10 % PVA solution **B.** 12 % PVA solution; **C.** 10 % PVA–CaL-B biocatalyst)

Next the activity and selectivity of the immobilized lipase were evaluated in the kinetic resolution of (*rac*)-1-phenylethanol with vinyl acetate as acyl donor [48]. The selective formation of (*R*)-1-phenyl-ethylacetate was monitored by high performance liquid chromatography (HPLC), using a chiral LUX Cellulose-3 column (250 mm x 4.6 mm x 5 μ m). The other parameters were the following: 40 bar column pressure, flow rate 1 mL/min at 25°C mobile phase hexane:isopropanol 98:2 v/v%, detection wavelength was set at 254.16 nm.

First the pure racemic substrate and the pure racemic product separation were performed by HPLC analysis by injecting the racemic mixtures to identify each enantiomer based on their retention time, important parameters for reaction mixture analysis. The retention times in the case of the 1-phenylethyl acetate mixture were found to be 8.6 and 9.5 minutes, respectively. According to literature data [44] retention time of (*R*)-1-phenyl-acetate is 9.5 minutes; therefore, the elution order is *S*, *R*.

To evaluate the effect of the polymer concentration on the lipase activity and to determine the optimal biocatalyst amount, 9 batch reactions were performed simultaneously. In each case the substrate, acylating agent and solvent volumes were identical, the biocatalyst type (8%–PVA–CaL-B, 10%–PVA–CaL-B, 12%–PVA–CaL-B) and quantity of the enzyme prepare (8 mg, 10 mg, 12 mg) varied, while the setted temperature of the shaker

(1350 rpm) equipped with a heating module was 30 °C. Samples were taken from the reaction mixture at fixed time intervals (after 2, 4, 6, and 12 hours) and analyzed by HPLC. A control experiment was conducted without any biocatalyst. A set of obtained chromatograms are illustrated in **Figure 3** and the results are presented in **Table 1**.

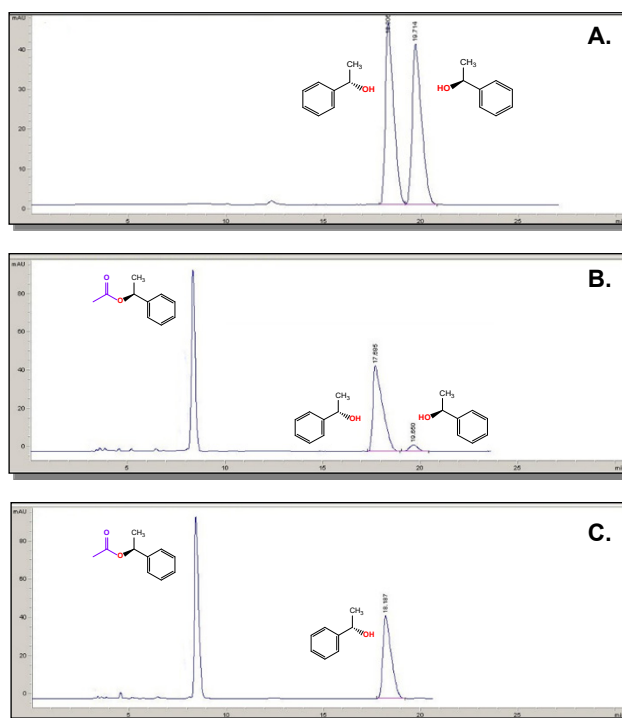


Figure 3. HPLC analysis of reaction samples after 12 hours **A.** control reaction; **B.** 12 mg of 8%–PVA–CaL-B biocatalyst (enzyme loading 14 $\mu\text{g}/\text{mg}$); **C.** 12 mg of 10%–PVA–CaL-B biocatalyst (enzyme loading 13.07 $\mu\text{g}/\text{mg}$)

However, in the case of 12%–PVA–CaL-B biocatalyst the maximum conversion was achieved after 12 hours, but not in case of 8%–PVA–CaL-B (**Table 1, entry 28-30**). This was analyzed also after 24 hours, when conversion reached 50%.

Based on the recorded chromatograms, after 4 hours the maximum conversion was achieved when 12 mg of 10%–PVA–CaL-B was used (**Figure 4**).

Table 1. PVA–CaL-B biocatalytic activity evaluation (*1st catalytic cycle*)

Reaction time (h)	C PVA (w/w %)	m PVA–CaL-B (mg)	Enzyme loading (µg/mg)	ees (%)	Conversion *	
2	8	4	4.7	19	16	
		8	9.3	31	24	
		12	14.0	41	30	
	10	4	4.4	40	29	
		8	7.5	52	34	
		12	13.1	69	41	
		12	4	3.4	31	24
			8	6.2	45	31
			12	10.1	61	38
	4	8	4	4.7	30	23
			8	9.3	40	29
			12	14.0	58	37
10		4	4.4	57	36	
		8	7.5	71	42	
		12	13.1	> 99	50	
12		4	3.4	45	31	
		8	6.2	62	39	
		12	10.1	81	45	
6		8	4	4.7	45	31
			8	9.3	57	36
			12	14.0	69	41
	10	4	4.4	71	42	
		8	7.5	88	47	
		12	13.1	> 99	50	
	12	4	3.4	62	39	
		8	6.2	81	45	
		12	10.1	> 99	50	
	12	8	4	4.7	62	39
			8	9.3	71	42
			12	14.0	88	47
10		4	4.4	> 99	50	
		8	7.5	> 99	50	
		12	13.1	> 99	50	
12		4	3.4	> 99	50	
		8	6.2	> 99	50	
		12	10.1	> 99	50	

* **ees** > 99% in all cases

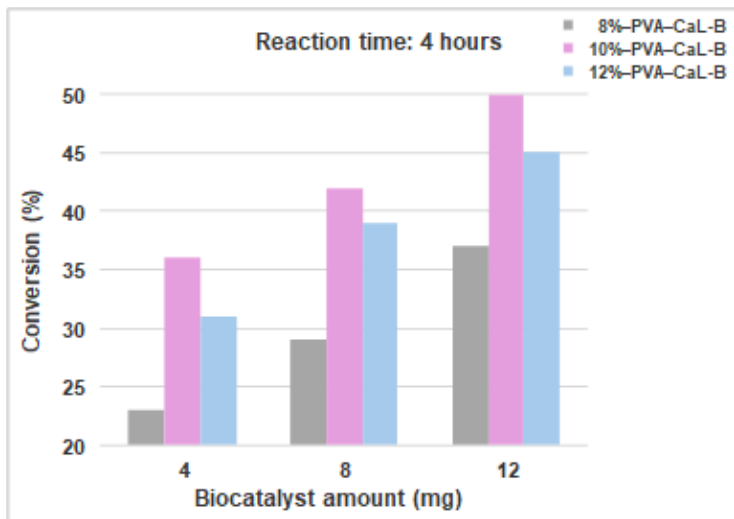


Figure 4. Conversion variation after 4 hours (*1st catalytic cycle*)

For reusability studies, in each case after the first catalytic cycle the biocatalyst was removed from the reaction media, was washed 2 times with isopropanol, 2 times with hexane and was stored in the refrigerator in a sealed glass container until further use regarding reusability.

The second catalytic cycle was performed as previously described. Samples were taken from the reaction mixture at fixed time intervals, analyzed by HPLC and conversion rates were calculated based on the chromatograms. The values indicate no decrease in activity, the 50% conversion rate was achieved after 4 hours using 12 mg of 10%–PVA–CaL–B biocatalyst in this case also. However, in all cases, maximum conversion was observed after 24 hours.

Based on this finding, we decided to test the reusability of the most promising biocatalyst (10%–PVA–CaL–B), starting from the third catalytic cycle, using 12 mg of prepared biocatalyst. The experiments were stopped when conversion dropped below 40% after 4 hours. The results are plotted in **Figure 5**.

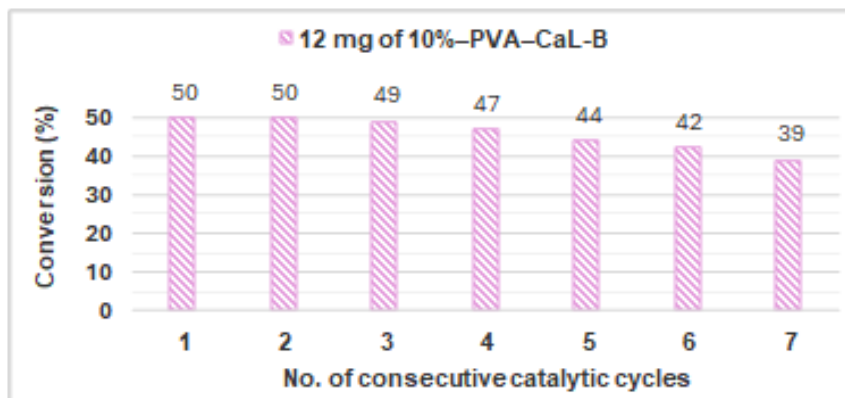


Figure 5. The reusability of 10%-PVA-CaL-B biocatalyst (12 mg) in the EKR of (*rac*)-1-phenylethanol with vinyl acetate after 4 hours

Further, the 10%-PVA-CaL-B biocatalyst was tested on halogenated (*rac*)-1-phenylethanol derivatives as substrates, namely (*rac*)-4-bromo-1-phenylethanol and (*rac*)-4-chloro-1-phenylethanol, under the previously described reaction conditions: substrate/acylating agent *ratio* 1:2, solvent hexane, incubation temperature 30°C, shaking at 1350 rpm with 12 mg biocatalyst (enzyme loading 13.1 µg/mg).

The samples taken from the reaction mixture at fixed time intervals were analyzed by gas chromatography on a Supelco Analytical Astec CHIRALDEX® B-DM Silica capillary column (30m × 0.32mm × 0.12µm) under the following conditions: N₂ as carrier gas, 1 µL injection volume, 100:1 split *ratio*, FID detector and injector temperature 250°C, head pressure 60 psi, operating at 120°C in case of (*rac*)-4-Br-1-phenyl-ethanol and with temperature gradient from 120°C to 160°C with 2.6°/min increment in case of (*rac*)-4-Cl-1-phenylethanol.

Considering the data from **Table 2**, the samples taken from the reaction mixture at fixed time intervals were subjected to GC analysis. Based on the recorded chromatograms, the calculated conversions are summarized in **Table 3**.

Table 2. Chromatographic chiral separation of racemic halogenated 1-phenylethanol derivatives (left) and their acetates (right) [49]

Compound	Retention time (min)		Compound	Retention time (min)	
	S	R		S	R
(<i>rac</i>)-4- Br -1-phenylethanol	28.3	31.3	(<i>rac</i>)-4- Br -1-phenylethyl acetate	24.9	26.6
(<i>rac</i>)-4- Cl -1-phenylethanol	11.6	11.3	(<i>rac</i>)-4- Cl -1-phenylethyl acetate	9.4	9.8

Table 3. EKR of racemic halogenated 1-phenylethanol derivatives with vinyl acetate over 12 mg of 10%–PVA–CaL–B biocatalyst in batch mode

Reaction time (h)	Substrate			
	(±)-4- Br -phenylethanol		(±)-4- Cl -phenylethanol	
	ees (%)	c* (%)	ees (%)	c* (%)
2	31	24	41	30
4	45	31	> 99	50
6	> 99	50		

* ee_P > 99% in all cases

The reaction rate was higher in the case of the chlorinated substrate than in the case of the brominated 1-phenylethanol derivative.

CONCLUSIONS

Candida antarctica B lipase was successfully immobilized into polyvinyl alcohol nanofibers *via* electrospinning technique using polymer solutions of different concentrations. The prepared biocatalysts were structurally characterized by transmission electron microscopy which confirmed the fiber formation and structural changes were observable in the case of prepared biocatalysts.

The activity and selectivity upon immobilization were investigated in batch mode in the acylation of racemic 1-phenylethanol with vinyl acetate. In the first catalytic cycle, maximum conversion was obtained after 4 hours in the case of using 12 mg of 10%–PVA–CaL–B noted biocatalyst with enzyme loading equal to 13.07 µg/mg instead of expected 12 mg of 10%–PVA–CaL–B biocatalyst with a higher enzyme loading (14.0 µg/mg). This could be explained with the fact that higher enzyme loading can cause steric hindrance between the protein molecules resulting in a less active biocatalyst.

In the second catalytic cycle the obtained results were in concordance with the previous findings, therefore only 10%–PVA–CaL–B biocatalyst was subjected further to reusability studies. A slight decrease in activity was observed starting with the third cycle. However, after the 7th consecutive catalytic cycle the biocatalyst maintained 78% of its initial activity.

The 10%–PVA–CaL–B biocatalyst proved to be suitable also for EKR of racemic halogenated 1-phenylethanol derivatives as well, returning the highest conversion after 4 hours when (*rac*)-4-chloro-1-phenylethanol was used as substrate.

EXPERIMENTAL SECTION

Materials and methods

Polyvinyl alcohol (molecular weight 130.000), vinyl acetate, (*rac*)-1-phenylethanol and sodium phosphate monobasic hydrate were products of Sigma-Aldrich. (*Rac*)-4-Bromo-1-phenylethanol, (*rac*)-4-chloro-phenyl-ethanol, (*rac*)-4-bromo-phenylethyl acetate and (*rac*)-4-chloro-phenylethyl acetate were synthesized by our colleagues [35] and used as received. Lipase B from *Candida antarctica* was purchased from Chiral Vision; HPLC grade solvents were procured from PromoChem.

For enzyme immobilization into polymeric nanofibers, the Fluidnatek Bioinicia electrospinning system was used. Transmission electron microscopy analyses were conducted on Hitachi H-7650 apparatus, at 80 keV. 460/H Ultrasonic bath operating at 100 W, 40 kHz served for ultrasonication. The shaking and incubation of the enzymatic reactions were performed on a shaker equipped with a heating module (Titramax 1000).

High-performance liquid chromatography analyses were performed with an Agilent 1200 instrument, while gas chromatography determinations were conducted on an Agilent 7890A GC equipped with a flame ionization detector.

The enantiomeric excess values of the substrate (ee_S) and of the product (ee_P) were calculated from the peak areas of HPLC chromatograms and the conversion (c) was determined from the following well-known equation [50]:

$$c (\%) = \frac{ee_S}{ee_S + ee_P} * 100$$

1. Immobilization of CaL-B into PVA nanofibers by electrospinning

The first step consisted of the preparation of stock solutions: CaL-B enzyme solution of 2,8 mg/mL concentration in 100 mM phosphate buffer, pH 7.5 and aqueous polyvinyl alcohol solutions of 8%, 10% and 12% concentration, respectively.

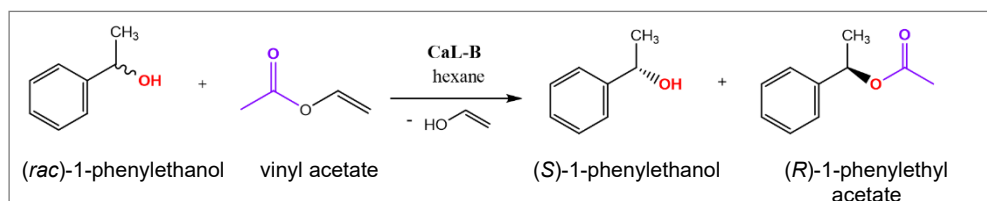
The polymer solution concentration values were chosen based on prior attempts to produce PVA nanofibers since the success of nanofiber production is also viscosity-dependent.

In the second step, the polymer-enzyme mixtures were prepared by adding 200 μ L of CaL-B solution to 6 mL polymer solution ($c_1 = 8\%$, $c_2 = 10\%$, $c_3 = 12\%$) followed by 30 minutes of ultrasonication and 1 h shaking at room temperature for optimal homogenization.

To obtain electrospun nanofibers, the dispensing syringe of the electrospinning equipment was filled with 5 mL of polymer-enzyme mixture and the vertical collector was wrapped with aluminium thin foil to facilitate the collecting of the produced nanofibers afterwards. The sample feeding rate varied between 560-750 μ L/h and the applied voltage between 18-19.5 kV depending on the viscosity of the polymer-enzyme mixture. The distance between the emitter and the collector was set to 13 cm in all cases. The as-produced solid biocatalyst (abbreviated further as 8%-PVA-CaL-B, 10%-PVA-CaL-B and 12%-PVA-CaL-B) was removed from the aluminium foil using a sharp tweezer, placed in a sealed glass container and stored in the refrigerator until use.

2. Activity and selectivity investigation of the prepared nanofiber-based biocatalysts

The chosen model reaction used for biocatalyst testing is illustrated in **Scheme 1**.



Scheme 1. Enzymatic kinetic resolution of racemic 1-phenylethanol with vinyl acetate mediated by immobilized lipase B from *Candida antarctica*

Batch reactions were performed in 1.5 mL screw-capped glass vials. To 1 mL hexane, 12 μL (*rac*)-1-phenylethanol (1.5 mmol), 36.8 μL vinyl acetate (3 mmol) and nanofiber-based biocatalyst (4 mg, 8 mg, 12 mg) were added. The vials were placed on a thermostated shaker (1350 rpm) at 30°C. At fixed time intervals (2 h, 4 h, 6 h, 24 h) 50 μL of the reaction mixture was removed, diluted with 450 μL hexane, centrifuged, filtered and injected into HPLC chiral chromatographic column.

3. Activity investigation of the prepared 10%–PVA–CaL-B biocatalyst on *p*-halogeno-1-phenylethanol derivatives

1.5 mmol racemic *p*-halogeno-phenylethanol derivative, 3 mmol vinyl acetate and 12 mg 10%–PVA–CaL-B were added to 1 mL hexane in a screw-capped glass vial. The vials were placed on a thermostated shaker (1350 rpm) at 30°C. At fixed time intervals (2 h, 4 h, 6 h, 12 h) 50 μL of the reaction mixture was withdrawn from the reaction media, diluted with 450 μL hexane, centrifuged, filtered and analyzed by gas chromatography.

REFERENCES

1. A. Frenot; I. S. Chronakis; *COCIS*, **2003**, 8, 64–75.
2. W. J. Morton; Patent no. US 705,691, **1902**.
3. J. F. Cooley; Patent no. US 745,276, **1903**.
4. K. Shafer; H. Thomas; P. Dalton; M. Moeller; Nano-Fibers for Filter Materials in *Multifunctional Barriers for Flexible Structure*, Springer, **1991**, Chapter 7, pp.125–138.
5. A. A. Babar; N. Iqbal; X. Wang; J. Yu; B. Ding; Introduction and historical overview in *Electrospinning: Nanofabrication and Applications*, William Andrew, **2019**, Chapter 1, pp. 3–20.
6. C. Cleeton; A. Keirouz; X. Chen; N. Radacsi; *ACS Biomater. Sci. Eng.*, **2019**, 5, 4183–4205.
7. S. Ramakrishna; K. Fujihara; W. E. Teo; T. Yong; Z. Ma; R. Ramaseshan; *Mater. Today*, **2006**, 9, 40–50.
8. X. Zhang; R. Lv; L. Chen; R. Sun; Y. Zhang; R. Sheng; T. Du; Y. Li; Y. Qi; *ACS Appl. Mater. Interfaces*, **2022**, 14, 12984–13000.
9. C. Z. Mosher; P. A. P. Brudnicki; Z. Gong; H. R. Childs; S. W. Lee; R. M. Antrobus; E. C. Fang; T. N. Schiros; H. H. Lu; *Biofabrication*, **2021**, 13, 035049.
10. A. B. J. de Barbosa; C. A. de França; J. J. de S. Gouveia; G. V. Gouveia, M. M. da Costa, H. P. de Oliveira, *J. Appl. Polym. Sci.*, **2019**, 136, 47479.

11. D. Li; Q. Wang; F. Huang; Q. Wei; Electrospun nanofibers for enzyme immobilization in *Electrospinning: Nanofabrication and Applications*, William Andrew, **2019**, Chapter 26, pp. 765–781.
12. Z. G. Wang; L. S. Wan; Z. M. Liu; X. J. Huang; Z. K. Xu; *J. Mol. Catal. B Enzym.*, **2009**, *56*, 189–195.
13. M. M. Aldahr; Y. Q. Almulaiky; R. M. El-Shishtawy; W. Al-Shawafi; A. Alngadh; R. Maghrabi; *ACS Omega*, **2018**, *3*, 6346–6350.
14. D. N. Tran; K. J. Balkus Jr.; *Top. Catal.*, **2012**, *55*, 1057–1069.
15. A. Greiner; J. H. Wendorff; *Angew. Chem., Int. Ed.*, **2007**, *46*, 5670–5703
16. Z. Vargas-Osorio; F. Ruther; S. Chen; S. Sengupta; L. Liverani; M. Michálek; D. Galusek; A. R. Boccaccini; *Biomed. Mater.*, **2022**, *17*, 045019.
17. V. Korniienko; Y. Husak; J. Radwan-Pragłowska; V. Holubnych; Y. Samokhin; A. Yanovska; J. Varava; K. Diedkova; Ł. Janus; M. Pogorielov; *Molecules*, **2022**, *27*, 3343.
18. Y. Samokhin; Y. Varava; K. Diedkova; I. Yanko; Y. Husak; J. Radwan-Pragłowska; O. Pogorielova; Ł. Janus; M. Pogorielov; V. Korniienko; *J. Funct. Biomater.*, **2023**, *14*, 414.
19. A. Al-Abduljabbar; I. Farooq; *Polymers*, **2023**, *15*, 65.
20. N. Rao; R. Singh; L. Bashambu; *Mater. Today: Proceedings*, **2021**, *44*, 608–614.
21. P. Adlercreutz, *Chem. Soc. Rev.*, **2013**, *42*, 6406–6436.
22. M. L. E. Gutarra; L. S. M. Miranda; R. O. M. A. de Souza, Enzyme Immobilization for Organic Synthesis in Organic Synthesis Using Biocatalysis, ed. A. Goswami and J. D. Stewart, Academic Press, Amsterdam, **2016**, Chapter 4, pp. 99–126.
23. R. C. Rodrigues; J. J. Virgen-Ortíz; J. C. S. dos Santos; Á. Berenguer-Murcia; A. R. Alcantara; O. Barbosa; C. Ortiz; R. Fernandez-Lafuente; *Biotechnol. Adv.*, **2019**, *37*, 746–770.
24. A. F. de Almeida; C. R. F. Terrasan, C. C. Terrone; S. M. Tauk-Tornisielo; E. C. Carmona; *Process Biochem.*, **2018**, *65*, 71–80.
25. L. de Abreu; R. Fernandez-Lafuente; R. C. Rodrigues; G. Volpato; M. A. Z. Ayub; *J. Mol. Catal. B Enzym.*, **2014**, *99*, 51–55.
26. T. Liu; X. Wang; Q. Li; J. Wang; Y. Yan; *J. Mol. Catal. B Enzym.*, **2011**, *71*, 45–50.
27. B. Stauch; S. J. Fisher; M. Cianci; *JLR*, **2015**, *56*, 2348–2358.
28. P. Nicolás; V. L. Lassalle; M. L. Ferreira; *Enzyme Microb. Technol.*, **2017**, *97*, 97–103.
29. J. Cassani; H. Luna; A. Navarro-Ocaña; E. Castillo; *Electron. J. Biotechnol.*, **2007**, *10*, 508–513.
30. E. M. Anderson; M. Karin; O. Kirk; *Biocatal. Biotransform.*, **1998**, *16*, 181–204.

31. M. Habulin; Ž. Knez; *J. Mol. Catal. B Enzym.*, **2009**, *58*, 24–28.
32. A. Idris; A. Bukhari; *Biotechn. Adv.*, **2012**, *30*, 550–563.
33. L. F. Solares; R. Brieva; M. Quiros; I. Llorente; M. Bayod; V. Gotor; *Tetrahedron: Asymmetry*, **2004**, *15*, 341–345.
34. C. A. Gál; L. E. Barabás; J. H. Bartha-Vári; M. E. Moisă; D. Balogh-Weiser; L. C. Bencze; L. Poppe; C. Paizs; M. I. Toşa; *React. Chem. Eng.*, **2021**, *6*, 2391–2399.
35. Q. Li; F. Fan; Y. Wang; W. Feng; P. Ji; *Ind. Eng. Chem. Res.*, **2013**, *52*, 6343–6348.
36. L. C. Bencze; J. H. Bartha-Vári; G. Katona; M. I. Toşa; C. Paizs; F. D. Irimie; *Bioresour. Technol.*, **2016**, *200*, 853–886.
37. E. P. Cipolatti; M. C. C. Pinto; J. M. de Robert; T. P. da Silva; T. D. C. Beralto; J. G. F. Santos Jr.; R. Fernandez-Lafuente; E. A. Manoel; J. C. C. D. S. Pinto; D. M. G. Freire; *J. Appl. Polym. Sci.*, **2018**, *135*, 46727.
38. Y. Poojari; S. J. Clarson; *Biocatal. Agric. Biotechnol.*, **2013**, *2*, 7–11.
39. J. Sun; Y. Jiang; L. Zhou; J. Gao; *New Biotechnology*, **2010**, *27*, 53–58.
40. X. Geng; O.-H. Kwon; J. Jang; *Biomater.*, **2005**, *26*, 5427–5432.
41. K. Sun; Z. H. Li; *EXPRESS Polym. Lett.*, **2011**, *5*, 342–361.
42. C. Ortiz; M. L. Ferreira; O. Barbosa; J. C. s. dos Santos; R. C. Rodriguez; Á. Berenguer-Murcia; L. E. Briand; R. Fernandez-Lafuente; *Catal. Sci. Technol.*, **2019**, *9*, 2380–2420.
43. C. José; R. D. Bonetto; L. A. Gambaro; M. P. Guauque Torres; M. L. Foresti; M. L. Ferreira; *J. Mol. Catal. B: Enzym.*, **2017**, *71*, 95–107.
44. C. José; L. E. Briand; *React. Kinet., Mech. Catal.*, **2010**, *99*, 17–22.
45. C. G. Spelmezan; A. Bacoş; G. Katona; *Studia UBB Chemia*, **2023**, *LXVIII*, *2*, 53–71.
46. C. G. Spelmezan; G. Katona; L. C. Bencze; C. Paizs; M. I. Toşa; *React. Chem. Eng.*, **2023**, *8*, 1109.
47. P. L. Sóti; D. Weiser; T. Vigh; Zs. K. Nagy; L. Poppe; G. Marosi; *Bioprocess. Biosyst. Eng.*, **2015**, *39*, 449–459.
48. A. Goswami; J. Goswami; *Tetrahedron Lett.*, **2005**, *46*, 4411–4413.
49. *Electronic Supplementary Material (ESI)* for C. A. Gál; L. E. Barabás; J. H. Bartha-Vári; M. E. Moisă; D. Balogh-Weiser; L. C. Bencze; L. Poppe; C. Paizs; M. I. Toşa; *React. Chem. Eng.*, **2021**.
50. C.-S. Chen; Y. Fujimoto; G. Girdaukas; C. J. Sih; *J. Am. Chem. Soc.*, **1982**, *14*, 7294.

INSIGHTS INTO CLOZAPINE'S KINETIC INTERACTIONS: ENZYMATIC INHIBITION OF CYP1A2 BY CIPROFLOXACIN AND NORFLOXACIN

Ana-Elena CHIRALI^a, Iulia Maria CIOCOTIȘAN^a ,
Ana-Maria VLASE^{b,*} , Dana Maria MUNTEAN^a , Laurian VLASE^a 

ABSTRACT. This study aimed to evaluate the kinetic interactions between clozapine (CLZ) and the fluoroquinolone antibiotics ciprofloxacin and norfloxacin using a systematic three-step compartmental modelling approach. Clozapine, primarily metabolized by CYP1A2 and CYP3A4, is known to exhibit altered kinetics when co-administered with fluoroquinolones due to their inhibitory effect on CYP1A2. The proposed models evaluated the absorption, distribution, metabolism, and elimination (ADME) of clozapine and its active metabolite, N-desmethyl clozapine (CLZ-M), under both reference conditions and in the presence of these antibiotics. The selected kinetic models demonstrated a strong correlation between experimental data and predictions ($R^2 > 0.96$), providing robust insights into the mechanisms underlying these interactions. Ciprofloxacin and norfloxacin significantly affected CLZ's presystemic and systemic metabolism, with ciprofloxacin altering relative bioavailability more prominently. These findings emphasize the necessity of dose adjustments for clozapine in clinical practice to mitigate potential adverse effects due to modified drug exposure when co-administered with fluoroquinolones. This study offers a mechanistic framework for understanding complex drug-drug interactions and optimizing dosing strategies in combined therapeutic regimens.

Keywords: kinetic modelling, drug-drug interaction, preclinical study, clozapine, fluoroquinolone antibiotics.

^a Iuliu Hațieganu University of Medicine and Pharmacy, Faculty of Pharmacy, Department of Pharmaceutical Technology and Biopharmacy, 8 Victor Babeș Street, RO-400347 Cluj-Napoca, Romania

^b Iuliu Hațieganu University of Medicine and Pharmacy, Faculty of Pharmacy, Department of Pharmaceutical Botany, 8 Victor Babeș Street, RO-400347 Cluj-Napoca, Romania

* Corresponding author: gheldiu.ana@umfcluj.ro



INTRODUCTION

Clozapine (8-chloro-11-(4-methylpiperazin-1-yl)-5H-dibenzo[b,e][1,4]diazepine) is a chemically distinct second-generation antipsychotic. Its unique molecular structure contributes to its wide receptor-binding profile, which includes dopaminergic, serotonergic, and adrenergic receptors, making it particularly effective for managing patients with treatment-resistant schizophrenia. Despite its advantages, clozapine therapy presents significant challenges, including a narrow therapeutic index and a high inter-individual variability in plasma concentration due to its complex kinetics and metabolism [1].

The kinetic behavior of clozapine is mainly directed by its extensive hepatic metabolism mediated by cytochrome P450 enzymes, particularly CYP1A2 and CYP3A4. Other isoforms, such as CYP2C19, and CYP2D6, contribute to a lesser extent to its biotransformation, as supported by kinetic data of expressed enzymes [1-3]. The metabolization processes of clozapine include N-demethylation, hydroxylation, N-oxidation, and conjugation before it is excreted. Clozapine presents two major metabolites, N-desmethylclozapine (or norclozapine), chemically known as 8-chloro-11-(1-methylpiperazin-4-yl)-5H-dibenzo[b,e][1,4]diazepine whose formation is attributed to both CYP1A2 and CYP3A4, and clozapine N-oxide, chemically known as 8-chloro-11-(4-methylpiperazin-1-yl)-5H-dibenzo[b,e][1,4]diazepine N-oxide, whose formation is mainly attributed to CYP3A4 [4-6].

Clozapine presents a rather poor bioavailability after oral administration due to extensive first-pass metabolism, resulting in a low and highly variable systemic bioavailability with an average around 30% [4]. The variability in clozapine metabolism is influenced by factors such as smoking, gender, co-medications, genetic polymorphisms, and drug-drug interactions, particularly those affecting CYP1A2 activity [5].

Ciprofloxacin (1-cyclopropyl-6-fluoro-1,4-dihydro-4-oxo-7-(1-piperazinyl)-3-quinolinecarboxylic acid) and norfloxacin (1-ethyl-6-fluoro-1,4-dihydro-4-oxo-7-(1-piperazinyl)-3-quinolinecarboxylic acid) [7,8] are fluoroquinolone antibiotics known to inhibit CYP1A2, the primary enzyme responsible for clozapine metabolism [6]. These interactions can significantly alter the kinetic profile of clozapine, leading to elevated plasma levels, prolonged therapeutic effects, and an increased risk of adverse reactions. From a chemical perspective, these interactions underscore the importance of understanding the molecular mechanisms by which enzyme inhibitors affect the metabolism of clozapine and its metabolites.

Unlike the non-compartmental approach, the compartmental modelling approach provides a valuable tool for describing and quantifying the movement of clozapine and its metabolites within the body [9]. This approach enables the

characterization of CLZ's disposition in the body following oral administration, providing a detailed mechanistic understanding of its absorption, distribution, metabolism, and elimination (ADME) processes [10]. By incorporating kinetic parameters and their modulation by enzyme inhibitors, such as ciprofloxacin and norfloxacin, it is possible to simulate and predict the impact of drug-drug interactions on systemic drug behavior of clozapine.

This study aims to provide a detailed chemical and kinetic analysis of clozapine and its primary metabolite, N-desmethylozapine, in the presence of ciprofloxacin and norfloxacin. Using experimental data from adult male Wistar rats, a comprehensive kinetic model was developed and used to characterize the interactions at the enzymatic and systemic levels. The results of this study are expected to enhance the understanding of the chemical and molecular insights of these drug-drug interactions and their implications for current practice.

RESULTS AND DISCUSSION

Figure 1 presents the mean plasma concentration-time profiles of CLZ and its primary metabolite, CLZ-M. These graphics highlight the extent of drug exposure following the co-administration of CLZ with fluoroquinolone antibiotics, providing valuable insights into the kinetic interactions and their potential implications for CLZ's metabolism and disposition.

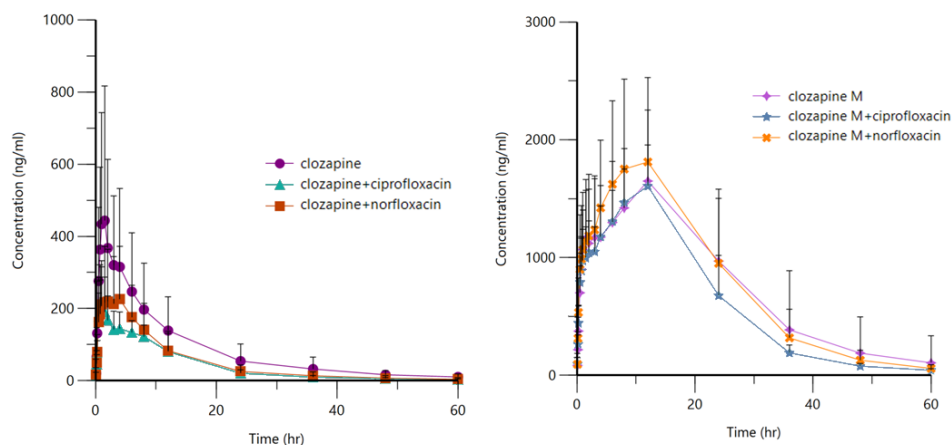


Figure 1. The mean plasma concentration-time profile of clozapine, administered as a single oral dose (20 mg/kg body weight), is depicted under three treatment conditions: as monotherapy (\circ), after a 6-day pretreatment with ciprofloxacin (15 mg) (Δ), and after a 6-day pretreatment with norfloxacin (30 mg) (\square). Data are presented as mean values + standard deviation (left). The corresponding mean plasma concentration-time profile for N-desmethylozapine under the same conditions is shown on the right

In the first stage, the focus was on optimizing a model specifically for the parent compound, CLZ, without including the metabolite or potential kinetic interactions. This initial model was aimed and consequently designed to isolate and characterize the kinetic properties of clozapine, establishing a foundational framework for incorporating more complex variables in following stages. A summary of the model parameters evaluated for clozapine kinetics is presented in Table 1.

Table 1. Kinetic models of **clozapine** used in compartmental analysis

Kinetic model	Lag Time	Absorption kinetics	Number of compartments
M1	No	1st order	1
M2	Yes	1st order	1
M3	No	1st order	2
M4	Yes	1st order	2

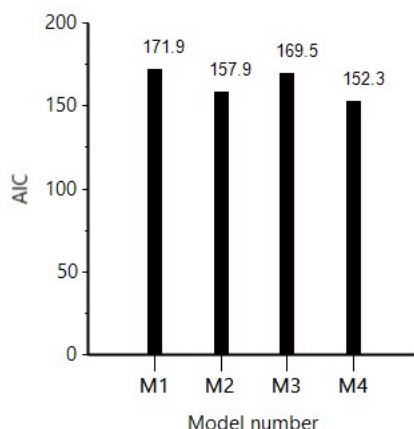


Figure 2. AIC values of M1-4 kinetic models describing the ADME processes of **clozapine** following oral administration

After evaluating multiple models and their respective Akaike Information Criterion (AIC) values, Model 4 (M4) was identified as the most suitable for further analysis. M4 was therefore selected as the baseline for subsequent modelling steps. This model employs first-order absorption kinetics with a lag time and assumes a bi-compartmental distribution for the parent compound, CLZ. The AIC values supporting this selection are illustrated in Figure 2.

Building on M4, four additional models were developed, with their specific differences summarized in Table 2. After re-evaluating AIC values (Figure 3), Model 43 (M43) was determined to be the best representative model.

Table 2. Kinetic models of **clozapine (CLZ)** and **N-desmethyl clozapine (CLZ-M)** assessed during the compartmental modelling approach

Kinetic model	Number of compartments for CLZ-M	Presystemic metabolism	Systemic metabolism	Other elimination routes from central compartment for CLZ
M41	1	No	Yes	Yes
M42	1	Yes	Yes	Yes
M43	2	No	Yes	Yes
M44	2	Yes	Yes	Yes

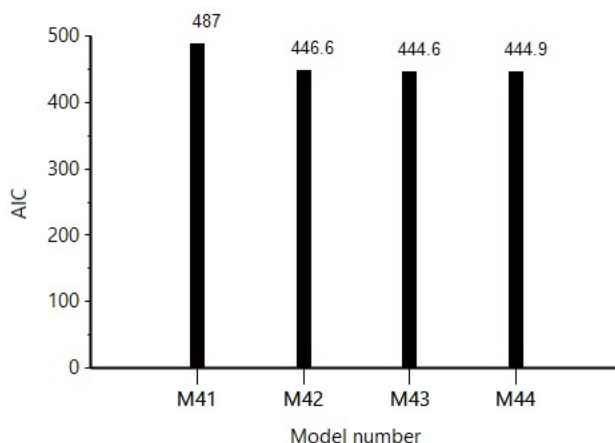


Figure 3. Akaike Index Criteria (AIC) results for the four models describing the kinetics of **N-desmethyl clozapine** after oral administration of clozapine

M43 is characterized by first-order absorption kinetics with a lag time, bi-compartmental distribution for CLZ, no presystemic metabolism, and a bi-compartmental distribution for its primary metabolite, N-desmethyl clozapine (CLZ-M). This preference for M43 over M42 aligns with the fact that most medications exhibit bi-compartmental rather than mono-compartmental distribution patterns.

In the third stage, two parallel models were developed to explore the interaction between CLZ and the selected fluoroquinolones, ciprofloxacin and norfloxacin. The specific differences between these models are detailed in Table 3.

Table 3. Kinetic models of clozapine (CLZ) and N-desmethyl clozapine (CLZ-M) used in compartmental analysis of the interactions with both fluoroquinolone antibiotics

Kinetic model	Number of compartments for CLZ and CLZ-M	Presystemic metabolism	Other elimination routes for CLZ	Relative bioavailability
M431	2	No	No	Same
M432	2	No	No	Different

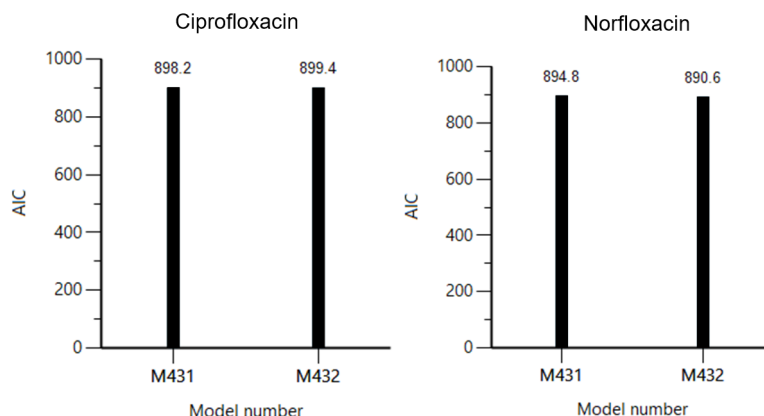


Figure 4. Akaike Index Criteria (AIC) results for the compartmental kinetic modelling of drug-drug interactions between **clozapine** and ciprofloxacin and norfloxacin

Based on the AIC scores (Figure 4), Model 431 (M431) was the best fit for the interaction between CLZ and ciprofloxacin, while Model 432 (M432) proved optimal for CLZ-norfloxacin interaction. Both models assumed first-order absorption kinetics with a lag time for CLZ, bi-compartmental distribution for CLZ and CLZ-M, and the elimination of CLZ exclusively via metabolism to CLZ-M. The distinct feature of M432 is the assumption of a relative bioavailability different than 100%.

Figure 5 illustrates the kinetic processes described by the M43 model, depicting the distribution of CLZ and CLZ-M between compartments, along with their associated kinetic processes and rate constants. This comprehensive framework provides valuable insights into the kinetic behaviours of CLZ and its interactions with the selected fluoroquinolones. Additionally, it offers important details about the processes of absorption, distribution, metabolism, and elimination for both CLZ and CLZ-M.

INSIGHTS INTO CLOZAPINE'S KINETIC INTERACTIONS: ENZYMATIC INHIBITION OF CYP1A2 BY CIPROFLOXACIN AND NORFLOXACIN

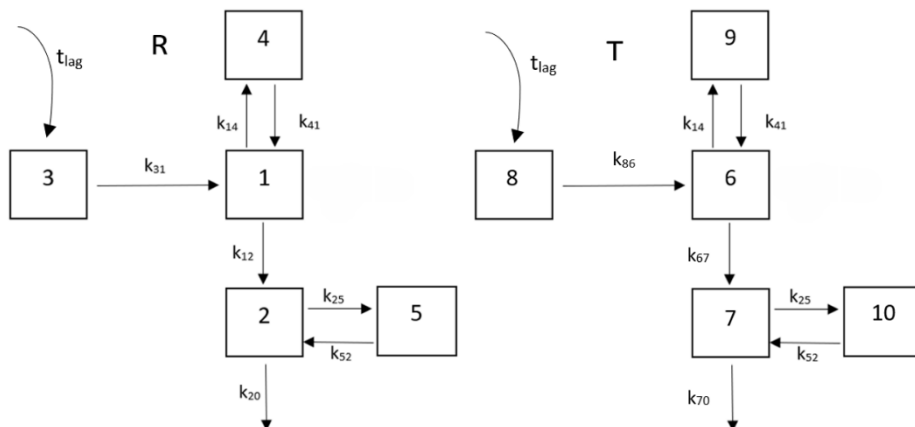


Figure 5. Schematic representation of the kinetic processes in model M43. On the left: "3" denotes the extravascular absorption site; "1" and "2" represent the central compartments for clozapine and N-desmethyl clozapine, respectively, while "4" and "5" are their peripheral distribution compartments. On the right: "8" represents the extravascular absorption site; "6" and "7" correspond to the central compartments for clozapine and N-desmethyl clozapine during the reference period, with "9" and "10" being their respective peripheral compartments during the test periods. The absorption latency time is represented as t_{lag} , and the absorption rate constant of clozapine is k_{31} . Distribution rate constants are k_{14} and k_{41} for the reference period, and k_{25} and k_{52} for the test periods. The systemic metabolism rate constant from clozapine to its metabolite is k_{12} . The elimination rate constants for clozapine (non-metabolic) and N-desmethyl clozapine are k_{20} and k_{70} , respectively, across both reference and test periods.

In this kinetic modelling study, compartmental models were employed to describe the disposition of CLZ and its primary metabolite, N-desmethyl clozapine (CLZ-M), between central and peripheral compartments over time [11,12]. These models are described by partial differential equations that quantify the rate of change in parent drug and metabolite concentration or amount within each compartment, reflecting the kinetic processes of absorption, distribution, metabolism, and elimination (ADME). The equations are based on the principle of mass balance, which mentions that the rate of change within a compartment is determined by the net balance of drug entering and leaving that compartment [13,14].

Rate constants incorporated into these equations provide the mathematical foundation for depicting the time-dependent kinetics of CLZ and CLZ-M across compartments. Specifically, the equations for the M43 kinetic model, used to describe the kinetics of CLZ and CLZ-M during both

the reference period (absence of inhibitors) and test periods (presence of CYP1A2 inhibitors ciprofloxacin or norfloxacin), were formulated using the general mass balance equation:

$$\frac{\partial A_i}{\partial t} = (\text{Rate of drug entering the compartment}) - (\text{Rate of drug leaving the compartment})$$

where A_i denotes the amount of drug in compartment i , and t represents time.

The complete set of equations underlying the M43 model is presented in Figure 6, offering a detailed depiction of the kinetic processes governing CLZ and CLZ-M under the respective experimental conditions. The results of the kinetic analysis are summarized in Table 4.

$$\begin{cases}
 \frac{\partial QC_{c1}}{\partial t} = k_{31} * QC_{abs3} * (1 - f_1) - k_{12} * QC_{c1} - k_{14} * QC_{c1} + k_{41} * QC_{p4} \\
 \frac{\partial QN_{c2}}{\partial t} = k_{12} * QC_{c1} * 0.997 - k_{20} * QN_{c2} - k_{25} * QC_{c2} + k_{52} * QC_{p5} + k_{31} * f_1 * QC_{abs3} * 0.997 \\
 \frac{\partial QC_{abs3}}{\partial t} = -k_{31} * QC_{abs3} \\
 \frac{\partial QC_{p4}}{\partial t} = k_{14} * QC_{c1} - k_{41} * QC_{p4} \\
 \frac{\partial QN_{p5}}{\partial t} = k_{25} * QN_{c2} - k_{52} * QN_{p5} \\
 \frac{\partial QC_{c6}}{\partial t} = k_{31} * QC_{abs8} * (1 - f_2) - k_{67} * QC_{c6} - k_{14} * QC_{c6} + k_{41} * QC_{p9} \\
 \frac{\partial QN_{c7}}{\partial t} = k_{67} * QC_{c6} * 0.997 - k_{70} * QN_{c7} - k_{25} * QN_{c7} + k_{52} * QN_{p10} + k_{31} * f_2 * QC_{abs8} * 0.997 \\
 \frac{\partial QC_{abs8}}{\partial t} = -k_{31} * QC_{abs8} \\
 \frac{\partial QC_{p9}}{\partial t} = k_{14} * QC_{c6} - k_{41} * QC_{p9} \\
 \frac{\partial QN_{p10}}{\partial t} = k_{25} * QN_{c7} - k_{52} * QN_{p10}
 \end{cases}$$

Figure 6. Mathematical equations for the kinetic model M43 in which $QC_{c1/6}$ and $QC_{p4/9}$ represent the amounts of clozapine in the central and peripheral compartments, respectively, while $QN_{c2/7}$ and $QN_{p5/10}$ denote the amounts of the metabolite (N-desmethyl clozapine) in its central and peripheral compartments. A molar ratio of 0.997 between clozapine and N-desmethyl clozapine was calculated and used as a conversion factor for translating molar units to mass units in the metabolic processes. Additional parameters for the model are provided in the legend of Figure 5.

Table 4. The kinetic parameters of clozapine and **N-desmethyl clozapine** determined with models M431 and M432

Parameter	Unit	M431 – T1	Standard error	M432 – T2	Standard error
f_{rel}	-	-	-	1.2945	0.2559
k_{12}	hr ⁻¹	3.7684	1.3288	3.7684	1.0440
k_{14}	hr ⁻¹	3.2326	2.2127	4.1156	1.8304
k_{20}	hr ⁻¹	1.1346	0.3606	1.2576	0.2186
k_{25}	hr ⁻¹	3.4353	0.8887	3.7578	0.8570
k_{31}	hr ⁻¹	0.1292	0.0550	0.1292	0.0373
k_{41}	hr ⁻¹	0.2437	0.2471	0.3155	0.2361
k_{52}	hr ⁻¹	0.3993	0.0720	0.4212	0.0667
k_{67}	hr ⁻¹	8.2529	3.1144	6.6553	2.3678
k_{70}	hr ⁻¹	0.8666	0.3758	0.7659	0.4752
k_{86}	hr ⁻¹	0.1053	0.0317	0.0931	0.0311
t_{lag}	hr	0.0690	0.0170	0.0715	0.0144
V F	L	1.0434	0.4097	1.1709	0.3100

To model the drug-drug kinetic interaction of CLZ with ciprofloxacin, the best-fitting model selected based on AIC values (M431) assumed no change in CLZ's bioavailability following co-administration with the inhibitor. In this scenario, the extent and rate of absorption, as reflected by the parameters k_{31} and k_{86} , were affected by the interaction (0.1292 hr⁻¹ vs. 0.1053 hr⁻¹ for the interaction of CLZ with ciprofloxacin; 0.1292 hr⁻¹ vs. 0.0931 hr⁻¹ for the interaction of CLZ with norfloxacin), as the effect of ciprofloxacin occurred primarily at the metabolic level, impacting both presystemic and systemic metabolism without interfering with the absorption dynamics.

On the other hand, model M432, used to assess the interaction with norfloxacin, assumed a relative bioavailability (f_{rel}) different from 100%, compared to the reference period (monotherapy). Specifically, during the test period with norfloxacin co-administration, f_{rel} was 30% higher than in the reference period ($f_{rel}=1.2945$). This increase was attributed predominantly to hepatic inhibition of CYP1A2, the primary enzyme involved in CLZ metabolism, and potentially to intestinal inhibition of CYP3A4 during the absorption phase, which plays a lesser but still relevant role. This altered presystemic metabolism during the absorption phase modified CLZ's oral bioavailability. Additionally, the extent and rate of absorption (k_{31} and k_{86}) were slightly impacted (0.1292 hr⁻¹ vs. 0.0931 hr⁻¹) due to metabolic-level interactions during presystemic and systemic metabolism.

Throughout the reference and test periods, extensive metabolism of CLZ to CLZ-M was observed, even under enzymatic inhibition of CYP1A2. This is evidenced by supra-unitary values for systemic metabolization constants ($k_{12}=3.7684$ hr⁻¹ during the reference period, $k_{67}=8.2529$ hr⁻¹ for co-administration with ciprofloxacin, and $k_{67}=6.6553$ hr⁻¹ for co-administration with norfloxacin). Notably, the magnitude of interaction was greater with ciprofloxacin than norfloxacin, as indicated by the higher k_{67} value for ciprofloxacin.

Further analysis of the metabolization rate constants for CLZ-M between study periods (k_{20} for the reference period and k_{70} for the test periods) revealed decreased elimination of CLZ-M during the test periods ($k_{20}=1.1346 \text{ hr}^{-1}$ vs. $k_{70}=0.8666 \text{ hr}^{-1}$ for ciprofloxacin and $k_{20}=1.2576 \text{ hr}^{-1}$ vs. $k_{70} = 0.7659 \text{ hr}^{-1}$ for norfloxacin co-administration). This reduction is likely due to the involvement of a metabolic pathway in CLZ-M elimination, which becomes saturated at higher metabolite concentrations during the test periods. This assumption is further supported by alterations in metabolism rate constants.

The graphical outputs from fitting model M431 for the interaction between CLZ and ciprofloxacin, and model M432 for the interaction with norfloxacin, are presented in Figures 7 and 8, respectively. These figures highlight the dynamics of absorption, distribution, and metabolism, providing a visual representation of the kinetic interactions under each test condition.

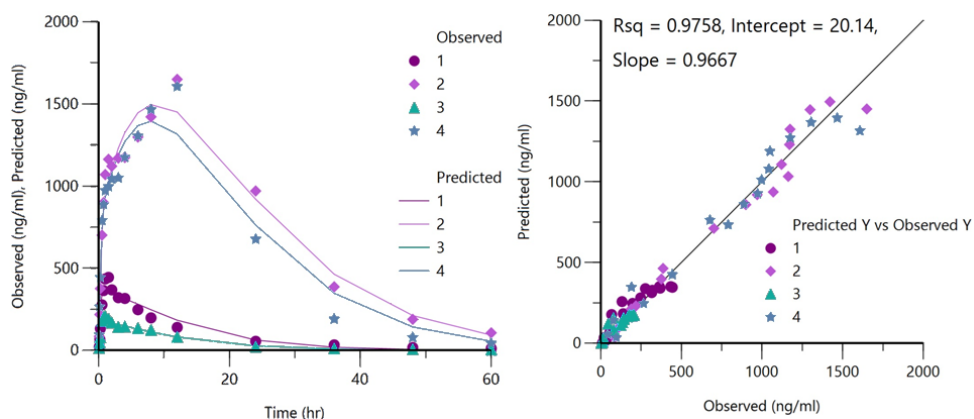


Figure 7. The kinetic fitting of model M431 during the first test period is shown on the left, along with the correlation between experimental and fitted values on the right. In the model, "1" represents **clozapine** in the central compartment during the reference period, "2" denotes **N-desmethyl clozapine** in the central compartment during the reference period, "3" represents **clozapine** in the central compartment during the first test period (with ciprofloxacin), and "4" corresponds to **N-desmethyl clozapine** in the central compartment during the first test period.

The experimental data align closely with the model predictions, as evidenced by the high correlation coefficients (R^2). For the CLZ-alone and CLZ-ciprofloxacin dataset, the R^2 value is 0.9667 (Figure 7), while for the CLZ-alone and CLZ-norfloxacin dataset, the R^2 value is 0.9725 (Figure 8). These values reflect a high level of correlation between the experimental observations and the model's predictions, underscoring the robustness and reliability of the kinetic model.

INSIGHTS INTO CLOZAPINE'S KINETIC INTERACTIONS: ENZYMATIC INHIBITION OF CYP1A2 BY CIPROFLOXACIN AND NORFLOXACIN

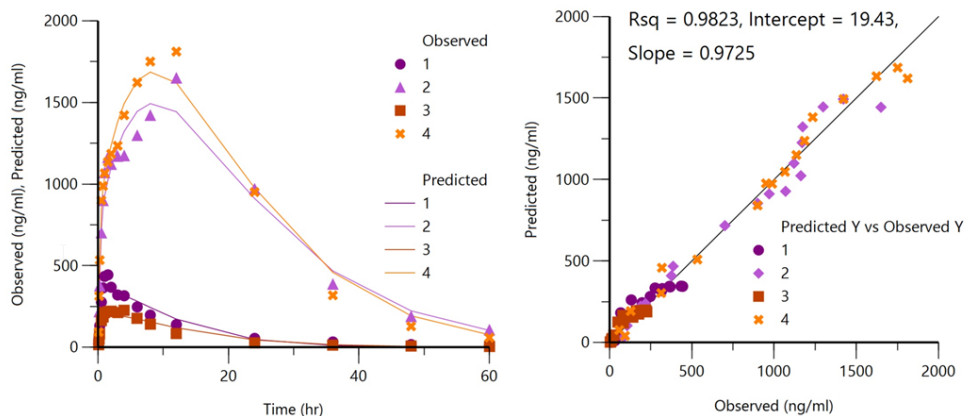


Figure 8. The kinetic fitting of model M432 during the second test period is displayed on the left, alongside the correlation between experimental and fitted values on the right. In this model, "1" represents **clozapine** in the central compartment during the reference period, "2" denotes **N-desmethyl clozapine** in the central compartment during the reference period, "3" represents clozapine in the central compartment during the second test period (with norfloxacin), and "4" corresponds to **N-desmethyl clozapine** in the central compartment during the second test period.

CONCLUSIONS

This study presents a comprehensive kinetic modelling framework for clozapine (CLZ) and its primary metabolite, N-desmethyl clozapine (CLZ-M), focusing on the interactions between CLZ and the fluoroquinolone antibiotics ciprofloxacin and norfloxacin. By employing a systematic three-tier modelling approach, the kinetic behaviour of CLZ and CLZ-M was elucidated across reference and test conditions, incorporating key processes such as absorption, distribution, metabolism, and excretion (ADME).

In the first step, compartmental modelling focused exclusively on the parent compound, clozapine, as its kinetics influence the kinetics of its metabolite, but not vice versa. This stage established the foundational kinetics of CLZ using a bi-compartmental model with first-order absorption and lag time.

In the second step, the metabolite was incorporated into the model, enabling simultaneous fitting of two datasets (clozapine and its metabolite) while accounting for additional parameters such as metabolite distribution and the effects of presystemic and systemic metabolism.

The third step involved simultaneous fitting of four datasets, considering the kinetic interactions between clozapine and ciprofloxacin or norfloxacin. This step addressed changes in presystemic and systemic metabolism mediated by CYP1A2 enzymatic inhibition, as well as variations in the relative bioavailability of clozapine between the reference and test periods due to changes in the extent of absorption. This final step also integrated the metabolite's kinetics, also altered by the assessed drug-drug interactions.

The selected models demonstrated excellent predictive accuracy, with high correlation coefficients ($R^2 > 0.96$) between experimental data and model predictions, underscoring the robustness of the proposed approach.

Key findings highlight the significant impact of ciprofloxacin and norfloxacin on CLZ kinetics, including altered presystemic and systemic metabolism and changes in bioavailability. These results provide critical insights into the molecular and kinetic interplay between CLZ and fluoroquinolones, offering valuable guidance for optimizing dosing strategies in clinical settings where these drugs are co-administered.

This rational and mechanistic modelling framework not only advances the understanding of CLZ-fluoroquinolone interactions but also sets a precedent for investigating complex kinetic scenarios involving metabolic inhibitors. The findings have significant implications for both clinical practice and future research into drug-drug interactions.

EXPERIMENTAL SECTION

Chemical and reagents

Clozapine (Leponex[®]) for animal administration was purchased from Mylan (Hatfield, Hertfordshire, UK), while analytical standards for clozapine and N-desmethyl clozapine used in LC-MS analysis were purchased from Sigma-Aldrich/Merck Group (Darmstadt, Germany). Ciprofloxacin (Ciprinol[®]) and norfloxacin (Nolicin[®]) were acquired from KRKA (Novo Mesto, Slovenia). For animal anesthesia, ketamine (Vetased[®]) was purchased from Farmavet (Romania), xylazine (XylazinBio[®]) from Bioveta (Czech Republic), and diazepam from Terapia (Cluj-Napoca, Romania). Heparin sodium (5000 IU/mL) was obtained from Belmedpreparaty (Minsk, Belarus). Analytical-grade formic acid and methanol were purchased from Merck (Darmstadt, Germany), and carboxymethyl cellulose was acquired from Sigma-Aldrich (Taufkirchen, Germany).

Study design

This study was approved by the local Ethics Committee of the “Iuliu Hațieganu” University of Medicine and Pharmacy, Cluj-Napoca, Romania, and the National Sanitary Veterinary and Food Safety Authority, in compliance with Romanian Law 43/2014, which governs the protection of animals used for scientific purposes. The legislation aligns with Directive 2010/63/EU of the European Parliament and Council, dated 22 September 2010, as published in the Official Journal of the European Union. Ethics approval was granted under reference number 313, dated 20 May 2022. The study was conducted at the Centre for Experimental Medicine and Practical Skills, Cluj-Napoca, Romania, using an open-label, three-period sequential design.

The experimental design involved three periods and involved the use of 16 white male Wistar rats, for each study period, weighing between 240 and 415 g. In the initial reference period, the rats received a single oral dose of clozapine (20 mg/kg body weight, b.w.). In the first test period, the animals were pretreated with 15 mg of ciprofloxacin administered orally for five days in order to reach the steady-state plasma concentration for this enzymatic inhibitor, followed by a combination of ciprofloxacin and clozapine (20 mg/kg b.w.) on the sixth day. In the second test period, the same protocol was followed, replacing ciprofloxacin with a 30 mg dose of norfloxacin. Both clozapine and norfloxacin were suspended in 1% carboxymethylcellulose and vortexed for 5 minutes before oral administration by intragastric gavage.

Sample preparation

To determine the plasma concentration of each analyte, namely the parent drug clozapine (CLZ) and its metabolite (CLZ-M), venous blood samples were collected from each rat during each study period. Cannulation of the left femoral vein was performed one day before clozapine administration under general anesthesia induced by a combination of ketamine, xylazine, and diazepam (1:1:1) via intramuscular injection. This procedure was done for each rat and allowed for automated blood sampling using the BASi Culex ABC® system (BASi Research Products, West Lafayette, IN, USA), ensuring consistency and reducing variability.

Blood samples (200 µL each) were collected at multiple time points: 5, 10, 15, 30, and 45 minutes; 1, 1.5, 2, 3, 4, 6, 8, 12, 24, 36, 48, and 60 hours after clozapine administration. Samples were stored at -20°C until analysis. Sample preparation involved mixing 60 µL of blood with 180 µL of methanol, vortexing for 10 seconds, and centrifuging at 10,000 rpm for 8 minutes. The resulting supernatant was transferred to autosampler vials for quantification via HPLC-MS.

Drug analysis from plasma samples

Clozapine and its active metabolite concentrations in rat plasma samples were simultaneously determined using a validated liquid chromatography-tandem mass spectrometry (LC-MS/MS) method. The HPLC system used was an Agilent 1100 series, featuring a binary pump, autosampler, and thermostat (Agilent Technologies, Santa Clara, CA, USA), coupled to an Agilent Ion Trap 1100 SL mass spectrometer. Chromatographic separation was achieved on a Zorbax SB-C18 column (100 mm x 3.0 mm i.d., 3.5 μm) (Agilent Technologies, Santa Clara, CA, USA). The mobile phase consisted of 0.3% formic acid in water (v/v) and methanol in a 68:32 ratio, with isocratic elution maintained for 3 minutes. The injection volume was set to 3 μL , with a flow rate of 1 mL/min, and the column temperature was kept at 45°C. Under these chromatographic settings, the retention times were 2.4 min for clozapine and 1.9 min for its metabolite. Mass spectrometric detection utilized multiple reaction monitoring (MRM) mode with an electrospray ionization source in positive ion mode. The monitored mass transitions were m/z 270 from m/z 328 for clozapine and m/z (253, 270) from m/z 314 for its metabolite. Calibration curves for both clozapine and its metabolite were linear within the concentration range of 5 to 1000 ng/mL.

Kinetic and statistical analysis of data

A three-tiered modelling strategy was utilized to manage the extensive number of variables, which would otherwise result in numerous model combinations, making computation infeasible.

In the first stage, the focus was on optimizing a model specifically for the parent compound, CLZ, without including the metabolite or potential kinetic interactions. This initial model was aimed and consequently designed to isolate and characterize the kinetic properties of clozapine, establishing a foundational framework for incorporating more complex variables in following stages. A summary of the model parameters evaluated for clozapine kinetics was presented in Table 1.

Figure 9 depicts the three-tier modelling approach used to further analyze the kinetics of clozapine's primary metabolite, N-desmethyl clozapine (CLZ-M), as well as the combined kinetics of CLZ and CLZ-M in the context of drug-drug interactions with ciprofloxacin and norfloxacin.

INSIGHTS INTO CLOZAPINE'S KINETIC INTERACTIONS: ENZYMATIC INHIBITION OF CYP1A2 BY CIPROFLOXACIN AND NORFLOXACIN

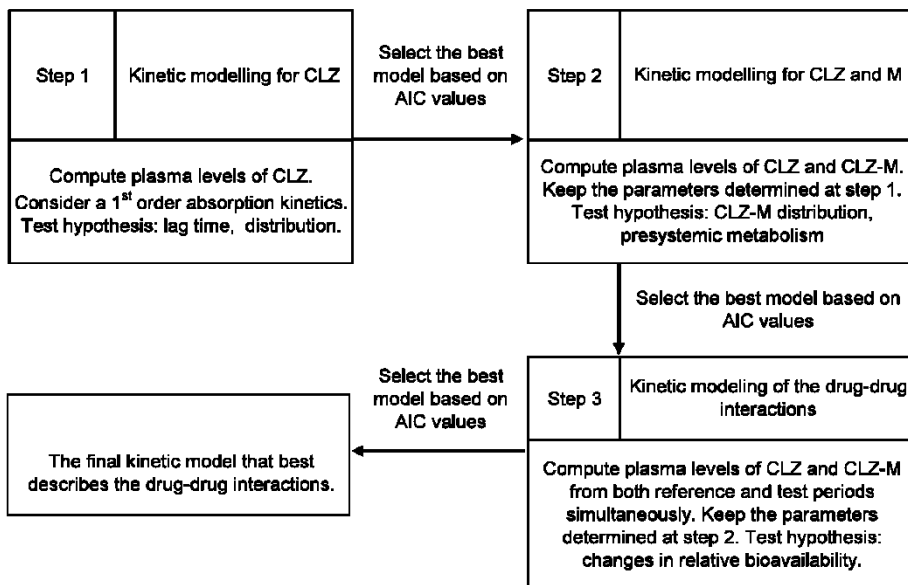


Figure 9. The three-tier framework utilized for kinetic modelling of clozapine (CLZ), its primary metabolite (N-desmethyl clozapine, CLZ-M), and the drug-drug interactions involving clozapine and the fluoroquinolone antibiotics ciprofloxacin and norfloxacin.

The Akaike Information Criterion (AIC) was employed as the primary method for model selection and evaluation to determine the kinetic model that best fit the experimental data [15]. AIC considers the number of observations, the quality of the fit, and model complexity. It is calculated using the formula:

$$AIC = m * \ln(WSSR) + 2 * p,$$

where m represents the number of observations, WSSR is the weighted sum of squares of residuals, and p is the number of structural parameters in the model [11-14,16]. A lower WSSR value indicates an improved fit, which results in a lower AIC score and a better overall fit to the data [16].

The AIC disadvantages models with more parameters, as its final value increases proportionally with p. Therefore, when comparing two models with similar fit quality (e.g., identical WSSR values), the model with fewer parameters will yield a lower AIC and be considered the better choice. Overall, a lower AIC value signifies a superior fit, provided the same data and error assumptions apply across the models [11,14].

CONFLICT OF INTEREST

The authors declare no conflict of interest regarding the publication of this research article.

ACKNOWLEDGMENTS

This work was supported by PCD grant, no 1032/15 from 13th January 2021.

REFERENCES

1. E. Wagner; S. Siafis; P. Fernando; et al.; *Transl Psychiatry*, **2021**, *11*, 487.
2. G. Schaber; I. Stevens; H.J. Gaertner; K. Dietz; U. Breyer-Pfaff; *Br. J. Clin. Pharmacol.*, **1998**, *46*, 453-459
3. P. Wickramarachchi; J.M. Boyd; D.J. Orton; *Clin. Chim. Acta*, **2022**, *531*, 183-187
4. R.J. Flanagan; S. Gee; S. Belsey; L. Couchman; J. Lally; *BJPsych Adv.*, **2023**; *29(2)*, 92–102
5. Á. Menus; Á. Kiss; K. Tóth; et al.; *Sci. Rep.*, **2020**, *10*, 21283
6. NCBI; **2024**, [cited 2024 Oct. 9] from:
<https://pubchem.ncbi.nlm.nih.gov/compound/91695433>
7. NCBI; **2024**, [cited 2024 Oct. 9] from
<https://pubchem.ncbi.nlm.nih.gov/compound/Ciprofloxacin>.
8. NCBI; **2024**, [cited 2024 Oct. 9]. Available from:
<https://pubchem.ncbi.nlm.nih.gov/compound/Norfloxacin>
9. A.E. Chirali; I.M. Ciocotișan; A.M. Vlase; D.M. Muntean; L. Vlase; *Farmacia*, **2024**, *72(5)*, 1092-1097
10. A.E. Chirali; I.M. Ciocotișan; A.M. Vlase; D.M. Muntean; L. Vlase; *Ovidius University Annals of Chemistry*, **2024**, *35(2)*, 137-145
11. A.M. Gheldiu; D.M. Muntean; I. Cristea; I. Antonescu; R. Chira; C.Ureche; L.Vlase; *Rev. Chim.*, **2016**, *67*, 702-705
12. A.M. Gheldiu; A. Csavdari; M. Achim; L. Vlase; I. Tomuța; D. Muntean; *Studia UBB Chemia*, **2017**, *62*, 179-188
13. M. Oroian; A. Marcovici; D.I. Pop; S. Bhardwaj; A. Khuroo; AM. Gheldiu; L. Vlase; *Studia UBB Chemia*, **2019**, *64*, 297-308
14. D.I. Pop; A. Marcovici; M. Oroian; A.M. Gheldiu; L. Vlase; *Studia UBB Chemia*, **2020**, *65*, 187-196
15. G. Glatting; P. Kletting; S.N. Reske; K. Hohl; C. Ring; *Med. Phys.*, **2007**, *34*, 4285-4292
16. H. Akaike; *IEEE Transactions on Automatic Control*, **1974**, *19*, 716-723.

EFFECTS OF SOME TURKISH PLANT EXTRACTS ON CARBONIC ANHYDRASE AND CHOLINESTERASE ENZYMES

İbrahim Seyda URAS^{a,*}, Murat KÜRŞAT^b, Belma KONUKLUGIL^c,
Murat ŞENTÜRK^d

ABSTRACT. Cholinesterase inhibitors are valuable compounds that can be used in many different therapeutic applications, including Alzheimer's disease. Carbonic anhydrase (CA) inhibitors constitute a pharmacological intervention employed for the management and alleviation of various medical conditions, including glaucoma, idiopathic intracranial hypertension. Turkey has a large and diverse flora, home to thousands of plant species. Hundreds of compounds of medicinal importance have been identified from the many plants in this flora. In this study, the inhibitory properties of seven different plant extracts on CA I and II, acetylcholinesterase (AChE) and butyrylcholinesterase (BChE) enzymes were investigated. The tested extracts showed AChE inhibitory activity with values ranging from 1.26 to 4.20 µg/mL, BChE inhibitory activity with values ranging from 1.32 to 4.24 µg/mL, CA I inhibitory activity with values ranging from 0.74 to 1.82 µg/mL and CA II inhibitory activity with values ranging from 0.033 to 0.067 µg/mL. The extract of *Zosima absinthifolia* showed a very active inhibition profile against both AChE and BChE (IC₅₀ 1.26 ± 0.01 µg/mL for AChE and 1.32 ± 0.02 µg/mL for BChE). The results indicate that these extracts are potent cholinesterases inhibitors and specifically *Zosima absinthifolia* extract could be evaluated for further studies.

Keywords: enzyme inhibition, Turkey flora, *Zosima absinthifolia*.

^a Agri Ibrahim Cecen University, Faculty of Pharmacy, Department of Pharmacognosy, Ağrı, Türkiye

^b Bitlis Eren University, Faculty of Science and Arts, Department of Biology, Bitlis, Türkiye

^c Lokman Hekim University, Faculty of Pharmacy, Department of Pharmacognosy, Ankara, Türkiye

^d Agri Ibrahim Cecen University, Faculty of Pharmacy, Department of Biochemistry, Ağrı, Türkiye

* Corresponding author: isuras@agri.edu.tr



INTRODUCTION

In this study, the enzyme inhibitory properties of seven plants growing in Turkey, one of which is endemic, were investigated. It was aimed to investigate the various enzyme activities of plants grown in Bitlis province and used among the public to relieve various symptoms. The selection of plants carried out based on their traditional use. *Diplotaenia cachrydifolia* is used traditionally for treating diabetes and rheumatism [1]. In Turkish folk medicine, the mixture made from the *Zosima absinthifolia* leaves is used in the treatment of diabetes [2]. In European folk medicine, *Salvia* species has been used to treat gastrointestinal disorders (dyspepsia, flatulence, abdominal spasms, diarrhea, inflammation of intestinal mucosa), inflammation of the mouth and throat [3]. Significant medicinal benefits from *Fumaria* species have been reported in traditional medicine, especially as a remedy for hepatobiliary disorders, cough, eczema treatment, and skin diseases [4]. *Anarrhinum* species [5], *Ferulago* species [6], and *Rhabdosciadium* species [7] are used in the treatment of various diseases in folk medicine.

The *Zosima* genus, which belongs to the Apiaceae family and spreads over a wide area from the Middle East to Turkey, Iran and Afghanistan, has been used as a medicinal plant for centuries. Essential oils and extracts of this plant have many biological activities such as anti-inflammatory, antimicrobial and cytotoxic activity. The essential oil of “peynir otu” (*Zosima absinthifolia*) fruits has a high antibacterial effect and it was found effective against some bacteria such as *Bacillus pumilus* and *B. subtilis* [8]. Another study concluded that flower and fruit extracts of *Z. absinthifolia* have high antioxidant and anticholinesterase properties.

Bahadır, Çitoğlu [9] stated that n-hexane extract obtained from the aerial part of *Z. absinthifolia* has anti-inflammatory properties in rats. In another study, it was found that the methanol extract of *Z. absinthifolia* fruits exhibited significantly higher free radical scavenging, antibacterial, anti-inflammatory, and cytotoxic activities [9]. Additionally, studies on the essential oil compositions of *Z. absinthifolia* fruits have shown that the main components of the essential oil are octyl acetate, octyl octanoate, octyl hexanoate and 1-octanol [10, 11].

Salvia species are represented by about a hundred species, half of which are endemic, in Turkey. In a study on “fırat şalbası” (*Salvia pseudeuphratica*), the main components of the plant’s essential oil were found to be camphor, 1,8 cineole and linalool by GC-MS analysis. It was thought that the essential oil of the plant could be used as an insect repellent due to its high camphor content [12]. In another study, researchers focused on the anticholinesterase

activity of *S. pseudoeuphratica* essential oil. The study found that the essential oil of the plant showed high anticholinesterase activity with an IC₅₀ value of 26 µg/mL [13].

Fumaria L. (Papaveraceae) has about 60 species and is found on the European continent, especially in the Mediterranean region and Eastern and Western Europe. Extracts obtained from *Fumaria* spp. has been used traditionally to treat rheumatism, abdominal pain, abdominal cramps, fever, diarrhoea, some skin diseases (rash or conjunctivitis), syphilis and leprosy.

Studies have presented extremely rich sources in terms of the alkaloid content of *Fumaria* species. In addition to the alkaloid content, the presence of different types of flavonoids, steroid structures and organic acids is also constant. Studies conducted with *Fumaria* extracts have also found that they have strong antihypertensive, hepatoprotective, diuretic, laxative effects, and antifungal, antibacterial, anti-inflammatory activities. These biological activities have mostly been associated with the presence of isoquinoline alkaloids [14].

The result of the GC-MS analysis of “akşahtere” (*Fumaria asepala*) essential oil conducted by Yılmaz Sancar in 2023, Phytol (20.74 %) was the major substance, followed by Thymol (20.42%), Benzyl Benzoate (15.89 %) and Hexahydrofarnesyl acetone (12.92 %). As a result of the antimicrobial analysis, *F. asepala* essential oil showed the best antimicrobial effect against *S. aureus*-ATCC 25923 (24 mm) and *K. pneumoniae* (24 mm). To determine antioxidant effects, total antioxidant level (TAS) and total oxidant level (TOS) were examined and it was found that the total oxidant level was high [15].

“Köse otu” (*Diplotaenia cachrydifolia*) is a member of the Apiaceae family and a perennial plant that grows wild in the eastern parts of Turkey. In previous studies, compounds such as jatamansin, xanthotoxin, bergapten and isopimpinellin were isolated from different parts of this plant [16]. In another study, alpha phellandrene and isomyristin substances were found in high amounts in the oil obtained from the roots of the plant, while terpinolene isodillapiol substances were found in high amounts in the oil obtained from the leaves and fruits. The researchers compared their results with those of other studies and evaluated that the difference in the major substances could be due to climatic factors, plant collection location, plant nutrition status and genetic differences [17]. In a more recent study, antimicrobial, antioxidant and antigenotoxic activity analyses were performed on the extracts prepared with different solvents (ethanol, acetone, hexane) from the plant. The highest antioxidant activity (DPPH IC₅₀: 2.5234 µg/mL) and phenol content (55.36 ± 0.035 µg/mL) were observed in the ethanol extract, which also showed protective effect against genotoxicity induced by mitomycin C [1].

The *Rhabdosciadium* genus, belonging to the Umbelliferae family, is distributed with two species in Turkey. “Som handok” (*Rhabdosciadium microcalycinum*) is a plant native only to Turkey. In Turkey, it can only be seen in the upper Euphrates region, in the provinces of Bingöl and Elazığ. In a GC-MS analysis on the composition of the essential oil obtained from *Rhabdosciadium microcalycinum* plant collected from the Elazığ region, the major component of the oil was found to be germacrene D [18]. In a recent study, different activities of the ethanolic extract of *R. microcalycinum* plant collected from the Bingöl region were investigated. The plant extract showed remarkable inhibitory effects on AChE and alpha glucosidase enzymes, and the IC₅₀ values were found to be 35.86 mg/mL and 10.14 mg/mL, respectively [19].

Plants belonging to the genus *Ferulago* are members of the Apiaceae family. When the essential oil of “yıldız kişnişi” (*Ferulago stellata*) plant collected from Iran was investigated, GC-MS analysis revealed that 2,4,5-trimethyl benzaldehyde and alpha and beta pinene compounds were the major components of the oil [20]. In another study, the inhibitory effects of the ethanolic extract of the plant collected from the Çatak region of Van province on AChE, alpha glucosidase and alpha amylase enzymes were remarkable, and the IC₅₀ values were 1.772 µg/mL, 33.56 µg/mL, and 0.639 µg/mL, respectively [6].

The treatment of various diseases is greatly influenced by enzyme inhibitors. AChE (EC 3.1.1.7) plays a crucial role in terminating cholinergic signaling by hydrolyzing acetylcholine (ACh), a vital neurotransmitter for memory and motor function [21].

Located postsynaptically, AChE terminates neuronal signaling by rapidly hydrolyzing ACh. Unlike AChE, butyrylcholinesterase (BChE) (EC 3.1.1.8) is primarily synthesized in the liver and distributed throughout the body, including blood plasma and the nervous system [22]. Clinical evidence demonstrates that AChE inhibitors enhance cholinergic activity by elevating ACh levels within cholinergic synapses [23]. While AChE primarily mediates ACh hydrolysis, BChE contributes to regulating ACh levels and plays a crucial role in drug metabolism and detoxification [24]. Selective inhibitors for both AChE and BChE are valuable therapeutic tools for managing motor neuron diseases like dementia, myasthenia gravis, and Alzheimer’s disease [21].

CAs (EC 4.2.1.1) are metalloenzymes catalyzing the conversion of CO₂ to HCO₃⁻ and H⁺. These ubiquitous enzymes are encoded by six distinct gene families across diverse species [25]. Humans possess fifteen CA isoforms, with cytosolic hCA I/II being most prevalent across tissues. Understanding CA modulation holds therapeutic potential for various clinically significant disorders [26, 27]. Notably, specific CA inhibitors have enabled the development of novel drugs for treating epilepsy, edema, and glaucoma. Therefore, exploring and identifying novel CA isoenzyme inhibitors represents a promising avenue for therapeutic discovery [26, 28, 29].

RESULTS AND DISCUSSION

An evaluation of seven plant extracts against the AChE enzyme identified extract of *Z. absinthifolia* as possessing the most potent inhibitory activity, exhibiting an IC₅₀ value of 1.26 µg/mL (Figure 1).

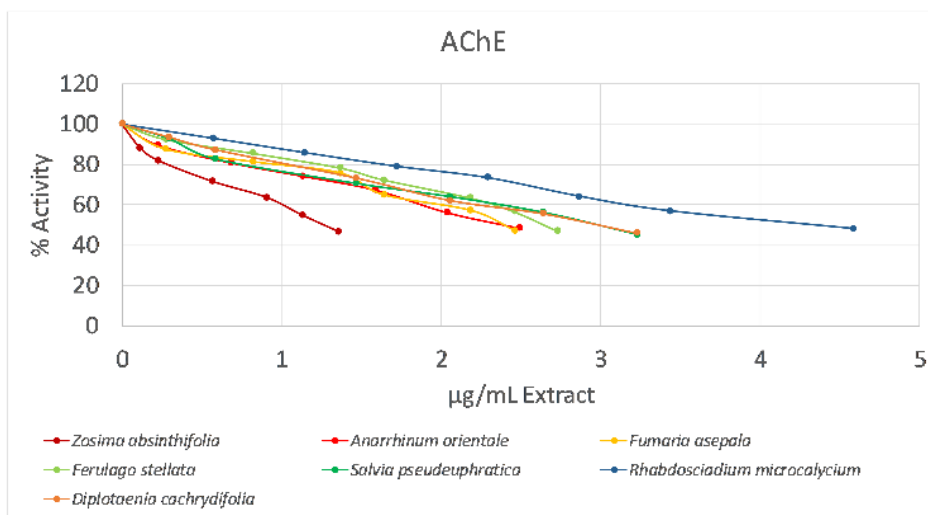


Figure 1. Decreasing in the AChE enzyme activity against tested extracts.

Conversely, extract of *R. microcalycinum* demonstrated the weakest inhibitory effect, as reflected by its IC₅₀ value of 4.2 µg/mL. Notably, all tested extracts displayed close inhibitory activity compared to the reference molecule, galantamine, which possessed an IC₅₀ value of 0.4 µg/mL (Table 1).

Table 1. Inhibition values of AChE and BChE enzymes with the tested extracts.

Plant Extracts	AChE IC ₅₀ value (µg/mL)	Galantamine Equivalents for AChE (µg/mL)	BChE IC ₅₀ value (µg/mL)	Galantamine Equivalents for BChE (µg/mL)
<i>Zosima absinthifolia</i>	1.26 ± 0.01	3.15	1.32 ± 0.02	0.6
<i>Anarrhinum orientale</i>	2.47 ± 0.03	6.175	2.92 ± 0.03	1.327
<i>Fumaria asepalae</i>	2.42 ± 0.03	6.05	2.43 ± 0.03	1.104
<i>Ferulago stellata</i>	2.81 ± 0.03	7.025	2.96 ± 0.03	1.345
<i>Salvia pseudeuphratica</i>	2.87 ± 0.03	7.175	2.95 ± 0.03	1.34
<i>Rhabdosciadium microcalycinum</i>	4.20 ± 0.04	10.5	4.24 ± 0.04	1.927
<i>Diplotaenia cachrydifolia</i>	2.90 ± 0.03	7.25	2.90 ± 0.03	1.318
Galantamine ^[a]	0.40 ± 0.10		2.20 ± 0.30	

[a] [30].

An assessment of the inhibitory potential of various plant extracts against the BChE enzyme revealed that extract of *Z. absinthifolia* exhibited the most pronounced inhibitory activity, with an IC_{50} value of 1.32 $\mu\text{g}/\text{mL}$ (Figure 2).

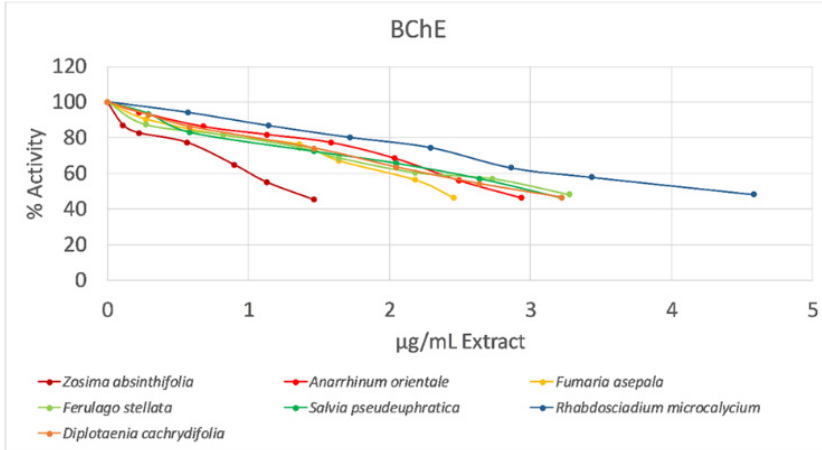


Figure 2. Decreasing in the BChE enzyme activity against tested extracts.

Among the seven extracts tested against the AChE enzyme, *R. microcalycium* ($IC_{50} = 1.82 \mu\text{g}/\text{mL}$) showed the weakest inhibitory effect among the seven extracts against the hCA I enzyme. However, extract *Z. absinthifolia* (0.74 $\mu\text{g}/\text{mL}$) showed the best inhibitory profile among all plant extracts (Figure 3).

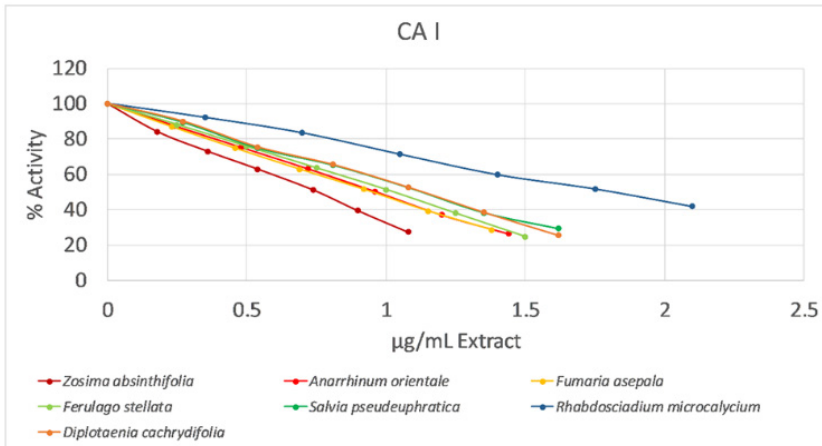


Figure 3. Decreasing in the CA I enzyme activity against tested extracts.

EFFECTS OF SOME TURKISH PLANT EXTRACTS ON CARBONIC ANHYDRASE AND CHOLINESTERASE ENZYMES

Additionally, in this study, the values obtained for the hCA I enzyme (0.74-1.82 µg/mL) were compared with the reference molecule acetazolamide (1.652 µg/mL). All of these plant extracts showed better or similar values than acetazolamide (Table 2).

Table 2. Inhibition values and acetazolamide equivalents (AE) of CA I and CA II enzymes with the tested extracts.

Plant Extracts	CA I IC ₅₀ value (µg/mL)	Acetazolamide Equivalents for CA I (µg/mL)	CA II IC ₅₀ value (µg/mL)	Acetazolamide Equivalents for CA II (µg/mL)
<i>Zosima absinthifolia</i>	0.74 ± 0.02	0.456	0.033 ± 0.001	2.062
<i>Anarrhinum orientale</i>	0.97 ± 0.03	0.587	0.041 ± 0.001	2.562
<i>Fumaria asepala</i>	0.95 ± 0.03	0.575	0.038 ± 0.001	2,375
<i>Ferulago stellata</i>	1.01 ± 0.03	0.611	0.047 ± 0.001	2.937
<i>Salvia</i>	1.13 ± 0.03	0.684	0.051 ± 0.001	3.187
<i>pseudeuphratica</i>				
<i>Rhabdosciadium microcalycinum</i>	1.82 ± 0.08	1.123	0.067 ± 0.001	4.187
<i>Diplotaenia cachrydifolia</i>	1.11 ± 0.04	0.671	0.053 ± 0.001	3.312
Acetazolamide	1.652 ± 0.03		0.016 ± 0.001	

R. microcalycinum extract (IC₅₀ = 0.067 µg/mL) showed the weakest inhibitory effect among the seven extracts against the hCA II enzyme. However, extract *Z. absinthifolia* (0.033 µg/mL) showed the best inhibitory profile among all plant extracts (Figure 4).

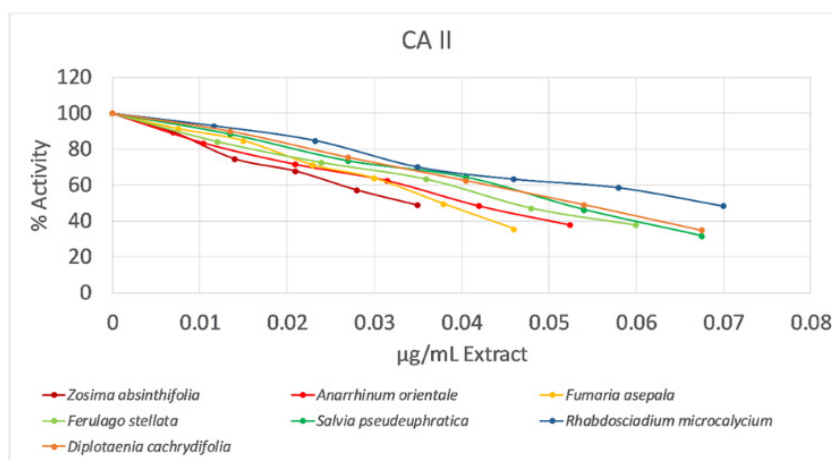


Figure 4. Decreasing in the CA II enzyme activity against tested extracts.

Additionally, in this study, the values obtained for the hCA II enzyme (0.033-0.067 µg/mL) were compared with the reference molecule acetazolamide (0.016 µg/mL). All of these plant extracts showed values close to acetazolamide (Table 2).

When comparing our results with those from other studies on the same plants, we observe significant variations in the outcomes. For AChE inhibition, the experiment using *Fumaria asepalae* extract at a concentration of 1 µg/mL resulted in 21 % inhibition in our study. However, the same plant's extract prepared using a chloroform: methanol (1:1) solvent system exhibited 9.76 % inhibition at the same concentration. Since both plants were extracted using solvents of similar polarity, the observed differences in results may be attributed to solvent selection for extraction or the geographical origin of the plants in different studies (Sivrihisar, Ankara – Baskil, Elazığ) [31].

Another group working with *Zosima absinthifolia* conducted a comprehensive study using different parts of the plant collected from Erzurum. In their research, extracts prepared from different parts of the plant using various solvents such as methanol, hexane, dichloromethane, and ethyl acetate and some of the secondary metabolites of plant isolated. Results showed significant variations in terms of cholinesterase inhibition. The highest inhibitory activity among extracts was observed in dichloromethane fruit extracts at 20 µg/mL, against both AChE and BChE (31.46% and 82.27% respectively). Among the isolated compounds pimpinellin showed highest activity against BChE (66.55% inhibition at 20 µg/mL) while umbelliferon presented best results against AChE (61.09% inhibition at 20 µg/mL) [32]. This results aligned with our findings and it points that the enzyme inhibitory activity of *Z. absinthifolia* could be related to its coumarin compounds.

In a study conducted on the ethanolic extract of *Ferulago stellata* collected from the Çatak region in Van province, it was determined that it exhibited activity with a lower IC₅₀ value compared to our results (IC₅₀: 2.42 and 1.77 µg/mL) [6].

In a conducted study, the acetylcholinesterase inhibitory activity of the ethanolic extract obtained from *R. microcalycinum* collected in Bingöl was found to be lower compared to our own results. This endemic species, which grows exclusively in Bingöl and Elazığ, yielded significantly different results when samples were collected from two distinct regions (IC₅₀: 35.86 and 4.20 µg/mL). The observed variation in activity is likely due to compositional differences in the bioactive compounds, influenced by solvent selection or the specific geographical location of plant growth [19].

In another study, the IC₅₀ value obtained from the AChE inhibitor activity test on the essential oil of *S. pseudeuphratica* was significantly higher than the IC₅₀ value demonstrated by plant's methanol extract in our study (IC₅₀: 26 and

1.13 µg/mL). Since both studies utilized plants collected from the same region, the difference in results is attributed to the fact that the activity test was performed on volatile oil in the initial study and on methanol extract in our study [13].

CONCLUSIONS

The evaluation of the inhibitory effects of Turkish plant extracts against various key enzymes, including AChE, BChE, CA I and II, has yielded significant insights into their potential therapeutic applications.

The anticholinesterase and carbonic anhydrase inhibitor activity analysis on *Diplotaenia cachrydifolia* and *Anarrhinum orientale* plant extracts has been conducted for the first time in this study. High activity was observed at the reference substance level in both butyrylcholinesterase and carbonic anhydrase inhibition. These findings highlight the potential pharmacological significance of these plant species.

EXPERIMENTAL SECTION

Chemicals and laboratory

All enzymes and chemicals used for experiments were bought from Sigma Aldrich (Germany). Extract preparation and enzyme inhibition studies were carried out in Central Research Laboratory of Agri İbrahim Cecen University.

Sample collection

All plants collected and identified by Murat Kürşat in 2020 from different regions of Turkey. *Diplotaenia cachrydifolia* Boiss. was collected in September from Karz Mountain, Bitlis at 2250 m. *Ferulago stellata* Boiss. and *Rhabdosciadium microcalycinum* Hand.-Mazz. were collected in September from Kambos Mountain, Bitlis at 1750 m. *Anarrhinum orientale* Benth. was collected in August from Kambos Mountain, Bitlis at 1600 m. *Fumaria asepala* and *Zosima absinthifolia* (Vent.) Link was collected in May from the Baskil region of Elazığ. *Salvia pseudeuphratica* Rech.f. was collected in July from Keban, Elazığ. Voucher specimen for each plant is available at Bitlis Eren University.

Preparation of plant extracts

For each plant, 50 g of dried plant material was taken. The coarsely ground parts were extracted with methanol at room temperature. The extraction process was repeated 4 times, and plants were extracted with a magnetic

stirrer for 12 hours by adding 1 L of fresh methanol each time. The methanolic phases obtained at the end of the extraction were combined and the methanol was evaporated with a rotavapor and the dry crude extracts were obtained for each plant. Extracts of *Z. absinthifolia*, *A. orientale*, *F. asepala*, *F. stellata*, *S. pseudeuphratica*, *R. microcalycinum* and *D. cachrydifolia* were numbered 1 to 7, respectively.

Carbonic anhydrase I/II inhibition

The activities of carbonic anhydrase I and II (CA I/II) were assessed spectrophotometrically at 348 nm by monitoring the conversion of 4-nitrophenyl acetate (NPA) to 4-nitrophenolate (NP) per minute over 3 minutes incubation at 25 °C. Each reaction mixture comprised:

- 1.4 mL of 50 mM Tris-SO₄ buffer (pH 7.4)
- 1 mL of 3 mM NPA
- 0.5 mL of deionized water
- 0.1 mL of enzyme solution

for a total volume of 3.0 mL [33].

Cholinesterase enzymes inhibition

The inhibitory activity against acetylcholinesterase (AChE) and butyrylcholinesterase (BChE) was evaluated using a standardized assay system. Each reaction mixture contained:

- 5-60 µL of inhibitor sample solution
- 200 µL of buffer (1 M Tris-HCl for AChE, PB for BChE; pH 8.0)
- 50 µL of 5,5'-dithiobis-(2-nitrobenzoic acid) (DTNB) (0.5 mM)
- 50 µL of acetylthiocholine iodide/S-butrylthiocholine chloride (10 mM)
- 10 µL of enzyme solutions at concentration of 0.28 U/mL for AChE and 0.32 U/mL for BChE [34].

The reaction was initiated by adding the enzyme, and the absorbance at 412 nm was monitored at 25° every two minutes for a total of 6 minutes incubation. A control lacking the inhibitor was included for comparison [35].

General enzyme inhibition studies

The inhibitory activities of plant extracts against carbonic anhydrases I and II (CA I/II), acetylcholinesterase (AChE), and butyrylcholinesterase (BChE) were determined using spectrophotometric methods (Agilent BioTek Epoch Microplate Spectrophotometer, California, USA). Acetazolamide and galantamine served as reference molecules for CA I/II and AChE/BChE, respectively. Meticulously prepared stock solutions of the investigated extracts

and reference molecules were dissolved in dimethyl sulfoxide at a concentration of 1 mg/mL. Subsequent dilutions using distilled water were performed to achieve a 1000-fold dilution. The inhibitory activity of these extracts on the aforementioned enzymes was assessed at seven distinct concentration points. The detailed methodology employed in this study adheres to procedures established in previously published works. Inhibitory properties for all extracts and standard drugs were calculated as IC₅₀ values determined graphically from inhibition curves against the log inhibitor concentration and the percentage of inhibition. IC₅₀ values represent the inhibitor concentration required for 50% inhibition of the enzyme. [29, 36, 37].

Statistical analysis of data

The SPSS program was used for the analysis of the experimental data. The standard deviation for IC₅₀ values were calculated and results were reported as mean ± standard deviation.

ACKNOWLEDGMENTS

There are no acknowledgements.

REFERENCES

1. S. Ugras; S. Ulger; P. Goc Rasgele; *Istanbul Journal of Pharmacy*, **2019**, 49, 45-52.
2. N. Alikhanova; E. Novruzov; *Chemical Bulletin of Kazakh National University*, **2022**, 34-42.
3. S. V. Luca; K. Skalicka-Woźniak; C. T. Mihai; A. C. Gradinaru; A. Mandici; N. Ciocarlan; A. Miron; A. C. Aprotosoia; *Antioxidants (Basel)*, **2023**, 12.
4. M. Mohseni; A. A. Azimi; B. D. Hashemloian; M. Farzamisepehr; *Turkish Journal of Botany*, **2023**, 47, 244-255.
5. A. Abdelsalam; E. Mahran; K. Chowdhury; A. Boroujerdi; *Journal of Genetic Engineering and Biotechnology*, **2021**, 19.
6. H. Kiziltas; Z. Bingol; A. C. Goren; L. P. Kose; L. Durmaz; F. Topal; S. H. Alwasel; I. Gulcin; *Molecules*, **2021**, 26.
7. A. Bakir; S. Ekin; M. Firat; *Kahramanmaraş Sütçü İmam Üniversitesi Tarım ve Doğa Dergisi*, **2023**, 26, 966-976.
8. S. Mollaei; S. Hazrati; V. Lotfizadeh; D. Dastan; P. Asgharian; *International Journal of Food Properties*, **2020**, 23, 1556-1567.
9. O. Bahadir; G. Çitoğlu; H. Özbek; *Journal of Medicinal Plants Research*, **2010**, 4.

10. K. H. C. Başer; T. Özek; B. Demirci; M. Kurkcuoglu; Z. Aytaç; H. Duman; *Flavour and Fragrance Journal*, **2000**, 15, 371-372.
11. S. Karakaya; M. Koca; S. V. Yılmaz; K. Yıldırım; N. M. Pınar; B. Demirci; M. Brestic; O. Sytar; *Molecules*, **2019**, 24, 722.
12. A. Ertas; M. Akdeniz; I. Yener; M. Ozturk; O. Tokul Olmez; M. Firat; U. Kolak; *Chem Biodivers*, **2022**, 19, e202100408.
13. H. E. Temel; B. Demirci; F. Demirci; F. Celep; A. Kahraman; M. Doğan; K. Hüsnü Can Başer; *Journal of Essential Oil Research*, **2016**, 28, 322-331.
14. R. Vrancheva; I. Ivanov; I. Aneva; I. Dincheva; I. Badjakov; A. Pavlov; *J. BioSci. Biotech*, **2014**, 3, 195-201.
15. P. Yılmaz Sancar; *International Journal of Pure and Applied Sciences*, **2023**, 9, 29-37.
16. M. H. Salehy Surmaghy, *The pharmacognosy of Diplotaenia cachrydifolia: characterisation of the coumarins and volatile principles and the histology of d. Cachrydifolia boiss. (Apiaceae)*. **1988**, University of Bradford (United Kingdom): England. p. 243.
17. M. Özcan; Y. Bağcı; K. Ertuğrui; J. Novak; *Journal of Essential Oil Research*, **2004**, 16, 211-213.
18. K. H. C. Başer; G. Özek; T. Özek; A. Duran; H. Duman; *Flavour and Fragrance Journal*, **2006**, 21, 650-655.
19. M. K. Erdogan; R. Gundogdu; Y. Yapar; I. H. Gecibesler; M. Kirici; L. Behcet; B. Tuzun; P. Taslimi; *ChemistrySelect*, **2022**, 7.
20. S. Masoudi; H. Eghbali; V. K. Abadi; *Journal of Essential Oil Bearing Plants*, **2016**, 19, 592-605.
21. H. Khan; Marya; S. Amin; M. A. Kamal; S. Patel; *Biomedicine & Pharmacotherapy*, **2018**, 101, 860-870.
22. M. M. Mesulam; A. Guillozet; P. Shaw; A. Levey; E. G. Duysen; O. Lockridge; *Neuroscience*, **2002**, 110, 627-639.
23. S. I. Zacks; J. M. Blumberg; *Journal of Histochemistry & Cytochemistry*, **1961**, 9, 317-324.
24. C. G. Carolan; G. P. Dillon; D. Khan; S. A. Ryder; J. M. Gaynor; S. Reidy; J. F. Marquez; M. Jones; V. Holland; J. F. Gilmer; *Journal of Medicinal Chemistry*, **2010**, 53, 1190-1199.
25. H. Yakan; G. Bilir; Ş. Çakmak; Ö. Taş; N. Türköz Karakullukçu; E. Soydan; H. Kütük; C. Güçlü; M. Şentürk; T. Arslan; S. Öztürk; E. Aksakal; D. Ekinci; *Journal of Enzyme Inhibition and Medicinal Chemistry*, **2023**, 38, 2194573.
26. R. Yaseen; D. Ekinci; M. Senturk; A. D. Hameed; S. Ovais; P. Rathore; M. Samim; K. Javed; C. T. Supuran; *Bioorganic & Medicinal Chemistry Letters*, **2016**, 26, 1337-1341.
27. A. H. Poslu; Ş. E. Aslan; G. Koz; E. Senturk; Ö. Koz; M. Senturk; A. Nalbantsoy; A. Öztekin; D. Ekinci; *Archiv der Pharmazie*, **2024**, 357, 2300374.
28. C. T. Supuran; *Nature Reviews Drug Discovery*, **2008**, 7, 168-181.
29. M. Özil; H. T. Balaydın; M. Şentürk; *Bioorganic Chemistry*, **2019**, 86, 705-713.

EFFECTS OF SOME TURKISH PLANT EXTRACTS ON CARBONIC ANHYDRASE AND
CHOLINESTERASE ENZYMES

30. K. Ingkaninan; W. Ekasari; D. Poerwanto; S. Suciati; E. R. Lail; K. Rabgay; L. Z. Gifanda; A. P. Hapsari; *Journal of research in pharmacy (online)*, **2020**, 24, 472-478.
31. I. Orhan; B. Şener; M. I. Choudhary; A. Khalid; *Journal of Ethnopharmacology*, **2004**, 91, 57-60.
32. S. Karakaya; M. Koca; S. V. Yılmaz; K. Yıldırım; N. M. Pınar; B. Demirci; M. Brestic; O. Sytar; *Molecules*, **2019**, 24.
33. J. A. Verpoorte; S. Mehta; J. T. Edsall; *J Biol Chem*, **1967**, 242, 4221-9.
34. G. L. Ellman; K. D. Courtney; V. Andres, Jr.; R. M. Feather-Stone; *Biochemical Pharmacology*, **1961**, 7, 88-95.
35. T. Arslan; M. Senturk; L. Karagoz; Y. Karagoz; D. Ekinci; A. Efe; E. A. Türkoğlu; F. Uras; *ChemistrySelect*, **2022**, 7, e202202993.
36. T. Arslan; M. Buğrahan Ceylan; H. Baş; Z. Biyiklioglu; M. Senturk; *Dalton Transactions*, **2020**, 49, 203-209.
37. H. Cavdar; M. Senturk; M. Guney; S. Durdagi; G. Kayik; C. T. Supuran; D. Ekinci; *Journal of Enzyme Inhibition and Medicinal Chemistry*, **2019**, 34, 429-437.

CHEMOMETRIC INSIGHTS INTO GRAPE STEMS: ANTIOXIDANT CAPACITY, PHENOLIC COMPOSITION, AND MINERAL PROFILE

Milan MITIĆ^{a,*}, Vesna STANKOV-JOVANOVIĆ^a,
Jelena MITIĆ^b, Jelena NIKOLIĆ^a, Anastasia KARIOTI^c and
Diamanto LAZARI^c

ABSTRACT. The primary objective of this investigation was to assess the total polyphenolic content (TPC), identify and quantify individual polyphenols, and evaluate their radical scavenging activity (RSA), as well as determine the mineral composition in stem extracts from nine distinct *Vitis vinifera* varieties. The total phenolic content in grape stem extracts ranged from 34.87 to 76.95 mg gallic acid equivalents (GAE) per gram of dry weight (d.w.). These extracts exhibited significant free radical scavenging activity, ranging from 0.344 to 0.898 mmol Trolox equivalents (TE) per gram d.w. Stem extracts were predominantly characterized by flavan-3-ols, flavonols, and phenolic acids. Catechin and quercetin-3-glucuronide were identified as the most abundant components, with concentrations of up to 1.858 mg/g d.w. and 1.315 mg/g d.w., respectively. Potassium (K) emerged as the most abundant element in all samples, with content ranging from 7.297 mg/g d.w. to 16.695 mg/g d.w., followed by calcium (Ca), phosphorus (P), and magnesium (Mg).

Keywords: *Vitis vinifera*, stem extracts, flavonols, potassium.

INTRODUCTION

The food processing sector generates a substantial volume of waste, posing environmental threats and causing considerable economic losses.

^a Faculty of Sciences and Mathematics, University of Nis, Visegradska 33, 18000 Nis, Serbia

^b Institute for Artificial Intelligence Research and Development of Serbia, Fruškogorska 1, 21000 Novi Sad, Serbia

^c Laboratory of Pharmacognosy, School of Pharmacy, Faculty of Health Sciences, Aristotle University of Thessaloniki, 54124 Thessaloniki, Greece

* Corresponding author: milan.mitic1@pmf.edu.rs



Grape stems, a byproduct of the winery industry, are often utilized partially as a source of astringent compounds, primarily comprising proanthocyanidins [1-2]. These stems are typically removed prior to vinification processes to prevent excessive astringency in wine or adverse effects on its sensory properties. Stem quantities typically range from 1.4% to 7.0% of the processed raw material [3]. Presently, grape stems hold low commercial value, primarily serving as animal fodder or soil enhancers. Limited available data on the composition of grape stems suggests their potential as a valuable source of dietary fiber and antioxidants [4-5]. Phenolic compounds represent a significant category of substances due to their well-established health-promoting properties. The phenolic composition of grape stems typically includes flavan-3-ols, hydroxycinnamic acids, monomeric and oligomeric flavonols, and stilbenes [6-7]. It has been reported that phenolics constitute approximately 5.8% of the dry weight of grape stems [2]. While phenolic compounds are commonly found in various plant-based foods, there is a preference for extracting them from agri-industrial by-products [8-9]. Consequently, there has been notable interest in recent years in acquiring polyphenols from plant residues. These polyphenols are sought for applications in the pharmaceutical sector, as food additives and supplements, or in cosmetics.

In addition to the organic constituents, the significance of both major and trace elements in grape stems cannot be overlooked. Findings from Leal et al. [5] underscored that the essential trace elements present in stems offer notable nutritional value. Conversely, concentrations of toxic elements such as arsenic (As), cadmium (Cd), and lead (Pb) were minimal and posed no threat to human health.

This study aims to explore the composition of grape stems to assess their potential utilization in the food and/or pharmaceutical industries. Stems from nine distinct grape cultivars underwent extraction via maceration. The resulting extracts were then subjected to analysis to establish their phenolic profiles using the HPLC method. Additionally, the mineral composition of the stems was assessed utilizing the ICP-OES method.

RESULTS AND DISCUSSION

Mineral contents of grape stems

The data about the mineral contents of the stems are presented in Tables 1-3. Statistical analysis showed that mineral contents of the stems differ significantly among the cultivars ($p < 0.05$).

The plant materials with high concentrations of the nutrient elements will play an essential role in maintaining human health when taken at recommended levels [10]. This study determined that grape stems are also useful dietary supplements that can provide K, P, Ca, Mg, Fe, and Zn.

All the grape stems were characterized by high potassium and low sodium contents. The concentration of Na varied and ranged from 2.01 $\mu\text{g/g}$ in the Tamjanika Black cultivar to 4.85 $\mu\text{g/g}$ in the Merlot cultivar.

Merlot cultivar had the highest levels of K (16.695 mg/g), whereas cv. Župljanka had the lowest K concentration (0.761 mg/g). K is essential for human health. High-potassium diet lowers blood pressure and reduces cardiovascular disease morbidity and mortality [10]. Since K is necessary for the growth and development of plants, this may be the main reason why it is the most abundant element in grape stems. Romero et al. [11] also analyzed K in stems, and obtained values were in accordance with values obtained in our study. However, Kondi et al. [12] found slightly lower (1.4 mg/g) whereas Leal et al. [5] values were higher (18.10-39.36 mg/g).

The highest P concentration was in the stems of Plovdiva (3.349 mg/g) and Merlot (3.017 mg/g) cultivars and it was lowest in the Župljanka cultivar (1.232 mg/g). P can be found most as phosphates in the environment as well as in plant tissues.

The results from the present study also showed that grape stems are rich in Ca. Ca concentrations in grape stems varied from 3.328 to 8.410 mg/g. The average results of Ca (5.016 mg/g) were higher compared to results reported by Kondi et al. [12] (1.92 mg/g), but lower obtained by Romero et al. [11] (14.9 mg/g). Ca is an essential mineral for human health because it is the major component of the bone, assists in tooth development, helps regulate endo- and exo-enzymes, and plays a significant role in regulating blood pressure [13].

Mg is one of the minerals found in high concentrations in grape stems. Mg concentrations varied between 0.546 mg/g (cv. Prokupac) and 2.142 mg/g (cv. Smederevka). Mg is essential to all living cells, where they play a major role in manipulating important biological polyphosphate compounds like ATP, DNA, and RNA. Also, more than 300 enzymes require magnesium ions to function [14].

Merlot Cultivar had the highest concentration of Fe, whereas the Muscat Hamburg cultivar had the highest concentration of Zn (139.82 $\mu\text{g/g}$ and 33.14 $\mu\text{g/g}$, respectively). The optimum range of the iron content in grapevine petioles ranges from 40 to 180 $\mu\text{g/g}$ [15]. The previous results obtained in grape stems in India, Portugal, and Spain's vineyards were 65.80-98.56 $\mu\text{g/g}$, 17.51-84.15 $\mu\text{g/g}$, 19.96-77.62 $\mu\text{g/g}$ for Fe content Fe [12, 5]. Also, the previous results obtained in grape stems in Poland, India and Spain vineyards for Zn

content were 30.8 µg/g, 90.22 µg/g, 21.7 µg/g respectively [11-12]. The deficiency of Zn and Fe in the diet is a widespread problem and a matter of great concern, especially in developing countries where people rely more on vegetarian diets. These essential trace elements are involved with the vital immune system (Zn) and metabolic functions and are intrinsic components of hemoglobin, myoglobin, and cytochrome (Fe) [15]. They are also recognized as potential antioxidants [10].

The most significant levels of manganese were noted in the stems of cv. Merlot (123.07 µg/g), compared with only 10.27 µg/g d.w. in the stems of cv. Tamjanika Blank (Table 2). Generally, manganese shows the most significant variation in stem tissues because root uptake of this nutrient depends on the soil solution concentration of Mn²⁺ [16]. Adequate Mn values for grape petioles are 18 to 100 µg/g. Gastol and Domagala-Swiatkiewicz [17] suggested that the high Mn levels, could be linked to increased availability of Mn in acid soils.

The copper content in grape stems ranged from 5.90 µg/g in stems of Tamjanika Black to 48.80 µg/g in stems of Cabernet Sauvignon. The previous study by Kondi et al. [12] found that Cu content in vine and table grape stems cultivated in India varied from 11.23 µg/g to 29.97 µg/g. The studies of Cu content in grape stems range from 16.00-159.25 µg/g in Portugal [5] and 8.9-21.7 µg/g Spain [11]. Many studies indicated that grapefruit, leaf, and stem are contaminated with Cu worldwide. Copper is generally slightly mobile element in plants as it is strongly bound by nitrogen and proteins. However, some plant species have a great tolerance to increased content of Cu and can accumulate high amounts in their tissues [18]. The content of Cu in the vineyards' soil usually depends on the age because the long-term use of the same parcels for grapevine growing could cause Cu accumulation in the soil due to the application of Cu-fungicides.

However, can find other elements in the vineyard soils, and consequently, in the vines, namely toxic or heavy metals (As, Al, Cd, Pb, and Hg). These elements appear in the soil, mainly due to the fertilizers and chemical pesticides used, and due to industrial activities or traffic. Thus, in the last years there has been a growing concern by the population about the increase in the quantity of toxic elements in plants [19], since these metals, when accumulated in the human body, can have negative effects, causing damage, for example, in the kidneys, nervous and immune systems, and even having carcinogenic effects [20]. For this reason, maximum levels of toxic metals in food have been set in most countries to prevent possible poisoning [22]. In this way, to verify the possibility of using grape stems in distinct industry areas, their content toxic metals were determined, if this by-product can be used safely in new and innovative products on food, cosmetic, and pharmaceutical industries.

The contents of toxic elements Al, Cd, and Pb in grape stems are also presented in Table 3. The most abundant toxic element in grape stems was Al, with concentrations ranging from 3.74 $\mu\text{g}/\text{kg dw}$ (cv. Župljanka) to 48.13 $\mu\text{g}/\text{kg d.w.}$ (cv. Cabernet Sauvignon). Pb content, an element with no known function in human organism, varied between 0.56 $\mu\text{g}/\text{g}$ (cv. Cabernet Sauvignon) and 1.70 $\mu\text{g}/\text{g}$ (cv. Plovdina).

Cd was detected only in three cultivars in range 0.01 (cv. Italian Rizling) to 0.04 $\mu\text{g}/\text{g}$ (cv. Merlot), whereas As was not detected.

Concerning the literature, Bustamante et al. [22] also quantified Cd and Pb in grape stems, obtaining average concentrations of 0.80 $\mu\text{g}/\text{g d.w.}$ and 26.2 $\mu\text{g}/\text{g d.w.}$, respectively. Compared to the present study, these concentrations are much higher, since the average value obtained for the nine cultivars analysed were 0.08 $\mu\text{g}/\text{g DW}$ for Cd and 0.99 $\mu\text{g}/\text{g d.w.}$ for Pb. These differences between studies can be justified by the above mentioned, namely, genetic characteristics, pollution, and de-stemming process.

Table 1. The content of essential macroelements $\pm\text{SD}^{\text{a}}$ ($\mu\text{g}/\text{g}$) in grape stems

Sample	K	Mg	Na	P	Ca
Žu	7612 \pm 35	645 \pm 3	2.48 \pm 0.02	1232 \pm 13	7287 \pm 45
TB	14800 \pm 60	1194 \pm 11	2.01 \pm 0.01	2099 \pm 30	4477 \pm 18
MH	11836 \pm 60	771 \pm 5	2,92 \pm 0.01	2656 \pm 26	5571 \pm 20
Sm	9905 \pm 40	2142 \pm 19	3.73 \pm 0.06	2194 \pm 21	8410 \pm 55
Pr	11344 \pm 20	547 \pm 4	2.08 \pm 0.01	1402 \pm 12	3329 \pm 20
PI	7297 \pm 40	1832 \pm 13.	3.80 \pm 0.01	3350 \pm 27	4534 \pm 27
IR	9685 \pm 45	1492 \pm 13	4.37 \pm 0.06	2727 \pm 5	4197 \pm 15
CS	10412 \pm 180	665 \pm 6	2.07 \pm 0.02	2757 \pm 7	3515 \pm 27
Me	16695 \pm 132	823 \pm 9	4.85 \pm 0.05	3017 \pm 17	4232 \pm 30

^aSD-standard deviation

Table 2. The content of essential trace and probably essential elements $\pm\text{SD}^{\text{a}}$ ($\mu\text{g}/\text{g}$) in grape stems

Sample	Mn	Ni	V	Zn	Fe	Cu
Žu	29.40 \pm 0.06	2.60 \pm 0.01	1.04 \pm 0.02	11.61 \pm 0.04	35.38 \pm 0.3	8.67 \pm 0.07
TB	10.27 \pm 0.04	1.72 \pm 0.02	2.04 \pm 0.05	11.03 \pm 0.06	75.3 \pm 0.1	5.90 \pm 0.09
MH	80.3 \pm 0.4	2.04 \pm 0.02	2.28 \pm 0.02	33.1 \pm 0.1	49.7 \pm 0.2	18.59 \pm 0.06
Sm	16.61 \pm 0.05	1.93 \pm 0.01	3.81 \pm 0.02	29.75 \pm 0.08	58.6 \pm 0.1	9.34 \pm 0.04
Pr	45.60 \pm 0.09	3.03 \pm 0.00	1.01 \pm 0.02	17.18 \pm 0.06	70.3 \pm 0.2	57.2 \pm 0.3
PI	45 \pm 0.2	3.04 \pm 0.02	3.40 \pm 0.06	13.5 \pm 0.1	115.5 \pm 0.2	9.19 \pm 0.04
IR	37.3 \pm 0.1	2.23 \pm 0.00	1.41 \pm 0.06	11.87 \pm 0.01	44.1 \pm 0.3	72.7 \pm 0.2
CS	72.9 \pm 0.4	1.09 \pm 0.00	1.3 \pm 0.1	10.68 \pm 0.06	53.80 \pm 0.07	48.7 \pm 0.1
Me	123 \pm 2	1.81 \pm 0.01	1.31 \pm 0.08	30.7 \pm 0.4	139.8 \pm 0.8	43.6 \pm 0.3

^aSD-standard deviation

Table 3. The content of toxic and probable toxic elements \pm SD^a (μ g/g) in grape stems

Sample	Si	Ba	Cr	Co	Al	Pb	Cd
Žu	3.80 \pm 0.01	24.5 \pm 0.1	3.16 \pm 0.01	0.06 \pm 0.01	3.7 \pm 0.8	0.61 \pm 0.03	- ^b
TB	35.5 \pm 0.2	6.17 \pm 0.02	2.88 \pm 0.02	0.05 \pm 0.01	27 \pm 1	1.41 \pm 0.04	-
MH	7.4 \pm 0.2	7.01 \pm 0.03	2.86 \pm 0.02	0.03 \pm 0.00	16.8 \pm 0.5	0.72 \pm 0.04	-
Sm	10.9 \pm 0.2	17.4 \pm 0.1	2.97 \pm 0.01	0.04 \pm 0.01	14.7 \pm 0.5	1.18 \pm 0.02	-
Pr	25.7 \pm 0.4	42.4 \pm 0.3	3.00 \pm 0.05	0.04 \pm 0.01	21.8 \pm 0.3	1.40 \pm 0.01	-
PI	24.2 \pm 0.1	16.45 \pm 0.05	3.30 \pm 0.01	0.06 \pm 0.01	62.1 \pm 0.8	1.70 \pm 0.04	-
IR	17.44 \pm 0.08	7.78 \pm 0.06	0.05 \pm 0.00	0.21 \pm 0.01	24.96 \pm 0.07	0.68 \pm 0.05	0.010 \pm 0.001
CS	31.80 \pm 0.05	17.8 \pm 0.1	0.24 \pm 0.06	0.20 \pm 0.01	48.1 \pm 0.4	0.56 \pm 0.03	0.021 \pm 0.002
Me	62.5 \pm 0.7	29.45 \pm 0.05	0.14 \pm 0.02	0.34 \pm 0.02	40.0 \pm 0.7	0.64 \pm 0.04	0.042 \pm 0.010

^aSD-standard deviation; ^b-<LOD (<limit of detection)

Total phenolic content

According to the results for total phenolic content and (Table 4), noticeable difference among investigated grape stem samples is observed. The highest TPC was identified in cv. Merlot stem extract (76.95 mg GAE/g d.w.). The lowest value for TPC was obtained in the sample of Plovdivina (34.87 mg GAE/g d.w.). The results of TPC for different grape stems obtained here in agree with those reported in another publication ([7]- 47.04/115.25 mg GAE/g d.w.; [5]- 30.91-96.12 mg GAE/g d.w.). However, Spigno et al. [23] observed total phenolic values considerably lower than those reported in the present research (3.30 mg GA/g d.w. in Barbera variety). All these differences may be attributed to the different vintage, geographical origin, and viticultural conditions of the samples and to the solvent used during the polyphenol extraction process [24].

Phenolic profile

It is also important to note that, these colorimetric methods, namely the Folin-Ciocalteu assay, enclose some constraints related to the limited information provided, the overestimation of the phenolic concentration and the lack of qualitative information on individual bioactive phenolics [5]. However, this assay, and others spectrophotometric methods employed, do not require expensive equipment, are easy to use and are all used to complement the total phenolics determination. Furthermore, also determined the identification of the individual phenolic compounds of these stem samples by HPLC. A total of 13 polyphenols were quantified using the available

CHEMOMETRIC INSIGHTS INTO GRAPE STEMS: ANTIOXIDANT CAPACITY,
PHENOLIC COMPOSITION, AND MINERAL PROFILE

standards in the grape stem extracts, mainly phenolic acids, flavan-3-ols and flavonols (Table 4).

Table 4. Phenolic Profile of Grape Stems (mg/g d.w.), TPC- total phenolic content (mg GAE/g d.w.), RSA- radical scavenging activity (mmol TE/g d.w.)

Sample	Žu	TB	MH	Sm	Pr	PI	IR	CS	Me
(+)catechin	0.584	0.612	0.702	0.898	0.855	0.654	1.125	1.080	1.858
(-)epicatechin	0.011	0.014	0.020	0.032	0.018	0.014	0.028	0.022	0.018
Total flavan-3-ols	0.595	0.626	0.722	0.930	0.873	0.668	1.153	1.102	1.876
Q-3-rutinoside	0.034	0.110	0.012	0.110	0.205	0.005	0.044	0.017	0.022
Q-3-glucuronide	0.414	0.508	0.607	0.547	0.478	0.405	0.573	0.630	1.315
Q-3-glucoside	0.111	0.119	0.151	0.196	0.256	0.132	0.117	0.167	0.449
Quercetin	0.009	0.010	0.037	0.040	0.025	0.046	0.015	0.092	0.018
Kaemferol	0.008	0.009	0.013	0.011	0.020	0.018	0.017	0.015	0.016
Total flavonols	0.576	0.756	0.820	0.904	0.984	0.606	0.766	0.921	1.820
L-7-glucoside	0.055	- ^a	0.114	0.261	0.168	-	0.382	0.097	0.448
Total flavonon	0.055	-	0.114	0.261	0.168	-	0.382	0.097	0.448
t-caftaric acid	0.024	0.055	0.023	0.016	0.094	0.014	0.086	0.135	0.106
Caffeic acid	0.023	0.065	0.020	0.387	0.028	0.010	0.262	0.093	0.092
Syringic acid	0.008	-	0.049	0.061	0.021	0.019	0.115	0.065	0.036
p-Coumaric acid	0.014	0.463	0.083	0.184	0.176	0.012	0.235	0.198	0.213
Ferulic acid	-	-	-	-	0.014	0.016	0.026	0.030	0.028
Total phenolic acids	0.069	0.583	0.175	0.648	0.333	0.071	0.724	0.521	0.475
Total polyphenols	1.157	1.957	1.821	2.717	2.344	1.326	3.060	2.721	4.611
TPC	40.65	52.13	39.15	49.69	43.52	34.87	67.84	78.53	76,95
RSA	0.433	0.547	0.497	0.668	0.523	0.344	0.732	0.766	0.898

^a-<LOD (<limit of detection)

In this study, only (+)-catechin and (-)-epicatechin were identified in grape stems. This finding aligns with prior research by Souquet et al. [3], where similar constituents were reported. Apostolou et al. [4] identified additional compounds such as procyanidin B3, procyanidin B2, and epicatechin gallate in grape stem extracts from various Greek *Vitis vinifera* varieties. Similarly, Silva et al. [9] found catechin, epicatechin, gallic acid, and catechin gallate in grape stem extracts from Portuguese red grape varieties: Touriga Nacional and Preto Martinho. Conversely, Leal et al. [5] detected only catechin. These discrepancies contributed to establishing distinct flavan-3-ol profiles for stems of each grape variety, focusing on quantification of individual compounds [7].

Catechin emerged as the most abundant compound in all examined grape stems. Its concentration ranged from 1.858 mg/g in Merlot to 0.584 mg/g in Župljanka stems. Previous studies reported catechin content in grape stems from Portugal, Spain, and Mexico as 0.55-2.03 mg/g dw, 0.093-1.339 mg/g d.w., and 0.034 mg/g d.w., respectively [7,5]. Interestingly, the concentration of (+)-catechin in grape stems surpassed that found in skins and seeds [25]. This compound exhibits high lability under oxidative conditions, providing protective effects against free radicals [26]. Epicatechin concentrations in the stem extracts of nine cultivars ranged from 0.011 to 0.032 mg/g d.w. This aligns with findings from other studies indicating lower epicatechin concentrations compared to catechin in stems of grape cultivars from Spain (0.006-0.111 mg/g d.w.) [7] and Greece (0.012-0.099 mg/g d.w.) [27].

Although some European studies reported higher catechin concentrations than epicatechin, others found the opposite trend. For instance, Barros et al. [28] found epicatechin to be the most abundant, representing 68% and 75% of total proanthocyanidins in red and white grape cultivars' stems, respectively. These variations may arise from genetic differences between cultivars, light intensity, soil composition, and regional factors [29].

Flavonol content in grape stems ranged from 0.576 to 1.820 mg/g dw. Quercetin, presented in both aglycon and glycoside forms, was consistently detected in all stem extracts. The average amount of aglycon quercetin was 0.032 mg/g d.w., ranging from 0.009 to 0.092 mg/g d.w. Kaempferol was found in relatively low amounts, ranging from 0.008 to 0.020 mg/g d.w. The most abundant glycoside forms of quercetin were quercetin-3-glucuronide and quercetin-3-glucoside, ranging from 0.405 to 1.315 mg/g d.w. and 0.111 to 0.449 mg/g d.w., respectively. Quercetin-3-glucuronide was the major flavonol, representing 48.57% to 74.80% of the total. Luteolin-7-glucoside was also detected in stem samples, albeit in extremely low concentrations compared to major flavonols such as catechin.

The phenolic acid composition, including t-caftaric, caffeic, syringic, p-coumarin, and ferulic acids, varied significantly among different cultivars. T-caftaric acid ranged from 0.014 mg/g d.w. to 0.135 mg/g d.w., consistent with previous reports [27]. Grape stem cultivars Smederevka and Italian Riesling exhibited richness in caffeic acid, while syringic acid content varied across cultivars. P-coumaric acid content was highest in cv. Tamjanika Black and lowest in t-caftaric and caffeic acids.

Radical scavenging activity

The DPPH• test results for grape stem extracts are presented in Table 4, indicating notable antiradical activity in Merlot and Cabernet Sauvignon stem extracts (0.898 mmol TE/g d.w. and 0.766 mmol TE/g d.w., respectively), with the lowest RSA value observed in Plovdiv stems (0.344 mmol TE/g d.w.).

Correlating total phenolics, flavan-3-ols, flavonols, flavonones, and phenolic acids contents with DPPH•, yielded corresponding coefficients of determination R^2 of 0.8707, 0.7857, 0.5813, 0.6319, and 0.5466, respectively.

The exact mechanism by which phenolic compounds scavenge free radicals remains uncertain. However, it is evident that the structural composition, particularly the aromatic OH groups, notably the 3',4'-dihydroxy catechol group, play a crucial role, with their activity potentially enhanced by the electron-donating effects of other substituents [30]. For flavonoid compounds like quercetin and rutin, antioxidant activity is associated with O-dihydroxy groups in the B-ring, the presence of a C 2-3 double bond in conjunction with 4-oxo in the C-ring, and 3- and 5-hydroxy groups, along with the 4-oxo function in the A and C-rings.

Pearson's Correlation Analysis

Pearson correlation analysis was conducted to examine the relationship between metals in grape stem samples. Strong correlations ($r \geq |0.5|$) were observed between certain metals (Mn, Fe, Cd, Si, and Co), while others (Cr, Zn, Ba, and Mg) showed poor correlation. The distribution of trace metal ions generally follows a pattern of roots > stems > leaves > fruit > seeds. Metal uptake by plants depends on soil content and plant affinity for specific metals. Antagonistic interactions between ions, particularly mono- and divalent cations, affect uptake, transport, and accumulation in plants. For instance, a strong positive correlation was found between Mg and V, Si and Cd, and Al and P. Vanadium concentrations above certain levels can be toxic to animals and plants, causing oxidative stress and nutrient disruption. Conversely, synergistic interactions between V and mineral elements may occur. Excessive phosphorus reduces the uptake of cationic micronutrients like Ni, Ba, and Cr.

Potassium shows a negative correlation with Ca and Mg due to competitive binding strengths. Lead exhibits negative correlations with elements like K, Na, Ca, Mn, Zn, Cu, and Co, indicating potential atmospheric or soil origins and translocation into plant tissues. Excessive calcium reduces copper uptake, leading to decreased Ca content in stems. These findings suggest complex interactions influencing metal uptake and distribution in grape stems.

In this research, the correlation of all individual polyphenolic compounds in selected types of stems were also determined based on the Pearson correlation coefficient. A high positive correlation was observed between catechin and Q3 glucuronide, catechin and Q3 glucoside, catechin and L7 glucoside, epicatechin and Caffeic acid, Q3 glucuronide and Q3 glucoside, Q3 glucuronide and L7 glucoside. The highest correlation coefficient occurs between catechin and Q3 glucuronide.

Cluster Analysis

Ward's method was employed to classify stem types based on the content of selected elements. The dendrogram presented illustrates the association of wine types based on the elemental content (K, Mg, Na, P, Ca, Mn, Ni, V, Zn, Fe, Cu, Si, Ba, Cr, Co, Al, Pb, and Cd) therein. Through cluster analysis, the analyzed stems were delineated into two significant clusters.

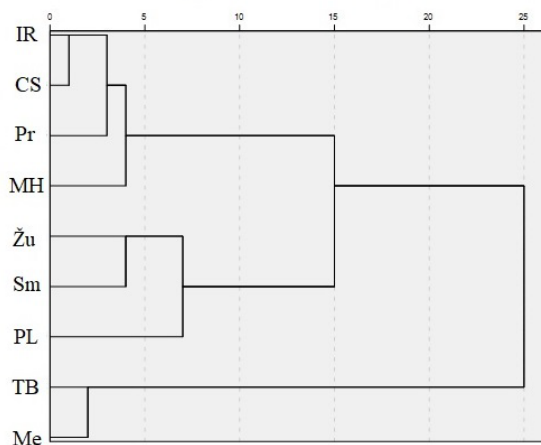


Figure 1. Dendrogram of stems type grouping according to mineral contents

The first cluster encompasses the stems of varieties: Žu, MH, Sm, Pr, PI, IR, and CS, divided into two subclusters. The first subcluster comprises IR, CS, Pr, and MH, while the second subcluster comprises Žu and Sm along

with PI. Through cluster analysis, based on the Euclidean distance, it's evident that the greatest similarity exists between wine types CS and IR due to their similar elemental content. Subsequently, Žu and Sm species are grouped together owing to their analogous elemental composition. The second cluster comprises wine types TB and Me, distinguished from other analyzed wines by their notably higher potassium (K) content.

The correlation between wine types regarding their phenol content (catechin, epicatechin, Q-3 - rutinoside, Q-3-glucuronide Q-3-glucoside, Quercetin, Kaemferol, L-7-glucoside, t-caftaric acid, and Caffeic acid) is depicted on Dendrogram 2. Through cluster analysis, the wine types are classified into two significant clusters.

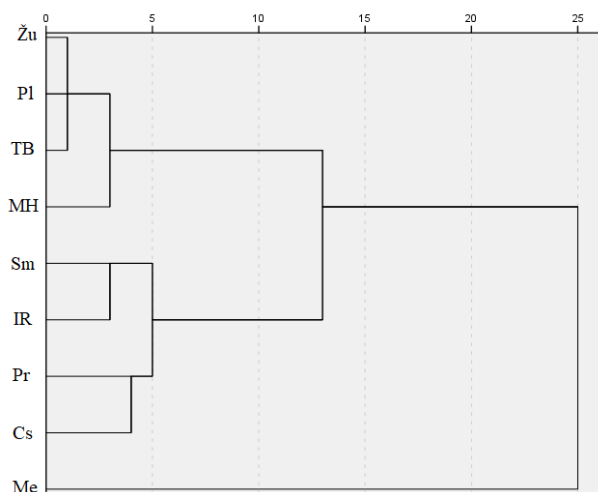


Figure 2. Dendrogram of stems type grouping according to individual polyphenols

The initial cluster comprises: Žu, TB, MH, Sm, Pr, PI, IR, and CS. Within this cluster, there are two subclusters: the first includes Žu, PI, TB, and MH, while the second subcluster comprises Sm, IR, Pr, and CS. Utilizing the Euclidean distance obtained from cluster analysis, it becomes evident that the greatest similarity exists among the stem types Žu, PI, and TB due to their similar element content. The second cluster is represented by the Me stem, distinguished from others by significantly higher levels of catechins, Q-3-glucuronide, and Q-3-glucoside.

CONCLUSIONS

Grape stems, as a by-product of the wine industry, could be further used to make the wine industry eco-friendlier and more sustainable. Results of the present study showed that grape stems have a high content of essential minerals, as the most represented Na, Mg, Ca, and K, as well as phenol compounds, as the most represented Q-3-glucuronide and catechin. In fact, the stems are richer in phenol compounds and minerals, in some cases higher than some food matrices consumed in our diet, whereby this by-product can be a good pledge in the production of value-added products.

EXPERIMENTAL SECTION

Samples

Well known international white and red wine varieties 'Cabernet Sauvignon' (CS), 'Merlot' (Me), 'Italian Riesling' (IR), 'Muscat Hamburg' (MH), together with Serbian autochthonous varieties 'Prokupac' (Pr), 'Plovdina' (Pl), and 'Smederevka' (Sm), Tamjanika Black (TB) and 'Župljanka' (Žu) were studied.

A total of 9 grapevine stem samples were collected in the south-east region of Serbia. For twenty days, samples were washed with water and dried on air, in the dark, and at room temperature. The dry plant material was then packed in paper bags and kept in the dark, dry, and cool place. Before being used, the plant material was comminuted by a hammer mill and sieved through a 6 mm sieve.

Samples preparation for HPLC analysis

The dried and ground stem (2.5 g) was macerated in 60%, v/v acetone/water for 24 h (at room temperature, in the shade). After the incubation, the extracts were filtered using the Whatman No. 1 filter paper. The residues were extracted twice with the same fresh solvent and extracts combined. The combined extracts were concentrated and freed of solvent under reduced pressure at 45 °C, using a rotary evaporator (BUCHI Rotavapor R-200). The dried crude concentrated extracts were dissolved using extraction solvent and kept in refrigerator until analyses.

Samples preparation for ICP-OES analysis

Homogenized dried stems (1.0 g) were digested in a solution containing HNO₃ and water (2:1). The samples were heated at 200 °C.

Then 1 ml 70% HClO₄ was added and reheated. The residue was taken up in 25 ml of 1 % HCl.

Determination of total polyphenolic content (TPC)

Total polyphenolic content in the stem extracts was determined using Folin-Ciocalteu method [31].

Determination of radical scavenging activity using DPPH test, RSA

Radical scavenging activity was determined spectrophotometrically using DPPH (1,1-diphenyl-2-picrylhydrazyl) method [32].

HPLC method

Quantification of individual phenolic compounds was performed using reversed-phase HPLC analysis according to research Mitić et al. 2012 [33]. The equipment used was an HPLC Agilent-1200 series with a UV–Vis DAD detector for multi-wavelength detection. The calibration curve, coefficient of correlation (R^2), the limit of detection (LOD) and the limit of quantification (LOQ) are shown in Table 5. The content of phenolic compound was expressed as micrograms per gram of dried plant material ($\mu\text{g/g}$).

Table 5. Analytical parameters for hydroxycinnamic acids used for HPLC-DAD analysis

Compound	Calibration curve	(R^2)	LOD ^a ($\mu\text{g/ml}$)	LOQ ^b ($\mu\text{g/ml}$)
Catechin	$y = 4628.36x + 0.97$	0.9996	0.33	1.10
Epicatechin	$y = 4785.17x - 0.18$	0.9998	0.30	1.00
Q-3-rutinoside	$y = 4879.79x - 5.55$	0.9996	0.39	1.18
Q-3-glucoside	$y = 5209.08x - 1.05$	0.9996	0.48	1.45
Quercetin	$y = 8143.54x + 5.62$	0.9999	0.52	1.57
Kaemferol	$y = 18921.26x + 1.82$	0.9999	0.55	1.67
Luteolin	$y = 3542.67x + 1.81$	0.9997	0.63	1.93
Caffeic acid	$y = 33621.18x - 0.67$	0.9998	0.30	1.00
Syringic acid	$y = 20540.50x + 0.98$	0.9997	0.29	0.97
p-coumaric acid	$y = 32964.76x - 2.39$	0.9992	0.52	1.57
Ferulic acid	$y = 18346.18x + 1.18$	0.9998	0.48	1.45

^aLOD-limit of detection, ^bLOQ-limit of determination

ICP-OES analysis

For the elemental analysis, an iCAP 6000 inductively coupled plasma optical emission spectrometer (Thermo Scientific, Cambridge, United Kingdom) with an Echelle optical design and a charge injection device (CID) solid-state detector was used under the operating conditions as follows: flush pump rate – 100 rpm; analysis pump rate – 50 rpm; RF power – 1150 W; nebulizer gas flow – 0.7 L min⁻¹; coolant gas flow – 12 L min⁻¹; auxiliary gas flow – 0.5 L min⁻¹; plasma view – axial; time of rinse – 30 s; measurement in three repetitions. All measurements were carried out in triplicate.

The precise method was optimized for each element. The choice of wavelength was performed based on the relative intensity of the signal as a measure of sensitivity, defects in response to the standards, and the extent of interference in the real sample. All calibration curves were prepared with four standard solutions, including the blank.

Statistical analysis

All measurements and analyses were performed in three replicates in the present study. The data in tables and graphs are presented as mean ± standard deviation. Differences were considered statistically significant at $p < 0.05$.

ACKNOWLEDGMENTS

This research was financially supported by the Ministry of Science, Technological Development, and Innovation of the Republic of Serbia (451-03-65/2024-03/200124).

REFERENCES

1. A. Llobera; J. Canellas; *Food Chem.*, **2007**, *101*, 659–666
2. A. Teixeira; N. Baenas; R. Dominguez-Perles; A. Barros; E. Rosa; D. A. Moreno; C. Garcia-Viguera; *Int. J. Mol. Sci.*, **2014**, *15*, 15638–15678
3. J. M. Souquet; B. Labarbe; C. Le Guerneve; V. Cheynier; M. Moutounet; *J. Agric. Food Chem.*, **2000**, *48*, 1076-1080
4. A. Apostolou; D. Stagos; E. Galitsiou; A. Spyrou; S. Haroutounian; N. Portesis; *Food Chem. Toxicol.*, **2013**, *61*, 60–68
5. C. Leal; C. M. Costa; A. I. R. Barros; I. Gouvinhas; *Waste Biomass Valori.*, **2021**, *12*, 1313–1325
6. E. Karvela; D. P. Makris; N. Kalogeropoulos; V. T. Karathanos; *Talanta*, **2009**, *79*, 1311–1321

7. M. R. Gonzalez-Centeno; M. Jourdes; A. Femenia; S. Simal; C. Rossello; P. L. Teissedre; *J. Agric. Food Chem.*, **2012**, *60*, 11850-11858
8. J. F. Ayala-Zavala; V. Vega-Vega; C. Rosas-Dominguez; H. Palafox-Carlos; J. Villa-Rodriguez; M. W. Siddiqui; J. Davila-Avina; G. Gonzalez Aguilar; *Food Res. Int.*, **2011**, *44*, 1866–1874
9. V. Silva; G. Igrejas; V. Falco; T. P. Santos; C. Torres; A. M. P. Oliveira; J. E. Pereira; J. S. Amaral; P. Poeta; *Food Control*, **2018**, *92*, 516–522
10. E. S. Cetin; D. Altinoz; E. Tarcan; N. G. Baydar; *Ind. Crops Prod.*, **2011**, *34*, 994-998
11. I. Romero; A. Benito; N. Dominguez; E. Garcia-Escudero; I. Martin; *Span J. Agric. Res.*, **2014**, *12*, 206-214
12. A. E. Kondi; S. Meti; B. V. Champa; M. S. Nagaraja; *Int. J. Curr. Microbiol. App. Sci.*, **2018**, *7*, 447-453
13. Brody T; *National Biochemistry*, Academic, San Diego, USA 1994
14. Schachter M; *The Importance of Magnesium to Human Nutrition*, 1996
15. S. Hemalatha; K. Patel; *Food Chem.*, **2007**, *102*, 1328-1336
16. L. P. Christensen; W. Peacock; 2000; *Mineral nutrition and fertilization. In: Raisin Production Manual*. University of California Division of Agricultural and Natural Resources Publication 3393, Oakland, CA. 102 – 114
17. M. Gastol; I. Domagala-Swiatkiewicz; *S. Afr. J. Enol. Vitic.*, **2014**, *35*, 217-225
18. Kabata-Pendias, A; *Trace Elements in Soils and Plants*. CRC Press, New York, USA, 2011
19. T. Milićević; M. Aničić Urošević; D. Relić; G. Vuković; S. Škrivanj; A. Popović; *Sci. Total Environ.*, **2018**, *626*, 528–545
20. M. G. Volpe; C. F. La; F. Volpe; De A Matia, V. Serino; F. Petitto; C. Zavalonni; F. Limone; R. Pellecchia; P. P. De Prisco; M. Di Stasio; *Food Chem.*, **2009**, *117*, 553–560
21. M. Edelstein; M. Benhur; *Sci. Hortic.*, **2018**, *234*, 431-444
22. M. A. Bustamante; R. Moral; C. Paredes; A. Pe; M. D. Pe; *Waste Manag.*, **2008**, *28*, 372–380
23. G. Spigno; D. M. De Faveri; *J. Food Eng.*, **2007**, *78*, 793-801
24. M. Monagas; S. C. Gomez-Cordove; B. Bartolome; O. Laureano; J. M. Ricardo Da Silva; *J. Agric. Food Chem.*, **2003**, *51*, 6475-6481
25. D. Villaño; M. S. Fernández-Pachón; A. M. Troncoso; M. C. García-Parrilla; *Anal Chim Acta.*, **2005**, *538*, 391-398
26. I. Gouvinhas; M. Queiroz; M. Rodrigues; I. R. N. A. Barros Ana; *Polyphenols in Plants*. **2019**, 381-394
27. M. Anastasiadi; H. Pratsinis; D. Kletsas; A. L. Skaltsounis; S. A. Haroutounian; *LWT-Food Sci. Technol.*, **2012**, *48*, 316-322
28. A. Barros; A. Girones-Valaplana; A. Teixeira; J. Collado-Gonzales; D. A. Moreno; A. Gil-Izquierdo; E. Rosa; R. Dominiguez-Perles; *Food Res. Int.*, **2014**, *65*, 375-384
29. A. Topalović; M. Mikulič – Petkovšek; *J. Food Agric. Environ.*, **2010**, *8*, 223-227
30. C. G. M. Heijnen; G. R. M. M. Haenen; J. A. J. M. Vekemans; A. Bast; *Environ. Toxicol. and Pharmacol.*, **2001**, *10*, 199-206

MILAN MITIĆ, VESNA STANKOV-JOVANOVIĆ, JELENA MITIĆ, JELENA NIKOLIĆ,
ANASTASIA KARIOTI, DIAMANTO LAZARI

31. V. L. Singleton; J. Rossi; *Am. J. Enol Vitric.*, **1965**, *16*, 144-158
32. W. Brand-Williams; M. E. Curelier; C. Berset; *Lebensm. Wiss. Technol.*, **1995**, *28*, 25-30
33. M. N. Mitić; J. M. Souquet; M. V. Obradović; S. S. Mitić; *Food Sci. Biotechnol.*, **2012**, *21*, 1619-1626

In memoriam Assoc. Prof. Dr. Marius Sălăjan (1952-2004)

RADIOCARBON DATING OF THE HISTORIC DERBY BOAB TREE FROM DERBY, KIMBERLEY, AUSTRALIA

Adrian PATRUT^{a,b*} , Laszlo RAKOSY^c , Karl F. VON REDEN^d 

ABSTRACT. The paper presents the AMS (accelerator mass spectrometry) radiocarbon dating investigation of the historic Derby Boab Tree from Derby, Kimberley, Australia. This well-known boab (*Adansonia gregorii*) is often considered a prison tree, where Aboriginal prisoners were temporarily incarcerated in its cavity. According to recent research, the Derby Boab Tree was never used as a prison tree. The boab has a closed ring-shaped structure, with 3 perfectly fused stems enclosing a false cavity. A number of six punctiform wood samples, the size of a grain of sand were collected from the cavity door wall. The radiocarbon date of the oldest dated punctiform sample was 1285 ± 21 BP, a value which corresponds to a calibrated age of 1185 ± 20 calendar years. This result indicates that the age of the Derby Boab Tree is 1250 ± 50 years. This is the first accurate dating result of a boab and demonstrates that the species is a millennial angiosperm.

Keywords: AMS radiocarbon dating, *Adansonia gregorii*, dendrochronology, Australia, age determination, false cavity.

^a Babeş-Bolyai University, Faculty of Chemistry and Chemical Engineering, 11 Arany Janos, RO-400028, Cluj-Napoca, Romania.

^b Babeş-Bolyai University, Raluca Ripan Institute for Research in Chemistry, 30 Fantanele, RO-400294 Cluj-Napoca, Romania.

^c Babeş-Bolyai University, Faculty of Biology and Geology, 44 Republicii, RO-400015 Cluj-Napoca, Romania.

^d NOSAMS Facility, Dept. of Geology & Geophysics, Woods Hole Oceanographic Institution, Woods Hole, MA 02543, U.S.A.

* Corresponding author: apatrut@gmail.com



INTRODUCTION

The *Adansonia* genus is classified into the Bombacoideae subfamily of the Malvaceae family, and comprises eight officially recognised species. One species is native to mainland Africa, six to Madagascar, and one can be found solely in northern Australia [1-7].

In 2005, we launched an extensive research program aimed at clarifying several controversial or poorly understood aspects related to the architecture, growth and age of the African baobab (*Adansonia digitata* L.).

Using our original methodology that enables the study and dating of living individuals rather than relying only on demised specimens, we conducted investigations based on AMS (accelerator mass spectrometry) radiocarbon dating of small wood samples. These samples were collected from inner cavities and/or from different areas of the trunk/stems of baobabs [8-21]. Our research revealed that all large African baobabs are multi-stemmed, featuring open and closed ring-shaped structures that allow them to attain old ages and exceptional sizes. We also identified false cavities, which are large natural empty spaces formed between perfectly fused stems that are disposed in a (semi)circular manner, in a so-called closed ring-shaped structure. The age of the oldest African baobabs exceeds 2,000 years old, establishing the African baobab as the longest living angiosperm [10, 11].

In 2013, we expanded our research on the *Adansonia* genus to Madagascar, where we investigated by radiocarbon large individuals of the most representative three *Adansonia* species, namely the fony baobab (*Adansonia rubrostipa* Jum. & H. Perrier), the za baobab (*Adansonia za* Baill.) and the Grandidier baobab (*Adansonia grandidieri* Baill.). These Malagasy species are found in the western and southern parts of the island [23-30].

Eventually, in 2015, we started to investigate superlative specimens of the Australian baobab, commonly known as boab (*Adansonia gregorii* F. Muell.) [4].

Adansonia gregorii is native to the Kimberley region of the Western Australia state and it extends to the closely adjacent parts of the Northern Territory (**Figure 1**). Its most common name is boab, but it had also other names, such as Australian baobab, boabab and baob [4, 31-33].

The Kimberley is the northernmost of the nine regions of the Western Australia state. It has a surface of 424,517 km² and a population of only 34,800 inhabitants. The population is concentrated in the major towns with Aboriginal settlements and scattered homesteads. Around 40% of the population is of Aboriginal descent. According to scientific studies and archaeological discoveries, the Aboriginal occupation of the region began 60,000 years ago [32, 34]. The boab is a prominent symbol in Aboriginal culture, spirituality and history. The stems of many specimens have inscriptions and drawings made by them. Such tree markings are also known as “dendroglyphs” [35].

RADIOCARBON DATING OF THE HISTORIC DERBY BOAB TREE
FROM DERBY, KIMBERLEY, AUSTRALIA

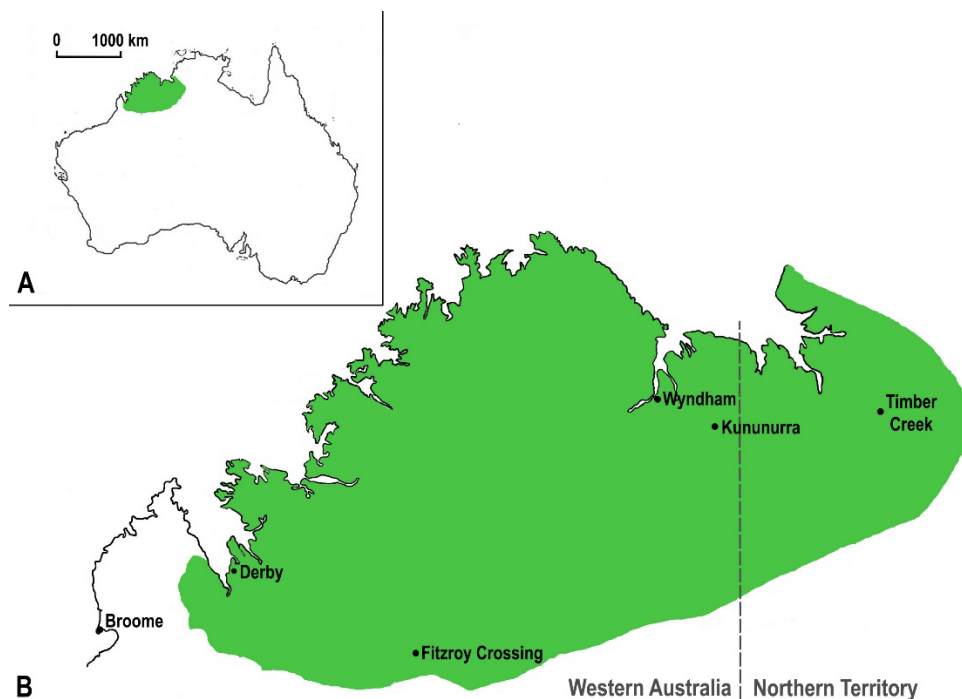


Figure 1. Geographic distribution of the Australian boab (green).

The boabs are concentrated along seasonal waterways and floodplains, suggesting that the presence of groundwater could be important for the species' distribution [32, 33]. Boabs are typically shorter than other *Adansonia* species, with heights between 5-12 m. The bottle-shaped trunks have girth values of 5-10 m for mature individuals. Exceptional specimens can reach heights close to 20 m and circumferences of up to 20 m [32, 33]. The boabs exhibit a very high morphologic variety, which shows that *A. gregorii* is a younger species with a high phenotypic plasticity [32, 36].

There are two gaps in the boab distribution, out of which the plateau gap is the most important, with a length of over 400 km along the Great Northern Highway. The existence of the plateau gap must be associated with two facts: i) the vast majority of boabs are young and very young (probably up to 100-150 yr); ii) the number of old boabs (with ages over 500-600 yr) is very low (probably up to a dozen individuals) for a species with a lifespan of over 1,000 yr [33, 37].

There was probably a critical period for boabs during the Little Ice Age (ca. 1500-1850), which reached a maximum around 1700. In the Northern Hemisphere, the Little Ice Age (LIA) was cold and wet. According to climate

research on baobabs of southern Africa, the LIA was cold and dry, in some areas and wetter in others [21]. The climate of western Australia during the LIA likely saw periods of increased rainfall, particularly in the southern part of the region. Evidence from flood deposits and other climate proxies indicates that while northern Australia experienced drier conditions, the south became wetter during this period. These wetter conditions are recorded in various hydrological studies, including extreme floods during the 1400-1850 period [38].

It is possible that the majority of old boabs have died during the LIA and many mature specimens stopped growing. It was a severe decline of the species across its entire distribution range and the boabs disappeared from the areas with the most severe climate conditions, such as the Kimberley plateau, by producing the gap.

According to the IUCN Red List of Threatened Species, *Adansonia gregorii* is listed as Least Concern, with a stable population [39].

In the case of African and Malagasy baobabs, we collected wood samples with long increment borers (from 0.60 to 1.50 m), out of which we extracted tiny segments, each 5×10^{-3} m long with a weight of 5×10^{-4} kg, for AMS radiocarbon dating. For boabs, we extracted for dating punctiform wood samples of the size of a grain of sand. This new methodology is described in the Experimental section.

Here we present the AMS radiocarbon dating results and the investigation of the historic Derby Boab Tree.

RESULTS AND DISCUSSION

The Derby Boab Tree and its area. Derby is a town in the Kimberley region of Western Australia. It was founded in 1883, when the new pastoral industry required a port from which to ship the wool. Derby has the highest tides in Australia, with a difference of 11.8 m between high and low tide. The population is 3,300, out of which over 40% are of Aboriginal descent. Derby is characterized by a hot semi-arid climate (*BSh* in Köppen classification), with a short wet season lasting from late December to March. The area in which the baobab grows has a mean annual temperature of 27°C and its mean yearly rainfall is 622 mm [34].

The Derby Boab Tree, which resembles a barrel in shape, grows on the outskirts of Derby, 6 km south of the town, at the end of a 0.5 km deviation towards east. The trunk is completely furrowed with deep signs and inscriptions carved by locals and tourists.

The indigenous people considered the Derby Boab Tree as a significant landmark before European settlement, calling it Kunumudj.

RADIOCARBON DATING OF THE HISTORIC DERBY BOAB TREE
FROM DERBY, KIMBERLEY, AUSTRALIA

The first photograph of the Derby Boab Tree dates back to 1916 and was captioned on glass plate by Herbert Basedow (**Figure 2**).



Figure 2. The first photograph of the Derby Boab Tree taken by Basedow in 1916.

The GPS coordinates of the Derby Boab Tree are 17°21.043' S, 123°43.191' E and the altitude of its location is 29 m. The height of the boab is 8.20 m (above the cavity level). The measured circumference revealed a value of 13.79 m at breast height (cbh, i.e. at 1.30 m above mean ground level), while at 2.03 m above ground it reached 14.40 m (**Figure 3**).



Figure 3. General view of the Derby Boab Tree as taken from the east.

The boab has a closed ring-shaped structure, with a ring of 3 perfectly fused stems around a false cavity which was never filled with wood.

The false inner cavity reaches a height of 3.90 m, with its base at 0.77 m under the ground level (Figure 4). The interior of the cavity has the following dimensions: 1.51 (WE) x 2.29 m (NS) (at the base: ground level – 0.77 m); 2.50 (WE) x 2.69 m (NS) (at the cavity door level: ground level + 0.10 m); 2.98 (WE) x 3.76 m (NS) (ground level + 2.20 m). The cavity door has a height of 1.60 m and a maximum width of 0.47 m. The side walls of the cavity door measure 0.45 m (to the left of the entrance) and 0.40 m (to the right of the entrance). The thickness of the trunk bark is between 0.05-0.15 m.

RADIOCARBON DATING OF THE HISTORIC DERBY BOAB TREE
FROM DERBY, KIMBERLEY, AUSTRALIA



Figure 4. The image shows the base of the false cavity of Derby Boab Tree.

The canopy has several large branches, and its horizontal dimensions are 14.4 (NS) x 14.8 (WE) m. The overall volume of the tree is 60 m³ (trunk and branches, including the false cavity).

The trunk and also the primary branches, which show tears and gaps, appear to be very old. However, according to the photos, the boab has not changed its appearance over the last hundred years.

The Derby Boab Tree is also frequently named Derby Prison Tree, Boab Prison Tree or Derby Boab Prison Tree. These names are associated with the Prison tree myth and with the conceptual framework of Dark Tourism. The Derby Boab Tree is a major attraction for tourists, who visit it each year by the thousands. It is presented as a major historic site, where Aboriginal prisoners, chained by the neck, were temporarily incarcerated in its hollow trunk by colonial police en route to the townships [34].

Officially signposted as a prison tree, the site of the Derby Boab Tree has undergone several upgrades over the years, becoming a major Kimberley tourism attraction. The concept of Dark Tourism is applied to tourism sites associated with death, crime and destruction, including 'dark dungeons', such as former courthouses or prisons.

New research by the academics Elisabeth Grant and Kristyn Harman, which were published in 2017 challenges the claim that the Derby Boab Tree once served as a temporary prison for Aboriginal captives. The authors contend that there is insufficient evidence to support the notion that the tree was ever used as a prison. They suggest that the belief in its use as an overnight holding cell for Aboriginal prisoners during the colonial 1890s stems from misinformation and that the rise of dark tourism has fueled this growing myth [34]

However, the site was listed as protected in 1999 under the Aboriginal Heritage Act of 1972. A fence and sign were erected around the tree to protect it from excessive human traffic, carvings and compacting of surrounding soil by vehicles. However, many tourists are still posing within the perimeter sign and inside the cavity [34].

Wood samples. Six punctiform wood samples of the size of a grain of sand, weighing each around 10^{-6} kg (0.001 g), were collected from the right side wall of the cavity door at a height of 1.35 m. At this height, the width of the right side wall of the cavity door (inside bark) is 0.40 m. The samples are labelled from 1 to 6.

AMS results and calibrated ages. Radiocarbon dates of the six punctiform samples are listed in Table 1. The radiocarbon dates are expressed in ^{14}C yr BP (radiocarbon years before present, i.e., before the reference year 1950). Radiocarbon dates and errors were rounded to the nearest year.

Calibrated (cal) ages, expressed in calendar years CE (CE, i.e., common era), are also displayed in Table 1. The 1σ probability distribution (68.3%) was selected to derive calibrated age ranges. For one sample (DBT-2), the 1σ distribution corresponds to one range of calendar years. Instead, for two samples (DBT-4, DBT-5) the 1σ distribution corresponds to two ranges, for three samples (DBT-1, DBT-6) it is consistent with three ranges, while for one sample (DBT-3) it corresponds to four ranges. In these cases, the confidence interval of one range is considerably greater than that of the others; therefore, it was selected as the cal CE range of the sample for the purpose of this discussion.

For obtaining single calendar age values of samples, we derived a mean calendar age of each sample, called assigned year, from the selected range (marked in bold). Sample ages represent the difference between the year 2024 CE and the assigned year, with the corresponding error. Sample ages and errors were rounded to the nearest 5 yr.

RADIOCARBON DATING OF THE HISTORIC DERBY BOAB TREE
FROM DERBY, KIMBERLEY, AUSTRALIA

This approach for selecting calibrated age ranges and single values for sample ages was used in all our previous articles on AMS radiocarbon dating of large and old angiosperm trees.

Dating results of punctiform samples. As mentioned, the tri-stemmed Derby Boab Tree exhibits a closed ring-shaped structure, that consists of a ring of three perfectly fused stems disposed around a false cavity. This false cavity represents an empty space that was never filled with wood and is covered by bark. Over time, stem growth determines the false cavities to become progressively smaller. Even more, false cavities may close completely or incompletely, by maintaining a small opening/door. In such cases, the age sequence of samples extracted from the cavity walls shows a continuous increase up to a certain depth into the wood, after which it decreases toward the exterior. Research revealed that the oldest part of the fused stems is found between the false cavity walls and the outer part (exterior) of each stem, being always closer to the cavity than the exterior [10].

Table 1. AMS Radiocarbon dating results and calibrated ages of punctiform samples collected from the Derby Boab Tree

Sample code	Distance from cavity wall / from exterior [height] (m)	Radiocarbon date [error] (¹⁴ C yr BP)	Cal CE range 1σ [confidence interval]	Assigned year [error] (cal CE)	Sample age [error] (cal CE)
DBT-1	0.01 / 0.39 [1.35]	210 [± 18]	1672-1685 [13.5%] 1732-1782 [46.9%] 1797-1805 [7.9%]	1777 [± 25]	245 [± 25]
DBT-2	0.08 / 0.32 [1.35]	445 [± 20]	1450-1486 [68.3%]	1468 [± 18]	555 [± 20]
DBT-3	0.17 / 0.23 [1.35]	1285 [± 21]	690-704 [10.2%] 718-737 [12.7%] 787-797 [5.9%] 819-855 [39.6%]	837 [± 18]	1185 [± 20]
DBT-4	0.24 / 0.16 [1.35]	930 [± 18]	1153-1188 [56.8%] 1197-1209 [11.5%]	1170 [± 17]	855 [± 15]
DBT-5	0.32 / 0.08 [1.35]	352 [± 17]	1510-1584 [63.8%] 1625-1628 [4.5%]	1757 [± 37]	265 [± 35]
DBT-6	0.39 / 0.01 [1.35]	151 [± 19]	1698-1723 [16.6%] 1834-1891 [35.3%] 1924-... [16.4%]	1862 [± 28]	160 [± 30]

The oldest investigated punctiform sample DBT-3 originated from a depth of 0.17 m from the cavity walls and 0.23 m from the exterior. Its radiocarbon date of 1285 ± 21 BP corresponds to a calibrated age of 1185 ± 20 calendar yr.

The two youngest samples, DBT-1 and DBT-6, were extracted from wood layers adjacent to the false cavity (DBT-1) and to the external bark (DBT-6). Their radiocarbon dates of 210 ± 18 BP and 151 ± 19 BP correspond to calibrated ages of 245 ± 25 and 160 ± 30 calendar yr. These values demonstrate that the stem which corresponds to the right side of the cavity door stopped growing around 245 yr ago from the false cavity and 160 yr ago toward the exterior, due to old age.

The other three punctiform samples, DBT-2, DBT-4 and DBT-5, have intermediary radiocarbon dates and calibrated ages between the oldest sample DBT-3 and the youngest samples DBT-1 and DBT-6.

Age of the Derby Boab Tree. The age of the stem corresponding to the right side of the cavity door was determined by extrapolating the age of the oldest punctiform sample DBT-3 to the point of maximum age at sampling height. The oldest dated sample DBT-3 had a calibrated age of 1185 ± 20 calendar yr, and it was extracted from a depth of 0.17 m into the cavity walls, at 0.23 m from the corresponding exterior of the tree. This point, must also be very close to the point of maximum age. We consider that the stem is between 1200 -1300 old, i.e. its age is of 1250 ± 50 years.

According to our research, for baobabs with a closed ring-shaped structure and a quasi-spherical or cylindrical trunk, the stems that build the ring have close or identical ages. Thus, the age of the investigated stem can also be considered as the age of the Derby Boab Tree.

CONCLUSIONS

The study reports the AMS radiocarbon investigation results of the historic Derby Boab Tree from Derby, Kimberley, Australia. The tree is usually presented as a prison tree, where chained Aboriginal prisoners were temporarily incarcerated in its hollow trunk by colonial police. However, according to recent research, there is no evidence to support the myth that the Derby boab was ever used as a prison tree. The boab has a closed ring-shaped structure that comprises three perfectly fused stems around an empty space called false cavity, a common feature among very large individuals of the *Adansonia* genus. Six punctiform samples were collected from the cavity door, by using a novel methodology. The oldest dated punctiform sample had

RADIOCARBON DATING OF THE HISTORIC DERBY BOAB TREE
FROM DERBY, KIMBERLEY, AUSTRALIA

a radiocarbon date of 1285 ± 21 BP, which corresponds to a calibrated age of 1185 ± 20 calendar years. This result shows that the Derby Boab Tree is 1250 ± 50 years old. It can be stated that the Derby Boab Tree started growing around 775 CE.

EXPERIMENTAL SECTION

Sample collection. The punctiform wood samples were extracted in a non-invasive manner from predetermined positions with a stainless steel pair of tweezers. The extracted punctiform sample was introduced in a small conical aluminium tube for preventing contamination. Next, the punctiform sample was pretreated and investigated by AMS. The AMS, which counts directly C-14 atoms, needs less than 10^{-6} kg (0.001 g) wood for an accurate dating.

Sample preparation. The modified α -cellulose extraction method was used for removing soluble and mobile organic components [40]. The pretreated samples were combusted to CO_2 by using the closed tube combustion method [41]. Next, CO_2 was reduced to graphite on iron catalyst [42]. Eventually, the resulting graphite samples were investigated by AMS.

AMS measurements. AMS radiocarbon measurements were performed at the NOSAMS Facility of the Woods Hole Oceanographic Institution (Woods Hole, MA, U.S.A.), by using the Pelletron ® Tandem 500 kV AMS system. The obtained fraction modern values, corrected for isotope fractionation with the normalized $\delta^{13}\text{C}$ value of -25‰ , were converted to a radiocarbon date.

Calibration. Radiocarbon dates were calibrated and converted into calendar ages with the OxCal v4.4 for Windows [43], by using the SHCal20 atmospheric data set [44].

ACKNOWLEDGEMENTS

The research was funded by the Romanian Ministry of Research CNCS-UEFISCDI under grants PN-II-ID-PCE-2013-76 and PN-III-P4-ID-PCE-2020-2567, No. 145/2021. Authors thank Susan O'Connor and Jack Pettigrew for useful discussions about boabs and the Derby Boab Tree.

REFERENCES

1. G.E. Wickens, *Kew Bulletin*, **1982**, 37(2), 172-209.
2. D.A. Baum, *Annals of the Missouri Botanical Garden*, **1995**, 82, 440-471.
3. G.E. Wickens, P. Lowe, "The Baobabs: Pachycauls of Africa, Madagascar and Australia", Springer, Dordrecht, **2008**.
4. P. Lowe, "The Boab Tree", Lothion, Port Melbourne, Victoria, **1998**.
5. J.D. Pettigrew, L.K. Bell, A. Bhagwandin, E. Grinan, N. Jillani, J. Meyer, E. Wabuyele, C.E. Vickers, *Taxon*, **2013**, 61, 1240-1250.
6. A. Petignat, L. Jasper, "Baobabs of the world: The upside down trees of Madagascar, Africa and Australia", Struik Nature, Cape Town, **2015**.
7. G.V. Cron, N. Karimi, K.L. Glennon, C.A. Udeh, E.T.F. Witkowski, S.M. Venter, A.E. Assobadjo, D.H. Mayne, D.A. Baum, *Taxon*, **2016**, 65, 1037-1049.
8. A. Patrut, K.F. von Reden, D.A. Lowy, A.H. Alberts, J.W. Pohlman, R. Wittmann, D. Gerlach, L. Xu, C.S. Mitchell, *Tree Physiology*, **2007**, 27, 1569-1574.
9. A. Patrut, K.F. von Reden, R. Van Pelt, D.H. Mayne, D.A. Lowy, D. Margineanu, *Annals of Forest Science*, **2011**, 68, 93-103.
10. A. Patrut, S. Woodborne, R.T. Patrut, L. Rakosy, D.A. Lowy, G. Hall, K.F. von Reden, *Nature Plants*, **2018**, 4(7), 423-426.
11. A. Patrut, K.F. von Reden, D.H. Mayne, D.A. Lowy, R.T. Patrut, *Nuclear Instruments and Methods in Physics Research Section B*, **2013**, 294, 622-626.
12. A. Patrut, S. Woodborne, K.F. von Reden, G. Hall, M. Hofmeyr, D.A. Lowy, R.T. Patrut, *PLOS One*, **2015**, 10(1), e0117193.
13. A. Patrut, L. Rakosy, R.T. Patrut, I.A. Ratiu, E. Forizs, D.A. Lowy, D. Margineanu, K.F. von Reden, *Studia UBB Chemia*, **2016**, LXI, 4, 7-20.
14. A. Patrut, R.T. Patrut, L. Rakosy, D.A. Lowy, D. Margineanu, K.F. von Reden, *Studia UBB Chemia*, **2019**, LXIV, 2 (II), 411-419.
15. A. Patrut, S. Woodborne, K. F. von Reden, G. Hall, R.T. Patrut, L. Rakosy, P. Danthu, J-M. Leong Pock-Tsy, D.A. Lowy, D. Margineanu, *Radiocarbon*, **2017**, 59(2), 435-448.
16. A. Patrut, S. Woodborne, R.T. Patrut, G. Hall, L. Rakosy, C. Winterbach, K.F. von Reden, *Forests*, **2019**, 10, 983-994.
17. A. Patrut, R.T. Patrut, M.J. Slater, L. Rakosy, D.A. Lowy, K.F. von Reden, *Studia UBB Chemia*, **2020**, LXV, 3, 149-156.
18. A. Patrut, A. Garg, S. Woodborne, R.T. Patrut, L. Rakosy, I.A. Ratiu, D.A. Lowy, *PLoS ONE*, **2020**, 15(1), e0227352.
19. A. Patrut, R.T. Patrut, L. Rakosy, I.A. Ratiu, D.A. Lowy, K.F. von Reden, *Dendrochronologia* **2021**, 70, 125898.
20. A. Patrut, R.T. Patrut, W. Oliver, I.A. Ratiu, D.A. Lowy, G. Shiimbi, L. Rakosy, D. Rakosy, S. Woodborne; K.F. von Reden, *Forests*, **2022**, 13, 1899.
21. R.T. Patrut, A. Patrut, G. Hall, C.W. Winterbach, I. Robertson, I.A. Ratiu, V. Bocos-Bintintan, L. Rakosy, S. Woodbourne, *Forests*, **2023**, 14, 1917.

RADIOCARBON DATING OF THE HISTORIC DERBY BOAB TREE
FROM DERBY, KIMBERLEY, AUSTRALIA

22. A. Patrut, R.T. Patrut, M. Molnar, L.S. Al Harthy, J.J. Brown, L. Rakosy, K.A. Al Farsi, A.R. Al Hinai, I.A. Ratiu, J. Bodis, *Studia UBB Chemia*, **2020**, *LXIX*, 2, 109-120.
23. A. Patrut, K.F. von Reden, P. Danthu, J-M. Leong Pock-Tsy, R.T. Patrut, D.A. Lowy, *PLOS One*, **2015**, *10*(3), e0121170.
24. R.T. Patrut, A. Patrut, J-M Leong Pock-Tsy, S. Woodborne, L. Rakosy, P. Danthu, I.A. Ratiu, J. Bodis, K.F. von Reden, *Studia UBB Chemia*, **2019**, *LXIV*, 4, 131-39.
25. A. Patrut, R.T. Patrut, J-M. Leong Pock-Tsy, S. Woodborne, L. Rakosy, I.A. Ratiu, J. Bodis, P. Danthu, *Studia UBB Chemia*, **2020**, *LXV*, 4, 151-158.
26. A. Patrut, R.T. Patrut, J-M. Leong Pock-Tsy, P. Danthu, S. Woodborne, L. Rakosy, I.A. Ratiu, *Forests*, **2021**, *12*, 1258.
27. A. Patrut, K.F. von Reden, P. Danthu, J-M. Leong Pock-Tsy, R.T. Patrut, D.A. Lowy, *PLoS ONE*, **2015**, *10*(3), e0121170.
28. A. Patrut, R.T. Patrut, P. Danthu, J-M. Leong Pock-Tsy, L. Rakosy, D.A. Lowy, K.F. von Reden, *PLOS One*, **2016**, *11*(1), e146977.
29. A. Patrut, R.T. Patrut, L. Rakosy, I.A. Ratiu, P. Danthu, J-M. Leong Pock-Tsy, K.F. von Reden, *Studia UBB Chemia*, **2023**, *LXVIII*, 1, 119-129.
30. A. Patrut, R.T. Patrut, J-M. Leong Pock-Tsy, L. Rakosy, P. Danthu, I.A. Ratiu, J. Bodis, S. Woodbourne, *Studia UBB Chemia*, **2023**, *LXVIII*, 3, 141-151.
31. D.M.J.S. Bowman, *Australian Journal of Botany*, **1997**, *45*, 893-904.
32. C. Done, *Bois et Forêts des Tropiques*, **2010**, *306*(4), 17-22.
33. K. L. Bell, H. Rangan, R. Fowler, R. Fowler, C.A. Kull, J. Pettigrew, C.E. Vicker, D. J. Murphy, *Australian Journal of Botany*, **2014**, *62*(2), 164-174.
34. E. Grant, K. Harman, "Inventing a colonial dark history: the Derby Boab 'Prison' Tree", in J. Wilson, S. Hodgkinson, J. Piché, K. Walby (eds.) "Palgrave Handbook of Prison Tourism", Palgrave MacMillan, London, **2017**, pp.735-759.
35. S. O'Connor, J. Balme, U. Frederick, B. Garstone, R. Bedford, J. Bedford, A. Rivers, A. Bedford, D. Lewis, *Antiquity*, **2022**, 1-18.
36. J. Deane, "Histress: Boabographies", Vocational Education & Training, Osborne Park, WA, **2008**.
37. H. Rangan, K.L. Bell, D.A. Baum, R. Fowler, P. McConvell, T. Saunders, S. Spronck, K.A. Kull, D.J. Murphy, *PLoS ONE*, **2015**, *10*(4), e0119758.
38. H.N. Pollack, S. Huang, J.E. Smerdon, *Journal of Quaternary Science*, **2006**, *21*, 701-706.
39. IUCN. 2019. The IUCN Red List of Threatened Species. Version 2024-1.
40. N.J. Loader, I. Robertson, A.C. Barker, V.R. Switsur, J.S. Waterhouse, *Chemical Geology*, **1997**, *136*(3), 313-317.
41. Z. Sofer, *Analytical Chemistry*, **1980**, *52*(8), 1389-1391.
42. J.S. Vogel, J.R. Southon, D.E. Nelson, T.A. Brown, *Nuclear Instruments and Methods in Physics Research Section B*, **1984**, *5*, 289-293.
43. C. Bronk Ramsey, *Radiocarbon*, **2009**, *51*, 337-360.
44. A.G. Hogg, T.J. Heaton, Q. Hua, J.G. Palmer, C.S.M. Turney, J. Southon, A. Bayliss, P.G. Blackwell, G. Boswijk, C.B. Ramsey, C. Pearson, F. Petchey, P.J. Reimer, R.W. Reimer, L. Wacher, *Radiocarbon*, **2020**, *62*(4), 759-778.

VALUATION OF THE ENERGY POTENTIAL OF AGROZOOTEHNIC WASTE

Roxana MITROI^a , Cristina Ileana COVALIU-MIERLĂ^a ,
Cristina-Emanuela ENĂȘCUȚĂ^b , Grigore PSHENOVSCHI^b,
Iuliana DELEANU^c 

ABSTRACT. The anaerobic digestion of animal manure is a promising treatment solution allowing its partial conversion to energy, in the form of biogas. Anaerobic digestion technology is thus considered not only as a way to solve environmental problems, but also as a potential source of energy, while also contributing to solving economic and social problems.

This research investigates the potential of poultry, cattle and pig wastes for biogas production through the anaerobic digestion process. A number of 15 recipes had been prepared and studied, each consisting of a mixture of organic materials with a concentration of 10% total solids (animal waste, vegetable waste, food waste), in different proportions. The raw material mixtures (representing the substrates) respected a C/N ratio between 15 and 25. The substrate composition influence on the production of biogas was investigated. Different types of animal manure have been found to produce varying rates of biogas, with certain types yielding higher or more stable levels. In this installation, efficient biogas production was observed after seven days of anaerobic digestion, with the most effective mixtures being those with a higher proportion of grass.

Keywords: animal waste, organic waste, anaerobic digestion, biogas, agro-food byproducts.

^a University Politehnica of Bucharest, Faculty of Biotechnical Systems Engineering, 313 Splaiul Independenței, 060042, Bucharest, Romania.

^b National Institute for Research & Development in Chemistry and Petrochemistry – ICECHIM, 202 Spl. Independenței, 060021, Bucharest, Romania.

^c University Politehnica of Bucharest, Faculty of Chemical Engineering and Biotechnologies, 313 Splaiul Independenței, 060042, Bucharest, Romania

* Corresponding author: cristina_covaliu@yahoo.com



INTRODUCTION

Biogas can be generated in many ways, using different materials as substrates: plants, trees, grass, seeds, fruit and vegetable solid wastes, animal farm manure, algae, sludge, sewage, agri-food wastes and even urban solid organic materials (household wastes) [1, 2]. Table 1 presents typical examples of raw materials used in anaerobic digestion (AD) processes.

Table 1. Raw materials used in the anaerobic digestion process [3]

Waste	Types of waste
Agricultural waste and crop residues	Straws, green grass, potatoes, etc
Animal manure	Cattle, pig, and poultry manure

The AD process (anaerobic fermentation) is one of the most suitable for organic materials (wastes) valorization. It consists in a sequence of biological processes, in which the biodegradable part of the substrate is broken down into simple products, in the presence of bacteria. Overall, the process follows four slightly distinct steps of fermentation: hydrolysis, acidogenesis, acetogenesis and methanogenesis, occurring simultaneously in an oxygen free medium (Figure 1A). Each stage is well defined by specific chemical reactions (Figure 1B).

The final product is biogas (a mixture of gases, mainly methane and carbon dioxide) and digestate as byproduct (or sludge, as can be seen in Figure 1A). The amount of biogas that can be theoretically obtained from different substrates can be estimated using Buswell approximate equation taking elementary composition into account [4]:

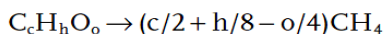


where

$$x = 0.125(4c + h - 2o - 3n + 2s)$$

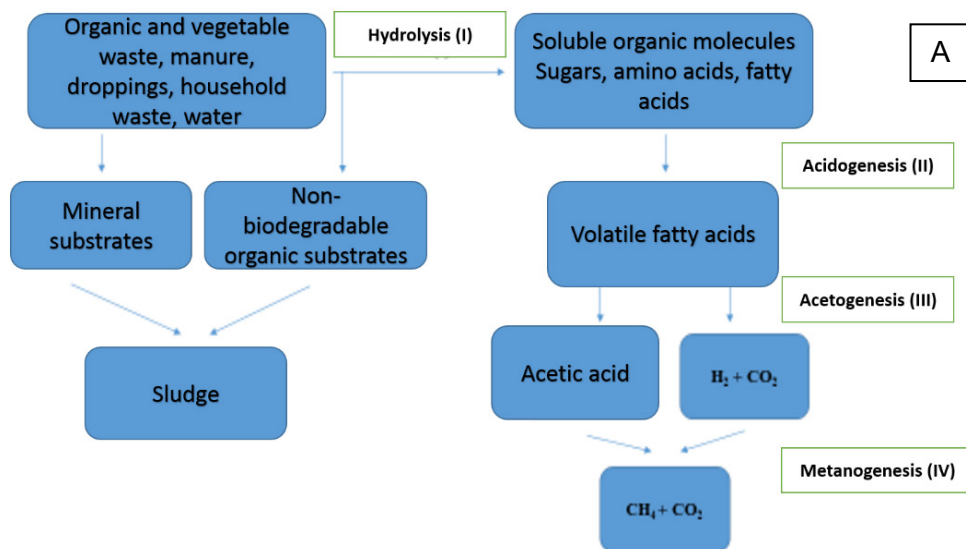
$$y = 0.250(4c - h - 2o + 3n + 2s)$$

or, simplified



For instance, carbohydrate is represented by $C_6H_{12}O_6$, fat by $C_{16}H_{32}O_2$, and protein by $C_6H_{10}O_2$ characterizing formulas.

VALUATION OF THE ENERGY POTENTIAL OF AGROZOOTEHNIC WASTE



AD Phase	Associated Chemical Reactions
Hydrolysis	$C_6H_{10}O_4 + 2H_2O \rightarrow C_6H_{12}O_6 + 2H_2$
	$C_6H_{12}O_6 \leftrightarrow 2CH_3CH_2OH + 2CO_2$
	$C_6H_{12}O_6 + 2H_2 \leftrightarrow 2CH_3CH_2COOH + 2H_2O$
Acidogenesis	$C_6H_{12}O_6 \rightarrow 3CH_3COOH$
	$C_3H_7O_2N + 2H_2O \rightarrow C_2H_4O_2 + NH_3 + CO_2 + 2H_2 + ATP$
	$C_4H_9O_3N + H_2O \rightarrow C_3H_6O_2 + NH_3 + CO_2 + H_2 + ATP$
	$4CH_3COCOO^- + 4H_2O \rightarrow 5CH_3COO^- + 2HCO_3^- + 3H^+$
Acetogenesis	$CH_3CH_2COO^- + 3H_2O \leftrightarrow CH_3COO^- + H^- + HCO_3^- + 3H_2$
	$C_6H_{12}O_6 + 2H_2O \leftrightarrow 2CH_3COOH + 2CO_2 + 4H_2$
	$CH_3CH_2OH + 2H_2O \leftrightarrow CH_3COO^- + 2H_2 + H^-$
Methanogenesis	$CH_3COOH \rightarrow CH_4 + CO_2$
	$CO_2 + 4H_2 \rightarrow CH_4 + 2H_2O$
	$2CH_3CH_2OH + CO_2 \rightarrow CH_4 + 2CH_3COOH$

Figure 1. A) Pathways for biomass conversion into biogas; **B)** Chemical reactions in anaerobic digestion (AD) phases [5]

Organic wastes are rich in carbohydrates, proteins and fats, which are important energy sources and generate considerable amounts of methane in biogas [6], as can be seen in Figure 1A.

Animal manure, in particular, is suitable for anaerobic digestion for several reasons: it has a high-water content, which facilitates the dilution of concentrated by-products and simplifies the pumping process; it has a high buffering capacity, essential to prevent sudden fluctuations in the pH value; and contain a wide range of nutrients necessary for the development of microorganisms [7]. Poultry manure however, has a low availability of nutrients, which makes regular supplementation with carbon sources necessary to ensure a stable and efficient anaerobic digestion process and therefore the exclusive use of poultry manure is not recommended, because the anaerobic fermentation process will be slow and will not produce a high yield of biogas [8]. However, this disadvantage can be compensated by co-digestion with other raw materials.

In this work was chosen to explore complex substrate compositions, including poultry, cattle, and pig waste, given the limited number of studies addressing the use of various animal wastes in a single digester. Thus, the main objective of the research is the development of an optimal mixture of animal manure and agro-food by-products to obtain high yield biogas conversions. Higher biogas production minimizes methane emissions into the atmosphere and contributes to a net reduction in greenhouse gas emissions [1,9].

The process of obtaining biogas through anaerobic digestion is a focus of research and is considered the best solution for managing animal waste, transforming organic waste into green energy and organic fertilizer for agriculture.

Since the topic of obtaining biogas is very current, I noticed that in the specialized literature only mixtures of organic matter with animal wastes that come from a single category of animals are presented, which is why I chose to study some waste mixtures that to lead to higher biogas yields than in the specialized literature, using both poultry manure, cattle manure, and pig manure in the same digester.

RESULTS AND DISCUSSION

As shown before, the complex process of AD is typically described as comprising four main stages: hydrolysis, acidogenesis, acetogenesis, and methanogenesis. Initially, lipids, carbohydrates, and proteins are broken down by fermentative bacteria into smaller components and soluble organic

substrates, such as fatty acids, glucose, and amino acids. This step is often the rate-limiting factor in the AD of solid organic wastes, and various pre-treatment methods, including mechanical grinding, ultrasound, microwave, thermal, chemical, and biological treatments, have been proposed to enhance hydrolysis. In the second stage, the intermediate compounds are converted into volatile fatty acids (VFAs) like acetate, propionate, and butyrate, along with by-products such as NH_3 , CO_2 , and H_2S . In the next stages, VFAs are further digested into acetate, H_2 , and CO_2 , which serve as precursors for the production of CH_4 and CO_2 by methanogens [10].

The 15 experiments that were conducted had as a substrate a complex mixture of organic materials with a concentration of 10% solids (animal waste, vegetable waste, food waste) based on the same materials, but in different proportions to see how the composition influences the production of biogas.

In order for the distribution of anaerobic bacteria to be uniform throughout the substrate, and to achieve the anaerobic co-digestion process, we combined several substrates with 40 g of the inoculum and then we introduced them into the fermentation reactors, having a useful volume of 400 g, as can be seen in Table 2.

The raw material mixtures respected a C/N ratio between 15 and 25.

The reactor uses the technique of continuous stirring in the fermentation process in order to maintain a constant and uniform movement of the mixture of substances. Thus, the uniform distribution of nutrients, or other essential elements in the fermentation solution is ensured.

In the sample incubation unit, up to 15 test vessels containing small amounts of a sample with appropriate microbial inoculum were incubated at the desired temperature in a thermostatic water bath.

In the gas absorption unit, the gas produced in each flask passes through an individual vessel containing a solution that can absorb certain fractions of the gas, undesired in biogas. In this case the produced gas was directed through an alkaline solution. Several gas fractions were retained through chemical interaction with the solution: when the alkaline solution like NaOH here is used, acidic fractions like CO_2 and H_2S are retained. Only CH_4 (and remaining traces such as H_2) will then proceed to the gas monitoring unit. A pH indicator was added to each vessel to monitor the acid-binding capacity of the solution.

In the gas volume measurement device, the volume of gas released from the incubation unit or from the gas absorption unit was measured using a wet gas flow meter with a multi-cell arrangement (15 cells). This measurement device operates on the principle of liquid displacement and buoyancy, and it can monitor ultra-low gas flow rates. A digital pulse is generated when a defined volume of gas flows through the device (2 ml or 9 ml, depending on the chosen resolution). An integrated data acquisition system is used to record, display, and analyze the results [11].

Table 2. Experiment Composting with Green Grass, Potatoes, and Wheat Straw

Exp.	Raw material (g)							
	Grass	Potatoes	Straw	Pig	Cattle	Poultry	Inoculum	Total
EXP 1	20.00	20.00	0.00	70.39	23.53	53.79	212.29	400.00
EXP 2	40.00	10.00	0.00	70.39	23.53	53.79	202.29	400.00
EXP 3	50.00	20.00	0.00	70.39	23.53	53.79	182.29	400.00
EXP 4	60.00	10.00	0.00	16.00	17.14	12.63	284.23	400.00
EXP 5	70.00	10.00	0.00	12.00	17.14	12.63	278.23	400.00
EXP 6	60.00	20.00	0.00	12.00	17.14	12.63	278.23	400.00
EXP 7	50.00	30.00	0.00	12.00	17.14	12.63	278.23	400.00
EXP 8	40.00	40.00	0.00	12.00	17.14	12.63	278.23	400.00
EXP 9	45.00	35.00	0.00	12.00	17.14	12.63	278.23	400.00
EXP 10	45.00	25.00	10.00	12.00	17.14	12.63	278.23	400.00
EXP 11	20.00	10.00	10.00	70.39	23.53	53.79	212.29	400.00
EXP 12	50.00	10.00	10.00	16.00	17.14	12.63	284.23	400.00
EXP 13	60.00	10.00	10.00	12.00	17.14	12.63	278.23	400.00
EXP 14	30.00	30.00	20.00	12.00	17.14	12.63	278.23	400.00
EXP 15	50.00	0.00	20.00	12.00	17.14	12.63	288.23	400.00

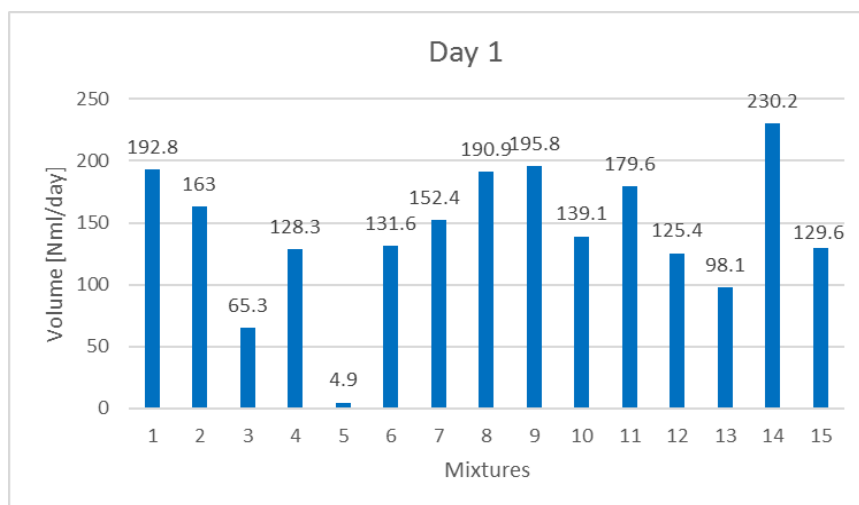


Figure 2. Results of biogas experiments generated using a mixture of pig manure, poultry manure, cattle manure, green grass, potatoes and straw, Volume [Nm³] – Day 1

On the first day of anaerobic digestion, experiment no. 14 generated the largest volume of biogas, which had as raw material: green grass 30 g, potatoes 30 g, straw 20 g, pig manure 12 g, cattle manure 17.14 g and poultry manure 12.63 g.

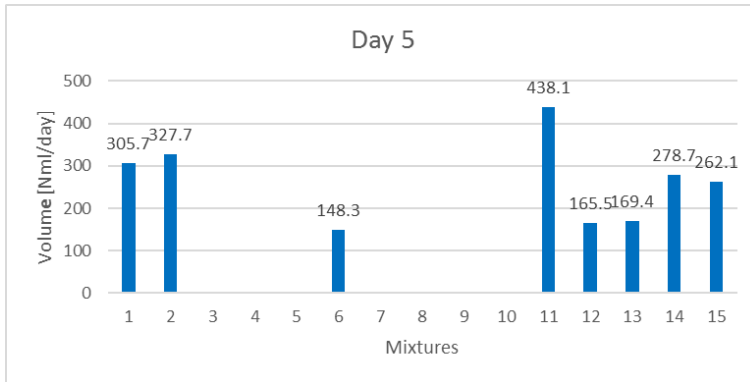


Figure 3. Results of biogas experiments generated using a mixture of pig manure, poultry manure, cattle manure, green grass, potatoes and straw, Volume [NmL] – Day 5

A low rate of biogas production was observed after the fifth day of anaerobic digestion, indicating that the anaerobic digestion was largely complete after this period. The maximum level of biogas was obtained after 5 days of anaerobic digestion.

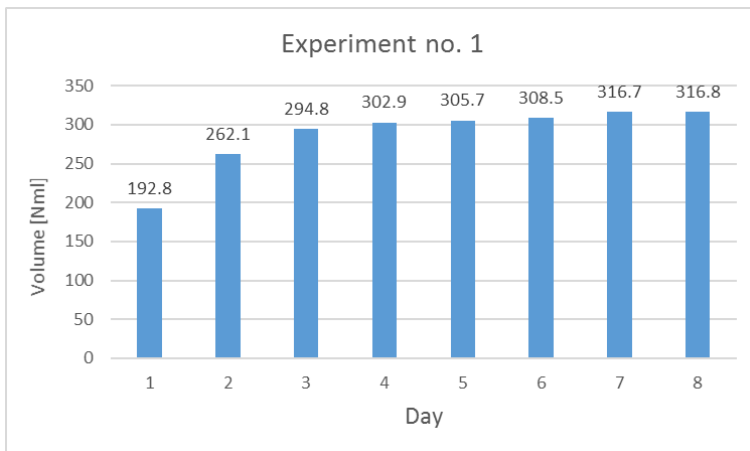


Figure 4. Results of experiment no. 1 biogas generated, using a mixture of pig manure 70.39 g, poultry manure 53.79 g, cattle manure 23.53 g, green grass 20 g, potatoes 20 g, Volume [NmL]

Starting with the sixth day of biogas production, the laboratory experiment recorded a decrease in the volume of biogas generated.

The highest volume of biogas generated was recorded in experiment no. 1 which consisted of a mixture of green grass 20 g, potatoes 20 g, pig manure 70.39 g, cattle manure 23.53 g, poultry manure 53.79 g, inoculum 212.29 g, followed by experiment no. 2 which it consisted of a mixture of green grass 40 g, potatoes 10 g, pig manure 70.39 g, cattle manure 23.53 g, poultry manure 53.79 g and inoculum 202.29 g.

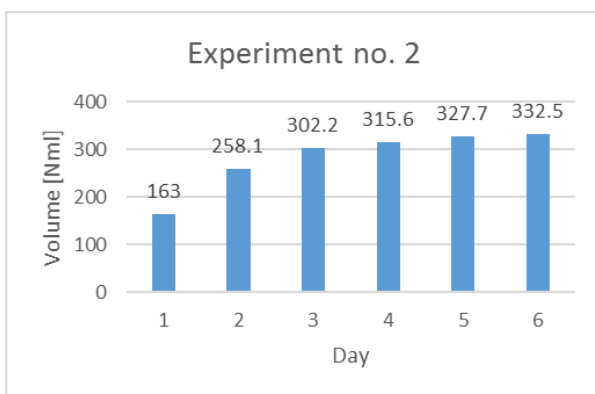


Figure 5. Results of experiment no. 2 biogas generated, using a mixture of pig manure 70.39 g, poultry manure 53.79 g, cattle manure 23.53 g, green grass 40 g, potatoes 10 g, Volume [Nm³]

The level of biogas generated recorded the highest flow on the first day of anaerobic digestion, then started to decrease in the following days.

The highest flow of biogas generated by experiment no. 1 consisted of a mixture of green grass 20 g, potatoes 20 g, pig manure 70.39 g, cattle manure 23.53 g, poultry manure 53.79 g, inoculum 212.29 g was recorded on the first day, having the value of 192.75 m³/day for the substrate with green grass and potatoes.

The observation that mixtures containing green grass generated a higher volume of biogas than those also containing wheat straw may be the result of differences in the chemical composition and degradation characteristics of these materials. Green grass may have a higher content of fermentable substances, such as carbohydrates and other water-soluble components, which are more easily accessible to the microorganisms involved in the anaerobic digestion process. This can lead to more efficient decomposition and higher biogas production. In contrast, wheat straw contains higher amounts of components that are more resistant to degradation. These components, such as lignin [12], may

require more extensive degradation conditions or more intense microbial activity to be fully broken down, which could explain the lower volume of biogas generated in mixtures containing wheat straw. Wheat straw is a suitable substrate for biogas production, although its lignin content slows down the degradation process. Song and Zhang [13], in a study in 2015, investigated the monodigestion and codigestion of wheat straw, which they pretreated with four concentrations of H_2O_2 (1%, 2%, 3%, and 4%) before digesting it with cattle manure. They recorded a higher methane yield when the wheat straw was treated with H_2O_2 and codigested with cattle manure, while the codigestion of untreated wheat straw resulted in a lower yield.

The low biogas production may be due to a lack of water. Sadaka and Engler [14] reported that the solid and water content are key parameters in biogas production, directly influencing anaerobic digestion. Water facilitates bacterial movement and growth, aids in nutrient transport, and reduces mass transfer limitations.

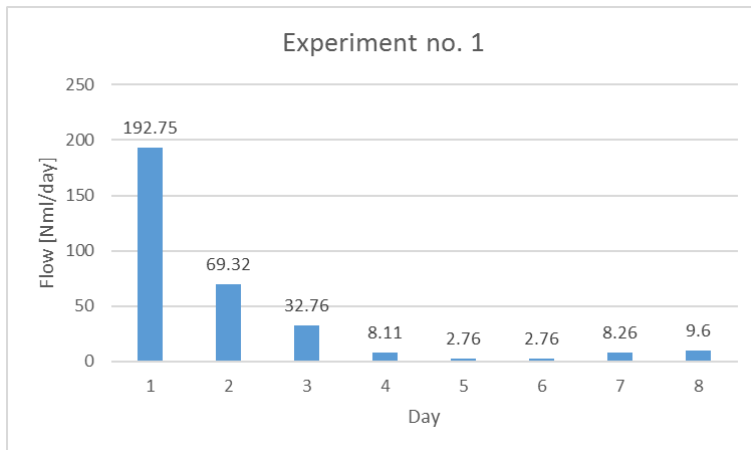


Figure 6. Biogas flow rate generated by experiment no. 1, using a mixture of pig manure 70.39 g, poultry manure 53.79 g, cattle manure 23.53 g, green grass 20 g, potatoes 20 g, Flow [Nml/day]

Figure 7 includes a centralized presentation of the experiments:

- Experiment no. 3 which consisted of a mixture of green grass 50 g, potatoes 20 g, pig manure 70.39 g, cattle manure 23.53 g, poultry manure 53.79 g, inoculum 182.29 g recorded the highest flow of biogas generated with the value of 392.21 m³/day.

- The mixture that generated biogas for 6 days is mixture no. 3 which it consisted of a mixture of green grass 50 g, potatoes 20 g, pig manure 70.39 g, cattle manure 23.53 g, poultry manure 53.79 g and inoculum 182.29 g.
- The best yields were given by the experiments that had in their composition both green grass and animal droppings.

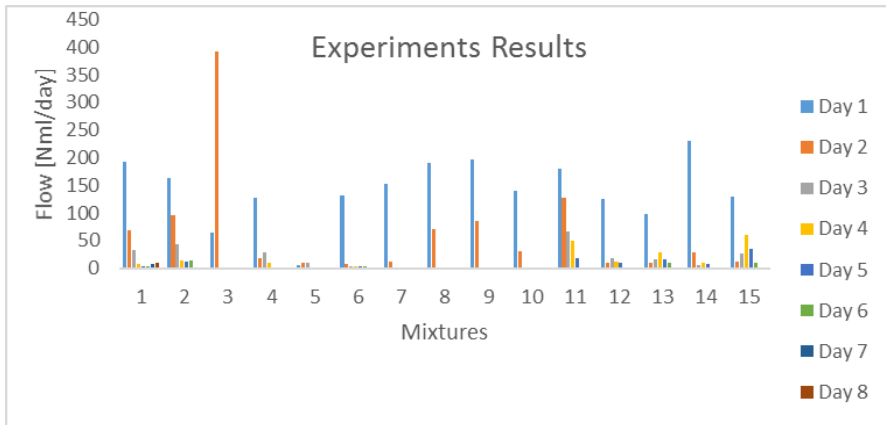


Figure 7. Experimental results using a mixture of pig manure, poultry manure, cattle manure, green grass, potatoes and straw, Flow [Nml/day]

CONCLUSIONS

The aim of the research was to develop an optimal mixture of animal manure and agro-food by-products in order to obtain high yields of biogas.

The experimental research consisted in the preparation and testing of 15 mixture recipes in which we used droppings from poultry, pig and cattle farms located in Teleorman county. We kept the animal manure samples at a temperature of $(-4)^\circ\text{C}$, in a closed container, protected from light. To speed up the anaerobic digestion process, we used wastewater as inoculum, collected from a sewage treatment plant located in Teleorman county.

The experiments were carried out using the Gas Endeavor biogas plant with a small capacity (15 glass reactors of 500 ml) and a constant temperature of 37°C .

Each set of experiments was carried out in four phases that included the collection and preparation of samples, the calculation of recipes, the preparation and commissioning of the installation and the collection and analysis of experimental data.

The installation has registered an efficient production of biogas since the first days, while the maximum level being recorded after 5 days of anaerobic digestion, the optimal mixtures being those that have a greater amount of green grass in their composition.

These differences between mixtures containing green grass and those containing wheat straw highlight the importance of biomass composition and characteristics in the biogas production process. The detailed analysis and understanding of these differences can provide valuable information for optimizing the composition of the mixtures used in biogas production and for increasing the efficiency of the process.

EXPERIMENTAL SECTION

The experiments were carried out using the Gas Endeavor biogas plant with a small capacity (15 reactors of 500 ml) and a constant temperature of 37°C.

The experiments were carried out in four phases:

Sample preparation phase: it consisted in the collection of samples from the site and the characterization of the organic substance by determining the content of dry substance and volatile substance. The samples were collected in the morning, to keep the biological characteristics intact and not to contaminate the samples.

The recipe calculation method was made taking into account that the C/N ratio should be between 15 and 25 and that the mixture should have solids content of 10%.

Preparation and commissioning of the installation Gas Endeavour consisted in the preparation and loading of the 15 glass reactors with substrate, according to the previously calculated mixture recipes.

After completing these phases, the installation is ready to be put into operation, and the reactors will be connected to the biogas treatment module, where the CO₂ retention takes place. The monitoring and control of the installation was done with the help of a laptop, which recorded and processed the data.

Recording of experimental data was carried out over a period of 8 days, during which the installation worked continuously. The installation calculated the value of the biogas production potential for each experiment.

The experiments were carefully monitored to maintain the best conditions for the development of anaerobic bacteria in the fermentation reactor: an optimal temperature, pH, continuous supply of substrate.

ACKNOWLEDGMENTS

The results presented in this article has been funded by the Ministry of Investments and European Projects through the Human Capital Sectoral Operational Program 2014-2020, Contract no. 62461/03.06.2022, SMIS code 153735.

This work was supported by a grant from the Ministry of Research, Innovation and Digitization through Program 1 – Development of the national research – development system, Subprogram 1.2 – Institutional performance in RDI, Contract no. 15PFE/2021.

REFERENCES

1. A. Vijin Prabhu, A.R. Sivaram, N. Prabhu, A. Sundaramahalingam, *Materials Today: Proceedings*, **2021**, *45*, 7994-7999.
2. A. Hilkiyah Igoni, M.J. Ayotamuno, C.L. Eze, S.O.T. Ogaji, S.D. Probert, *Appl. Energy*, **2008**, *85*, 430–438.
3. R.S. Khoiyangbam, N. Gupta, S. Kuma, *Biogas technology towards sustainable development*, Edition: 1, Publisher: *TERI Press The Energy and Resources Institute Darbari Seth Block IHC Complex Lodhi Road, New Delhi*, **2011**.
4. D. Deublein, A. Steinhauser, *Biogas in Biogas from Waste and Renewable Resources: An Introduction*, Edition: 1, Publisher: **2008**, online, Chapter 1, pp. 49-56.
5. N. Nwokolo, P. Mukumba, K. Oibileke, M. Enebe, *Processes*, **2020**, *8*, 1224.
6. A. Schnürer, Å. Jarvis, *Microbiological handbook for biogas plants, Swedish Waste Management U2009:03, Swedish Gas Centre Report 207*, **2010**.
7. S. Sutaryo, Department of Engineering, Aarhus University, Technical Report BCE-TR-E, **2012**, *1*, 3.
8. A. Babae, J. Shayegan, A. Roshani, *Journal of Environmental Health Sciences & Engineering*, **2013**, *1*, 11–15.
9. H. Fredriksson, A. Baky, S. Bernesson, Å. Nordberg, O. Norén, P. Hansson, *Agricultural Systems*, **2006**, *89*, 184–203.
10. J. G. Neto, L. V. Ozorio, T. C. Campos de Abreu, B. Ferreira dos Santos, F. Pradelle, *Fuel*, **2021**, 285.
11. BPC Instruments AB - Gas Endeavour, Automatic Gas Flow Measuring System - Operation and Maintenance Manual, Version 1.2.1, **2022**.
12. J. Baruah J., B. K. Nath, R. Sharma, S. Kumar, R. C. Deka, D. C. Baruah & E. Kalita, *Frontiers in Energy Research*, **2018**, *6*, 141.
13. Z. Song, C. Zhang, *Bioresource Technology*, **2015**, *186*, 128–135.
14. S.S. Sadaka, C.R. Engler, *Compost Science & Utilization*, **2003**, *11*, 2003, 361-369.

BIOSORPTION OF Cu (II) IONS USING RESIDUAL TOMATO POMACE BIOMASS. A STUDY OF ISOTHERMS AND KINETICS

Cerasella INDOLEAN^{a*}, Silvia BURCĂ^a

ABSTRACT. This work investigates the possible usage of tomato pomace biomass (TPB) as support for metabolic quantities of copper. Thus, biosorption potential of natural and biodegradable matrix formed from tomato residue, in suspension form was explored. The effect of biomass quantity, Cu(II) concentration and temperature were assessed.

Analysis of Fourier-transform infrared (FTIR) spectrum, scanning electron microscopy (SEM) images and elemental analysis suggested that the organic functional groups take part in the Cu (II) biosorption process, and some surface modifications and appearance of cavities onto the TPB surface were observed after biosorption.

Experimental data were analysed in terms of pseudo-first order, pseudo-second order, intraparticle diffusion and external diffusion kinetic models. The results showed that the biosorption process of Cu(II) ions followed well pseudo-second order kinetics. The biosorption data of Cu(II) ions at 295 K are fitted to Langmuir, Freundlich, Dubinin–Radushkevich (D–R) and Temkin isotherms. Biosorption of Cu(II) onto TPB followed the Freundlich isotherm model ($R^2 = 0.93$) with the maximum biosorption capacity of 2.05 mg/g. In conclusion, TPB showed appropriate adsorption capacity, 0.5 g of this biomaterial, as powder, containing Cu(II), could be used as a dietary supplement in order to supply the daily copper demand of the organism.

Keywords: *Lycopersicon esculentum*, tomato pomace biomass, Cu(II), lycopene, biosorption, dietary supplement

^a Babeş-Bolyai University, Faculty of Chemistry and Chemical Engineering, 11 Arany Janos str., RO-400028, Cluj-Napoca, Romania

* Corresponding author: liliana.indolean@ubbcluj.ro



INTRODUCTION

As one of the most popular vegetables in the world, tomatoes (*Lycopersicon esculentum*) are rich in lycopene, phenolics, organic acids, vitamins and many other beneficial components [1,2]. As is known, the tomatoes can be served as fresh vegetables or, as some processed products, such as paste, juice, sauce, puree and ketchup. In industry, processed tomatoes generate about 10–40% of by-products containing peel, seeds, as well as a small amount of pulp, known as tomato pomace, which is widely known as a rich source of β -carotene and lycopene [3]. Utilization of tomato pomace has been limited. Most studies have involved organic extraction of antioxidants from tomato peels, as over 50% antioxidants in tomato are in peels and seeds, and tomato peels have three times more lycopene, one of the major tomato antioxidants than whole tomato [4].

Every year, the alimentary industry generates significant amounts of tomato residues, in many cases considered as wastes, responsible of disposal problems and environmental pollution. In fact, the accumulation of these residues, predominantly in the warm periods, promotes uncontrolled anaerobic fermentations leading to environmental problems [5].

Copper, Cu (II), is an essential trace element in both humans and animals, required as a cofactor and/or structural component of numerous metalloenzymes. It uses copper to form red blood cells, bone and connective tissue. Copper is also involved in the processing of cholesterol, the proper functioning of your immune system and the growth and development of babies in the womb. [6]

The body of a healthy adult contains approximately 80–100 mg of copper, accumulated mainly in the bones, liver, and muscles [7].

The World Health Organization (WHO) and the Food and Agriculture Administration (FAA) suggest that the average daily intake of copper for a healthy adult should not exceed 0.9 mg/day, while during pregnancy it should be 1.0 mg/day and 1.3 mg/day during breastfeeding for women [6]. The food sources of copper include meat, crustaceans, nuts, wholemeal foods, and dried fruit. Around 50% of copper is absorbed in the stomach, duodenum, and the initial parts of the small intestine, and the remaining amount is excreted in faeces [7,8].

For this reason, the aim of this research is to purpose obtaining a functional food based on Cu(II), in metabolic quantity, biosorbed onto a tomato biomass waste matrix, rich in antioxidants, cheap and available from local alimentary industry.

The variables operation effect such as initial copper ion concentration, adsorbent dose, contact time and stirring rate were investigated.

RESULTS AND DISCUSSION

I. Biosorbent characterization

1.1. Fourier transform infrared spectroscopy (FTIR)

FTIR spectra were recorded using JASCO 615 FTIR spectrometer. The sample of dried biosorbents was grinded sufficiently with KBr by pallet method. The spectra were recorded in the range of 500–4000 cm^{-1} and resolution 2 cm^{-1} .

In Figure 1 are depicted the spectra of TPB before and after Cu(II) adsorption. The broad absorption peak at around 3255.2 cm^{-1} corresponds to the O–H stretching vibrations due to inter- and intra-molecular hydrogen bonding of polymeric compounds (macromolecular associations), such as alcohols, phenols and carboxylic acids, as in pectin, cellulose and lignin, thus, showing the presence of hydroxyl groups on the adsorbent surface [8]. After Cu(II) biosorption this band was shifted at 3261 cm^{-1} , fact which supports the Cu(II) presence onto TPB surface. The sharp bands at 2915.8 cm^{-1} and 2850 cm^{-1} can be attributed to the aliphatic saturated C-H stretching vibrations of the lignin, cellulose and hemicellulose polysaccharides. The presence of the peak at 1619.9 cm^{-1} indicates the carbonyl (C=O) stretching vibration of the carboxyl groups of pectin, hemicellulose and lignin, peak that was shifted at 1706.6 cm^{-1} after Cu (II) biosorption, fact that confirm the presence of the metal in the biomass structure [8,9]. The other prominent band is due to C=O (carbonyl) group, at 1022.08 cm^{-1} that was shifted at 1024.01 cm^{-1} . Moreover, in the case of TPB, after Cu(II) biosorption, a remarkable modification in positions and amplitude of –OH and C=O bands was observed, which indicates that Cu(II) was linked mostly at these groups, and it can be seen that some of the characteristic absorption bands of TPB biomass after biosorption were shifted at higher values than those of TPB before biosorption [10-12].

Peaks in the wavenumber region below 800 cm^{-1} can be attributed to the presence of bioligands. These spectra indicate that the studied biosorbent contains a wide variety of functional groups such as hydroxyl, carboxyl, amides, ethers, ketones, and esters that play important role for Cu (II) binding through different mechanisms. The changes in FTIR spectra confirm the binding of Cu with functional groups present in the biosorbent. Similar observations were also reported by Pandya et al. [13].

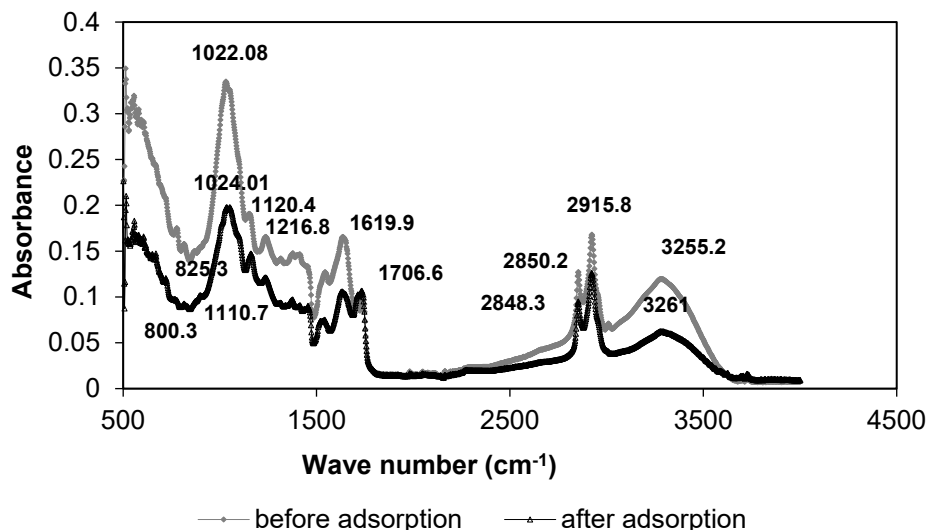


Figure 1. FTIR spectra before Cu (II) biosorption onto TPB (grey line) and after biosorption (black line).

1.2. Elemental analysis

Elemental analysis (EA) is, as is well-known, an analytical technique applied in chemistry to determine the elemental composition of chemical compounds and their composites.

The composition of the TPB sample was characterised by means of proximate and ultimate analyses. Elemental (C, H and N) analysis was performed using a Perkin Elmer PE2400 CHNS/O Elemental Analyzer.

The oxygen content was calculated by difference from the data obtained by the Perkin Elmer PE 2400 CHNS/O Elemental Analyzer machine.

Elemental composition (wt.% on dry basis) for TPB was % C = 45.77; % H = 6.67; % N = 3.35; % S = 0.14.

The results of elemental analysis reveal that TPB has high carbon content, which makes it a good precursor material for biosorbents.

1.3. Scanning Electron Microscope (SEM) analysis

Scanning electron microscopy (SEM) images for samples were obtained with a JEOL (USA) JSM 5510 LV apparatus. Prior to analyse, biosorbent samples were mounted on a stainless stab with a double stick tape. Then they were coated with a thin layer of gold under vacuum to improve electron conductivity and image quality.

In order to examine the morphological structure of biomass, SEM micrographs of TPB were taken before and after Cu (II) biosorption and presented in Figure 2. SEM micrograph of initial TPB material indicates a smooth structure of the biomass surface, Figure 2a. After metal loading, some surface modification and appearance of cavities onto the TPB surface were observed, Figure 2b.

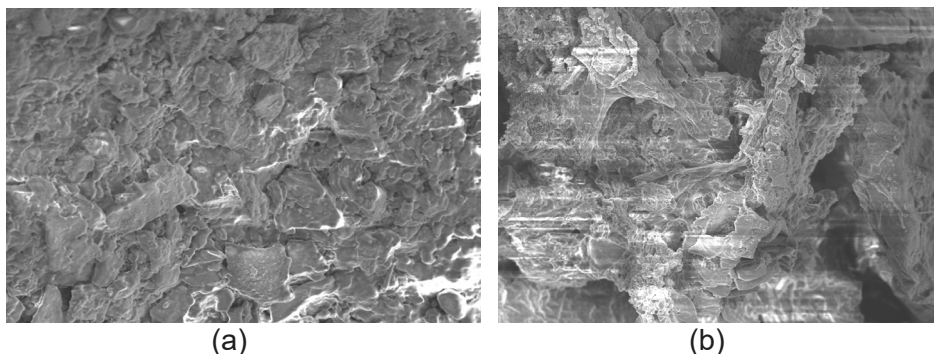


Figure 2. SEM micrograph (x1000) of (a) TPB before and (b) after Cu(II) biosorption.

II. Biosorption study

II.1. Effect of Cu(II) concentration on the biosorption process

Cu(II) concentration influence was studied using the following biosorption conditions: 1g TPB, $d = 200-400 \mu\text{m}$, 296 K, $\text{pH} = 5.41$, 300 rpm, contact time 240 min, with concentrations in 12.5-68 mg Cu(II)/L range. Time evolution was also followed for all concentrations used.

Experimental results showed that sorption capacity increases with increasing concentration of Cu^{2+} ions in aqueous solution, from 0.285 mg/g when a 12.5 mg Cu^{2+} /L aqueous solution was used up to 1.98 mg/g when a 68 mg Cu^{2+} /L aqueous solution was used, Figure 4. But as the initial concentration increases, sorption process equilibrium was reached more difficult, after about 125 minutes, by comparison with just 30 minutes for small concentrations (12.5 – 27.5 mg Cu^{2+} /L), Figure 3. However, for further experiments was chosen the initial metal concentration to be 68 mg Cu(II)/L, because the biosorption efficiency was the highest.

In addition, this value of 1.98 mg Cu^{2+} /L is in the range of the daily requirement of Cu(II) for a healthy adult, in an eventual dietary supplement formulation, requiring about 0.5 g of TPB with Cu (II) biosorbed [6,14].

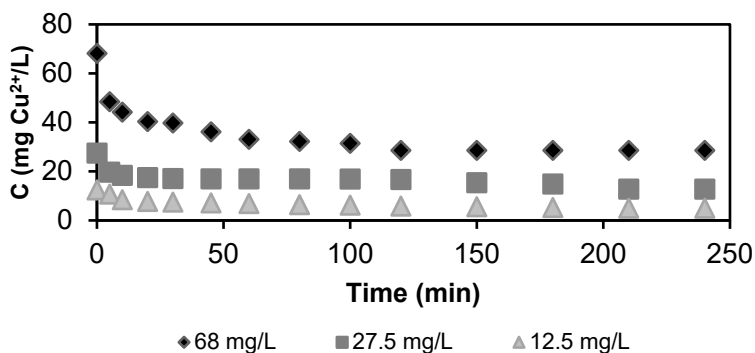


Figure 3. Cu(II) concentration time evolution for biosorption onto TPB; 1 g TPB, $C_i = 68$ mg Cu(II)/L, $d = 200\text{-}400$ μm , 296 K, pH = 5.41, 300 rpm.

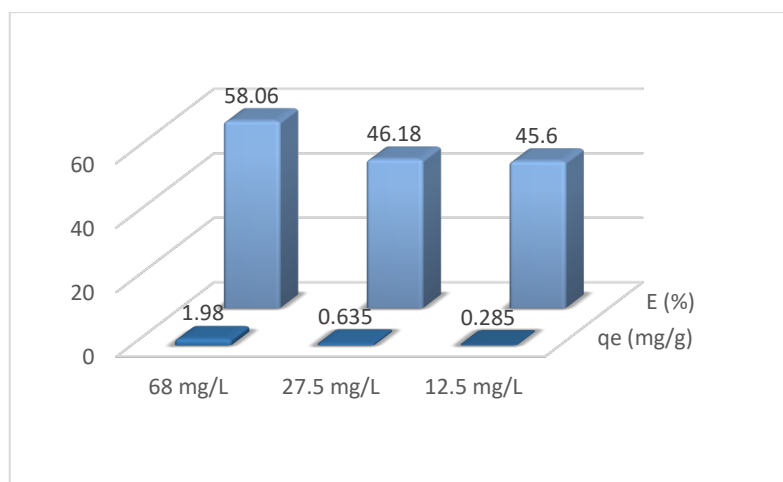


Figure 4. Initial concentration influence over equilibrium biosorption capacity (q_e) and biosorption efficiency (E,%) for Cu(II) biosorption on TPB; 1 g TPB/100 mL, $d = 200\text{-}400$ μm , 296 K, pH = 5.41, 300 rpm.

II.2. Effect of biomass quantity on the biosorption process

The effect of biomass quantity on Cu (II) biosorption was studied using different quantities of TPB powder, ranging from 1 to 3 g (Figure 5).

The increase in the biomass quantities, from 1 to 3 g, increases biosorption of Cu(II) ions onto TPB from 51.34% to 73.67%.

BIOSORPTION OF Cu (II) IONS USING RESIDUAL TOMATO POMACE BIOMASS.
A STUDY OF ISOTHERMS AND KINETICS

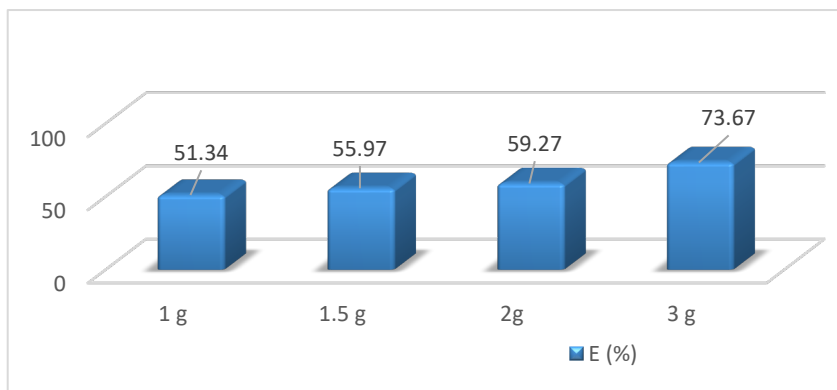


Figure 5. The effect of the TPB quantity on Cu (II) biosorption over the biosorption efficiency (E,%); ($C_i = 68 \text{ mg Cu(II)/L}$, $d = 200\text{-}400 \text{ }\mu\text{m}$, 296 K , $\text{pH} = 5.41$, 300 rpm).

More visible changes in the biosorption efficiency can be observed at quantities between 2 and 3 g. This effect could be explained by the availability of more adsorption sites on biosorbent surface and by increasing on total functional groups. Higher biomass quantities improve the biosorption efficiency, but not significantly, therefore the optimal amount of TPB for biosorption of Cu(II) was chosen to be 1 g TPB/100 mL Cu(II) solution for further experiments.

II.3. Effect of the stirring rate

Biosorption experiments were repeated with varying stirring speeds from 300 to 700 rpm (rotations per minute). As such, the curve for Cu (II) biosorption with respect to time, in terms of biosorption efficiencies, could be drawn for three different rotation speeds, 300, 500 and 700 rpm (Figure 6).

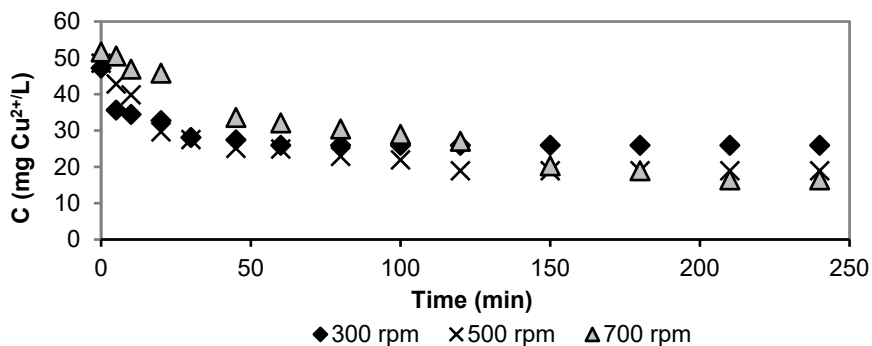


Figure 6. Influence of the stirring rate over time evolution of Cu (II) biosorption onto TPB ($C_i = 68 \text{ mg Cu (II) / L}$, 296 K , 1 g TPB , $d = 200\text{-}400 \text{ }\mu\text{m}$, $\text{pH} = 5.41$, 300 rpm)

The obtained curves showed that the biosorption process was intensified with stirring rate up to 500 rpm, but a further increase from 500 to 700 rpm will lead to a less increase, showing that after a certain stirring speed, the minimization of the thin film layer formed at the TPB surface will not lead to a further increase in the external diffusion rate.

As can be seen in Figure 7, even if the biosorption efficiency increases from 45.12 % to 65.21 %, by increasing the rotation speed from 300 rpm to 700 rpm, however, for energy saving reasons, for subsequent experiments the rotation speed of 300 rpm will be chosen.

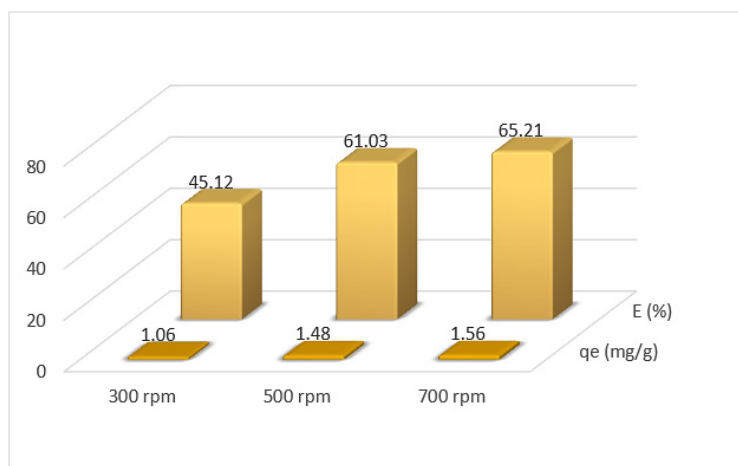


Figure 7. Influence of the stirring rate over the efficiency (E,%) and biosorption capacity at equilibrium (q_e, mg/g) of the Cu (II) retain onto TPB (C_i =68mg/L, 296 K, d = 200-400 μm, 1g TPB/100 mL, pH = 5.41, 150 min).

III. Adsorption isotherms

The adsorption isotherms describe the pathway of the interaction of a substrate from the bulk solution to the surface of adsorbate.

The equilibrium data were analysed using different isotherm models (Figures 8-11). In this article, four important isotherm models, namely Langmuir, Freundlich, Temkin and Dubinin–Radushkevich, were selected to fit the obtained experimental data. Each isotherm is characterized by definite constants whose values express the surface properties and affinity of the studied material.

There is a limitation of Langmuir equation because it assumes that adsorption is monolayer with no attraction between molecules on the surface of adsorbate.

BIOSORPTION OF Cu (II) IONS USING RESIDUAL TOMATO POMACE BIOMASS.
A STUDY OF ISOTHERMS AND KINETICS

Using Langmuir model, the maximum adsorption capacity (q_m) was found to be 2.959 mg g^{-1} (Table 1).

Temkin isotherm model takes into account the effects of indirect adsorbate/adsorbate interactions on the adsorption process; it is also assumed that the heat of adsorption (ΔH_{ads}) of all molecules in the layer decreases linearly as a result of increase surface coverage [15]. The Temkin isotherm equation has been applied to describe adsorption on heterogeneous surface.

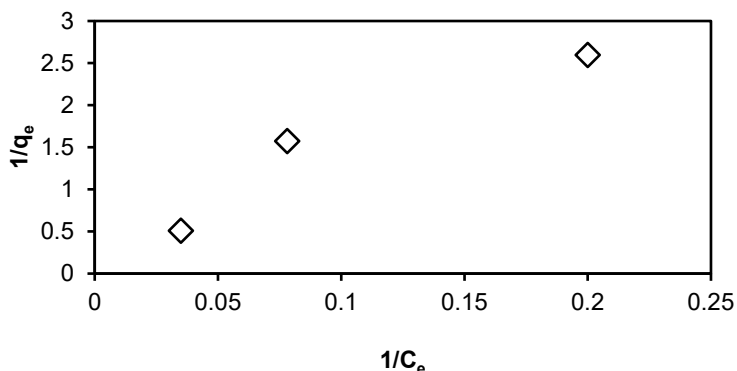


Figure 8. Langmuir plot for Cu^{2+} biosorption onto TPB ($C_i = 12.5\text{-}68 \text{ mg Cu}^{2+}/\text{L}$, 296 K , $\text{pH}=5.41$, 1 g TPB , $d = 200\text{-}400 \mu\text{m}$, 300 rpm).

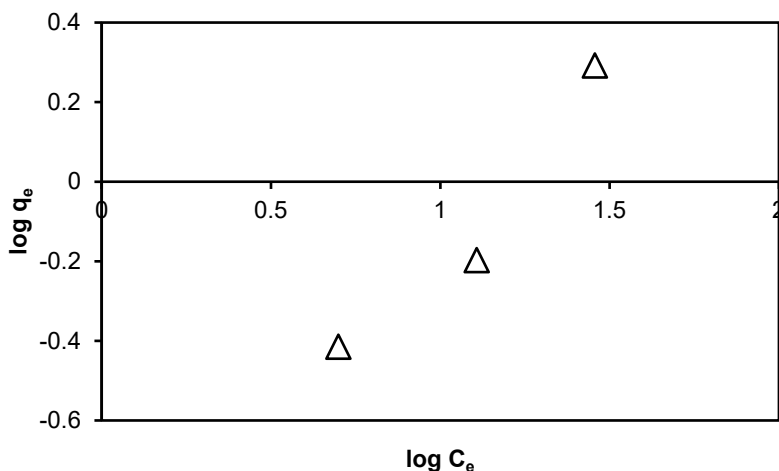


Figure 9. Freundlich plot for Cu^{2+} biosorption onto TPB ($C_i = 12.5\text{-}68 \text{ mg Cu}^{2+}/\text{L}$, 1 g TPB , $d = 200\text{-}400 \mu\text{m}$, 296 K , $\text{pH}=5.41$, 300 rpm).

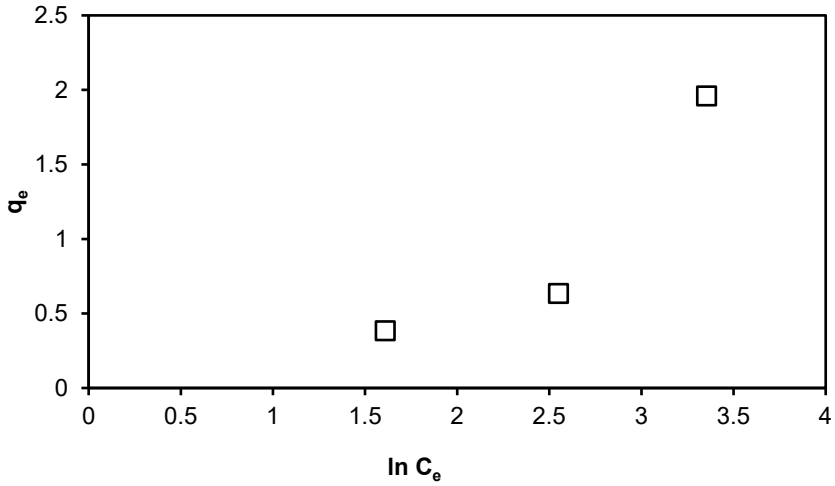


Figure 10. Temkin plot for Cu^{2+} biosorption onto TPB ($C_i = 12.5\text{-}68 \text{ mg Cu}^{2+}/\text{L}$, 296 K, $\text{pH}=5.41$, 1 g TPB, $d = 200\text{-}400 \mu\text{m}$, 300 rpm).

Therefore, by plotting q_e versus $\ln C_e$, enables the determination of the constants A_T and B . B is the Temkin constant related to heat of sorption (J/mol) and A_T is the Temkin isotherm constant (L/g) (Figure 10, Table 1).

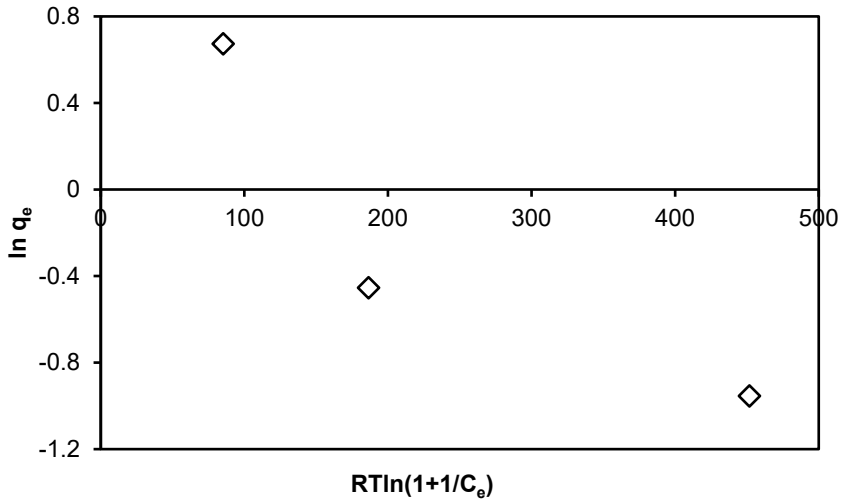


Figure 11. Dubinin–Radushkevich plot for Cu^{2+} biosorption onto TPB ($C_i = 12.5\text{-}68 \text{ mg Cu}^{2+}/\text{L}$, 296 K, $\text{pH}=5.41$, 1 g TPB/100 mL, $d = 200\text{-}400 \mu\text{m}$, 300 rpm).

Dubinin-Radushkevich isotherm model [16] is an empirical adsorption model that is generally applied to express adsorption mechanism with Gaussian energy distribution onto heterogeneous surfaces. This isotherm model was developed to account for the effect of the porous structure of the adsorbents. It was based on the adsorption potential theory and assumed that the adsorption process was related to micropore volume filling as opposed to layer-by-layer adsorption on pore walls.

Dubinin-Radushkevich isotherm model is superior to the Langmuir isotherm since it did not consider a homogeneous surface or constant adsorption potential [17]

It is usually applied to differentiate between physical and chemical adsorption of metal ions. A distinguishing feature of the Dubinin-Radushkevich isotherm is the fact that it is temperature dependent; hence when adsorption data at different temperatures are plotted as a function of logarithm of amount adsorbed versus the square of potential energy, all suitable data can be obtained [18].

From the linear plot of Dubinin-Radushkevich model, q_s was determined to 2.013 mg/g (Table 1). The mean free energy was calculated and has value $E = 16$ KJ/mol, that indicating a chemisorption process.

The coefficient of determination $R^2 = 0.89$ for Dubinin-Radushkevich model is higher than that of Tempkin model ($R^2 = 0.83$), so, the first is preferred.

From literature [19], is well-known that, if E value is between 8 and 16 kJ/mol, the adsorption follows an ion-exchange process (chemisorption), and if $E < 8$ kJ/mol, the adsorption process is physical.

Table 1. Langmuir, Freundlich, Temkin and Dubinin–Radushkevich coefficients calculated using linear regression analysis for Cu^{2+} adsorption on TPB; $C_i = 12.5$ -68 mg Cu^{2+}/L , 296 K, pH = 5.41, 1 g TPB/100 mL, $d = 200$ -400 μm , 300 rpm.

Langmuir			Freundlich			Temkin			Dubinin–Radushkevich		
b (L/mg)	q_m (mg/g)	R^2	n	K_f ($mg^{(1-1/n)}$ $L^{1/n}/g$)	R^2	B (J/mol)	A_T (L/g)	R^2	q_s (mg/g)	K_{ad} (mol^2/KJ^2)	R^2
0.028	2.959	0.92	1.084	0.077	0.93	0.885	0.999	0.83	2.013	0.002	0.89

IV. Kinetics models

The data obtained from adsorption kinetic experiments were simulated using five kinetic models, which are pseudo-first order, pseudo-second order reaction rate, Elovich, Weber-Morris intra-particle diffusion and Boyd external film diffusion models. Coefficient of correlation (R^2), which represent the percentage of variability in the dependent variable (the variance about the mean) is employed to analyse the fitting degree of isotherm and kinetic models with the experimental data [20] and as is well known, may vary from 0 to 1. The values of k_1 and q_e calculated from the slope and intercept obtained from the linear plot of $\ln(q_e - q_t)$ vs. t (Figure 12) and the R^2 values of fitting the first-order rate model at the three concentrations are presented in Table 2.

Linear plot of t/q_t vs. t (Figure 13) was used for calculating the q_e (cal) of pseudo-second order and k_2 , and these values are also shown also in Table 2.

IV.1. Pseudo-first-order kinetic model

This model – Lagergren [21] – describes the adsorption of one adsorbate molecule onto one active site of the biosorbent.

The constants K_1 and q_e were estimated from the slope and intercept by plotting $\ln(q_e - q_t)$ vs. time, respectively (see Figure 12 and Table 2). Calculated adsorption capacity values (q_e) of Cu (II) biosorption on TPB are much lower ($q_{\text{calc}} = 1.02$ mg/g, Table 2) in comparison to experimental ones ($q_e = 1.98$ mg/g, Figure 4) and R^2 (regression coefficient) values are small (no. 0.74, Table 2), suggesting that the pseudo-first-order model cannot describes the studied system.

IV.2. Pseudo-second-order kinetic model

Experimental data were also tested using the Ho and McKay [22] pseudo-second-order equations. The rate constants (k_2), R^2 and q_e values are given in Table 2, Figure 13.

As the table shows, the linearized pseudo second-order kinetics model provides much better R^2 values (0.999 for all tree concentrations) than those for the pseudo-first-order model.

The good agreement between the experimental data and the pseudo-second order kinetic model (Figure 13, Table 2) show that in the studied biosorption process, the rate-limiting step is the chemical interaction between the Cu(II) ions and the functional groups on the TPB biosorbent surface. Moreover, for retention on the biosorbents surface, Cu(II) ions need two functional groups, which must be geometrically favorable.

BIOSORPTION OF Cu (II) IONS USING RESIDUAL TOMATO POMACE BIOMASS.
A STUDY OF ISOTHERMS AND KINETICS

Since studied TPB biosorbent has a large number of functional groups on their surface (FTIR analysis, Figure 1), it can be assumed that there is no reason why biosorption should not takes place according to the pseudo-second-order kinetics.

The theoretical q_e (cal) = 2.05 mg/g for C_i = 68 mg Cu (II)/L (Table 2) value were also found in concordance with the experimental value q_e (exp) = 1.94 mg/g for the C_i = 68 mg Cu (II)/L (Figure 4).

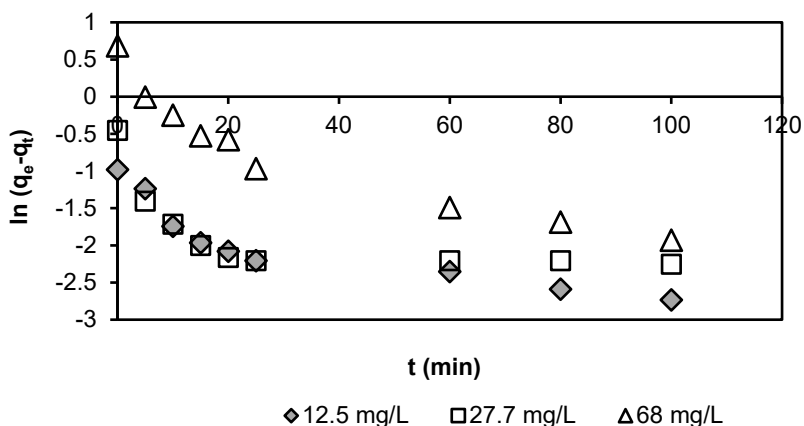


Figure 12. Plots of the pseudo-first-order kinetic models for Cu (II) biosorption using TPB; C_i = 12.5-68 mg Cu²⁺/ L, 1g TPB/100 mL, d = 200-400 μ m, 296 K, pH = 5.41, 300rpm.

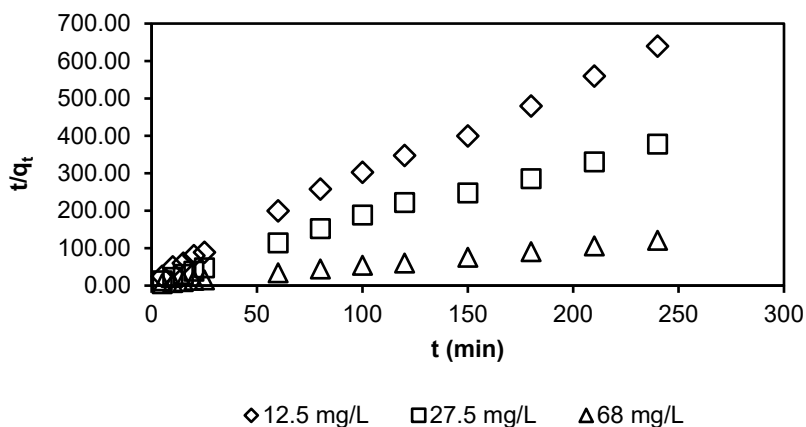


Figure 13. Plots of the pseudo-second-order kinetic models for Cu (II) biosorption using TPB; C_i = 12.5-68 mg Cu²⁺/ L, 1g TPB, d = 200-400 μ m, 296 K, pH = 5.41, 300rpm.

IV.3. Elovich equation

The Elovich equation has been widely used in adsorption kinetics, which describes chemical adsorption (chemical reaction) mechanism in nature. The model of Elovich and Larinov [23] is based on a kinetic principle assuming that the adsorption sites increase exponentially with adsorption, which implies a multilayer adsorption.

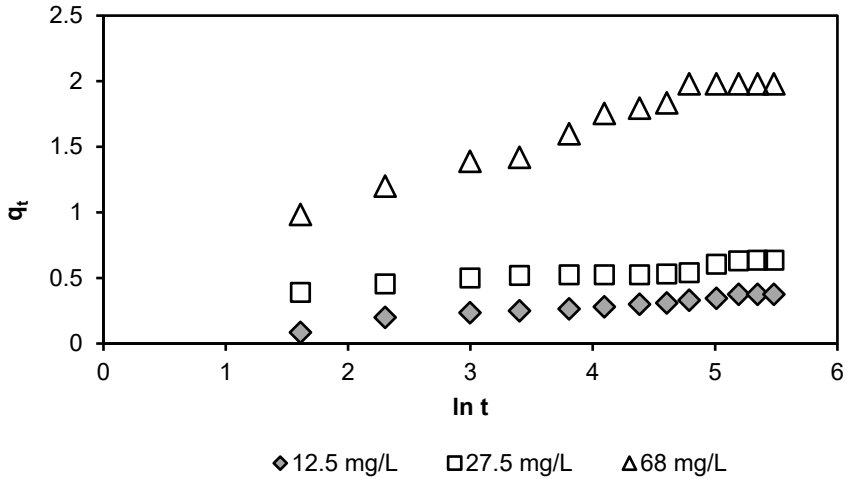


Figure 14. Elovich plots for Cu^{2+} biosorption onto TPB ($C_i = 12.5\text{--}68 \text{ mg Cu}^{2+}/\text{L}$, $1 \text{ g TPB}/100\text{mL}$, $d = 200\text{--}400 \mu\text{m}$, 296 K , $\text{pH}=5.41$, 300 rpm).

Table 2. Pseudo-first-order, pseudo-second-order rate constants and Elovich kinetic models calculated and experimental q_e values for Cu (II) biosorption onto TPB using different initial concentrations; $C_i=12.5\text{--}68\text{mg Cu}^{2+}/\text{L}$, $1\text{g TPB}/100 \text{ mL}$, $d=200\text{--}400 \mu\text{m}$, 296K , $\text{pH} = 5.41, 300 \text{ rpm}$.

Concentration (mg Cu^{2+}/L)	Pseudo-first order			Pseudo-second order			Elovich		
	q_m (mg/g)	K_{ad} (min^{-1})	R^2	q_m (mg/g)	K_2 (g/mg·min)	R^2	α (mg/g·min)	β (g/mg)	R^2
12.5	0.224	0.014	0.74	0.391	0.215	0.99	0.081	14.025	0.95
27.5	0.225	0.010	0.37	0.643	0.172	0.99	1.394	7.85	0.90
68	1.018	0.022	0.85	2.052	0.061	0.99	2.093	3.63	0.97

In the case of Elovich kinetic model, the low values of the correlation coefficients, between 0.90 and 0.97 (see Figure 14, Table 2), suggest that this model is not suitable to describe the Cu(II) on TPB biosorption process.

IV.4. Intra-particle diffusion kinetic model

This model was developed by Weber and Moris, in 1962 [24]. According this model, adsorption is a mass transport process that can be viewed as a diffusion. The adsorption mechanism is through three steps, i.e., the external mass transfer, the intraparticle diffusion, and the final equilibrium step [25, 26].

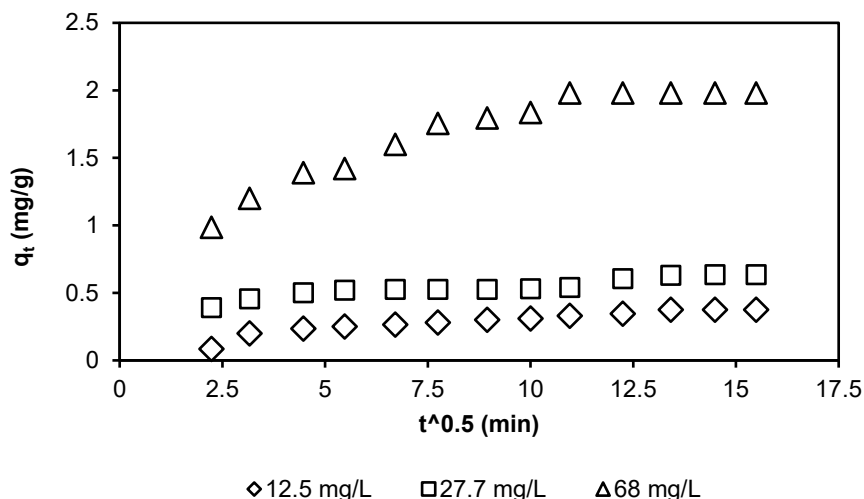


Figure 15. Intraparticle diffusion kinetics for biosorption of Cu(II) onto TPB at 296K.

The intra particle diffusion Weber and Morris [24] was considered in order to establish how mass transfer through the biomass pores influences the biosorption process.

Plots of q_t against $t^{1/2}$ are linear, but with intercepts +0.13, +0.90 and +1.94 (Table 3), suggesting that early stages of the diffusion process could be rate-limitative at small concentrations ($C_i = 12.5$ mg Cu (II)/L).

IV.5. External diffusion kinetics model.

The external diffusion models assume that the diffusion of adsorbate in a bounding liquid film around the adsorbent is the slowest step.

Several equations have been developed to model the external mass transfer process.

Boyd's external diffusion model [27] simulates the external diffusion of adsorbate in a liquid film.

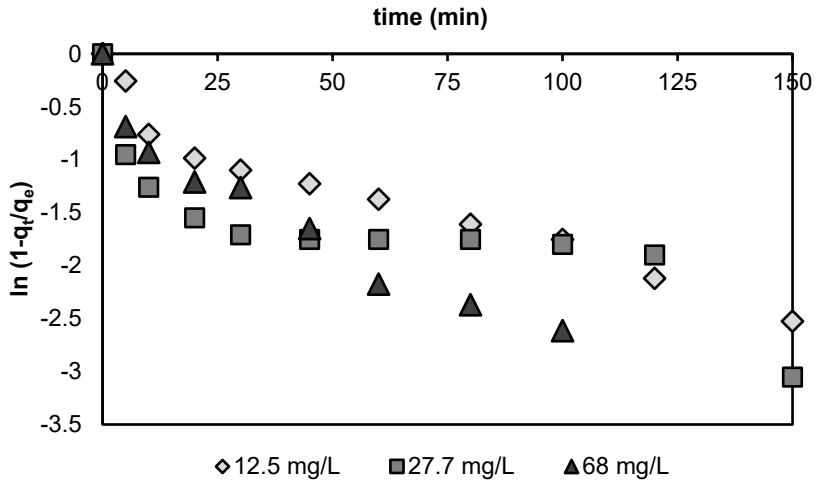


Figure 16. Boyd's external diffusion kinetics model for biosorption of Cu(II) onto TPB at 296K.

The liquid film model [27] plots $(-\ln(1 - q_t/q_e))$ against t do not exhibit zero intercepts (Table 3, +0.44, +0.61 and +0.53), suggesting that the process is not controlled by diffusion through the liquid film surrounding the TPB biosorbent particles.

Table 3. Intra-particle and external (film) diffusion rate coefficients for Cu^{2+} biosorption on TPB; 12.5 - 68 mg Cu^{2+}/L , 300 rpm, 296 K. pH = 5.41.

Concentration (mg Cu^{2+}/L)	Intra-particle diffusion			External (Film) Diffusion		
	K_p (min^{-1})	Intercept	R^2	K_{fd} (min^{-1})	Intercept	R^2
12.5	0.178	0.128	0.87	0.014	0.439	0.91
27.5	0.015	0.900	0.88	0.012	0.613	0.97
68	0.072	1.038	0.87	0.023	0.529	0.91

CONCLUSION

In the present work, a modified biomass (TPB) for biosorption of Cu(II) ions from aqueous solution, in a batch adsorption study was investigated, in order to obtain a biomaterial that could be used as a base for a dietary supplement with Cu(II) and significant amounts of lycopene from TPB.

The surface modifications after Cu(II) biosorption on TPB were analysed by the FTIR and SEM analyses.

The biosorption Cu(II) ions on TPB depends on the initial Cu(II) ions concentration, contact time and stirring rate. 68 mg/L of biosorbent dose, 150 min of contact time and 300 rpm, at room temperature for Cu(II)/TPB system was used. The adsorption of Cu(II) ion from aqueous solution increased with increase in the contact time. The biosorption percentage of Cu(II) ions increased with increase with the biosorbent quantity and stirring rate. However, for energy saving reasons, the rotation speed of 300 rpm will be chosen.

The adsorption kinetics and mechanism were analysed by using kinetic models such as pseudo-first-order, pseudo-second-order, Elovich, intraparticle diffusion and external diffusion film model.

The pseudo-second-order was fitted very well compared to all other kinetic models.

Freundlich model was fitted well with the maximum R^2 value (0.93) compare to Langmuir, Temkin and Dubinin-Radushkevich models for TPB.

Taking into consideration that pore diffusion coefficients have higher values than the rate-determining range, that none of the plots of the liquid film model exhibit a zero intercept, and that the biosorption fits the pseudo-second-order kinetics, the considered process that takes place is chemisorption.

Finally, we concluded that TPB biosorbent is an effective material to adsorb the Cu(II) ions from aqueous solution.

Taking into consideration the values obtained for the adsorption capacity and knowing the WHO suggested intake of copper for males and females, 0.5 g of TPB, in powder form containing Cu(II), could be used as a dietary supplement in order to supply the daily copper demand of the organism.

EXPERIMENTAL SECTION

Materials

The stock solution, 1 g/L of Cu (II), was prepared by dissolving $\text{CuSO}_4 \cdot 5\text{H}_2\text{O}$ in distilled water. Analytical grade, without further purification, from E. Merck Ltd., Germany was used. The required concentrations were obtained by diluting the stock solution to the desired concentrations, in 12.5–68 mg Cu^{2+} /L range.

The tomato waste material (peel, seeds and pulp), TPB, required as starting material for this work was collected locally, after tomato juice extraction. Initially, for the preparation of biosorbent, the biomass was crushed, washed several times with distilled water, and dried in the oven at 70 °C, for 48 h until the biosorbent constant weight is obtained. The dried TPB samples were ground to fine powder and the this was sieved through different sizes and 200–400 μm fractions was used. This was stored in a desiccator and used in further experiments.

Biosorption experiments.

Biosorption process took place under established conditions in a beaker (thermostated batch conditions, 296K ±2K) containing 100 mL of Cu (II) solution of different concentrations (12.5–68 mg/L) and different quantities (1–3 g) of TPB. The different solutions were placed on a magnetic stirrer and stirred at a different speed (300-700 rpm) in a continuous manner. In order to determine the exact concentration of copper and to establish the evolution of the biosorption process, water samples from the supernatant, diluted as required, were collected at different time intervals, until equilibrium was reached. The maximum contact time used was 240 min to ensure that biosorption equilibrium was reached.

The concentration of copper ions in the solution was determined using a flame atomic absorption spectrophotometer (Sens AA Dual GBS Scientific Equipment, Australia).

Biosorption efficiency, expressed as percentage, was calculated with equation (1):

$$E = \frac{C_0 - C_e}{C_0} \times 100 \quad (1)$$

where C_0 and C_e are the initial and equilibrium concentrations of Cu (II), respectively (mg/L).

The amount of Cu(II) biosorbed per gram of TPB (mg/g) was calculated using equation (2):

$$q_e = \frac{(C_0 - C_e) \cdot V}{m} \quad (2)$$

where V is solution volume (L) and m is TPB quantity (g).

All parametrical values presented are the averaged mean of three series of data recorded from repetitions of the same experiment.

REFERENCES

1. G. Giovanelli and A. Paradiso, *J. Agric. Food Chem.*, **2002**, *50*, 7277–7281; doi.org/10.1021/jf02559r.
2. Z. Lu, J. Wang, R. Gao, F. Ye, G. Zhao, *Trends Food Sci. Technol.*, **2019**, *86*, 172-187.
3. G.S. Dhillon, S. Kaur, H.S. Oberoi, M.R. Spier, S.K. Brar, Chapter 2 -Agricultural-Based Protein By-Products: Characterization and Applications; in Protein byproducts, Academic Press, **2016**, p21-p36; doi.org/10.1016/B978-0-12-802391-4.00002-1.
4. F. Jiang, Y.-L. Hsieh, *Carbohydrate polymers*, **2015**, *122*, 60-68.
5. G. Toscano, A. Pizzi, E. Foppa Pedretti, G. Rossini, G. Ciceri, G. Martignon, D. Duca, *Fuel*, **2015**, *143*, 89-97.
6. <https://www.healthline.com/nutrition/food-high-in-copper>
7. Wiecek, S., Paprocka, J., *Metabolites*, **2024**, *14*, 38-51.
8. S. Azabou, I. Louati, F. Ben Taheur, M. Nasri, T. Mechichi, *Environ. Sci. Pollut. Res.*, **2020**, *27*, 39402–39412.
9. A.Ş. Yargıç, R.Z. Yarbay Şahin, N. Özbay, E. Önal, *J. Clean. Prod.*, **2015**, *88*, 152-159.
10. M. Changmai, P. Banerjee, K. Nahar, M. K. Purkait, *J. Environ. Chem. Eng.*, **2018**, *6*, 246-257.
11. H. Saygılı, F. Güzel, Y. Onal, *J. Clean. Prod.*, **2015**, *93*, 84–93.
12. H. Saygılı, F. Güzel, *J. Clean. Prod.*, **2016**, *113*, 995–1004 K. Y.
13. Pandya, R. V. Patel, R. T. Jasrai, N. Brahmhatt, *Int. J. Eng. Res. Gen. Sci.*, **2017**, *5(4)*, 137-148.
14. N. Ayawei, A. N. Ebelegi, D. Wankasi, *J. Chem.*, **2017**, *7*, 1-11.
15. C. Indolean, A. Măicăneanu, M. Cristea, *The Canadian Journal of Chemical Engineering*, **2017**, *95*, 615-622.
16. N. Ayawei, A. Newton Ebelegi, D. Wankasi, *J. Chem.*, **2017**, *50*, 1-11.
17. Qi. Hu, Z. Zhang, *J. Mol. Liq.*, **2019**, *277*, 646-648.
18. A. G`unay, E. Arslankaya, I. Tosun, *J. Hazard. Mat.*, **2007**, *146(1-2)*, 362–371M. A Al-Ghouti, D. A. Da'ana, *J. Hazard. Mat.*, **2020**, *393*, 122383-122392.
19. A. Sari, M. Tuzen, *J. Hazard. Mater.*, **2008**, *152*, 302 308.
20. N. Bar, T. Mitra, S. K. Das, *J. Environ. Eng. Land. Manag.*, **2021**, *29 (4)*, 441–448.
21. Lagergren, S., *Royal Swed. Acad. Sci.* **1898**, *24*, 1–39.
22. Ho, Y.S.; McKay, G., *Process Biochem.* **1999**, *34*, 451–65.
23. S.Y. Elovich, O.G. Larinov, *Izv. Akad. Nauk. SSSR, Otd. Khim. Nauk*, **1962**, *2*, 209–216.
24. W.J. Weber, C.J. Morris, *Proceed. Intern. Conf. Water Poll. Symp.* Oxford: Pergamon Press, **1962**, *2*, 231-266.
25. Y. Qu, C. Zhang, F. Li, X. Bo, G. Liu, Q. Zhou, *J. Hazard. Mat.*, **2009**, *169(1–3)*, 146–152.
26. R. Ratnawati, A. Prasetyaningrum, H. Hargono, M. F. Zakaria, *Period. Politech. Chem. Eng.*, **2023**, *10*, 1-14.
27. G.E. Boyd, A.W. Adamson, L.S. Jr. Myers, *J. Am. Chem. Soc.*, **1947**, *69*, 2836–2842.

IN VITRO – IN VIVO CORRELATION OF PENTOXIFYLLINE: A COMPREHENSIVE KINETIC ANALYSIS

Maria CODREANU^{a,b}, Diana IACOB^c, Maria Ioana ONOFREI^{d,e},
Ana-Maria VLASE^f , Dana Maria MUNTEAN^{a,*} , Laurian VLASE^a 

ABSTRACT. This study presents an analysis of *In Vitro-In Vivo* Correlation (IVIVC) for pentoxifylline modified-release tablets, with a focus on deriving robust predictive models. *In vitro* dissolution tests were conducted in three pH media (1.2, 4.5, and 6.8) to simulate various gastrointestinal conditions. Data was collected under fed conditions from a bioequivalence (BE) study. The modeling and calculations were performed using Phoenix WinNonlin[®] version 8.4 software, enabling estimation of drug absorption kinetics. A Level A IVIVC model was employed for each *in vivo* data to establish a direct and reliable correlation between the *in vitro* dissolution profiles and the *in vivo* pharmacokinetic data. The determination coefficient (R^2) exceeded 0.97, demonstrating a high degree of predictability and robustness in the established IVIVC.

Keywords: *In Vitro – In Vivo* Correlations (IVIVCs), pentoxifylline, *in vitro* dissolution, bioequivalence, Level A Correlation

^a Iuliu Hațieganu University of Medicine and Pharmacy, Faculty of Pharmacy, Department of Pharmaceutical Technology and Biopharmacy, 8 Victor Babeș Street, RO-400347 Cluj-Napoca, Romania

^b Antibiotice SA, Regulatory Affairs Department, 1 Valea Lupului Street, RO-707410 Iași, Romania

^c Antibiotice SA, Center for Drug Evaluation, 1 Valea Lupului Street, RO-707410 Iași, Romania

^d Sf. Parascheva Clinical Hospital of Infectious Diseases, Clinic of Infectious Diseases, 23 Iuliu Moldovan Street, RO-400003 Iași, Romania

^e Grigore T. Popa University of Medicine and Pharmacy, Department of Infectious Diseases, 16 Universității Street, RO-700115 Iași, Romania

^f Iuliu Hațieganu University of Medicine and Pharmacy, Faculty of Pharmacy, Department of Pharmaceutical Botany, 8 Victor Babeș Street, RO-400347 Cluj-Napoca, Romania

* Corresponding author: dana.muntean@umfcluj.ro



INTRODUCTION

In the field of pharmaceutical sciences, establishing a robust *In Vitro-In Vivo* Correlation (IVIVC) is pivotal for the development and regulatory approval of drug formulations and also for lifecycle management [1–5]. The continuous enhancement of drug development remains a key objective, with the industry committed to pioneering innovative approaches to achieve this goal. Within the increasing pressures to expedite product development timelines, it is imperative to foster integrated collaboration among scientists from diverse disciplines, including analytical chemistry, formulation science, clinical pharmacology, and other pharmaceutical fields. Such interdisciplinary teamwork is crucial to ensure the success of pharmaceutical products at every stage of development [2,6]. A critical tool is the establishment of IVIVC, a predictive model that bridges the gap between laboratory dissolution data and *in vivo* drug performance, offering a scientific basis for understanding drug behavior within the human body [7,8]. Both academia and the pharmaceutical industry, along with regulatory bodies, have concentrated efforts on utilizing IVIVC to address a variety of objectives [7–9]. IVIVC plays an important role in the development and post approval changes of a drug product [2,4,6] but also limiting the risk of *in vivo* failure [10].

In vitro release, typically illustrated through dissolution profiles in biorelevant or bio-predictive media, contrasts with *in vivo* release, which is primarily determined by pharmacokinetic studies measuring plasma drug concentration or the amount of drug absorbed [2,4,10]. Observed *in vivo* differences in the rate and extent of drug absorption between two pharmaceutically equivalent solid oral products may be attributed to variations in their *in vivo* dissolution profiles [11].

Over the years, IVIVC has seen significant evolution, driven by advances in analytical techniques and a deeper understanding of drug dissolution and absorption dynamics [2,10]. Originally applied to immediate release formulations, the scope of IVIVC has now expanded to include modified-release products, driven by advancements in dissolution testing methodologies and computational modelling [8].

Despite these advancements, the field of IVIVC faces several challenges, including variability in dissolution testing methods, inter-individual physiological differences, and the inherent complexities of modified-release formulations [3,7,9]. Most of the published studies still focus on early-stage applications rather than regulatory purposes, reflecting a gap in the adoption of advanced technologies [1–3,8,12].

The legislative framework for *In Vitro-In Vivo* Correlation (IVIVC) across Europe [13,14], USA [15], and Canada [16] is guided by a common scientific principle that seeks to establish a predictive mathematical model linking *in vitro*

drug release to *in vivo* pharmacokinetic responses [4,9]. While specific regulatory guidelines may vary, they all emphasize the importance of IVIVC in drug development and approval processes. This includes setting dissolution specifications, supporting bioequivalence studies, and facilitating drug product modifications post-approval [4,9,17]. The harmonization efforts by international regulatory bodies aim to streamline the IVIVC application across different jurisdictions, ensuring consistency and predictability in drug development and assessment [6].

In the United States, both innovator and generic drug companies employ IVIVC models in their regulatory submissions, particularly for oral extended-release (ER) drug products [7].

An IVIVC model should be applied strictly for interpolation within the data range used during its development, ensuring adherence to validated parameters and avoiding extrapolation beyond these bounds [13]. International regulatory guidelines provide comprehensive protocols for both internal and external validation of IVIVC models [18].

According to the United States Pharmacopeia (USP) and Food and Drug Administration (FDA) guidelines, IVIVC models are classified into three levels: A, B, and C, with Level A representing the highest standard of correlation. Level A IVIVC models establish a direct and point-to-point relationship between the *in vitro* dissolution and the *in vivo* input rates, providing the most comprehensive and predictive correlation. This high degree of correlation underscores the reliability and applicability of the IVIVC model in predicting *in vivo* drug behavior based on *in vitro* dissolution data. This level of correlation is particularly beneficial for obtaining biowaivers, which can expedite the drug approval process by reducing the need for extensive clinical trials. Biowaivers are often not granted for Level B, C, and multiple C correlations [3–7,15].

Regulatory authorities recommend IVIVC-based biowaivers for modified-release dosage forms, particularly those with extended release characteristics [2,15]. The Biopharmaceutics Classification System (BCS) is a scientific framework that classifies drug substances into four categories based on their aqueous solubility and intestinal permeability. BCS class I drugs exhibit high solubility and high permeability, while class II drugs have low solubility but high permeability. Class III drugs are highly soluble but poorly permeable, and class IV drugs are characterized by both low solubility and low permeability. This classification helps predict the rate-limiting step for drug absorption, either solubility/dissolution or permeability, and is instrumental in guiding regulatory decisions for *in vitro-in vivo* correlation (IVIVC) studies. For oral dosage forms, as emphasized by the FDA, it is feasible to correlate *in vitro* and *in vivo* data when the absorption of the drug substance is constrained by the dissolution

rate [15]. Consequently, establishing IVVC is more straightforward for BCS class II compounds and, in certain cases, BCS class III compounds, as well as extended-release (ER) formulations [3].

Pentoxifylline, chemically known as 3,7-dimethyl-1-(5-oxohexyl)-3,7-dihydro-1H-purine-2,6-dione or 1-(5-oxohexyl)-3,7-dimethylxanthin, is a methylxanthine derivative with significant therapeutic potential (Figure 1) [19]. This compound is characterized by its molecular formula $C_{13}H_{18}N_4O_3$ and a molecular weight of 278.3 g/mol [20,21].

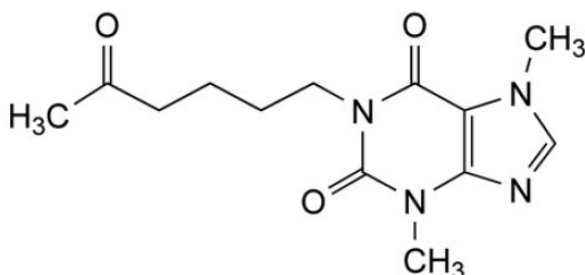


Figure 1. Chemical structure of pentoxifylline
(IUPAC name 3,7-Dimethyl-1-(5-oxohexyl) purine-2,6-dione)

Pentoxifylline, an anti-haemorrhagic medication utilized in the treatment of intermittent claudication but with much broader potential for protecting vascular health and optimising tissue perfusion [21], undergoes significant hepatic metabolism, resulting in a rapid decrease in therapeutic levels [18,22].

Following oral administration, pentoxifylline is well-absorbed, reaching peak plasma concentrations within an hour, although its bioavailability is subject to a non-linear, dose-dependent first-pass effect. Metabolized in the liver and erythrocytes, pentoxifylline and its active metabolites are primarily excreted *via* the urine, with a minor proportion eliminated through feces. These pharmacokinetic attributes underscore pentoxifylline's therapeutic potential and the necessity for precise formulation to optimize its clinical efficacy.

Classified under the BCS as a Class II compound, pentoxifylline is characterized by low solubility but high permeability, indicating that its absorption is predominantly solubility-limited [19].

IVVC plays a crucial role in the application of biowaivers, thereby expediting the drug approval process and reducing the necessity for human bioequivalence studies [11].

The primary objective of constructing an IVVC is to validate that the *in vitro* dissolution characteristics are predictive of the *in vivo* pharmacokinetic performance of the drug across various release rates [5]. This correlation is

crucial for ensuring that the predictive model remains reliable and robust, enabling the facilitation of manufacturing modifications without compromising the drug's therapeutic efficacy and safety [6,23]. The successful establishment of a Level A IVIVC thus provides a powerful tool for both regulatory assessment and the optimization of drug formulation development processes [6,10].

The development of Level A IVIVC typically involves multiple drug formulations exhibiting a range of dissolution rates, including slow, medium, and fast release profiles. These formulations undergo comprehensive *in vitro* dissolution testing to generate dissolution profiles, followed by *in vivo* pharmacokinetic studies to obtain plasma concentration profiles. Advanced deconvolution techniques are subsequently employed to accurately determine the *in vivo* absorption profiles from the plasma concentration data [4–6,15,23,24].

In this study, the focus is on the development of IVIVC model for Pentoxifylline modified-release tablets, using such a Level A IVIVC, by evaluating various dissolution media and considering physiological variables.

This research serves as an initial exploratory study, aiming not at the development of an industrial-scale IVIVC, but to serve as a support for subsequent, more comprehensive studies in this area. Accordingly, the *in vitro* experiments were conducted on two modified-release formulations of pentoxifylline, namely, the reference product Trental 400 mg modified-release tablets (R), Sanofi Aventis, France, and the prototype generic formulation Pentoxifylline 400 mg modified-release tablets (T) developed by Antibiotice SA, Iași, Romania.

RESULTS AND DISCUSSION

In vitro dissolution data analysis

The *in vitro* dissolution characteristics of two modified-release formulations of pentoxifylline were assessed through *in vitro* dissolution tests, in three distinct pH media: 1.2, 4.5, and 6.8. These pH conditions were carefully chosen to simulate the physiological conditions of the gastrointestinal (GI) tract: pH 1.2 represents the acidic gastric environment, pH 4.5 simulates the early intestinal transit, and pH 6.8 corresponds to the later stages of intestinal digestion [25].

The detailed methodology and sample preparation protocols are outlined in the experimental section. The percentage release of pentoxifylline was quantified, with results presented in Figure 2 as mean values \pm standard deviation (SD) of six replicates.

The results presented in Figure 2 demonstrate that the *in vitro* release of pentoxifylline from the generic modified-release product developed by Antibiotice SA and the reference product are independent of pH, as evidenced

by the almost superposable dissolution profiles across all three media. This pH independence represents a significant advantage, as the chosen dissolution media simulate a range of physiological and nutritional conditions encountered in the gastrointestinal (GI) tract. Specifically, pH 1.2 mimics the fasting state in the stomach (pH 1–3), while pH 4.5 simulates the fed state in the stomach (pH 4–6, depending on food composition). Lastly, pH 6.8 represents the pH of the small intestine, consisting in the duodenum (pH 5–6.5), jejunum (pH 6–7), and ileum (pH 7–8), as well as portions of the large intestine such as the cecum (pH 5.5–7) and colon (pH 6–7.5) [25]. This consistency in drug release across varying pH conditions ensures reliable drug performance regardless of the fed or fasting state, reflecting a stable release mechanism suitable for the diverse physiological environments of the GI tract. Such properties enhance the predictability of the modified-release formulation and align well with the criteria for robust IVIVC models.

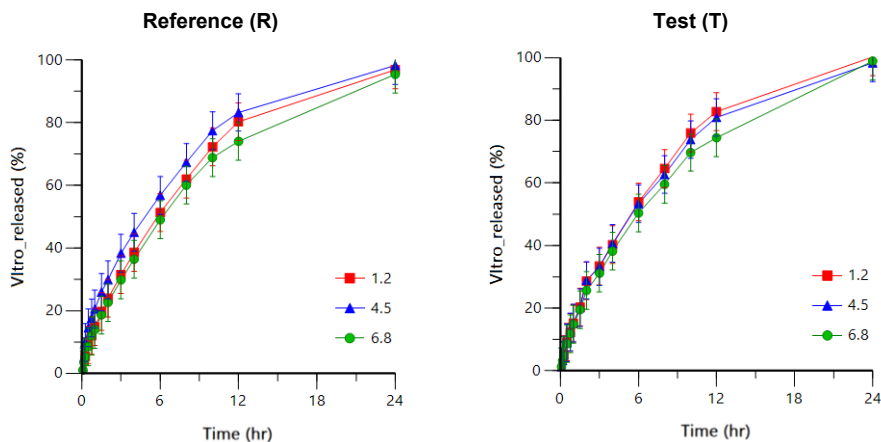


Figure 2. Dissolution profiles of pentoxifylline 400 mg modified-release tablets (Reference and Test) in three pH conditions (1.2, 4.5, and 6.8)

***In vivo* data**

The *in vivo* data used to establish the IVIVC for pentoxifylline were derived using mathematical deconvolution techniques. This method takes the known output function, represented by the mean plasma concentrations, to back-calculate the input function, which reflects the absorption kinetics of pentoxifylline [24]. As a result, the time-dependent relative fraction of pentoxifylline absorbed from the administration site was determined and is illustrated in Figure 3. The corresponding bioequivalence study was carried out at the Center for Drug Evaluation, Antibiotice SA, Iași, Romania.

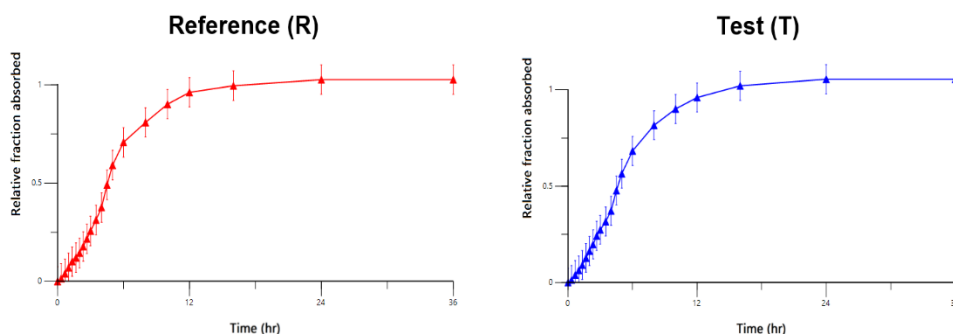


Figure 3. The relative fraction of pentoxifylline absorbed following the oral administration of a single 400 mg dose of the Reference and Test formulations under fed conditions of the *in vivo* clinical trial

In vitro – in vivo correlation

The *in vitro–in vivo* correlations (IVIVCs) were evaluated to establish a Level A correlation. Absorption profiles of Pentoxifylline 400 mg modified-release tablets were derived from individual plasma drug concentration *versus* time profiles obtained during bioequivalence study. These absorption profiles were assessed under fed conditions.

By correlating the percentage of *in vivo* absorbed pentoxifylline with the *in vitro* dissolution percentages, an IVIVC was established. The regression analysis, including slopes, intercepts, and determination coefficients for the IVIVCs, is detailed in Table 1.

The IVIVC plots from Figure 4 illustrate the relationship between *in vitro* dissolution and *in vivo* absorption of pentoxifylline 400 mg modified-release tablets under fed conditions of subjects enrolled in the clinical trial, evaluated using the deconvolution approach across three pH values for the dissolution media: 1.2, 4.5, and 6.8.

Table 1. *In vitro – in vivo* correlation results for pentoxifylline 400 mg modified-release tablets and statistical analysis of the correlations obtained for the clinical study under fed conditions

Dissolution media pH	IVIVC correlations					
	Reference (R)			Test (T)		
	Slope ¹	Intercept ²	Determination Coefficient (R ²)	Slope	Intercept	Determination Coefficient (R ²)
1.2	0.6491	12.52	0.9724	0.6703	13.83	0.9752
4.5	0.6260	19.24	0.9737	0.6442	14.47	0.9730
6.8	0.6126	11.98	0.9796	0.6046	13.47	0.9818

¹ Slope – expressed in $\Delta\%$ vitro released / $\Delta\%$ fraction absorbed; ² Intercept – expressed in % vitro released.

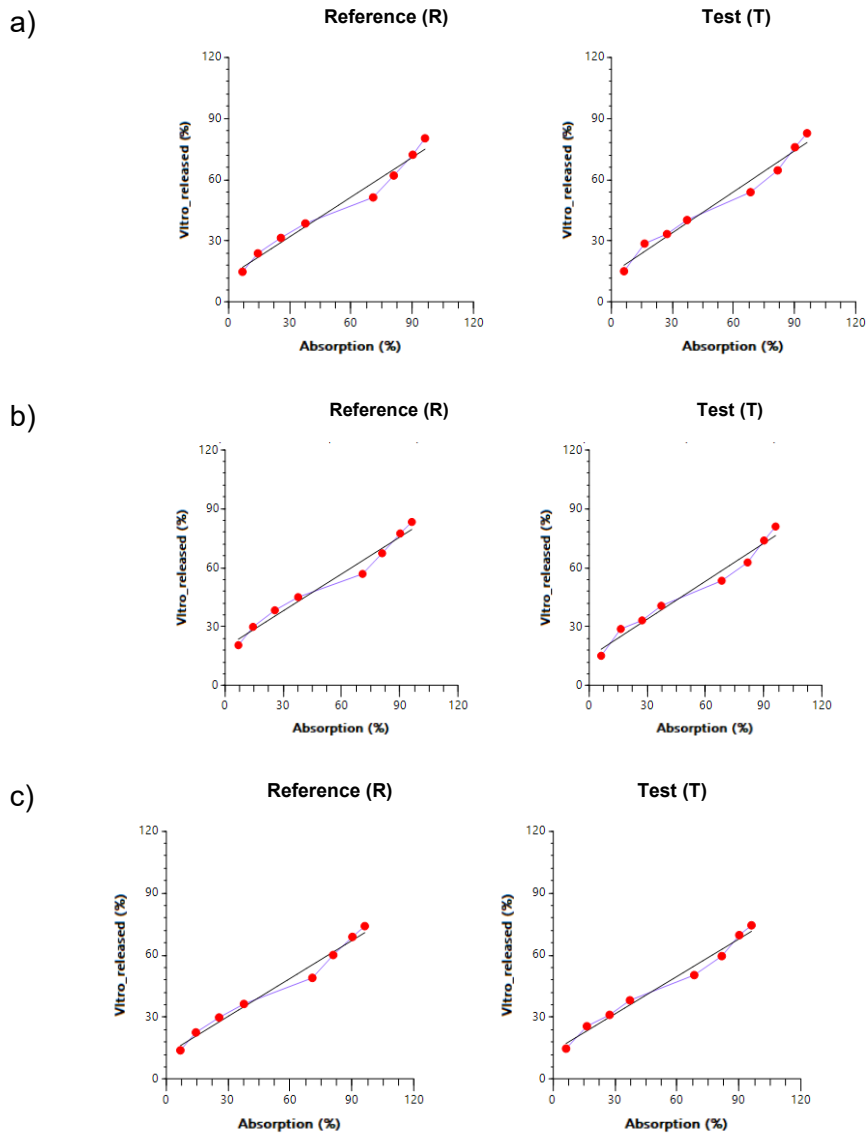


Figure 4. *In vitro* – *in vivo* correlation plots for pentoxifylline 400 mg modified-release tablets, generated using the deconvolution approach, at different pH levels of the dissolution media (1.2 [a], 4.5 [b], and 6.8 [c]) and under fed conditions of subjects in the clinical *in vivo* trial

The establishment of a robust IVIVC necessitates linking the pharmacokinetic profile of a drug substance with the formulation characteristics, ensuring that physiological factors do not limit drug absorption. According to the IVIVC guidelines, such correlations are particularly feasible for drugs classified under Biopharmaceutics Classification System (BCS) class II. Modified-release (MR) formulations are well-suited for IVIVC studies, as they can be designed to control drug release over an extended period, making pentoxifylline a reliable candidate for IVIVC development.

In this study, we evaluated the IVIVC of two formulations of pentoxifylline: the reference product Trental and the generic prototype of pentoxifylline 400 mg MR tablets. Data from a bioequivalence study conducted under fed conditions, alongside *in vitro* results in multiple dissolution media (at pH 1.2, 4.5, and 6.8), provides a comprehensive evaluation.

The tablet's design allows for the formation of a gel layer upon hydration, facilitating the slow release of pentoxifylline. Pentoxifylline MR tablets have demonstrated predictable and reproducible Active Pharmaceutical Ingredient (API) release, maintaining effective plasma concentrations over 24 hours with a single daily dose (400 mg), which supports a prolonged therapeutic effect.

The IVIVC was established by selecting eight common time points for both *in vivo* and *in vitro* studies (specifically 1, 2, 3, 4, 6, 8, 10 and 12 hours). The correlation, derived from data at selected time points, resulted in the establishment of six IVIVCs under fed conditions.

For an accurate IVIVC, the *in vivo* and *in vitro* profiles must exhibit similar shapes. The statistical evaluation of the IVIVC for Pentoxifylline 400 mg modified-release tablets revealed a high determination coefficient, consistently exceeding 0.97. This indicates a strong linear relationship between the *in vitro* dissolution profiles and the *in vivo* absorption data. The slope of the correlation was determined to be approximately 0.6, with intercept values ranging between 12 - 19.

The high determination coefficient, along with supportive slope and intercept values, validates the IVIVC model developed in this study. These results underscore the feasibility of using IVIVC as a reliable predictive tool for drug development and regulatory submissions, particularly for BCS class II compounds.

The findings align with current IVIVC guidelines, demonstrating that a Level A IVIVC is feasible for BCS class II drugs, characterized by low solubility and high permeability. According to these guidelines, a high determination coefficient (generally above 0.9) is essential to demonstrate the predictive power of the IVIVC. The slope and intercept values further support the robustness of the correlation, indicating that the dissolution characteristics of the modified-release formulation are effectively translated into *in vivo* absorption profiles [15].

A recent study by Taha et al (2024) was the only one identified in the scientific literature to investigate the IVIVC of pentoxifylline sustained-release (SR) formulations [18]. This study explored the role of different Flow-Through-Cell (FTC, USP IV) designs in predicting *in vivo* performance under fed and fasting conditions, proposing a closed-loop FTC system with a turbulent-flow pattern and gradient-buffer medium as the optimal setup for achieving a predictive IVIVC, with acceptable prediction error (PE%) values for pharmacokinetic parameters such as maximum plasma concentration (C_{max}) and area under the plasma concentration *versus* time curve (AUC) [18]. In contrast, our study focused on a more classical and regulatory-aligned approach to IVIVC development, using traditional dissolution testing in three pH media (1.2, 4.5, and 6.8) to simulate gastrointestinal conditions, alongside bioequivalence data obtained under fed conditions from an *in vivo* study conducted on healthy volunteers. This methodology enabled the successful establishment of six robust Level A IVIVC models with high determination coefficients ($R^2 > 0.97$), adhering to the standard requirements for biowaiver applications. In contrast to the aforementioned study, which used *in vivo* data sourced from the scientific literature, our study integrates *in vivo* data obtained in a clinical trial conducted in the same company that produced the generic formulation to be tested, ensuring better alignment with regulatory expectations.

Given that no previous studies have comprehensively evaluated IVIVCs for this drug molecule using classical approaches, our findings hold a very high degree of novelty and underscore the importance of this work in supporting the development of modified-release formulations for pentoxifylline.

Although these correlations were not intended for industrial scale-up, the promising preliminary results provide a strong foundation for further IVIVC development, potentially leading to a biowaiver application. This would reduce costs associated with additional studies required for post-approval changes, as the drug product could benefit from a biowaiver based on a Level A IVIVC, in accordance with regulatory guidelines.

CONCLUSIONS

The successful establishment of six Level A *In Vitro-In Vivo* Correlations (IVIVCs) for Pentoxifylline 400 mg modified-release tablets, with high determination coefficients ($R^2 > 0.97$), obtained from the point-to-point IVIVCs, signify a strong relationship between the *in vitro* dissolution data obtained in three pH media and *in vivo* absorption profiles. The robust IVIVC models presented here for both Reference product Trental 400 mg modified-release

tablets and for the prototype generic developed Pentoxifylline 400 mg modified-release tablets highlight the importance of controlled release formulations in achieving consistent therapeutic outcomes and underscores the utility of IVIVCs in regulatory submissions. Overall, this work contributes to the growing body of evidence supporting the use of IVIVC in drug development, particularly for modified-release formulations. It highlights the potential for IVIVCs to improve the efficiency and cost-effectiveness of bringing new pharmaceutical products to market, ultimately benefiting both industry and patients. This approach allows for the improvement of methodologies and accumulation of data critical for future IVIVC development efforts.

EXPERIMENTAL SECTION

In vitro studies

Dissolution studies were performed on 400 mg Reference and Test pentoxifylline modified-release tablets (EvoluPharm, Auneuil, France). The dissolution tests were carried out in a rotating paddle apparatus (USP Apparatus II) from Pharma Test (type PTWS 120s, Hainburg, Germany) at $37\pm 0.5^\circ\text{C}$ and rotational speed of 50 rpm, using 900 mL of various dissolution media (media pH 1.2, 4.5 and 6.8).

A high-performance liquid chromatography (HPLC) method with UV detection was employed to identify and quantify pentoxifylline in samples obtained during the dissolution test. The analysis was performed using a Zorbax C18 column (100 mm x 3.0 mm i.d., 3.5 μm particle size) under the following conditions: the mobile phase consisted of 25% acetonitrile (ACN) and 75% 0.1% phosphoric acid (H_3PO_4); the column temperature was maintained at 25°C ; the flow rate was set at 1 mL/min; the injection volume was 1 μL ; detection was carried out at a wavelength of 274 nm. Under these conditions, pentoxifylline had a retention time of 1.1 minutes, with the total analysis completed within 2 minutes per sample.

The dissolution media for the *in vitro* studies were prepared using the following protocols:

- pH 1.2 Hydrochloric Acid Solution: A 0.1 N hydrochloric acid solution was prepared by dissolving 9.9 g of 37% HCl in distilled water. The solution volume was adjusted to 1 L, achieving a pH of 1.2.
- pH 4.5 Acetate Buffer Solution: To prepare the buffer, 3 g of sodium acetate trihydrate was dissolved in distilled water, followed by the addition of 14 mL of 2N acetic acid. The final volume was adjusted to 1 L with distilled water, resulting in a buffer with a pH of 4.5.

- pH 6.8 Phosphate Buffer Solution: A phosphate buffer was prepared by dissolving 6.81 g of potassium dihydrogen phosphate and 0.9 g of sodium hydroxide in distilled water. The solution volume was adjusted to 1 L to achieve a pH of 6.8.

The dissolution media were prepared by thoroughly mixing the reagents until fully dissolved, and the final pH was confirmed using a calibrated pH meter to ensure consistency and accuracy during the dissolution tests. All reagents used in the preparation of the dissolution buffer were of United States Pharmacopoeia (USP) grade.

Samples (100 μ L each) were collected at specific intervals: before tablet release into the dissolution media (time 0), and subsequently at 0.25, 0.5, 0.75, 1, 1.5, 2, 3, 4, 6, 8, 10, 12, and 24 hours. The collected samples were filtered and analyzed for pentoxifylline content using an HPLC-UV method, as previously described.

In vivo data

The clinical study data, detailing plasma concentration versus time profiles, were obtained from a pilot bioequivalence study in which the test formulation was pentoxifylline 400 mg modified released tablets (developed by Antibiotice SA, Iași, Romania) and the reference drug was Trental® 400 mg modified release tablets (Sanofi-Aventis, Paris, France). The study was performed under fed conditions at the Centre for Drug Evaluation, Antibiotice SA, Iași, Romania. The study strictly adhered to all applicable European Union (EU) and International Council for Harmonization of Technical Requirements for Pharmaceuticals for Human Use (ICH) requirements and Ethical standards. The study protocol was approved by the National Ethics Committee, Romania, and by the National Agency for Medicines and Medical Devices, Romania.

Study subjects: Twenty-nine healthy male and female Caucasian subjects were screened and included in the study. All relevant study aspects were discussed with each volunteer, and written informed consent was provided by each participant prior to the commencement of the study. The study protocol clearly defined the inclusion and exclusion criteria. Only healthy volunteers who met the established criteria were selected by the investigator based on their medical history, physical examination, and clinical laboratory tests. These tests included haematology, clinical chemistry, urine analysis, urine drug screening, and pregnancy tests for female subjects. All participants were Caucasian adults aged 18 to 50 years, non-smokers or light smokers, with a body mass index (BMI) between 18.5 and 30 kg/m².

Drug products: All subjects received a single oral dose of 400 mg pentoxifylline, either test or reference drug, in accordance with the randomization scheme.

Study design: The study was designed as a pilot, single-center, open-label, analytically blind, randomized, single-dose, crossover study, with a wash-out period of 6 days between treatments.

At each treatment period, subjects were confined from at least 10 hours before dosing until after 24.0 hours post – dose. Follow-up ambulatory visits were scheduled for 36 hours post-dose.

The drug administration followed a standard high – fat high – calorie breakfast 30 minutes before drug administration and standardized meals at 4.0, 9.0, and 13.0 hours after drug administration. Liquid consumption was restricted from 1 hour before until 1 hour after drug administration, except 200 mL non – sparkling water for drug administration.

Blood plasma samples collection: Venous blood samples (6 mL each) were collected prior to drug administration (at 0 hours) and at predetermined time points post-dose, including 0.33, 0.67, 1.0, 1.33, 1.67, 2.0, 2.33, 2.67, 3.0, 3.5, 4.0, 4.5, 5.0, 6.0, 8.0, 10.0, 12.0, 16.0, 24.0 and 36.0 hours. The collected samples were rapidly frozen until analysis at a temperature of $(-25^{\circ}\text{C}) \pm 5^{\circ}\text{C}$.

Bioanalytical methodology: Quantification of the drug substance was performed using a high-throughput liquid chromatography-tandem mass spectrometry (LC/MS/MS) method, with pentoxifylline d5 serving as the internal standard. Calibration curves demonstrated linearity within the concentration range of 5–500 ng/mL.

Statistical analysis: Data analysis was conducted using Phoenix WinNonlin® software, version 8.4 (Certara, PA, USA). The results obtained for the Reference and Test products were utilized to develop the IVIVC models.

In vitro – in vivo correlations (IVIVCs)

The numerical deconvolution method was employed to evaluate the level of correlation. This approach involved deriving the absorption profile from *in vivo* data collected during clinical study. Subsequently, the percentage of the drug absorbed *in vivo* was plotted against the percentage dissolved in *in vitro* tests. The analysis and calculations were conducted using Phoenix WinNonlin® version 8.4 software (Certara, PA, USA), facilitating the estimation of drug absorption kinetics.

ACKNOWLEDGMENTS

This research study was supported by Antibiotice SA, Romania. Maria Codreanu, Diana Iacob, and Maria Ioana Onofrei were employees of the Antibiotice SA, Romania during the conduct of this study. Ana-Maria Vlase, Dana Maria Muntean, and Laurian Vlase are full-time employees of the University of Medicine and Pharmacy "Iuliu Hatieganu", Cluj-Napoca, Romania. All authors declare there is no conflict of interest.

REFERENCES

1. N. Alimpertis; A. Simitopoulos; A.A. Tsekouras; P. Macheras; *Pharm. Res.*, **2024**, *41*, 235–246.
2. M.G. Davanço; D.R. Campos; P.D.O. Carvalho; *Int J Pharm*, **2020**, *580*, 119210.
3. P.K. Tuszyński; J. Szlęk; S. Polak; R. Jachowicz; A. Mendyk; *Dissolution. Technol.*, **2018**, 20-24.
4. S. Jacob; A.B. Nair; *Drug Development Research*, **2018**, *79*, 97–110.
5. Y. Qiu; J.Z. Duan; *Pharmaceutical Theory and Practice*, 2nd ed.; *Academic Press*, Amsterdam, **2017**, chapter 16.
6. A. Fortuna; *J. Bioequiv. Availab.*, **2011**, *S3*, 1-12.
7. P. Kaur, X. Jiang, J. Duan, E. Stier.; *AAPS J*, **2015**, *17*, 1035–1039.
8. S. Suarez-Sharp, M. Li, J. Duan, H. Shah, P. Seo; *AAPS J*, **2016**, *18*, 1379–1390.
9. I. González-García, V. Mangas-Sanjuán, M. Merino-Sanjuán, M. Bermejo; *Drug Dev. Ind. Pharm.*, **2015**, 1-13.
10. J.M. Cardot, J.C. Lukas, P. Muniz; *AAPS J*, **2018**, *20*, 95.
11. U.S. Department of Health and Human Services, Food and Drug Administration, Center for Drug Evaluation and Research. Guidance for Industry. Waiver of In Vivo Bioavailability and Bioequivalence Studies for Immediate-Release Solid Oral Dosage Forms Based on a Biopharmaceutics Classification System, **2017** [cited 2024 Oct. 12]. Available at: <https://digi repo.nlm.nih.gov/master/borndig/101720038/UCM070246.pdf>
12. U.S. Department of Health and Human Services, Food and Drug Administration, Center for Drug Evaluation and Research. Draft Guidance, The Use of Physiologically Based Pharmacokinetic Analyses Biopharmaceutics Applications for Oral Drug Product Development, Manufacturing Changes, and Controls Guidance for Industry [cited 2024 Oct. 12]. Available at: <https://www.fda.gov/media/142500/download>
13. European Medicines Agency, Committee for Medicinal Products for Human Use (CHMP), Guideline on quality of oral modified-release products, **2014** [cited 2024 Oct. 12]. Available from: https://www.ema.europa.eu/en/documents/scientific-guideline/guideline-quality-oral-modified-release-products_en.pdf

14. European Medicines Agency, Committee for Medicinal Products for Human Use (CHMP), Guideline on the pharmacokinetic and clinical evaluation of modified-release dosage forms, **2014** [cited 2024 Oct. 12]. Available from: https://www.ema.europa.eu/en/documents/scientific-guideline/guideline-pharmacokinetic-and-clinical-evaluation-modified-release-dosage-forms_en.pdf
15. U.S. Department of Health and Human Services, Food and Drug Administration, Centre for Drug Evaluation and Research. Guidance for Industry. Extended-Release Oral Dosage Forms: Development, Evaluation, and Application of In Vitro/In Vivo Correlations, **1997** [cited 2024 Oct. 12]. Available at: <https://www.fda.gov/media/70939/download>
16. Health Canada. Guidance Document: Quality (Chemistry and Manufacturing) Guidance: New Drug Submissions (NDSs) and Abbreviated New Drug Submissions (ANDSs). **2017** [cited 2024 Oct. 12]. Available from: <https://www.canada.ca/en/health-canada/services/drugs-health-products/drug-products/applications-submissions/guidance-documents/chemical-entity-products-quality/guidance-document-quality-chemistry-manufacturing-guidance-new-drug-submissions-ndss-abbreviated-new-drug-submissions.html>
17. U.S. Department of Health and Human Services, Food and Drug Administration, Center for Drug Evaluation and Research. Guidance for Industry: SUPAC-MR: Modified-release Solid Oral Dosage Forms Scale-Up and Postapproval Changes: Chemistry, Manufacturing, and Controls; In Vitro Dissolution Testing and In Vivo Bioequivalence Documentation. **1997** [cited 2024 Oct. 12]. Available from: <https://www.fda.gov/regulatory-information/search-fda-guidance-documents/supac-mr-modified-release-solid-oral-dosage-forms-scale-and-postapproval-changes-chemistry>
18. N.F. Taha, L.H. Emara; *AAPS Pharm. Sci. Tech.*, **2024**, *25*, 243.
19. A.R. Pawar, N.A. Shete, P.V. Jadhav, V.K. Deshmukh, J.S. Mehetre; *Pharmaceut. Fronts*, **2021**, *3*, e200-e207.
20. European Directorate for the Quality of Medicines & HealthCare, European Pharmacopoeia, Pentoxifylline monograph 0851, *Ph. Eur. 11th ed.*, **2020**.
21. M.F. McCarty, J.H. O'Keefe, J.J. DiNicolantonio; *Open Heart*, **2016**, *3*, e000365.
22. A.M. Shailendrakumar, V.M. Ghatge, M. Kinra, S.A. Lewis; *AAPS Pharm. Sci. Tech.*, **2020**, *21*, 118.
23. D.I. Pop, A. Marcovici, M. Oroian, A.M. Gheldiu, L. Vlase; *Studia UBB Chemia*, **2019**, *64*, 217-229.
24. Certara. IVIVC Toolkit™ User's Guide Applies to: IVIVC Toolkit 8.3 for Phoenix WinNonlin® Phoenix WinNonlin 8.3 reference manual user. **2020** [cited 2024 Oct. 12]. Available from: https://onlinehelp.certara.com/phoenix/8.3/responsive_html5_!MasterPage!/IVIVC%20Toolkit%20User%27s%20Guide.pdf
25. J. Fallinborg; *Dan Med Bull*, **1999**, *46*(3), 183-196.